Transition Metal Fluorides as Lithium Ion Cathodes

Understanding Battery Mechanisms and Performance using Monodisperse Nanocrystal Samples

Albert W. Xiao
St. Catherine's College
University of Oxford

A thesis submitted for the degree of
Doctor of Philosophy
Hilary 2020

Abstract

More energy dense lithium ion batteries are essential for the production of long-range electric vehicles and all-electric aircraft. These next generation batteries will require high capacity cathode materials that move beyond the lithium intercalation chemistry of current electrodes. On paper, transition metal fluorides are among the most promising cathode materials, combining high electrode potentials (2.6 V to 3.5 V vs. Li^+/Li) with three to six times the theoretical capacity of conventional cathode materials. However, their commercial application has been hindered by their inability to cycle in a truly energy dense format (i.e. at high active material concentration) and ultimately the inadequate understanding of their electrochemical capabilities and limitations. Both of these issues have been largely resolved as a result of this DPhil project. First I design a materials system that is practically ideal for reversible high-capacity cycling as well as detailed mechanistic study. This is achieved through the development of a new colloidal synthesis method for single-crystalline, monodisperse transition metal fluoride (FeF_2, CoF_2) nanorods. Size and shape control are demonstrated, and a chemical reaction pathway and nucleation and growth mechanism are proposed. Next I present an ionic liquid electrolyte (1 molal lithium bis(fluorosulfonyl)imide in N-methyl-N-propylpyrrolidinium bis(fluorosulfonyl)imide) that forms a stable solid electrolyte interphase, prevents the fusing of particles, and consequently precludes the major failure mechanisms associated with transition metal fluoride cathodes. The use of this electrolyte with the iron(II) fluoride (FeF_2) nanorod system results in near theoretical capacity (570 mA h g^{-1}) on discharge and charge, with extraordinarily stable cycling (>90% capacity retention after 100 cycles). This stability is maintained for over 200 cycles at relatively high cycling rates (C/2) and temperatures (50 °C). By combining the unique vantage point afforded by this novel materials system with the morphology preserving qualities of our new electrolyte, I am further able to characterize the discharge/charge mechanism with an unprecedented level of detail. High-resolution analytical transmission electron microscopy reveals intricate morphological features, lattice orientation relationships, and oxidation state changes that that provide a new and comprehensive understanding of the discharge/charge (conversion) reaction mechanism. This new mechanistic understanding defines the structural and chemical origins of reversible cycling and cell failure in transition metal fluorides and unearths new concepts such as an inherently high discharge rate capability in FeF_2.

Some principal results of this work have been published in the following article:[1]

Xiao, A. W. et al. Understanding the conversion mechanism and performance of monodisperse FeF_2 nanocrystal cathodes. *Nature Materials* **19**, 644–654 (2020).

doi:10.1038/s41563-020-0621-z

To my wonderful family for their unwavering love and support.

Declaration

I certify that the work presented in this thesis is the result of my own original research and, unless otherwise stated, is written and produced entirely by myself.

Acknowledgements

I am beyond grateful for those who have helped to teach, guide, and support me through the course of my doctoral study. The success of this project would never have been possible without the scientific contributions of my professors, lab-mates, and collaborators nor the moral support of my friends and loved ones. I would first like to thank my DPhil supervisor professor Mauro Pasta for welcoming me into his research group, constantly pushing me to improve my science and the quality of my work, and inspiring me to expect more from myself. I would also like to thank all my fellow Pasta Group members—Sam-Wheeler, Isaac Capone, Jack Fawdon, Kevin Hurlbutt, and the young ones—for putting up with my terrible jokes, helping me with my experiments, and making my time in and out of the lab a genuine joy. The postdocs, Hyeon Jeong Lee and Zack Brown, have made an invaluable contribution to this work as well. I am grateful to my collaborators; Alex Robertson, Hyun-Wook Lee, and Tae-Ung Wi for their assistance in the collection and interpretation of HR(TEM)/STEM/EELS data. The research presented in this thesis was made possible by financial support from the John Fell Oxford University Press Research Fund and the Henry Royce Institute (through UK Engineering and Physical Science Research Council grant EP/R010145/1). Many thanks to the David Cockayne Center for Electron Microscopy for indispensable training and the use of their electron microscopes.

Finally, I must thank the members of my PhD support group (A.N.B.D.)—in particular Pablo Quijano Velasco, Dominique Piche, Jesus Antonio Acapulco Jr., Pierre Romain, and Eoin O'Sullivan—for making my journey in Oxford truly unforgettable, despite the number of brain cells I will never get back. Yumiko Ito, thank you for being my greatest motivation in writing this thesis and completing this PhD. Most of all, however, I thank my family—my Mom Iris, my Dad Jian, my stepdad Joe, Anny (the best older sister in the world), and my little siblings Jason and Jessica—for their overwhelming love and support throughout my life and especially in these last four years.

Contents

Abstract i

Dedication iii

Declaration v

Acknowledgements vii

1 Introduction 1
- 1.1 Transition Metal Fluorides in Lithium Ion Batteries . . . 1
- 1.2 Synthetic Methods for Metal Fluoride Nanoparticles . . . 7
- 1.3 Performance of Transition Metal Fluoride Cathodes . . . 14
- 1.4 The Conversion Mechanism in Metal Fluorides . . . 20

2 Synthesis 29
- 2.1 Colloidal Synthesis of Metal Fluoride Nanocrystals . . . 29
- 2.2 Single Source Precursors for Colloidal Synthesis . . . 32
- 2.3 Mechanism of Metal Fluoride Formation . . . 35
  - 2.3.1 Nanorod Structure and Composition . . . 39
- 2.4 Nucleation and Growth of FeF_2 Nanorods . . . 41
- 2.5 Size and Shape Control . . . 44
- 2.6 Ligand Exchange Techniques . . . 47
- 2.7 Alternative Precursors and Other Transition Metal Fluorides . . . 49

3 Electrochemical Performance 55
- 3.1 Electrochemistry Of Transition Metal Fluorides . . . 55
- 3.2 Electrode Preparation . . . 60
  - 3.2.1 Mixing Methods . . . 61
  - 3.2.2 Effects of Calendaring . . . 63
- 3.3 Failure Mechanisms . . . 65
  - 3.3.1 Cathode Dissolution . . . 66
  - 3.3.2 Electrolyte Decomposition . . . 69
  - 3.3.3 In-Situ TEM Technique and Limitations . . . 72
  - 3.3.4 Particle Fusing . . . 74
- 3.4 Ionic Liquid Electrolytes . . . 76
  - 3.4.1 SEI Composition and Stability . . . 79
  - 3.4.2 Morphology Preservation . . . 85
- 3.5 Differential Rate Capability on Charge and Discharge . . . 86
- 3.6 High Temperature Performance . . . 87

4 The Conversion Mechanism **89**
4.1 *Ex-Situ* Mechanistic Characterization 89
4.1.1 *Ex-Situ* XRD 90
4.1.2 Interpretation of TEM Data 92
4.1.3 FeF_2 Nanorod Structure and Morphology 96
4.2 Surface Reactions 99
4.3 Pseudo-Intercalation and the Activation Overpotential 103
4.4 Phase-Equilibria and Reaction Symmetry 105
4.5 Lattice Orientation Relationships 112
4.5.1 The Invariant Fluoride Lattice 112
4.5.2 Iron Particle Nucleation 115
4.5.3 Long Term Phase Evolution 120
4.6 Performance Implications 122

5 Conclusions **125**
5.1 Key Findings 125
5.2 Implications for the Field 127
5.3 Future Work 128

Appendix I: Methods **139**

List of Figures

1.1 The Lithium Ion Battery . . . 3
1.2 The Path to Higher Energy Densities . . . 4
1.3 Energy Densities of Cathode Materials . . . 5
1.4 Periodic Trends and Electrode properties . . . 8
1.5 Ionic Liquids for Metal Fluoride Synthesis . . . 13
1.6 Failure Mechanims in Transition Metal Fluoride Cathodes . . . 17
1.7 The Conversion Mechanism in Literature . . . 21
1.8 *In-situ* TEM Lithiation techniques . . . 23
1.9 *In-Situ* TEM lithiation of FeF_2 Nanorods . . . 24

2.1 Monodisperse FeF_2 Nanorods . . . 29
2.2 Transition Metal Trifluoroacetate Precursors . . . 34
2.3 FeF_2 Nanorods from Different Perspectives . . . 35
2.4 FeF_2 Nanorod Surface Chemistry . . . 36
2.5 Iron Oxide Formation . . . 37
2.6 Chemical Pathway of FeF_2 Formation . . . 38
2.7 Pristine Nanorod Crystal Structure . . . 39
2.8 Elemental Composition . . . 40
2.9 Supercrystallinity . . . 41
2.10 Nucleation and Growth . . . 43
2.11 Convergent Growth of Disparate FeF_2 nuclei. . . . 45
2.12 Size and Shape Control . . . 46
2.13 Polydisperse Nanorods . . . 47
2.14 Thermal Annealing . . . 48
2.15 Ligand Exchange . . . 49
2.16 Comparison of Precursor Structures . . . 49
2.17 CoF_2 Nanorods (TFA Precursor . . . 50
2.18 CoF_2 Nanorods (HFAC Precursor) . . . 51
2.19 NiF_2 Synthesis . . . 52
2.20 CuF_2 Synthesis . . . 53

3.1 Coin Cell Configuration . . . 57
3.2 Overpotentials and Reaction Hysteresis . . . 59
3.3 Structure of the Electrode Composite . . . 60
3.4 Mixing by Co-Dispersion . . . 61
3.5 Effect of Mixing Method of Electrode Structure . . . 62
3.6 The Effect of Densification . . . 64
3.7 Electrode Performance in Conventional Electrolytes . . . 65
3.8 Conventional LIB Electrolytes . . . 66
3.9 Iron Dissolution on Charge . . . 67

3.10 Iron Dissolution . . . 68
3.11 Electrolyte Stability on Cycling . . . 70
3.12 Uncontrolled SEI Growth . . . 71
3.13 The *In-Situ* TEM Lithiation Technique . . . 73
3.14 Particle Fusing . . . 74
3.15 Particle Fusing *In-Situ* . . . 75
3.16 The Ionic Liquid Electrolyte . . . 76
3.17 Superior Cycling Stability . . . 77
3.18 Effect of Electrolyte on Overpotentials . . . 78
3.19 IL Electrolyte Stability at Increased Cycling Rate . . . 79
3.20 Chemistry of the Uncycled Electrode Surface . . . 81
3.21 LP30 Derived SEI . . . 82
3.22 IL Derived SEI . . . 82
3.23 Chemical Composition of SEI Layers . . . 83
3.24 SEI Formation and Evolution in the IL Electrolyte . . . 84
3.25 Preservation of Nanorod Morphology . . . 85
3.26 High Discharge Rate Capability . . . 86
3.27 High Temperature Cycling Stability . . . 88

4.1 *Ex-Situ* Data Points . . . 89
4.2 Conventional Characterization by XRD . . . 90
4.3 Structural Data from HRTEM . . . 93
4.4 EELS Analysis . . . 94
4.5 L_3/L_2 Quantification . . . 95
4.6 FeF_2 Nanorod Crystal Structure and Lattice Orientation . . . 96
4.7 The Complete Conversion Reaction . . . 98
4.8 Stage 1—Discharge . . . 99
4.9 Formation of the Double-Layered Shell . . . 101
4.10 Crystal Structure of the Double-Layered Shell . . . 102
4.11 Stage 2—Discharge . . . 103
4.12 Discharge Disproportionation and Fe^{3+} Formation . . . 104
4.13 Stage 3a—Discharge . . . 106
4.14 Stage 3b—Discharge . . . 107
4.15 The Converted and Unconverted Regimes . . . 108
4.16 Stage 5—Charge . . . 109
4.17 Stage 6—Charge . . . 110
4.18 Oxidation to Fe^{3+} . . . 111
4.19 The Fluoride Anion Lattice . . . 113
4.20 Fully Coherent Fluoride Phases . . . 113
4.21 Stage 7—Fully Charged . . . 114
4.22 Nucleation of Metallic Iron . . . 116
4.23 Stage 4—Fully Discharged . . . 117
4.24 Lattice Matching at the Fe|LiF Interface . . . 118
4.25 Semicoherent Fe|LiF Interfaces . . . 119
4.26 Nanorod Morphology After 50 Cycles . . . 120
4.27 Structural Evolution in IL Electrolyte . . . 121
4.28 Structural Evolution in LP30 Electrolyte . . . 122

5.1 The New Conversion Mechanism . . . 126
5.2 Results and Next Steps . . . 128

Chapter 1

Introduction

1.1 Transition Metal Fluorides in Lithium Ion Batteries

In 1991 Sony released the CCD-TR1 8 mm camcorder, forever changing the world of amateur home videos with its portable lightweight design. Some, however, would argue that the battery within this camcorder has made an even larger impact on our lives. This so-called lithium-ion battery (LIB) exhibited nearly twice the energy density of the technologies that preceded it. Lithium ion batteries replaced legacy alkaline or acidic aqueous electrolytes with organic electrolytes employing reductively stable lithium ions as charge carriers; these stable electrolytes opened the door or rather the [electrochemical stability] window for the use of anode/cathode pairs with a much larger cell voltage. In a feat of (Nobel Prize worthy) materials engineering, the originators of the field combined two stable materials with interstitial space for lithium storage (graphite and $LiCoO_2$) into a redox pair of electrodes with immense potential (4 V when charged). Nearly 30 years of optimization later, and lithium-ion batteries (LIBs) have become the industry standard for electrical energy storage (170 $W\,h\,kg^{-1}$ to 200 $W\,h\,kg^{-1}$); however, the electrode materials underpinning this technology have hardly changed at all.[2]

While LIBs have seen commercial success in far more than just camcorders, higher energy densities are required to match the ever-increasing performance of consumer electronics and are particularly crucial for reducing the environmental impact of transporation through the development of next generation electric vehicles.[2] For example, benchmark specific energy values of 500 $W\,h\,kg^{-1}$ and 800 $W\,h\,kg^{-1}$ are required to in-

crease the driving range of electric vehicles and spur the development of all-electric aircraft respectively.[2,3]

Like all batteries, LIBs extract energy from the chemical potential change of electrons as they move from an electropositive material (anode) to an electronegative one (cathode) through an external circuit (Figure 1.1). Within the battery, the concomitant diffusion of lithium ions out of the anode, through the electrolyte, and into the cathode, maintains charge neutrality. Likewise, LIBs can store electrical energy as chemical potential if an external voltage is applied to reverse this reaction, moving electrons and lithium ions from cathode to anode. The energy density of LIBs is fundamentally a function of how much charge these electrodes can store (specific capacity) and the potential difference or "cell potential" between the oxidized cathode (high potential) and the reduced anode (low potential). The theoretical specific capacity of an electrode material is the amount of charge transferred per unit mass undergoing a complete stoichiometric (half)reaction, and can be calculated from molar values using equation 1.1.

$$
\begin{gathered}
Q_{theoretical} = \frac{n_{stoich} F}{3.6 * M} \\
n_{stoich} = \#\ of\ electrons\ in\ the\ stoichiometric\ reaction \\
F = Faraday's\ Constant\ (96\,485.3\,C\,mol^{-1}) \\
M = molecular\ weight\ of\ active\ material(s)\ (g\,mol^{-1}) \\
factor\ of\ 3.6\ is\ applied\ to\ give\ values\ in\ mA\,h\,g^{-1}
\end{gathered}
\tag{1.1}
$$

Equilbrium cell potentials can be calculated from the standard reduction potentials of the cathode and anode species (equation 1.2).

$$
E^{\circ}_{Cell} = E^{\circ}_{cathode} - E^{\circ}_{anode} \tag{1.2}
$$

The product of these two values gives the theoretical specific energy or gravimetric energy density of the electrode pair (equation 1.3).

$$
U = E^{\circ}_{Cell} \times Q^{cathode+anode}_{theoretical} \tag{1.3}
$$

Conventional intercalation based electrodes (such as graphite and $LiCoO_2$) store

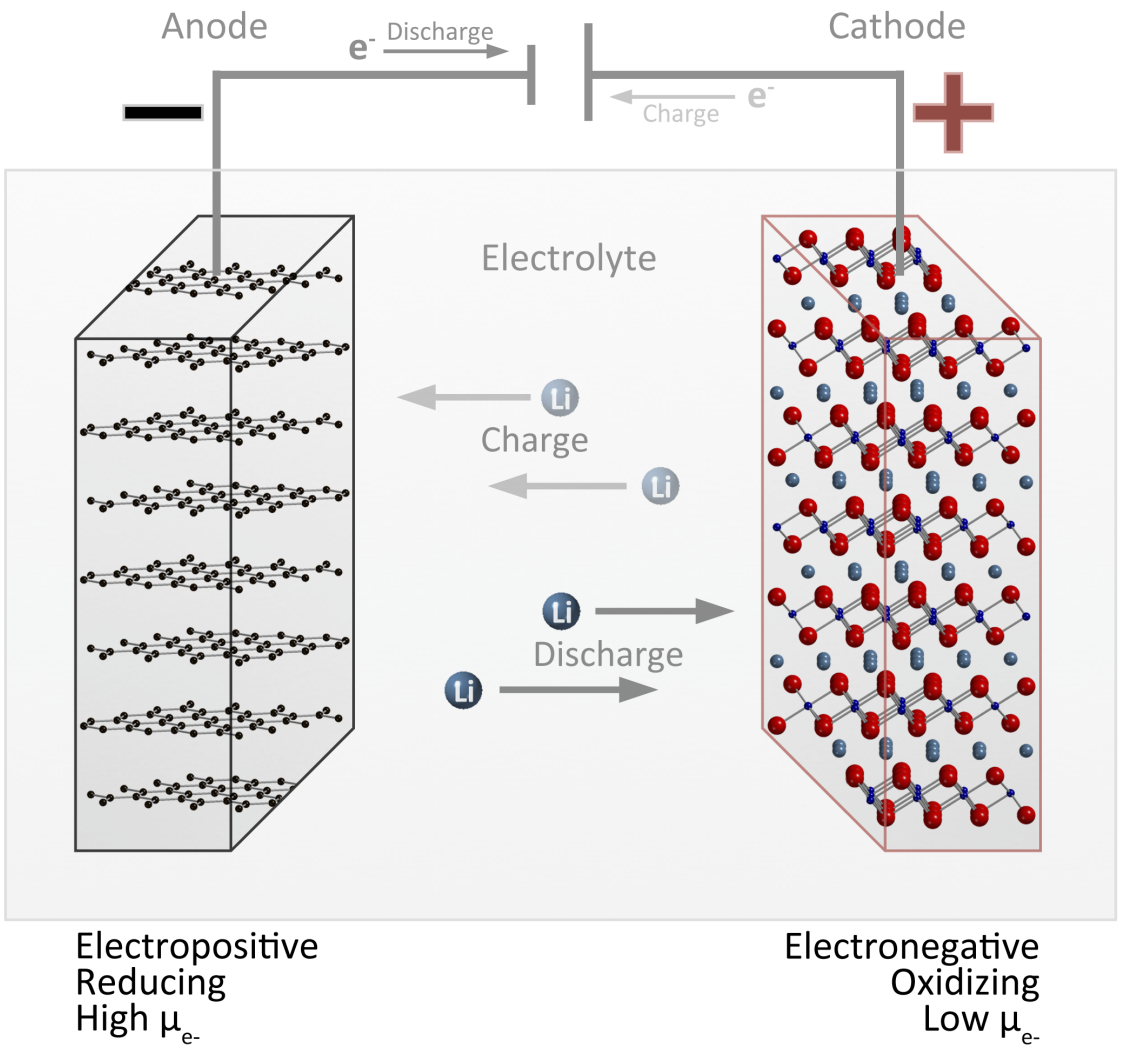


Figure 1.1: The Lithium Ion Battery. This schematic illustrates the working principle of a conventional lithium ion battery composed of the prototypical graphite anode and lithium cobalt oxide ($LiCoO_2$) cathode. Electrons flow spontaneously from anode to cathode on discharge. This flow can be reversed by an applied electric field to charge the battery.

lithium at a fraction of interstitial sites within a stable host lattice, and their charge storage capacities are thus intrinsically limited by their crystal structures.[4] A reactive host structure – where every molecule of active material reacts reversibly with Li^+ – is required to reach a higher level of energy density (Figure 1.2). Anodes based on the plating/stripping of Li metal or the alloying of Li with Si promise gravimetric capacities nearly ten times greater than that of conventional graphite anodes and are expected to predominate next generation LIBs.[5] However, to effectively utilize these anodes, higher capacity cathodes must also be achieved. Conversion electrodes are materials of the type MX_y (M = transition metal, X = O, S, N, P, F) that store lithium (Li^+) via a reversible reaction to form reduced metallic

nanoparticles contained within a matrix of a binary lithium compound (Figure 1.2).[6–10]. Depending on the metal oxidation state, conversion materials can store multiple Li^+ per metal center, yielding nearly three to six-fold increases in theoretical capacity.[6,8,11]

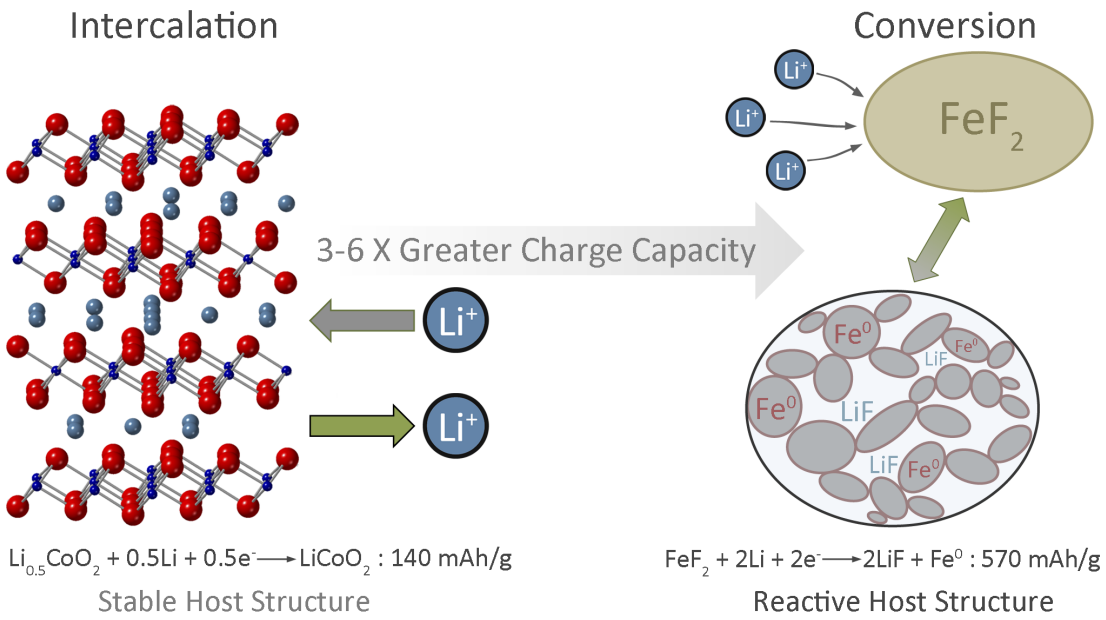


Figure 1.2: The Path to Higher Energy Densities. Any significant improvement on the energy density of current lithium ion batteries will necessarily involve a paradigm shift away from the conventional intercalation based materials. The high energy density of conversion based cathode materials stems from the sheer amount of charge transferred in the reaction of each transition metal atom.

Transition metal fluorides are unique among conversion compounds as the only materials with electrode potentials high enough to be practically viable cathodes. For example, oxides and sulfides are reduced at roughly 1 V lower than fluorides of the same transition metal (Figure 1.3). This translates to an approximately 30-40% loss in theoretical energy density, which is directly proportional to cell potential. This distinction arises from the ionic character of the metal-fluorine bond, which removes valence electrons from the metal atoms and decreases shielding of the d-electrons. These more strongly bound d-electrons undergo a larger chemical potential change on redox, in other words, transition metal fluorides are much more "electronegative" than their oxide and sulfide analogues.[12] Transition metal fluorides react with lithium to form a metallic phase embedded in a lithium fluoride (LiF) matrix.[11,13–15] For difluorides (MF_2), this conversion reaction involves two electrons per metal center, resulting in capacities nearly three to four times greater than conventional $LiCoO_2$ (Figure 1.2).[6,13,14,16]

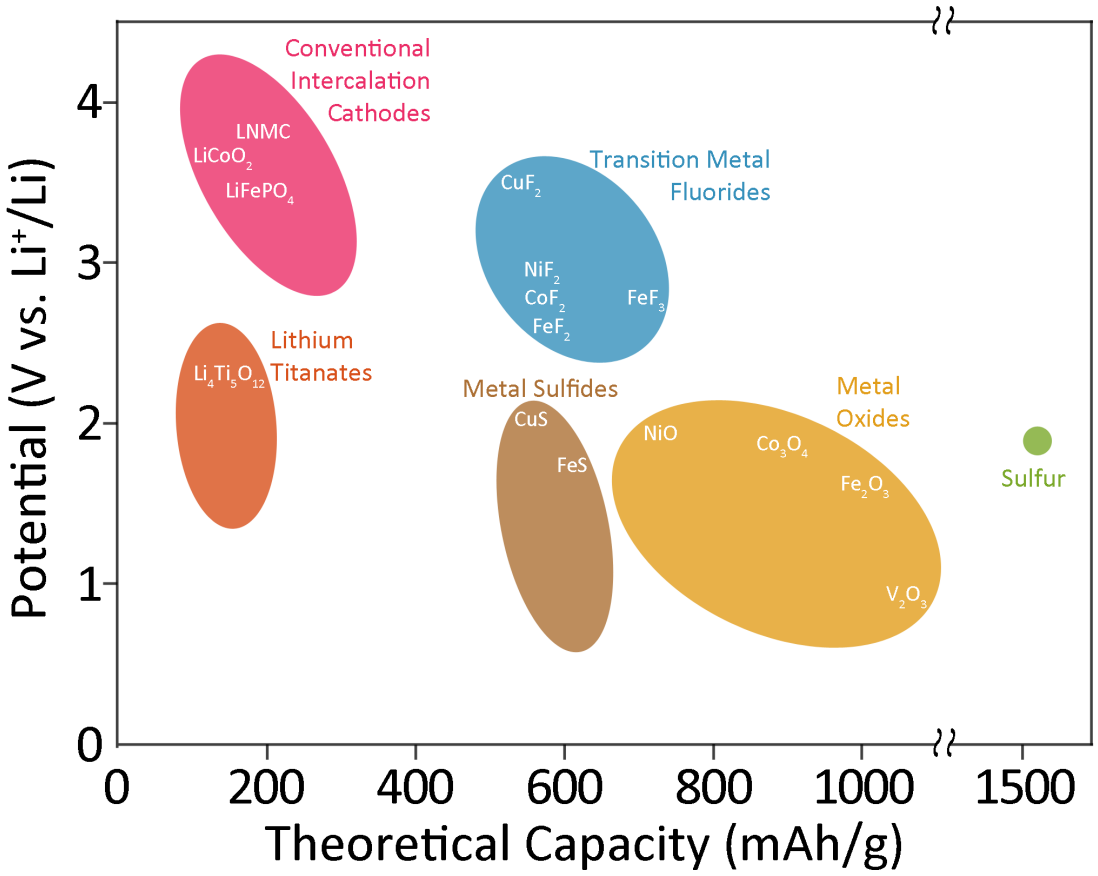


Figure 1.3: Energy Densities of Cathode Materials. This graph plots the equilibrium discharge voltage against the theoretical specific capacity for various classes of LIB cathode materials. The product of these two values gives the maximum specific energy density for each cathode system. Transition metal fluorides occupy a unique niche with high capacities resulting from the conversion reaction and high electrode potentials resulting from their ionic nature.

Unfortunately, the same ionic nature that makes transition metal fluorides promising also makes them difficult to implement in battery applications. In general, while increasing ionic character increases the transition metal reduction potential, it also unfortunately results in larger band gaps and decreased conductivity. The ionicity of a bond ultimately results from a large energy difference between the atomic orbitals on the cation (e.g. Fe 4s: −7.07 eV and those on the anion (e.g F 2p: −18.7 eV).[17] In the bulk solid, these cation (antibonding) and anion (bonding) orbitals combine to form the conduction and valence bands respectively, the greater ionic nature of transition metal fluorides results in larger band gaps (FeF_2: 3.24 eV) and consequently lower conductivity than their less ionic analogues (e.g. FeS_2: 0.87 eV).[18] The low electronic and ionic conductivity of the transition metal fluorides and the lithium fluoride discharge product are at odds with the widespread diffusion of lithium, electrons, and transition metal atoms required for the

conversion reaction.[15,19–21] This paradox dictates that nanoscale particles with short diffusion distances are necessary for the complete reaction of the active material. Several estimates have even suggested that even when a slow cycling rate is applied (C/20 or 20 hours/half-cycle), particle sizes less than 20 nm are required to utilize the full capacity of transition metal fluorides.[15,22] Even if such exceedingly small particles can be produced, in practice, copious amounts of conductive carbons are required to enable reversible cycling. This additional carbon dilutes the energy density of the electrode, effectively negating any gains resulting from the higher capacity of the conversion material. In contrast, several *in-situ* transmission electron microscopy (TEM) studies (including our own) have shown discharge over hundreds of nanometers at rates estimated between 5-20C.[23,24] Additionally, recent works have demonstrated that certain cathode failure mechanisms can be mitigated by electrolyte design.[25,26] However, the true prognosis for transition metal fluoride cathodes is unclear as current understanding of the charge/discharge mechanism in these materials is incomplete, incongruous, and lacks the detail to draw definitive conclusions. A better understanding of the mechanism is required to determine what capabilities/limitations are inherent to the material and how they can be improved by rational cell design.

This thesis describes recent breakthroughs in the application of transition metal fluorides as high energy density cathodes for lithium ion batteries. In this introductory chapter, I review the studies that form a context for our work, and highlight those that laid a foundation for the success of this project. **Chapter 2** describes the development of a new colloidal synthesis method to produce transition metal fluoride nanorods with unprecedented size and shape control. In **Chapter 3**, I detail the development of an ionic liquid electrolyte that precludes all the major failure mechanisms of transition metal fluorides, preserves particle morphology during cycling, and enables superior cycling stability at and above room temperature with the highest reported active material loading. Finally, in **Chapter 4**, I combine these advances with high resolution transmission electron microscopy (HRTEM) to redefine the conversion mechanism in transition metal fluorides and form tangible conclusions on the battery performance of transition metal fluroide cathodes.

1.2 Synthetic Methods for Metal Fluoride Nanoparticles

There are hundreds of known transition metal fluoride compounds and many more that are predicted to be stable.[18] However, studies on lithium ion battery cathodes have typically been limited to fluorides of the rightmost, first-row transition metal elements (Fe, Co, Ni, Cu). This can be rationalized based on cost per unit of energy density. The first row transition metal elements are among the most abundant on earth, and their relatively low molecular weights and high ionization energies yield the highest theoretical specific (or gravimetric) energy densities of all transition metal difluorides. The effective nuclear charge on d-orbital electrons increases with atomic number for elements in the same period, thus ionization energies and consequently reduction potentials increase from left to right across the first row (Figure 1.4).[27] Theoretical electrode potentials range from 2.6 V for FeF_2 to 3.5 V for CuF_2. The scope of this chapter is limited to the transition metal fluorides outlined above. MnF_2 has also been studied but it's lower reduction potential renders it less favorable. Hydrated phases, primarily $FeF_3 \bullet xH_2O$, have garnered some interest as intercalation compounds but will be excluded from the present discussion of conversion cathodes.

The short ionic and electronic diffusion lengths in metal fluorides demands uniformly small metal fluoride nanoparticles for use lithium ion battery applications;[9,11,24] however, the synthesis of such nanomaterials is not trivial. Compared to other elements, there is a lack of diversity in fluorine precursors. Commercially available transition metal fluorides are synthesized using gaseous F_2 or HF; however, such gases are dangerous and extremely reactive, and are typically not useful for nanoparticle syntheses.[28] Syntheses are further complicated by the fact the metal fluorides themselves can be reactive and are easily hydrated or hydrolyzed.[10,11,29] Although many recipes for transition metal fluoride nanoparticles have been reported, they generally follow one of only a few synthetic routes, which are outlined below.

The earliest and most common approach relies on the simplest of ideas: the solid-state mechanical attrition of bulk materials into nanoscale particles. These methods rely almost universally on some form of form of ball milling.[11,15,30] High-energy ball milling was first employed by Badway *et al.* to generate nanostructured metal fluorides cathodes in the

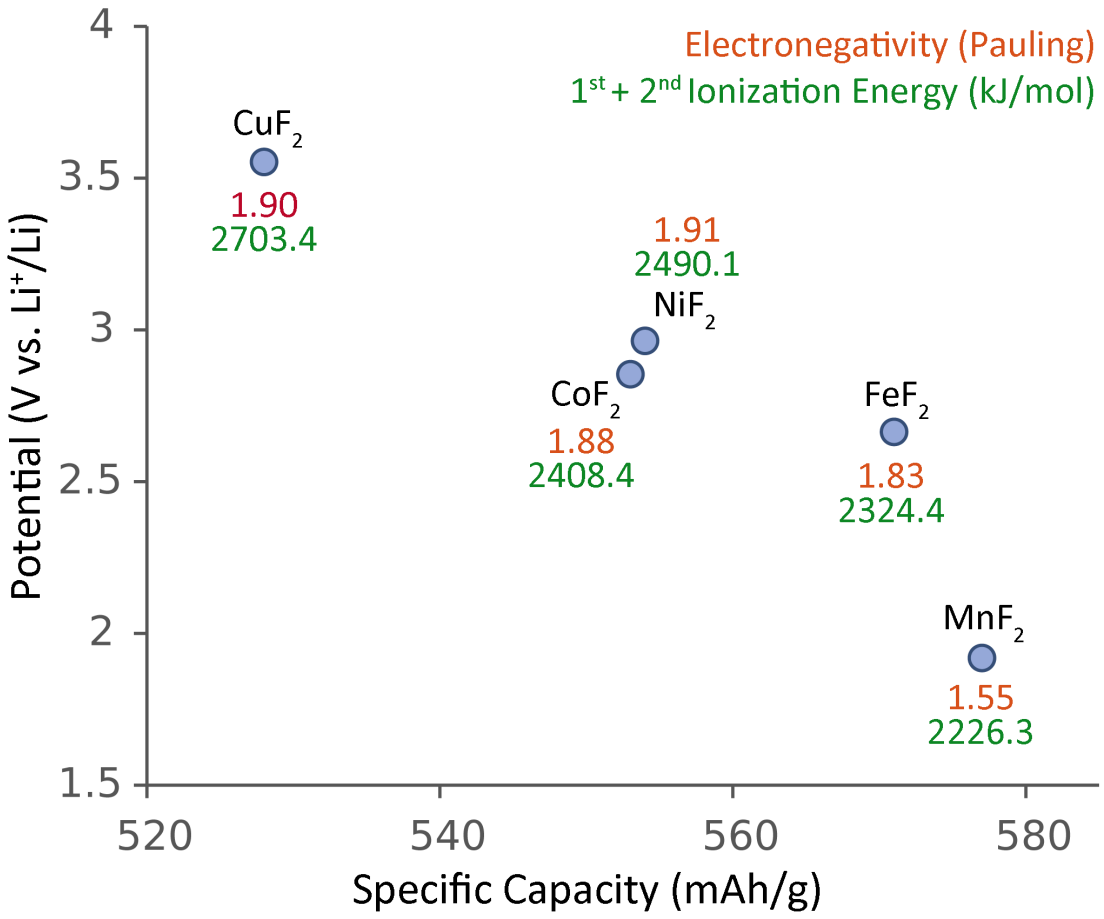


Figure 1.4: Periodic Trends and Electrode properties. This graph plots equilibrium cell potential and specific capacity for the rightmost first-row transition metal fluorides. The Pauling electronegativity and the cumulative two-electron ionization energy is shown for each transition metal. Electrode potentials increase with increasing electronegativity; specific capacity decreases as atomic mass increases.

earliest studies on transition metal fluoride cathodes.[15] The mechanism is quite simple; bulk metal fluoride powders are placed in sealed containers, typically with steel or zirconia balls, and moved at high speed (200 rev min^{-1} to 800 rev min^{-1}) through a planetary or eccentric orbit. Large particles are cleaved into smaller pieces by a combination of shear, compression, and impact stresses.[31]

Although ball milling is neither the most versatile synthetic method nor the most fundamentally interesting, it remains one of the most scalable methods of nanostructuring and must be considered if metal fluorides are to become commercially viable. The simplicity of ball milling enables its compatibility with the widest range of materials and further allows for the intimate integration of conductive carbon species (*e.g.* carbon black, graphene, carbon

nanotubes) with exact proportions.[13,15] As ball milling generally proceeds from standard commercially available materials, the fundamental electrochemical characterization and most basic mechanistic studies of metal fluorides have been performed on ball milled samples.[32–34]

The quality of ball milled samples, however, is quite poor. Although crude size control can be achieved by adjusting milling time (30 min-48 h) and speed, particle size distributions are extremely wide.[34,35] The milling process introduces structural defects and impurities from the milling equipment. Consequently, ball milled metal fluorides typically exhibit rapid loss of capacity on cycling and do not perform well at high discharge/charge rates; they are rarely employed in studies focused on optimizing performance (i.e. cycle life, capacity, rate capability).[34] Furthermore, the irregular and disordered morphology of ball-milled particles offers little information for detailed mechanistic study.

High-energy ball milling is purported to generate enough heat and mechanical energy to induce the solid-state interdiffusion of dissimilar materials.[30,31,36,37] These so-called "mechano-chemical" syntheses offer the supposed ability to produce homogeneous single-phase nanopowders of ternary or even more complex metal fluorides.[30,36,38] For example Gocheva *et al.* and Dimov *et al.* have demonstrated the facile preparation of $NaMF_3$ (M = Fe, Cu, Mn, Ni, Co) compounds via milling of NaF and MF_2 (figure 2).[30,38] Wang *et al.* have used ball milling to synthesize ternary metal fluorides ($Fe_{0.5}Co_{0.5}F_2$) from separate binary metal salts (FeF_2, CuF_2).[36] It is questionable whether these products are truly homogeneous, as they exhibit different redox behavior than their chemically synthesized ananlogues.[39]

Apart from ball milling, thermal decomposition methods based on a handful of precursors have dominated the nanoparticle synthesis literature. These precursors are typically fluoride containing salts that release a number of gaseous byproducts on heating, leaving behind the pristine metal fluoride.[40–43] In general, this thermal decomposition can take place in either liquid solutions or in an inert gas atmosphere.

In the liquid state, nanoparticles can be synthesized directly from the reaction of transition metal and fluorine precursors dissolved as molecular species. This kind of bottom up processing, allows for much greater morphology, composition, and phase control of the resulting nanomaterials than ball milling.[44–46] Composition and phase can

often be controlled simply by tuning precursor ratios, while morphology and size are governed by reaction temperatures and the presence of other surfactants or structure directing agents.[46–49]

Liquid phase syntheses have several limitations. For polar solvents, water can be difficult to remove; this can be particularly detrimental for transition metal fluorides as excess water may lead to the formation of hydrated phases with unwanted properties.[10,50] Additionally, for molecular precursors, side reactions are often possible and at the low temperatures imposed by liquid phases, it can be difficult to isolate a single thermodynamic product.[45] As the use of solvents is essential for liquid phase synthesis, a considerable amount of waste is often generated. In **Chapter 2** I will discuss how the more electronegative transition metals (Ni, Cu) can actually be readily reduced by certain organic functional groups, effectively limiting the range of transition metal fluorides that can be formed in a given solvent environment.

High temperatures and anhydrous conditions are more readily accessed in an inert gas, and the products of such syntheses are often highly crystalline and contain few defects.[41] Furthermore, reactions in an inert gas involve fewer reactive chemical species, and are more predictable, often resulting in a single thermodynamic product. The absence of condensed media also produces far less chemical waste. For these reasons, decomposition in an inert gas can also be cost-effective at scale depending on the precursors used.

Unfortunately, such thermal decomposition techniques offers few convenient ways to control particle morphology, or even limit particle growth to the nanoscale. Often transition metal fluorides synthesized in inert gas require some degree of ball milling. Nanostructuring is most-often achieved by confining the transition metal fluoride precursor(s) within a porous carbon scaffold prior to thermal decomposition; however, this significantly reduces energy density as will be discussed below. Synthesis in a closed system presents additional hazard due to relatively high pressures. While open systems allow chemically reactive species to diffuse away, making it complicated to control the yield and stoichiometry of the product.[43]

Most thermal decomposition synthesis methods rely on either ammonium fluoride mixtures or hexafluorosilicates; syntheses based ionic liquids or other organofluorine precursors are less popular but have demonstrated interesting results. Ammonium Fluoride

(NH_4F) is a solid salt that is stable and easily handled at room temperature. However, at elevated temperatures (as low as 80 °C), NH_4F sublimes and dissociates into reactive HF and NH_3.[43] This makes NH_4F extremely useful as a relatively safe source of a powerful fluorinating agent (HF).[43,51] NH_4F can be combined with a wide range of readily available transition metal salts as one of the most cost-effective precursors. Teng *et al.* first demonstrated this reaction with the NH_4F:$Co(NO_3)_2$ mediated synthesis of CoF_2.

$$\begin{gathered} 4NH_4F + M(NO_3)_2 \xrightarrow{heat} (NH_4)_2MF_4 + 2N_2O + 4H_2O \\ (NH_4)_2MF_4 \rightarrow MF_2 + 2NH_3 + 2HF \\ M = \text{Co, Ni, Cu} \end{gathered} \tag{1.4}$$

43

Chun *et al.* showcased the versatility of this method by infiltrating a mesoporous carbon scaffold with solutions of ammonium fluoride and a range of transition metal nitrates (Fe, Co, Cu) followed by heating between 200 °C to 270 °C to generate the final anhydrous fluorides (Equation 1.4).[43] However, this synthesis required several additions of NH_4F solution to achieve a stoichiometric product and the resulting composite contained a large proportion of carbon (45%). Zhou *et al.* presented a synthetic route based on the simultaneous sublimation and decomposition (400 °C) of NH_4F with ferrocene in an autoclave.[51] This simple reaction mixture produced FeF_2 rods (500 nm x 10 µm) coated in a thin layer of amorphous carbon. Ammonium fluoride is of particular interest to future work as its compatibility with colloidal synthesis techniques has been also been demonstrated.[52,53]

$$\begin{gathered} M(SiF_6)_2 \xrightarrow{heat} MF_2 + 2SiF_4 \\ M = \text{Mn, Fe, Co, Ni, Cu} \end{gathered} \tag{1.5}$$

39,42

Metal hexafluorosilicates, $M_x(SiF_6)_y$, decompose on heating, leaving behind metal fluorides and gaseous tetrafluorosilane (SF_4).[42] This decomposition mechanism well-defined and generates only a single volatile side product (Equation 1.5). The reliability and simplicity of this reaction has led to it's adoption as perhaps the most commonly used precursor in recent years. This technique was pioneered by Pereira *et al.* who demonstrated that

heating $FeSiF_6$ at 200 °C in an inert atmosphere could be used to fabricate anhydrous FeF_2 while annealing the same compound in air at temperatures between 150 °C and 300 °C produced rutile structured oxyfluorides FeO_xF_{2-x} with x between 0.33 and 1.[42] The $FeSiF_6$ precursor was also used by Wang *et al.* in several of the highest profile mechanistic studies to date.[24,32] Following their work, the group led by Gleb Yushin prepared carbon-metal fluoride nanocomposite materials by infiltrating nanocarbon scaffolds with an aqueous hexafluorosilicate solution prior to thermal decomposition.[25,36,39,40,54] This technique was demonstrated first using mesoporous carbon spheres and later carbon nanotubes, with the latter composites displaying some of the highest rate capabilities and longest cycle lives in the literature, albeit with very low active material loading. The versatility of hexafluorosilicate precursors was fully showcased as binary and ternary fluorides of Mn, Fe, Co, and Ni were all synthesized. Unfortunately, the hexafluorosilicic acid required to prepare these precursors exists in equilibrium with large proportions HF ($H_2SiF_6 + 2H_2O \rightarrow 6HF + SiO_2$), making these compounds extremely dangerous to synthesize. Furthermore, the hexafluorosilicate salts are insoluble in organic solvents, rendering them incompatible with solution-phase syntheses.

Prior to the work presented in this thesis, few solvothermal methods existed for the synthesis of anhydrous transition metal fluoride nanoparticles. Interestingly, the literature was primarily dominated by syntheses which employed ionic liquids as both the solvent and the fluorine precursor. This ionic liquid based technique was spearheaded by Jacob *et al.* who demonstrated a simple but versatile reaction scheme to produce a wide range of transition metal, main group, and lanthanide fluorides (FeF_2, CoF_2, ZnF_2, LaF_3, YF_3, SrF_2) using chloride, nitrate, and acetate salts.[55] Initial work centered around the 1-butyl-3-methylimidazolium tetrafluoroborate ionic liquids shown in Figure 1.5. The tetrafluoroborate (BF_4^-) anion decomposes at elevated temperatures to yield F^- anions that react with transition metal cations to quickly form insoluble metal fluorides.[47,55] It was later shown that ionic liquids containing hexafluorophosphate (PF_6^-) and triflate ($CF_3SO_3^-$) anions could also function as fluoride precursors (Figure 1.5).[48]

Ionic liquids exhibit negligible vapor pressures, a wide range of stable temperatures, and the ability to dissolve a wide range of compounds.[55,56] More remarkable, however, is their ability to stabilize extremely small particle sizes in the absence of a surfactant.

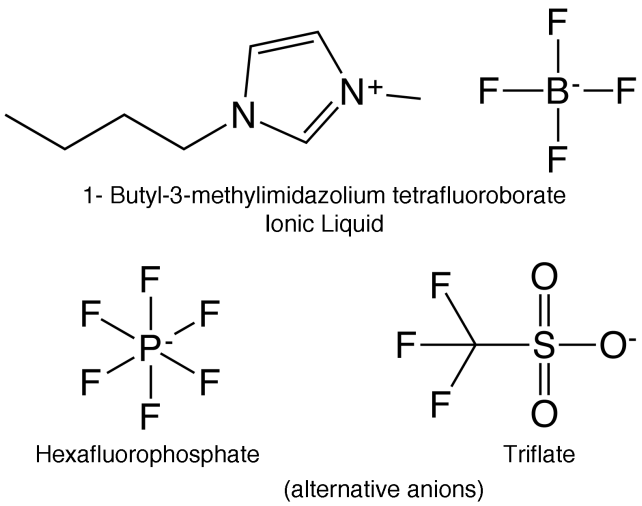


Figure 1.5: Ionic Liquids for Metal Fluoride Synthesis. Chemical structure of the 1-butyl-3-methylimidizolium (Bmim) tetrafluoroborate ionic liquid used for transition metal fluoride nanoparticle synthesis. Ionic liquids composed of Bmim cations and the other anions shown also function as fluoride precursors.

Electrostatic interactions in ionic liquids lead to ordered local environments around metal ions and growing nanoparticles, which allows for the nucleation of small particles and confines growth to the nanoscale.[44,55] This can even produce a soft templating effect, allowing for some degree of shape control. A similar phenomenon may also be responsible for the morphology preserving ability of the ionic liquid electrolytes employed in our electrochemical studies (**Chapter 3**). Despite the potential of IL liquid synthesis, transition metal fluoride nanoparticles produced in this way tend to be polydisperse and irregular.[48,55] At the moment, ionic liquids are prohibitively expensive to merely be used as reaction media.

Of the synthetic methods reviewed above, few are able to reliably produce particles with dimensions less than 100 nm, and none offer precise size or shape control. Colloidal synthesis methods, in which nanoparticles are nucleated and grown in a coordinating organic solvent, have long been used to produce particles between 3-30 nm in size and have demonstrated the highest degree of size and shape control, often producing particles with standard deviations of <5% from the mean. This field has become highly sophisticated – with syntheses extending from metals to metal oxides, chalcogenides and even rare earth fluorides.

In developing a colloidal synthesis for transition metal fluorides, I drew inspiration

from the syntheses of rare-earth metal fluorides, the majority of which use rare-earth trifluoroacetates as single-source precursors for both the metal and the fluorine. It has been known for some 50 years that metal salts of trifluoroacetic acid ($M^{x+}(CF_3COO^-)_x$) decompose on heating (generally between 250 °C to 350 °C) to generate metal fluorides and various fluorocarbon species (Equation 1.6).[41,57] Although, the fluorine atoms in these compounds are not labile, trifluoracetic acid has been demonstrated both experimentally and theoretically to decompose via a series of complex intermediates, releasing HF and other gases.[58,59]

$$\begin{gathered} M(CF_3COO)_x(CF_3COOH)_y \xrightarrow{heat} MF_x + CO_2 + CO + CF_3H \\ M = \mathrm{Mn},\ \mathrm{Fe},\ \mathrm{Co},\ \mathrm{Ni} \end{gathered} \tag{1.6}$$

41

Guntlin *et al.* synthesized trifluoroacetates of Fe(III), Fe(II), Co(II), and Mn(II), elucidated their structure and decomposed them in an inert atmosphere to generate the corresponding anhydrous metal fluorides.[41] It is apparent that the decomposition of the trifluoroacetate generates enough HF for full reaction with the metal centers. The resultant particles are microscale in size, and conventional ball milling was required to reduce their size for use in battery electrodes. In the next chapter I discuss how, under the correct conditions, these precursors can be used to produce monodisperse, single-crystalline transition metal fluoride nanorods.

1.3 Performance of Transition Metal Fluoride Cathodes

In this section I briefly review the progress that has been made on improving the electrochemical performance of transition metal fluoride cathodes. In academic reports, electrochemical performance is often reported in terms of three major metrics. The first is "reversible capacity" or the amount of charge that is stored after a full discharge/charge cycle; "coulombic efficiency" is the ratio of charge capacity to discharge capacity and is often used to quantify losses in reversible capacity. A second metric, "cycle life", is the number of complete cycles the cathode can endure before a 20% fade (80% retention) in reversible capacity is observed. A third commonly reported metric is "rate capability" or

the proportion of the full capacity that can be accessed with increasing discharge/charge current density (cycling rates). I first examine the major tactics used to improve these values for transition metal fluorides and later discuss the indicators of commercial viability that are often un-reported.

Reports on the common iron fluorides (FeF_2, FeF_3) have dominated the literature in studies of electrochemical performance/characterization as well as the conversion mechanism. As the only trifluoride among the high potential first row transition metal (Fe, Co, Ni, Cu) fluorides, FeF_3 exhibits the highest theoretical capacity (712 mA h g^{-1}). However, its canonical prevalence may partially be a result of precedence, as FeF_3 was the first transition metal fluoride cathode to be described in depth (by Amatucci's group in 2003).[15] This seminal work not only demonstrated the full theoretical capacity of the material, but also provided the first crystallographic description of a full discharge/charge cycle. Other authors were quick to follow suit, seeking to build on their results.

The related compound, FeF_2, presented a simpler system that exhibited a purely conversion-type reaction and was seen as more characteristic model compound. FeF_2 has the lowest reduction potential, and consequently the least oxidizing nature, of the fluorides outlined above, making it easier to synthesize, handle and process; FeF_2 also appears to exhibit greater inherent reversibility that the other fluorides. In any case, FeF_2 has become the prototypical transition metal fluoride cathode; the highest capacities, longest cycle lives, and greatest rate capability have all been demonstrated in the FeF_2 system.

Needless to say, the initial studies on transition metal fluoride cathodes, from the groups of Ammatucci and Maier, did not exhibit the best electrochemical performance. In their original work on FeF_3, Badway *et al.* used electrodes prepared by high-energy ball milling, consisting of only 48 wt.% active material, and performed their experiments at extremely elevated temperatures (70 °C where reaction kinetics are greatly accelerated.[15] Even so, extremely slow cycling rates of C/100 (corresponding to a 100 hr discharge) were required to achieve the full theoretical capacity, and this capacity faded by nearly 30% over the first 14 cycles. This experiment demonstrated the difficulty of working with an electronically and ionically insulating material. Several later studies demonstrated that the direct chemical synthesis of FeF_3 nanoparticles using solvothermal methods

allowed for room temperature cycling at near theoretical capacities and slightly higher rates (C/14-C/7); however, rapid capacity fade (60% capacity loss after 50 cycles) was still observed.[49,60] Li *et al.* suggested that this steady capacity fade was a result of an incomplete reconversion ($3LiF + Fe \rightarrow FeF_3 + 3Li^+$) reaction on each charging cycle without providing further explanation.[49] The section below describes how many authors have pointed instead to cathode dissolution as a major failure mechanism in transition metal fluorides. In **Chapter 4**, I will demonstrate how these two mechanisms are actually one and the same.

In more recent years, publications touting "high-performance" transition metal fluorides have focused on metal difluorides and FeF_2 in particular. These reports typically show stable cycling at near theoretical capacities with minimal capacity fade over at least 100 cycles. In certain cases extremely high rate capabilities are even demonstrated with between 300 mA h g^{-1} to 400 mA h g^{-1} (50-70% of the theoretical capacity) maintained at rates above 1C.[25,28,43] However, all of these studies rely on the same principle: the heterogeneous nucleation of transition metal fluoride nanoparticles on or within nanostructured carbon scaffolds. This trope, commonly referred to as "strongly-coupled" nanocomposites, has actually been tried with nearly every non-intercalation type LIB electrode from silicon anodes to metal oxides and sulfides with blanket promises of mitigating nearly every imaginable failure mechanism.[61] While these nanocomposite materials perform impressively based on capacity, cycle life, and rate capability, they actually are less favorable than previous works on benchmarks of commercial viability such as active material mass fraction, areal capacity, production line compatibility, and cost. In other words, the amount of carbon introduced in these nanocomposites is so high (40-60 wt.%) that they dilute the energy density of the electrode while also increasing materials cost and manufacturing complexity

The most important contribution of these works is that they demonstrate that capacity loss can be mitigated to a large extent. Initially this was achieved by growing transition metal fluoride nanoparticles inside various mesoporous carbon scaffolds.[43,62] As mentioned above, these mesoporous carbons limit crystal growth to the nanoscale. Additionally, they serve to anchor the transition metal fluoride particles to prevent exfoliation, seperate adjacent particles to prevent fusing, and physically passivate the particle surface to mitigate

electrolyte decomposition and electrode dissolution (corrosion) (Figure 1.6). These failure mechanisms were not investigated in the aforementioned reports, but they were identified in the course of this study and will be discussed in **Chapter 3**. Later reports demonstrated similarly stable cycling by growing transition metal fluoride nanoparticles on the surface of carbon nanotubes.[25,26,39] In these cases, the authors tailored the electrolytes to prevent cathode dissolution through the formation of a stable solid-electrolyte interphase (SEI). The anchoring effect of the carbon nanotubes was still required to prevent fusing and exfoliation. In **Chapter 3** I demonstrate how our ionic liquid electrolyte is able to prevent these issues as well.

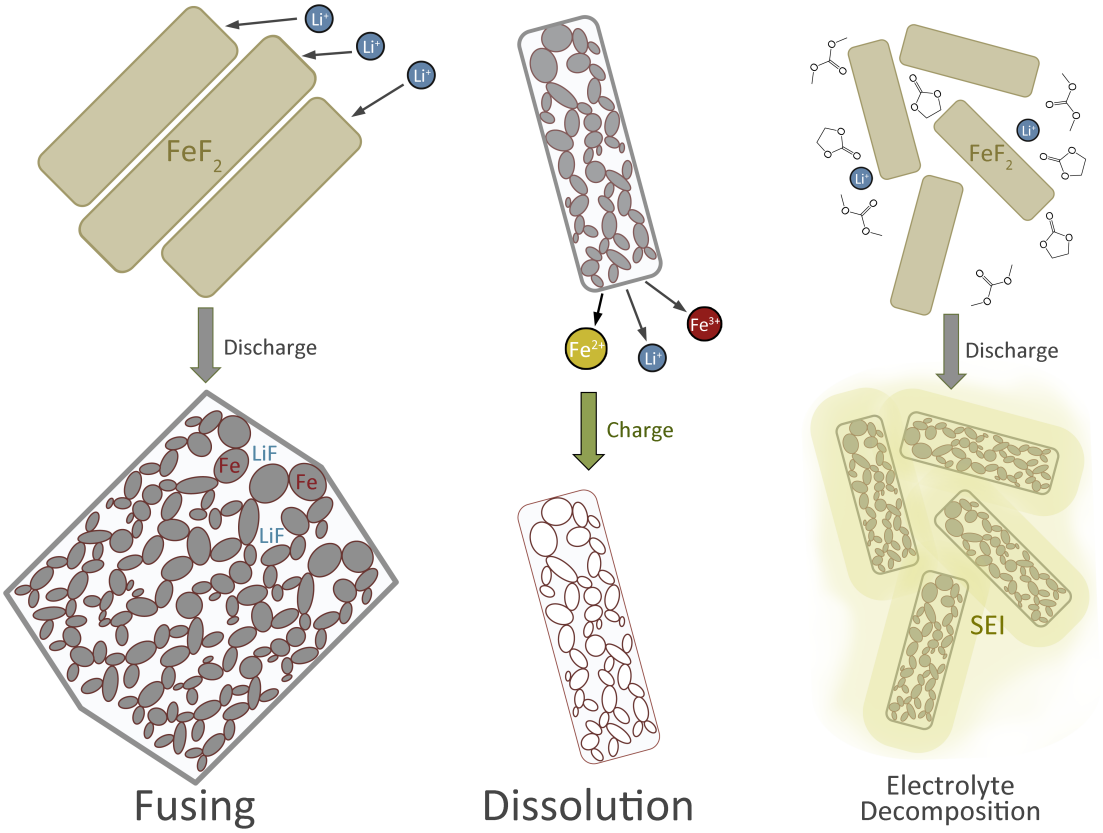


Figure 1.6: Failure Mechanims in Transition Metal Fluoride Cathodes. This schematic depicts the three major failure mechanisms present in transition metal fluoride LIBs as determined by our study.[1] For reference in the context of this thesis, FeF_2 is shown in the form of nanorods; however, these failure mechanisms are common to all nanoparticle morphologies. Further discussion of failure mechanisms is provided in **Chapter 3**.

In general, electrolyte engineering is a more favorable means of achieving cycling stability, as it avoids the use of excessive amounts of carbon and requires no change to the battery fabrication process. Beginning with the very first reports from Maier and Amatucci,

the electrolytes used in the electrochemical characterization of transition metal fluorides were those developed for conventional intercalation based lithium ion batteries, most commonly 1 M lithium hexafluorophosphate ($LiPF_6$) in 1:1 ethylene carbonate (EC):dimethyl carbonate (DMC) (trade name LP30).[13,15,63] Wang *et al.* were the first to demonstrate the systematic effect of varying the composition of the organic solvents in the electrolyte. In the context a CoF_2-CNT composite they prepared electrolytes composed of $LiPF_6$ dissolved in ethylmethyl carbonate (EMC):fluoroethylene carbonate (FEC) mixture, and demonstrated that cycling stability increased with increasing FEC content.[36] It has been speculated that FEC decomposes to form a more robust interphase between transition metal fluoride and the electrolyte that prevents the dissolution of the transition metal on charging (oxidation). In a much more recent work, Huang *et al.* of the same research group performed an extensive and systematic comparison of electrolytes for FeF_2 cathodes.[25] The authors prepared electrolytes of three different salts at three different concentrations, each in one of two different solvent systems. The electrolyte that produced the most stable cycling behavior was highly concentrated (3 M) fluorosulfonylimide (FSI) salt dissolved in the more electrochemically stable dimethoxyethane (DME) solvent. The stable SEI forming properties of FSI were also observed in my work and are discussed in **Chapter 3**.

Conventional layered metal oxide cathode materials decompose in organic electrolytes at elevated temperatures, resulting in violent and often televised exothermic reactions. In light of this glaring safety concern Zhou *et al.* published a series of works investigating the thermal stability of FeF_3 electrodes in organic $LiPF_6$ electrolytes.[51,64,65] Such electrode/electrolyte mixtures were stable to over 200 °C in both the charged and discharged states. Reactions above this temperature resulted entirely from electrolyte decomposition, and FeF_3 even appeared to quench the exothermic heat of these reactions. From a high temperature safety standpoint, FeF_3 even outperformed the industry standard for thermally stable cathodes, lithium iron phosphate ($LiFePO_4$), suggesting its suitability for next generation LIBs. However, the failure mechanisms that plague transition metal fluorides at room temperature (cathode dissolution in particular) are actually exacerbated above 40 °C. Recently, Huang *et al.* laminated their FeF_2-CNT cathode in a solid polymer electrolyte, which resulted in stable cycling at 50 °C. However, this came at the cost of greatly reduced rate capability and further decreased active material mass fraction.[25] In **Chapter 3** I

demonstrate how our ionic liquid electrolyte allows for both room temperature and high temperature performance, while providing greatly improved safety at high temperatures.

With the highest reduction potential among first row transition metal fluorides, CuF_2 exhibits an even higher theoretical energy density than FeF_3.[32,36] Yet, out of the aforementioned transition metal fluorides, CuF_2 is also the only compound that has never successfully been cycled. Much has been made of the anomalous behaviour of CuF_2, with its instability mainly attributed to the greater solubility of the Cu^{1+} ion. In light of the new mechanistic understanding presented in **Chapter 4**, I will highlight additional factors that may contribute to this distinct behavior.

Two promising chemical strategies have been employed to enhance the electrochemical properties of transition metal fluorides. The first involves the synthesis of ternary metal fluorides with two different transition metal species (i.e. $Fe_{0.5}Cu_{0.5}F_2$). In one case, $Fe_{0.5}Cu_{0.5}F_2$ exhibited significantly reduced hysteresis and a relatively high reduction potential (as a result of Cu substitution). This was attributed to a synergistic, stepwise reaction whereby converted Cu^0 particles were said to provide improved electron transport during the reconversion of Fe at low potentials ($\mathrm{Fe} + 2\mathrm{LiF} \rightarrow \mathrm{FeF_2} + 2\mathrm{Li^+} + 2\mathrm{e^-}$), while the existing FeF_2 framework facilitated the reconversion of Cu at high potentials.[36] Interestingly, other combinations of transition metals do not appear to produce such a beneficial effect, and the results of this report have yet to be reproduced.[39,66]

A second strategy introduces mixed anionic species in the form of transition metal oxyfluorides. Oxyfluorides (i.e. FeOF) take on the same rutile structure as transition metal difluorides, as O^{2-} can substitute for F^- at any lattice site.[42] The presence of oxygen increases the electrical conductivity of the active material, leading to a lower reaction hysteresis. To maintain charge neutrality, each O^{2-} anion introduces one Fe^{3+} cation to the lattice; the addition of this Fe^{3+}/Fe^{2+} redox couple results in a higher average reduction potential. Interestingly, FeOF cathodes produced by a simple ball-milling procedure exhibit a greater inherent reversibility than FeF_2; this has been attributed to the segregation of oxygen to the particle surface and the formation of an oxide shell which prevents excessive SEI formation and likely also reduces cathode dissolution.[22,67,68] This anion rearrangement is irreversible however and introduces some degree of built-in capacity loss for these materials.[68] While these strategies are not employed in the current work,

our electrolyte based framework (**Chapter 3**) for achieving stable cycling can be used in conjunction with ternary transition metal fluorides and oxyfluorides. Furthermore, the comprehensive mechanistic model (**Chapter 4**) developed herein for the simple FeF_2 system provides a detailed guide for the analysis of more complex materials.

1.4 The Conversion Mechanism in Metal Fluorides

Although CoF_2, NiF_2, and CuF_2 have higher theoretical energy densities, FeF_2 exhibits the greatest inherent reversibility and has thus become the prototypical system for examining conversion reactions in transition metal fluorides. These fluorides all share a common tetragonal rutile crystal structure ($P4_{/2}mnm$), with the exception of CuF_2, which exhibits a Jahn-Teller distortion.[69] A shared crystal system and similar chemistries suggests closely related conversion mechanisms.[13,39] Thus, a comprehensive understanding of the iron system would also elucidate methods for improving the performance of the more energy dense fluoride materials.

The overall reaction ($\mathrm{FeF_2 + 2Li^+ + 2e^- \leftrightarrow Fe^0 + 2LiF}$) belies the complex series of phase transformations that enable the reversibility of the conversion reaction. In their foundational study, Badway *et al.* characterized the reaction using X-ray diffraction (XRD) techniques; however they could only conclude that a Fe/LiF nanocomposite was formed on discharge and that a rutile structure was restored on charge.[15] The extreme broadening of XRD peaks at grain sizes below 10 nm obscures the presence of any minor phases or structural distortions. A handful of papers have successfully probed features of the conversion mechanism using advanced X-ray techniques, magnetic measurements, and electrochemical characterization.[22,32,70,71] However, these techniques provide no spatial resolution and cannot be used to form definitive mechanistic conclusions without the addition of a broader morphological context. Transmission electron microscopy (TEM) techniques offer high spatial resolution, but isolated images of disparate particles cannot accurately describe the progress of the reaction.

Much of the common understanding of the conversion mechanism in transition metal fluorides was built on the back of two mechanistic studies by Wang *et al.* in 2011 and 2012 (Figure 1.7).[24,32] The first study probed size of iron particles and amount of iron forming on

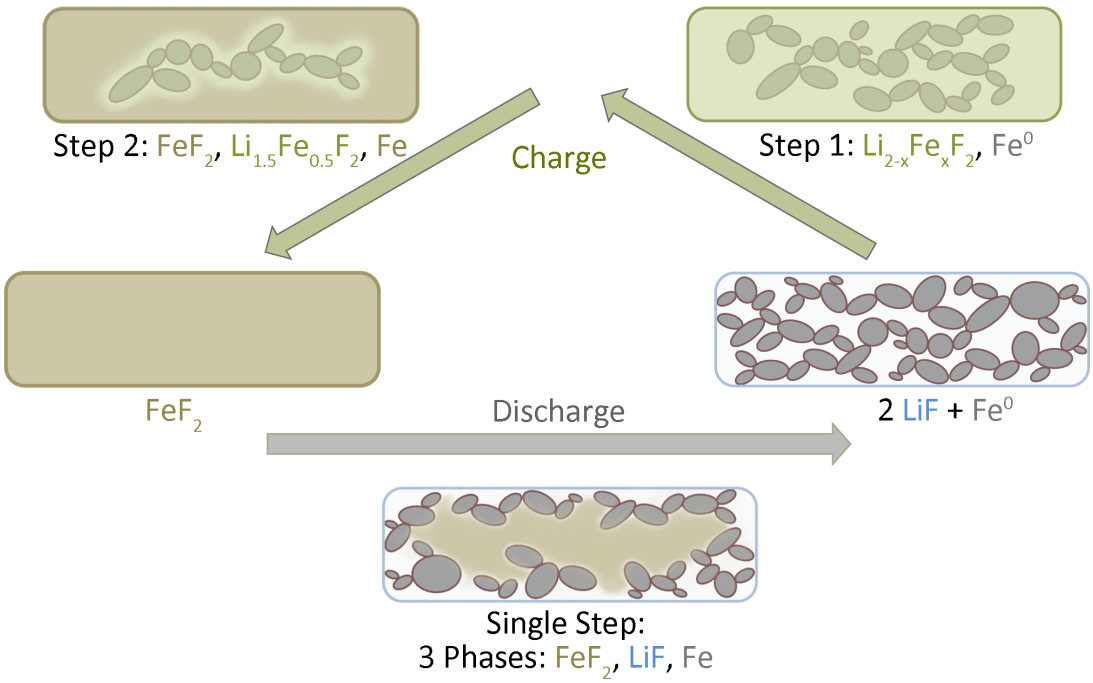


Figure 1.7: The Conversion Mechanism in Literature. This schematic depicts the conversion and reconversion mechanism of transition metal fluorides as commonly described in the literature before the publication of our work. The discharge reaction was defined as a 3-phase direct conversion of FeF_2 to LiF and Fe, while the charge reaction occurs in two steps with the formation of an $Fe_xLi_{2-x}F_2$ intermediate before recovery of the rutile FeF_2 structure. The reaction here is depicted with the spatial distribution of metallic iron particles reversed between charge and discharge (compositional inhomogeneity).[70] The preservation of particle morphology show here was first demonstrated in our work.[1] A new mechanism based on my findings is outlined in **Chapter 4**.

discharge, directly using X-r ay pair distribution function analysis (X-ray PDF) and indirectly using superconducting quantum interference device magnetometry (SQUID). Although the X-ray PDF measurements showed no obvious iron particle formation until nearly halfway through the discharge reaction, the SQUID measurements showed a near linear increase in magnetic material with degree of lithiation. The authors also used TEM in conjunction with electron energy loss spectroscopy (EELS) to confirm the presence of LiF in the fully discharged state. Although this set of measurements was inconclusive regarding the phase equilibria in the early stages of the reaction, the authors nonetheless concluded that the entire discharge reaction ($FeF_2 + 2e^- + 2Li^+ \rightarrow Fe + 2LiF$) occurs through a single step 3-phase reaction in which both LiF and Fe are simultaneously extruded from the FeF_2 lattice (Figure 1.7). The authors also claimed that the iron particles grown during the conversion reaction formed a "bi-continiuous" or "percolating" network of interconnected

iron particles within the FeF_2/LiF matrix that provided electronic and ionic conduction pathways within the material.[32] However, evidence for this was limited to a single TEM image which appeared to show several connected (or overlapping) particles with a shared lattice orientation. In any case, this claim was seemingly corroborated in their following report, which employed an *in-situ* technique to record the lithiation of FeF_2 nanoparticles using TEM (Figure 1.8).[24] This *in-situ* TEM technique visually demonstrated the direct and rapid nucleation of iron particles starting from the FeF_2 surface and propagating with a distinct conversion front into core of particle. We have recreated this *in-situ* experiment with the FeF_2 nanorods below (Figure 1.9). However, unlike a real battery, *in-situ* TEM experiments involve highly directional lithiation, steep concentration gradients, and a large negative bias between electrodes (Figure 1.8).[72,73] In **Chapter 4** we will present additional *in-situ* TEM data and examine how these experimental considerations can cause the morphological and even the chemical phase progression of the conversion reaction to deviate from real battery conditions.

The visually explicit nature of the *in-situ* TEM results presented by Wang *et al.* established the single-step, three-phase direct conversion of FeF_2 to LiF and Fe as the accepted discharge (lithiation) mechanism. Other authors appeared to corroborate this theory but provided little experimental evidence of their own.[22,70] Later reports primarily focused on describing the charge or de-lithiation mechanism, sometimes termed "re-conversion". Ko. *et al.* describe how the discharged mixture of metallic Fe and rocksalt LiF transforms back to a rutile iron fluoride through the formation of an iron substituted rocksalt intermediate.[22] Using X-ray pair distribution function (PDF), they demonstrated de-lithiation proceeds with the insertion of Fe into the LiF rocksalt structure to form a rocksalt $Fe_xLi_{2-x}F_2$ species up to a composition of x = 0.4-0.5 (Figure 1.7). Further Fe insertion (and lithium extraction) results in the formation of rutile iron fluoride in a two-phase mixture with the rocksalt phase (1.7). Li *et al.* followed the progression of the reconversion reactions in FeF_2 using *in-situ* X-ray absorption spectroscopy (XAS) to measure oxidation states and local bonding environments.[70] Interestingly they observed the oxidation of Fe^{3+} species upon charging to 3.3 V vs Li^+/Li. The fully charged state contained a mixture of Fe^0, Fe^{2+}, and Fe^{3+} species, with the dominant crystal structure related to that of rutile FeF_2. Unfortunately, the authors did not provide an explanation for these observations. In the same work, Li *et al.*

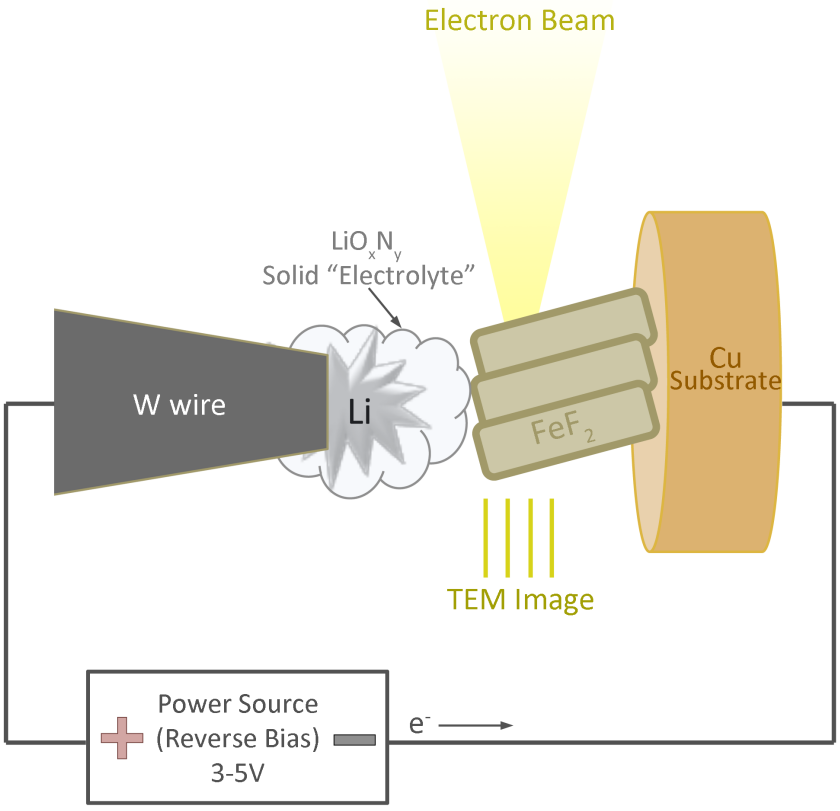


Figure 1.8: *In-situ* TEM Lithiation techniques. This schematic shows the setup of an *In-situ* TEM lithation experiment using a scanning tunneling microscopy (STM) biasing TEM sample holder. A small piece of lithium metal is mounted on the STM probe; exposure to air generates a layer of electrically insulating LiO_xN_y, which serves as a kind of solid Li^+ electrolyte. The Li probe is placed in contact with the nanoparticle sample, a large reverse bias is applied to drive lithiation. In general, this anisotropic lithiation produces a inhomogenous appearance and the large reverse bias places the active material at an unrealistic free energy with respect to lithium. *In-situ* TEM is, however, useful for visualizing broader morphological changes.

studied the phase evolution of FeF_3 and demonstrated the chemical pathways on charge and discharge are largely symmetric. Although the authors extended this claim to FeF_2, the experimental evidence was inconclusive. **Chapter 4** defines the full phase evolution on discharge and charge. I will demonstrate how the phases formed on discharge mirror those formed on charge and further provide a concrete mechanistic explanation for why the reconversion to phase pure FeF_2 is not observed.

Although the direct conversion of FeF_2 to LiF and Fe is the most common discharge mechanism found in the literature, it is actually not the equilibrium discharge pathway predicted by first principles calculations. Several authors, including the aforementioned Wang *et al.* and Li *et al.* used density functional theory (DFT) to calculate equilibrium reaction pathways for FeF_2 and FeF_3.[24,70] However, this approach was first pioneered in

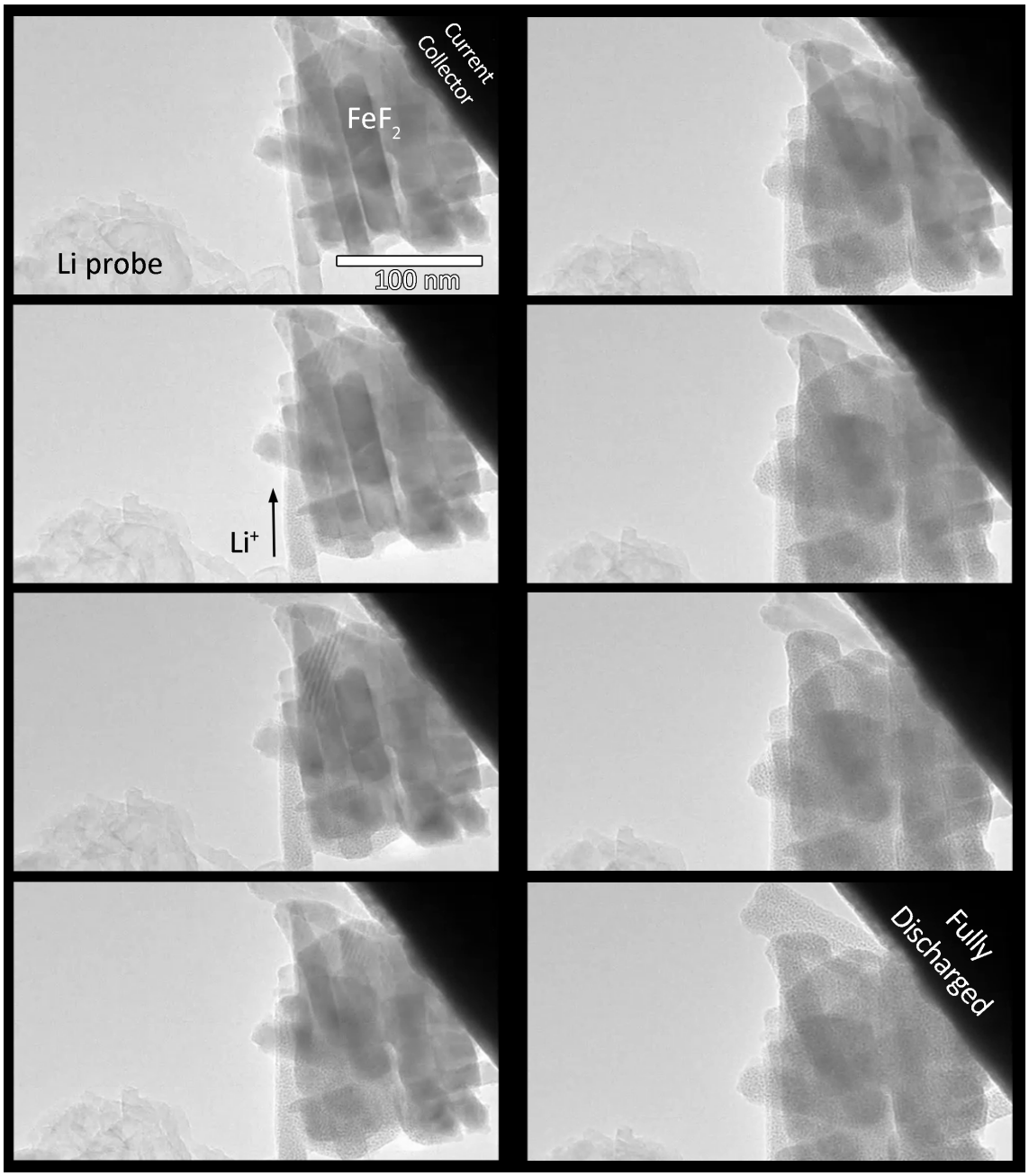


Figure 1.9: *In-Situ* TEM lithiation of FeF_2 Nanorods. (Bright field (BF) TEM with live view video capture.) Using the technique depicted in Figure 1.8, we performed *in-situ* TEM lithiation of my FeF_2 nanorod sample. When a large reverse bias is applied, the conversion reaction is observed to occur immediately at the point of Li contact and subsequently spread throughout the material. Similar results led Wang *et al.* to propose a direct conversion mechanism. Lithiation under real battery conditions follows a vastly different pathway. Interestingly, this experiment demonstrates fast lithiation over hundreds of nm. Fast lithiation (discharge) will be discussed in **Chapters 3 and 4**. Experiments were performed with our collaborator Prof. Hyun-wook Lee (Ulsan National Institute of Science and Technology. Ulsan, South Korea)

2008 by Doe *et al.* who defined a ternary phase diagram based on the most thermodynamically stable compounds of lithium, iron and fluorine.[74] Their results demonstrated that for FeF_3, intercalation up to 0.5 Li^+ per formula unit with a corresponding phase transition

to a tri-rutile $LiFe_2F_6$ phase before the onset of conversion to LiF and Fe represents an equilibrium pathway. This intercalation reaction is largely expected based on the presence of interstitial sites within the compound and the stability of the Fe^{3+}/Fe^{2+} redox couple, and it was verified experimentally several years later. For FeF_2, the equilibrium reaction pathway also involves the formation of the tri-rutile $LiFe_2F_6$ intermediate at the onset of lithiation. However, in this case intercalation would not be expected as accommodation of Li^+ within the FeF_2 structure would result in the concomitant reduction of Fe^{2+} to Fe^{1+}, which is highly unstable. The authors proposed that the insertion of lithium within the FeF_2 structure could take place via an electrochemical disproportionation to form reduced Fe^0 and oxidized Fe^{3+} in the form of $LiFe^{2+}Fe^{3+}F_6$.[74] However, a lack of experimental validation of this tri-rutile intermediate led to the exclusion of intercalation-like behavior, and the discharge pathway of FeF_2 was assumed to occure by non-equilibrium direct conversion.

Although the conversion mechanism on discharge remained largely undisputed until the publication of results from the present work,[1] several previous reports have presented evidence for the possibility of a contrary opinion. Most notably, Ma and Garofalini pioneered a new molecular dynamics approach which introduced functions to dynamically account for charge transfer and changing oxidation states during the electrochemical conversion reaction.[19] This approach was used to simulate lithium insertion into a ~3 nm wide nanorod of FeF_2 faceted on the $\{1\,1\,0\}$ and $\{0\,0\,1\}$ planes. Their simulations demonstrated that a short-lived and kinetically limited intercalation of Li^+ into the surface layers of FeF_2 was possible in the $\langle 0\,0\,1\rangle$ direction. The authors calculated that Li^+ diffusion could occur through open channels in the $\langle 0\,0\,1\rangle$ direction with a negligible potential energy barrier. The model showed that the one electron reduction of $Fe^{2+} \rightarrow Fe^{+}$ accompanying each intercalated Li^+ ion would be delocalized over several Fe centers in the vicinity, allowing for the intercalation of Li^+ through several atomic layers before the FeF_2 lattice was destabilized and decomposed into finely divided iron particles and amorphous LiF.[19] In the $\langle 1\,1\,0\rangle$ direction, this decomposition occured almost immediately in a layer by layer fashion. This model assumes the instantaneous and uninhibited transport of electrons to the reaction front, which may only be accurate for material in close contact with a conductive carbon phase. In a second work, Ma and Garofalini further calculated that F^- diffusion

was negligible compared to that of Li^+, and that Li^+ ion diffusion through crystalline lithium fluoride was possible, while insertion of lithium into crystalline lithium fluoride from the electrolyte was thermodynamically unlikely.[20] The authors also demonstrated that the interfaces between crystalline LiF and metallic Fe particles forming on discharge would be dominated by the $(1\,1\,0)_{Fe}|(0\,0\,1)_{LiF}$ interface. In **Chapter 4** I will re-examine these computational results in light of our highly detailed experimental data and analyze how these concepts manifest under real battery conditions.

In a report that preceeded the *in-situ* TEM work of Wang *et al.*, Yamakawa *et al.* actually observed several features that seemed to suggest an alternative picture of the discharge reaction pathway in FeF_2.[71] Using solid state nuclear magnetic resonance (NMR), they observed spin coupling between Li^+ ions and the unpaired electrons on the Fe ions early in the discharge reaction, suggesting insertion of lithium into the rutile lattice. Additionally, using conventional XRD, they observed a corresponding expansion in the rutile lattice parameters as the degree of lithiation increased. Their XRD data further suggested that the formation of substantial iron particles did not occur until late in the discharge reaction, while a rocksalt phase was observed early on. The authors even suggested that this rocksalt phase could correspond to Fe substituted LiF. However, in this case the resolution of both NMR and XRD was poor, and in the absence of more definitive data, the authors attributed this phenomena to oxidation of the FeF_2 during processing.[71] In **Chapter 4**, I discuss how the HRTEM technique allowed for the direct crystallographic measurement of fluoride intermediates in the discharge pathway and how the phenomena described by Yamakawa *et al.* can be explained by the new mechanism I propose herein.

Recently, Karki *et al.* re-examined the discharge mechanism in a new set of *in-situ* TEM experiments on a large single crystal of FeF_2.[23] Using *in-situ* electron diffraction, they revealed that the metallic iron phase formed on discharge had a distinct and well defined orientation relationship to the parent FeF_2 lattice. The authors hypothesized that this was a result of how the Fe was extruded from the FeF_2 lattice. In this case, the particle measured was over 200 nm thick, and the low resolution of the resulting images inhibited accurate analysis of the data. Interestingly, the authors performed molecular dynamics calculations to show that the diffusion coefficient of Fe^0 through the lattice was much greater than that of Fe^{2+} due to the decreased charge.[23] In the mechanistic study

(**Chapter 4**), I will expand on this principle of a topotactic reaction, and, in a much greater level of detail, define the true nature of the orientation relationships observed.

Ultimately, there is a large disconnect between the electrochemical performance of transition metal fluorides and the understanding of their discharge/charge mechanisms. The methods so often employed to achieve "high performance" in these materials are essentially agnostic to the specific problems that transition metal fluorides pose. On the other hand, mechanistic studies of these materials lack the detail and spatial resolution required to describe the inherent capabilities and limitations of transition metal fluorides. Moreover, these mechanistic studies are often performed in systems that exhibit poor reversibility or are not designed to cycle at all. The primary goal of the work presented herein is to bridge the gap between mechanism and performance of transition metal fluoride cathodes. This thesis deals first with the design of a materials system that is practically ideal for microscopic analysis. Secondly this work develops an electrolyte that enables the highly reversible discharge/charge cycling of transition metal fluorides in an energy dense format, while also preserving the morphology of my material system. Finally, this electrode/electrolyte system is examined using HRTEM and EELS to elucidate the comprehensive discharge/charge mechanism and to draw realistic conclusions about the performance of these materials and how this performance can be improved.

Chapter 2

Synthesis

2.1 Colloidal Synthesis of Metal Fluoride Nanocrystals

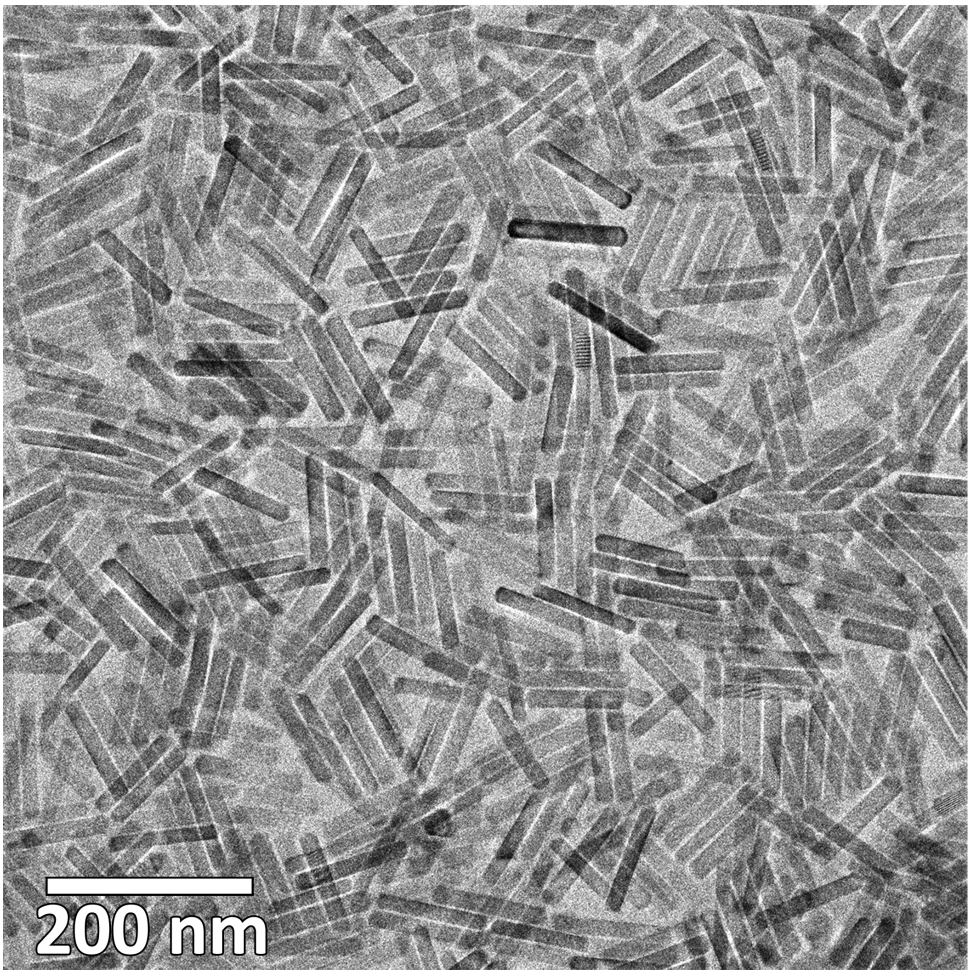


Figure 2.1: Monodisperse FeF_2 Nanorods. (Bright field [BF] TEM.) FeF_2 nanorods grown using our new colloidal synthesis method. Typical nanorod samples measure 110.5±13.5 nm by 20.6±2.9 nm.

High-resolution transmission electron microscopy (HRTEM) combined with analytical techniques such as electron energy loss spectroscopy (EELS), delivers morphological, structural, and chemical data with extremely high spatial resolution.[24,75,76] While it seems like the ideal tool for mechanistic study, the HRTEM approach is limited by the difficulty of isolating single crystals from a battery as well as the impossibility of correlating the structure and morphology of disparate particles through different states of charge and discharge. Additionally, it can be difficult to find particles oriented along an information-dense, high symmetry zone axis, and even multiple images are typically not representative of the whole battery. However, in a system where all particles of the active material are single crystalline and share the same size, morphology, lattice orientation, and exposed facets, HRTEM would provide an immense wealth of information and allow for the extrapolation of results from a single particle to the entire electrode.

As mythical as such a system may sound, colloidal synthesis methods, in which nanoparticles are nucleated and grown in a coordinating organic solvent, have a well-established track record for producing particles with near perfect uniformity. These syntheses typically produce particles with dimensions under 30 nm and can further be tuned to provide precise control over size and shape.[77,78] Recipes for entirely monodisperse samples—where the standard deviation in nanorod dimensions is ≤5%—have been developed for a wide variety of materials systems including metals, oxides, chalcogenides, and rare earth fluorides.[77–80] In this chapter, I present a new one-pot, single-step, high yield method for the colloidal synthesis of transition metal fluoride nanorods from a single source precursor (Figure 2.1). In the case of FeF_2, the resulting nanorods are single crystalline and nearly monodisperse, with typical standard deviations between 10–15%. These FeF_2 nanorods further exhibit 20 nm x 20 nm square cross sections and are faceted along their $\{1\,1\,0\}$ planes so that they naturally fall on their $\langle 1\,1\,0\rangle$ –zone axis (Figure 2.3). As cathode materials, the as-synthesized nanorods are small enough to reversibly deliver the full theoretical capacity of FeF_2 (571 mA h g^{-1}); in **Chapter 3** I assemble these FeF_2 nanorods into energy dense cathodes and explore their electrochemical performance. These FeF_2 nanorods are further utilized in **Chapter 4** to conduct a comprehensive study of the conversion mechanism.

In a colloidal synthesis, the growing nanoparticles form an inherently stable colloidal

dispersion within the liquid reaction media. This typically involves the thermal decomposition of dissolved precursors in the presence of one or more surfactant species. These surfactants reduce the interfacial energy between the nucleating particle and the solvent. The critical radius for nucleation is given by equation 2.1, where r^* is the smallest radius at which stable particles can form, γ is the interfacial free energy between the solid and the liquid, and ΔG_v is the volume free energy change for the reaction. The formation of any new particle involves a balance between the volumetric free energy change of the reaction and the surface free energy cost associated with the formation of new interface. Derivation of this equation reveals that a free energy maximum exists at $r = r^*$. To decrease the total free energy, particles larger than r^* will spontaneously grow, while particles smaller than r^* will shrink and disappear.[81]

$$\begin{aligned} \Delta G &= -\frac{4}{3}\pi r^3 \Delta G_v + 4\pi r^2 \gamma \\ \frac{dG}{dr} &= -4\pi r^2 \Delta G_v + 8\pi r^2 \gamma \\ r &= r^* when \Delta G = 0 \\ r^* &= \frac{2\gamma}{\Delta G_v} \end{aligned} \tag{2.1}$$

By reducing the interfacial energy, γ, surfactants facilitate the nucleation of nanoparticles with a smaller initial size. These surfactants can further be used to modulate particle growth rates by binding reactive species or slowing the diffusion of atoms to the particle surface.[78] In addition to reducing interfacial energies, surfactants typically provide a steric barrier preventing the agglomeration of particles and the consequent growth of irregular morphologies.[77,82]

Colloidal syntheses commonly employ high-boiling organic solvents (i.e. 1-octadecene or benzyl ether) to enable decomposition temperatures up to ~300 °C. As such, surfactants typically contain a long aliphatic tail with a polar head group that can bond to the nanoparticle surface with covalent or dative bonds (i.e. oleic acid, oleylamine, trioctylphosphine, etc.).[77] In many reactions, surfactants are chosen by design to double as precursors, reducing agents, or reagents that accelerate the decomposition of the precursor (as in the case of Oleylamine in the reaction below). However, the reactivity of functional groups on the surfactants and as well as the solvents can result in unforeseen side reactions and

even the synthesis of unintended nanoparticle products.

The decomposition of precursors releases elemental feedstock into the solution. However, these reactive elements exist as transient clusters of atoms until they reach the critical radius as defined by the by equation 2.1 above. Equivalently, once the amount of reactive elemental species in solution reaches a critical concentration, particles will nucleate and grow. In general, monodisperse size distribution can be achieved if there is a short-lived nucleation event after which the concentration of elemental feedstock does not exceed the threshold concentration to form additional nuclei.[77,82]

This work describes the first colloidal synthesis of transition metal fluoride nanoparticles. The goal of this chapter is to understand the chemical and physical principles that govern this reaction and further provide a framework for the synthesis of additional transition metal fluoride species. This chapter first considers the single-source transition metal-fluorine precursor and examines how it's reactivity changes as a function of the solvent/surfactant environment. Based on these results I propose a possible chemical breakdown pathway. I further examine the nucleation and growth process and develop a means of achieving size/shape control in this system. Although the present work primarily concerns FeF_2, I extend the synthetic method to CoF_2 and lay the groundwork for the synthesis of NiF_2 and CuF_2. Monodisperse samples of these more energy dense compounds would be instrumental in understanding how the conversion mechanism changes as a function of transition metal crystal structure and electronegativity.

2.2 Single Source Precursors for Colloidal Synthesis

In the absence of any preceding work, some instruction for the colloidal synthesis of transition metal fluorides can be gleaned from the case of rare-earth metal fluorides, for which a wealth of colloidal synthesis recipes, involving the full gamut of rare-earth metals, has been reported.[52,79,83,84] The majority of these methods use rare-earth trifluoroacetates as single-source precursors for both the metal and the fluorine. Trifluoracetates and trifluoroacetic acid do not contain labile fluorine atoms, making them relatively safe compared to other HF releasing precursors.

Since as early as the 70's, metal trifluoroacetates have been known to decompose

upon heating (250 °C to 350 °C) in inert gas to form the corresponding anhydrous metal fluorides.[57–59] Both experimental and theoretical experiments suggest that the breakdown of trifluoroacetic acid begins with a fluorine transfer reaction via a relatively high energy intermediate, followed by a fast, complex multistep mechanism, for which the ultimate products are CO_2, CO, CHF_3, H_2O, and HF.[58,59] The thermal decomposition of metal trifluoroacetates in inert gas is thought to follow similar mechanisms in which a fluorine atom or fluoride ion is directly transferred to the metal center. Little effort has been made to understand the reaction mechanism of rare-earth trifluoroacetates during colloidal synthesis, and the mechanism is often simply suggested to be analogous to thermal decomposition in the gaseous environment.[79,84]

Whereas the decidely electropositive rare earth metals easily form stable fluorides, the more electronegative transition metal fluorides that are interesting for cathode applications are necessarily oxidizing and consequently less stable. Nevertheless, transition metal trifluoroacetates present a possible synthesis pathway. Recently, Guntlin *et al.* demonstrated the synthesis of FeF_2, CoF_2, MnF_2, and FeF_3 via the thermal decomposition of the corresponding solid trifluoroacetates and showed that the synthesis was highly economical.[41] In this case, thermal decomposition in argon at 295 °C for 24 h was required to form the phase pure transition metal fluoride. In the next section, I demonstrate that the reactivity of these trifluoroacetate precursors is significantly altered in the presence of solvents and surfactants.

The trifluoroacetate precursors themselves are synthesized in the anhydrous form via the prolonged reflux of transition metal chlorides with pure trifluoroacetic acid. For a typical synthesis, a ratio of 1 g of metal chloride to 10 ml (a very large excess) of trifluoroacetic acid is used; the duration of reflux varies from 24 h for iron (II) trifluroacetate to 72 h for cobalt trifluoroacetate. A full, detailed description of the precursor synthesis including purification and processing is given in Appendix I. Crystallization of the trifluoroacetate salt from the trifluoroacetic acid solution yields $M(CF_3COO^-)_2(CF_3COOH)_2$ (M = Mn, Fe, Co) (Figure 2.2). This reaction, given by equation 2.2 below, has an equilbrium that lies far to the left due to the much lower pKa of hydrochloric acid compared to trifluoroacetic acid.

$$MCl_2 + 2CF_3COOH \leftrightarrow M(CF_3COO^-)_2 + 2HCl \tag{2.2}$$

$$M = Fe, Co, Ni, Cu$$

$$pKa_{CF_3COOH} = -0.25$$

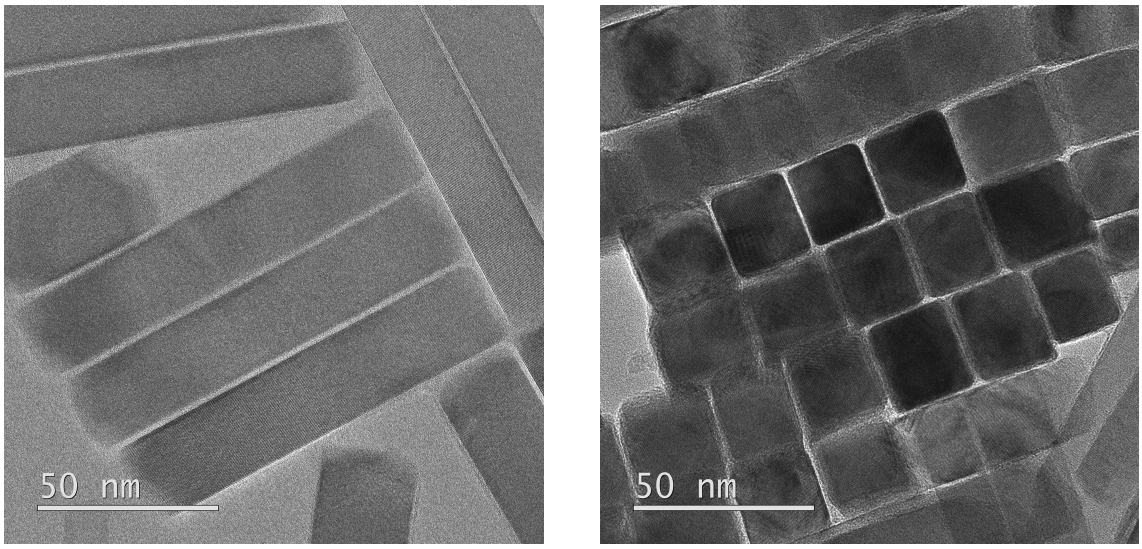
$$pKa_{HCl} = -8.0$$

However, this reaction is driven to completion as HCl (boiling point = –85.05 °C) is distilled off. Even so, as the electronegativity of the transition metal increases (from Fe → Cu) the equilibrium is shifted even more toward the metal chloride because Cl^- is a π electron donor and more polarizable than the CF_3COO^-.[27] For this reason, trifluoroacetates of Ni(II) and Cu(II) cannot be prepared in this way, as negligible yields are obtained even after many days of reflux. Instead Ni(II) and Cu(II) trifluoroacetates were prepared by reaction of $Ni(OH)_2$ and CuO with pure trifluoroacetic acid; however, these compounds exhibit a stoichiometry closer to $M(CF_3COO^-)_2$ (M = Ni, Cu) presumably to the coordination of water in place of trifluoracetic acid (Figure 2.2). The synthesis of FeF_2 nanorods from $Fe(CF_3COO^-)_2(CF_3COOH)_2$ is examined in detail below. Syntheses of CoF_2, NiF_2, and CuF_2 are discussed at the end of the chapter.



Figure 2.2: Transition Metal Trifluoroacetate Precursors. Trifluoracetate salts of Fe, Co, Ni, Cu synthesized via reaction of trifluoroacetic acid (CF_3COOH) with $FeCl_2$, $CoCl_2$, $Ni(OH)_2$, CuO respectively.

2.3 Mechanism of Metal Fluoride Formation



(a) Side view: ⟨1 1 0⟩ zone axis. **(b)** End-on view: ⟨0 0 1⟩ zone axis.

Figure 2.3: FeF_2 Nanorods from Different Perspectives. (BF TEM.) These complementary images reveal the full 3-dimensional morphology of the FeF_2 nanorods. This square prismatic morphology facilitates structural characterization of the conversion mechanism presented in **Chapter 4**. Curved surfaces are apparent between planar facets; their role in nanorod growth is described below.

A detailed synthetic recipe for the FeF_2 nanorods including chemicals, experimental setup, and purification procendure is given in Appendix I. Briefly, a typical FeF_2 nanorod synthesis begins with the dissolution of 0.75 mmol of iron(II) trifluoroacetate ($Fe(CF_3COO^-)_2(CF_3COOH)_2$) with 3.5 ml each of oleic acid (OLAC) and oleylamine (OLAM) in 7 ml of 1-octadecene (ODE). The mixture is attached to a Schlenk line, degassed and heated to 310 °C under inert gas (N_2) flow for 2 h. This recipe can be scaled linearly by up to a factor of four for yields as high as 250 mg of monodisperse FeF_2 nanorods. The reaction temperature can be varied between 290 °C to 320 °C to control the aspect ratio of the resulting nanorods, as discussed in Section 2.5 below. Formation of FeF_2 is indicated by the transition from a clear, light-yellow solution to a translucent, off-white suspension. The low concentration of precursor reduces the rate of nanoparticle growth and facilitates small particle sizes. The result of a typical synthesis is shown in Figure 2.3. The reaction temperature was chosen to align with that used for solvent-less decomposition.[41] The large excess of surfactants (OLAC and OLAM) was determined by surveying a number of colloidal synthesis recipes for rare-earth metal fluoride nanoparti-

cles. Other studies have demonstrated that OLAC is the primary surfactant in systems where both OLAC and OLAM are present. The acid-base equilibrium between oleylamine and oleic acid, shown in equation 2.3 below, increases the concentration of the oleate ion which bind more strongly to the nanoparticle surface.[85]

$$\begin{gathered} \mathrm{R{-}CH_2NH_2 + R{-}COOH \leftrightarrow R{-}CH_2NH_3^+ + R{-}COO^-} \\ R = \mathrm{C_8H_{17}CH{=}CH(CH_2)_7} \end{gathered} \tag{2.3}$$

Indeed, fourier transformed infrared spectroscopy (FTIR) of the washed nanorods shows that OLAC is present as the sole surfactant (Figure 2.4).

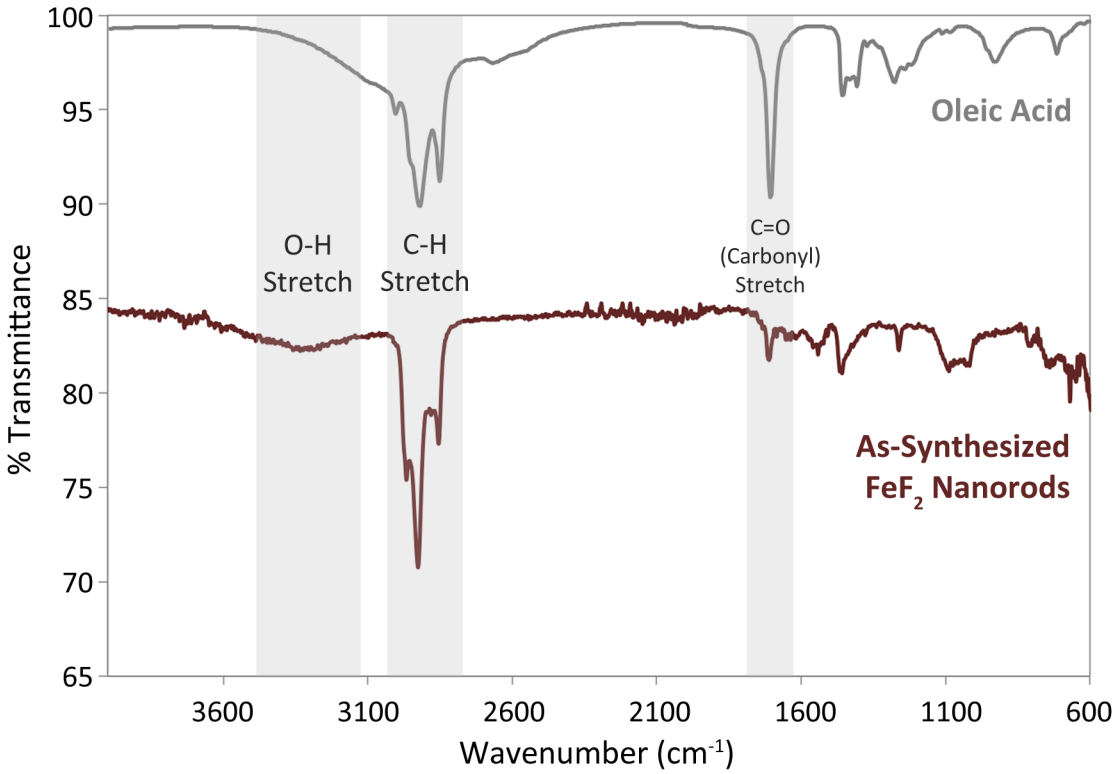


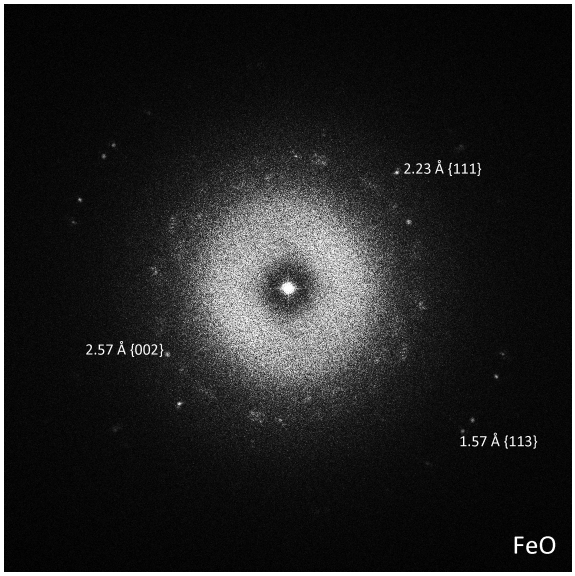
Figure 2.4: FeF_2 Nanorod Surface Chemistry. FTIR Spectra of pure OLAC and As-synthesized FeF_2 nanorods after washing. Vibrational modes characteristic of OLAM are not observed.

The reaction described above produces >90% yield of FeF_2 after 2 h as opposed to the 24 h reported by Guntlin *et al.*.[41] Clearly, the other species present in solution augment the reactivity of the trifluoroacetate precursor significantly. To empirically understand the role of each chemical species, a set of control experiments was performed by heating $Fe(CF_3COO^-)_2(CF_3COOH)_2$ to the reaction temperature in just one solvent/surfactant at a time. The solvent, ODE, was confirmed to be largely inactive, as virtually no visible reaction

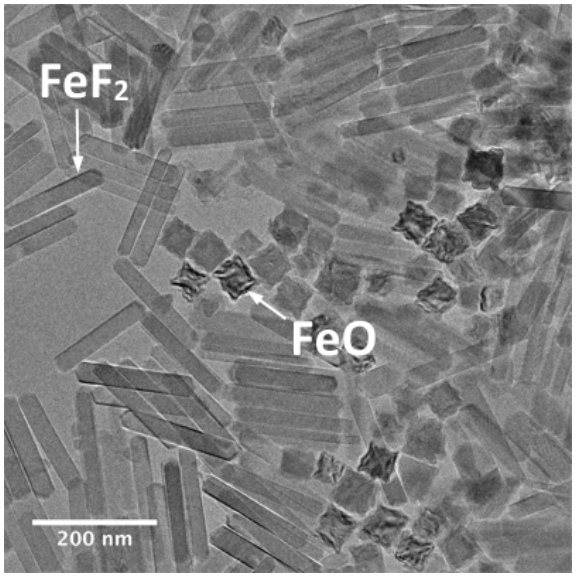
was observed apart from minute bubbling close to the reaction temperature. Likewise, no significant reaction was observed in the OLAC solution, suggesting that OLAM is primarily responsible for the increased reactivity. Interestingly, however, decomposition of the trifluoroacetate precursor in large excess (>2 ml) of pure OLAM results in an entirely different product, as evidenced by the rapid formation of a dark brown/black dispersion. HRTEM confirms lattice spacings characteristic of iron oxide (FeO). Smaller excesses (1 ml) produced a mixture of iron fluoride and oxide particles (Figure 2.5).



(a) Photograph of colloidal dispersion



(b) FFT of BF TEM image (not shown)



(c) Low mag BF TEM image

Figure 2.5: Iron Oxide Formation. FeF_2/FeO nanoparticle mixture produced by thermal decomposition of Fe(II) trifluoroacetate in the presence of a small excess of OLAM. The two different products are evidence of competing reaction pathways.

In order to understand this phenomenon, it is important to understand that iron(II) acetate ($Fe^{2+}(CH_3COO^-)_2$), the unfluorinated anologue to iron(II) trifluoroacetate, has played a large role in the colloidal synthesis of iron oxide particles. In fact, if iron(II) acetate is used in place of the trifluoroacetate under reaction conditions identical to those described above, iron oxide nanoparticles are formed as the sole product. It has been proposed that OLAM plays a critical role in the formation of iron oxide clusters via a mechanism similar to that shown in Figure 2.6 below).

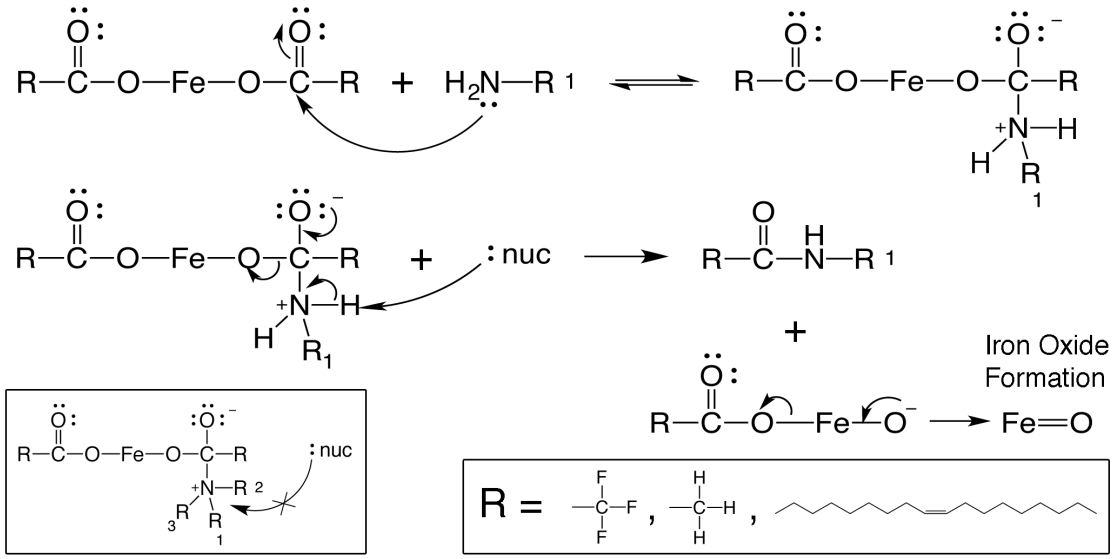


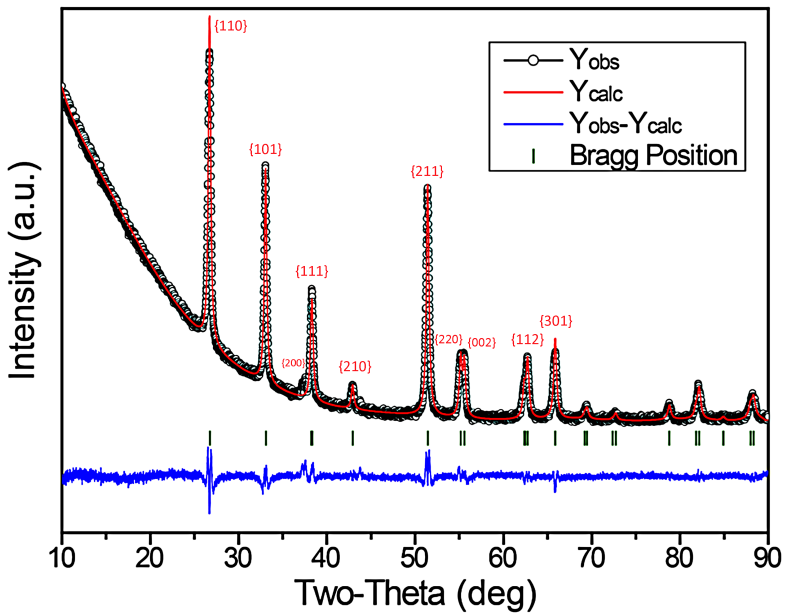
Figure 2.6: Chemical Pathway of FeF_2 Formation. The formation of iron-oxide particles is observed when the amount of OLAM exceeds the amount of OLAC. Empirical data suggests an iron oxide intermediate plays a role in the high yield synthesis of FeF_2 nanorods. This figure shows a possible chemical reaction mechanism for the OLAM mediated formation of Fe−O bonds. This mechanism requires either a primary or secondary amine and does not occur with tertiary amines.[86]

The electron withdrawing nature of the trifluoromethyl group would only serve to increase the likelihood of this reaction, suggesting that it would also be ongoing during synthesis of the transition metal fluoride. According to the reaction mechanism below, the formation of Fe-O bonds requires either a primary (i.e. oleylamine) or secondary amine, as tertiary amines lack the labile proton required to complete the reaction.[86] In order to determine whether this reaction was critical to the formation of the FeF_2, a control experiment was performed in which oleylamine was replaced with an equivalent molar amount of dimethylhexadecylamine (a tertiary amine). In this case, under otherwise identical reaction conditions, a negligible amount of FeF_2 was obtained. This indicates that the oxide intermediate formed through the reaction above is required for the accelerated

formation of the transition metal fluoride. The above discussion outlines the chemical mechanism for fluoride formation. The next section considers the physical basis for the formation of monodisperse nanorods.

2.3.1 Nanorod Structure and Composition

As mentioned in **Chapter 1**, oxygen substitution introduces Fe^{3+} and intercalation behavior on discharge that would complicate mechanistic analysis.[42] Although, the mechanism proposed above involves the reaction of transient Fe-O intermediates, the resulting product corresponds to phase pure FeF_2. The presence of any oxy-fluoride phase can be excluded by X-ray diffraction (XRD) (Figure 2.7) and energy dispersive X-ray spectroscopy (EDX) (Figure 2.8).



(a) Powder XRD pattern of the as-synthesized FeF_2 nanrods and calculated pattern generated by Rietveld refinement.

Parameters	FeF_2 Nanorods	Literature Standard[87]
a (Å)	4.7042(1)	4.6945(4)
c (Å)	3.3031(1)	3.3097(1)
$\alpha = \beta = \gamma$ (°)	90	90
V (Å^3)	73.096(5)	72.940(5)

(b) Refined lattice parameters and cell volume.

Figure 2.7: Pristine Nanorod Crystal Structure. Rietveld refinement of as-synthesized FeF_2 nanorods with calculated lattice parameters and cell volume. A close match is observed between the FeF_2 nanorods and the standard structure of FeF_2 from the literature.[87]

Pereira *et al.* demonstrated that the substitution of O^{2-} for F^- in the FeF_2 lattice results in a near linear contraction of the "c" lattice parameter from 3.304 Å for pure FeF_2 to 3.04 Å for stoichiometric FeOF (~ 0.008 Å for every 1 at.% O^{2-}).[42] The refined "c" lattice parameter from the powder XRD pattern of the FeF_2 nanorods (Figure 2.7) closely matches the literature value for chemically pure FeF_2. Based on the correlation presented by Pereira *et al.*, this "c" lattice parameter suggests an oxygen content no greater than 0.11 at.%. Additionally, EDX shows a shadow in the oxygen intensity in the area of the nanorods further indicating the absence of oxygen in the as-synthesized nanorods (Figure 2.8). Qualitatively, the EDX elemental maps suggest that the FeF_2 nanorods are composed primarily of Fe and F, as no other characteristic X-ray signals were localized to the region of the nanorods. However, a quantitative stoichiometry could not be obtained using EDX due to the strong overlap between the FKα, the FeLα, and other spurious X-rays from the microscope. Quantification of fluorine content is already inherently difficult due to its relatively low fluorescence yield and the tendency of the low energy FKα X-rays to be absorbed before detection. In the Chapter 3, we will demonstrate that the as synthesized nanorods exhibit a reversible capacity close to the theoretical value as well as a galvanostatic profile similar to that reported for commercially available FeF_2.[22,71] These observations, in conjunction with the close match in lattice parameters suggest a stoichiometry close to FeF_2.

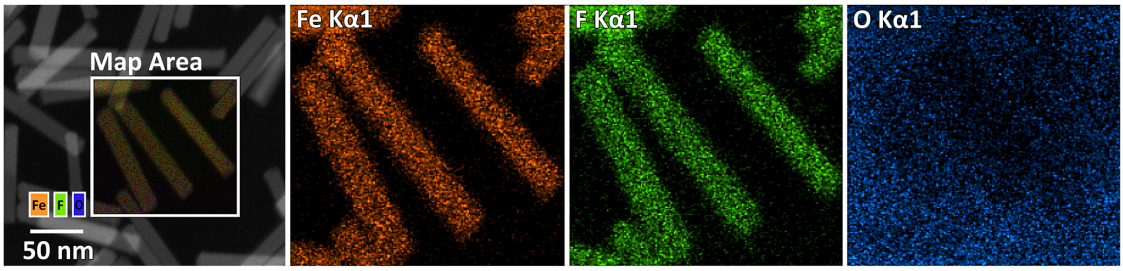


Figure 2.8: Elemental Composition. (Annular Dark Field [ADF] STEM and EDX) EDX map of as-synthesized FeF_2 nanorods, which shows strong Fe and F signals and excludes the presence of oxyfluoride.

2.4 Nucleation and Growth of FeF_2 Nanorods

The rate of precursor decomposition in the reaction described above is extremely slow compared to the majority of colloidal synthesis methods (2 h vs <30 min). However, this slow introduction of elemental feedstock to the reaction limits consecutive or continuous nucleation events and is actually conducive to the formation of a monodisperse sample.[77,78] Nanorod polydispersity decreases during the first hour of the reaction, and subsequent uniform growth results in >90% yield after 2 hours. The resultant nanorods are monodisperse (Figure 2.1) to the point of spontaneously packing into 2D and 3D superlattices, when dried as a powder (Figure 2.9).

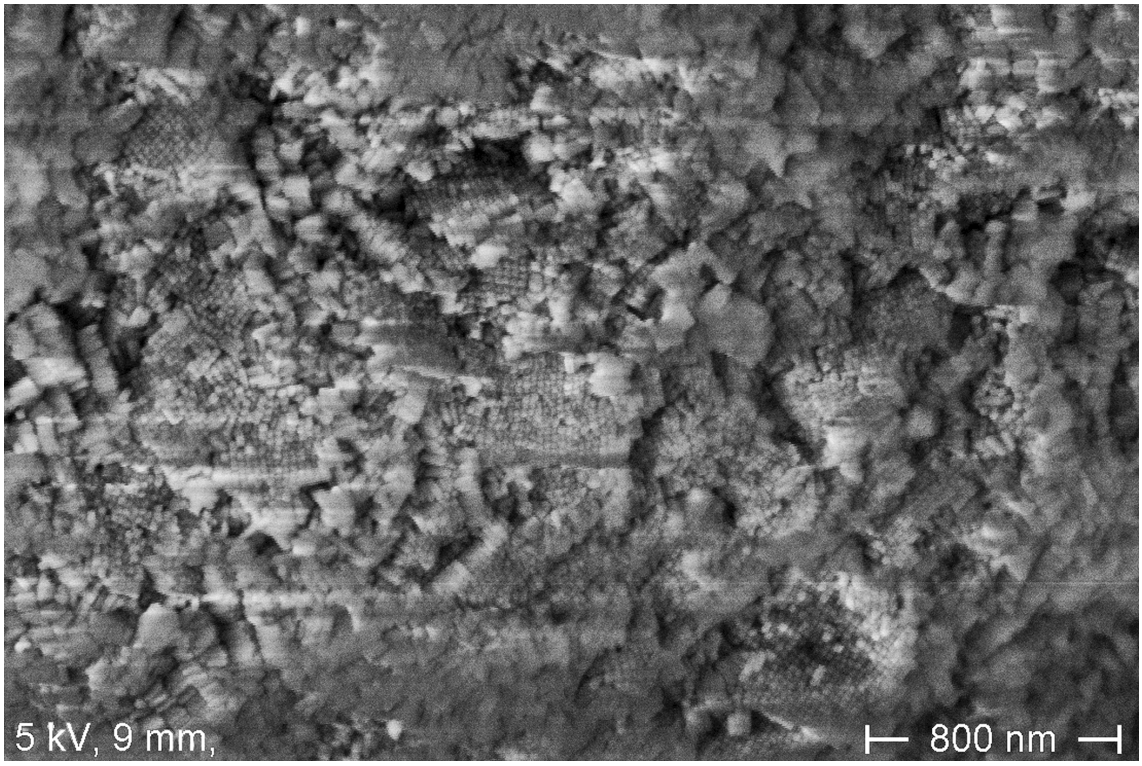


Figure 2.9: Supercrystallinity. (Secondary electron [SE] SEM.) SEM image of as-synthesized FeF_2 nanorods after centrifugation and precipitation and drying. FeF_2 nanorods pack into simple square superlattices in two dimensions. Layering of these square-packed layers produces three-dimensional superlattices. This supercrystallinity is enabled by the monodispersity of the FeF_2 nanrods.

The nanorods produced by the reaction above are defined by sharp surface facets and a highly anisotropic shape. During an equilibrium reaction, the free energies of atoms in the solid and the solution are equal by definition; however atoms at the interface between these phases exhibit a higher free energy.[81] Atomically sharp interfaces (faceting) occur

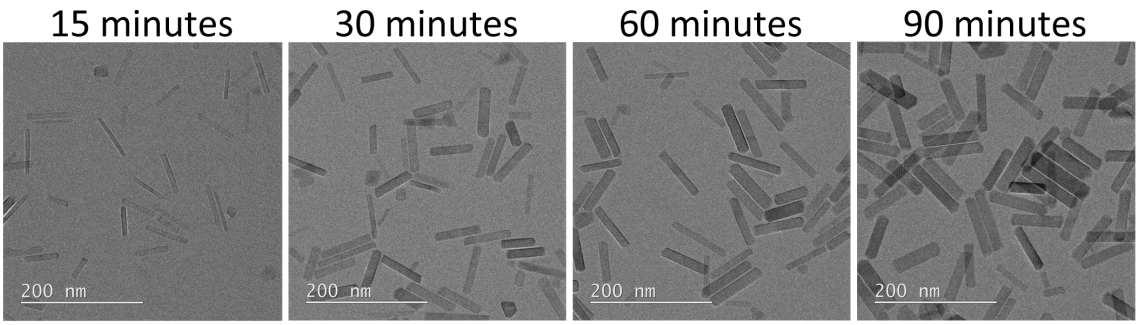
when the magnitude of this excess energy is sufficiently high. Empirically, faceting is predicted for systems where the enthalpy of dissolution divided by the reaction temperature yields a value larger than 4R, where R is the ideal gas constant (Equation 2.4). While the absolute value of this calculation is of little use to us, it is worth noting that faceting will occur unless the reaction temperature or the solubility of the metal fluoride in the reaction media is drastically increased.

$$\frac{\Delta H_{solv}}{T_{rxn}} > 4R$$
$$R = Ideal\ Gas\ Constant \tag{2.4}$$

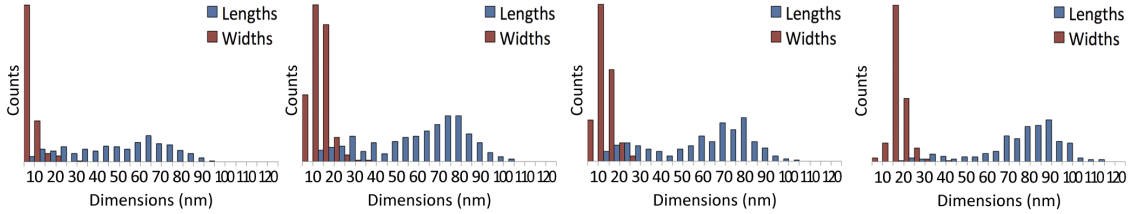
In the case of faceted systems, the equilibrium shape and lattice orientation of the nanocrystals are defined by the relative surface/interfacial energies on different crystallographic planes. The Wulff theorem indicates that a single crystal will be truncated along its lowest energy interfaces with the relative area of each facet inversely proportional to its interfacial free energy.[81] Ma and Garofalini calculated that $\{1\,1\,0\}$ and $\{0\,0\,1\}$ planes exhibit the lowest surface energies for FeF_2, and indeed these are the exact facets observed on my FeF_2 nanorods.[19] Thus, from a thermodynamic standpoint, the lattice orientation of every nanorod must be identical. These surface facets are important for understanding how monodisperse samples are formed.

The monodispersity of the as-synthesized nanorods is partially a result of slow precursor decomposition which maintains low concentrations of elemental feedstock to the reaction, preventing consecutive or continuous nucleation events. However, the formation of initial nuclei also plays a large role in defining the morphology of the final sample. Figure 2.10 below shows the progression in morphology of the growing FeF_2 nanorods. Interestingly, there are two distinct morphologies observed early in the reaction, as indicated by the bimodal distribution of lengths and aspect ratios (Figure 2.10b, 2.10c). This is a result of nucleation over a range of temperatures on heating and can be rationalized based on the critical particle size for nucleation. When the free energy of the reaction is large, nuclei will form with a higher surface area to volume ratio, yielding either smaller nuclei or nuclei with a larger aspect ratio. Assuming that the free energy of the reaction increases with temperature (as evidenced by an increasing reaction rate), the first nuclei to form at lower temperatures will exhibit a short and wide morphology, while those that form at the

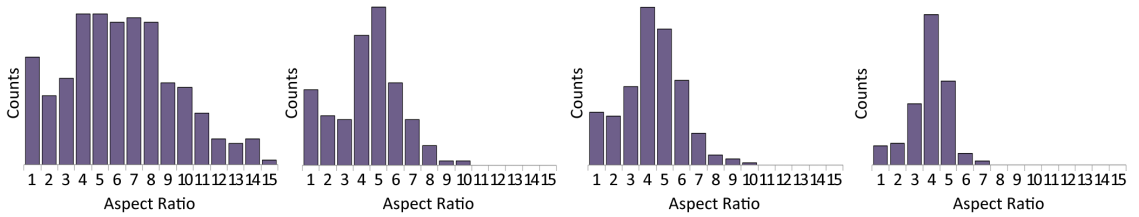
reaction temperature will be long and thin, as can be seen in Figure 2.10a.



(a) TEM images of FeF_2 nanorods at different reaction times.



(b) Progression of nanorod dimensions during synthesis.



(c) Progression of nanorod aspect ratios during synthesis.

Figure 2.10: Nucleation and Growth. (BF TEM.) Evolution of particle morphology during the colloidal synthesis of FeF_2 nanorods. Aliquots were taken from the reaction mixture after 15, 30, 60 and 90 min. Histograms were generated from ~300 unique particles per sample, measured from multiple TEM images. The average nanorod dimensions are 53.9±21.6 nm by 9.0±3.7 nm (15 min), 62.8±22.6 nm by 14.2±4.0 nm (30 min), 64.0±22.2 nm by 14.5±4.5 nm (60 min), 80.6±18.5 nm by 18.9±3.8 nm (90 min). The average aspect ratios are 6.7±3.3 (15 min), 4.8±2.0 (30 min), 4.7±1.8 (60 min), 4.4±1.2 (90 min).

This polydispersity can be lessened if a faster heating rate is applied so that initial nuclei form over a narrower temperature range. However, in even in the case of an initially non-uniform distribution, a monodisperse sample can still form. At 15 min, the reaction mixture contains long, thin precipitates as well as nearly cubic precipitates marked by a distribution of particles with an aspect ratio of ~1. As the reaction continues, both the mean lengths and widths increase, indicating that growth occurs on both the $\{1\,1\,0\}$ and $\{0\,0\,1\}$ facets. At 30 min, the bimodal distribution is clear; however, between 30 min and

90 min, the distributions of lengths, widths and aspect ratios begin to converge on a single morphology. Typically, growth is kinetically limited normal to low-energy planar interfaces such as the $\{1\,1\,0\}$, and one would expect growth to occur primarily in the $\langle 0\,0\,1\rangle$ direction, which is visibly curved. However, this would result in diverging rather than converging morphologies. Recall that the nanorods are curved where the $\{1\,1\,0\}$ surfaces meet (Figure 2.3, Figure 2.11). For the exceedingly thin rods observed early in the reaction, the sides of the nanorods would be dominated by curved surfaces and growth in the $\langle 1\,1\,0\rangle$ direction would be comparable to that in the $\langle 0\,0\,1\rangle$ direction. For the nuclei that form with initially larger widths, the sides of the nanorods would be dominated by planar $\{1\,1\,0\}$ surfaces, and growth will occur primarily in the $\langle 0\,0\,1\rangle$ direction (Figure 2.11). Given a sufficiently long reaction, the initial precipitates will converge on a similar morphology. This is evidenced by a decrease in the standard deviation of both lengths and widths from ~40% to ~20% over the first 90 min of reaction shown in Figure 2.10. The standard deviations decrease further as the reaction proceeds to completion at ~2 h (often to between 10% and 15% as shown in Figure 2.1).

2.5 Size and Shape Control

For non-cubic crystal systems such as the tetragonal FeF_2, there is generally one preferred direction of ion transport within the lattice. In **Chapter 4**, it will be shown that this anisotropy in transport properties plays a large role in defining the reaction mechanism. As such, control over the shape as well as the size of nanoparticles is essential for developing a truly optimized electrode. A degree of size and shape control in colloidal synthesis is most commonly achieved by tuning the ratios of surfactant mixtures.[88] In the case of the reaction above, OLAC is the primary surfactant, and while OLAM is sometimes considered a co-surfactant, it does not bind strongly to the nanoparticle surface. As demonstrated above, changing the OLAM:OLAC ratio greatly affects the reaction rates and even the reaction product, so this was excluded as a method of shape control. The further addition of other surfactants was also avoided for the sake of simplicity.

The growth mechanism outlined in the previous section can, however, can be manipulated to tune the aspect ratio of the FeF_2 nanorods. It was observed that if the reaction

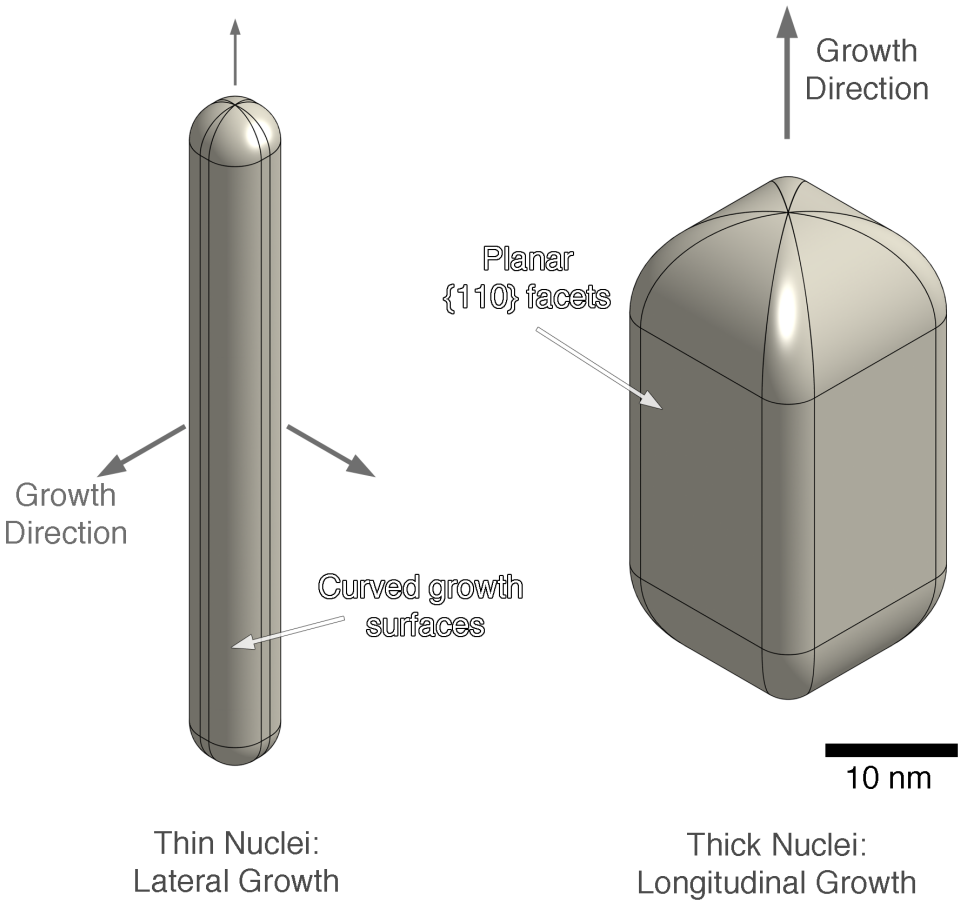
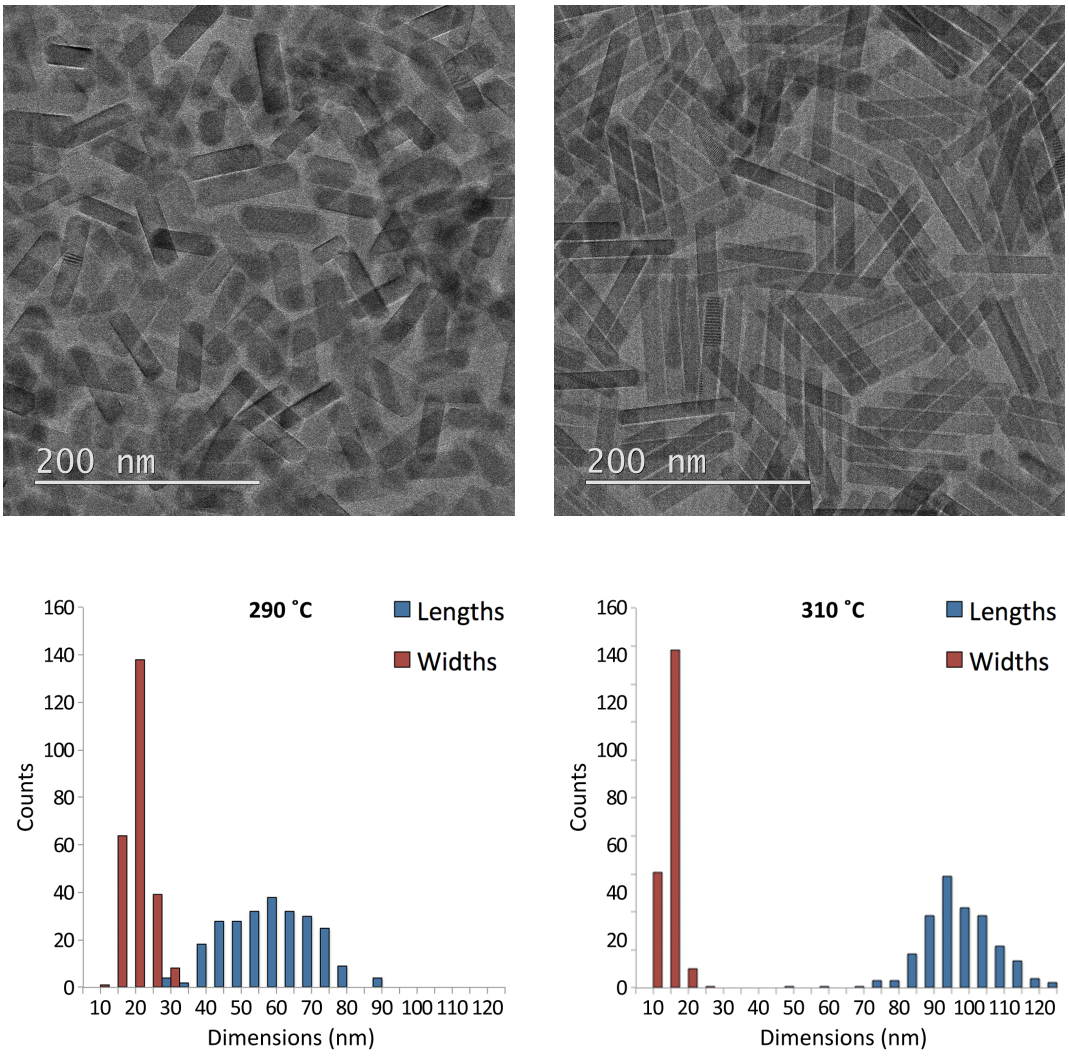


Figure 2.11: Convergent Growth of Disparate FeF_2 nuclei. This schematic shows the 3D morphology of the two types of nuclei observed early in the colloidal synthesis of FeF_2 (Figure 2.10a). Nuclei with different aspect ratios form at different temperatures. The addition of atoms to planar interfaces is thermodynamically unfavorable and growth typically occurs on high energy (curved) interfaces. The two nuclei morphologies have different predominant growth directions and converge on a similar morphology.

temperature is lowered to 290 °C, the entire product consists of short fat nanorods (aspect ratio 2.8±0.6) as opposed to the thinner ones (aspect ratio 6.2±0.9) produced at 310 °C (Figure 2.12). As the reaction temperature is decreased, the formation of nuclei is constrained to particles with low surface area to volume ratios. At sufficiently low temperatures, this condition is satisfied by nuclei with not only lower aspect ratios but also larger particle sizes. In this case, the large $\langle 110 \rangle$ dimensions of the nuclei limits growth to the $\langle 001 \rangle$ directions, meaning that nuclei elongate as they grow, resulting in nanorods with a larger horizontal cross-section.

In general, there is no mechanism by which the diameter of larger nanorods can shrink, and the initial diameter of wide nuclei is largely preserved. In Figure 2.13a below, the



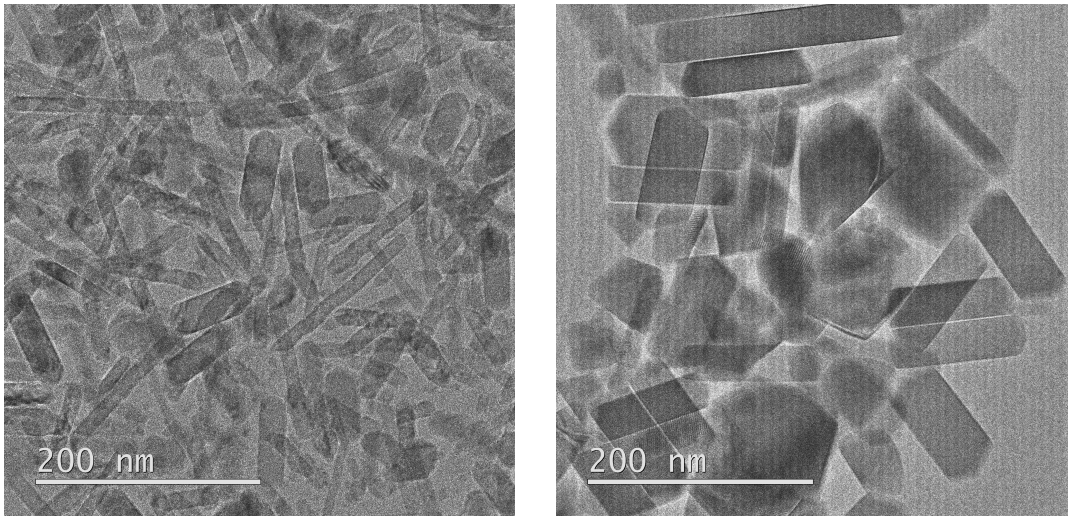
(a) FeF_2 nanorods synthesized at 290 °C **(b)** FeF_2 nanorods synthesized at 310 °C

Figure 2.12: Size and Shape Control. (BF TEM.) TEM images and histograms comparing the morphology of FeF_2 nanorods synthesized at 290 and 310 °C. The nanorod aspect ratio can be tuned by controlling the reaction temperature, with higher temperatures resulting in longer, thinner rods. a) Average dimensions: 61.6±12.2 nm by 22.2±3.5 nm; average aspect ratio: 2.8±0.6. b) Average dimensions: 100.8±10.4 nm by 16.5±2.1 nm; average aspect ratio: 6.2±0.9.

reaction was allowed to proceed at 290 °C for 1 h and then raised to 310 °C for a second hour. In the 1st hour, the short, wide nanorods have begun to form; however, the rate of reaction at this temperature is slow, and there is a significant concentration of unreacted precursor. As the temperature is raised to 310 °C, additional nuclei form with much smaller widths and the growth of long, thin nanorods is observed.

This example illustrates that narrowing of the size distributions is only observed if the widths of initial nuclei are very small, and if exceedingly large nuclei are formed below the final reaction temperature, than the final product is decidely polydisperse. This can also

occur in the case of high precursor concentrations which accelerate reaction rates at lower temperatures, Figure 2.13b below.



(a) Multiple reaction temperatures **(b)** High precursor concentration

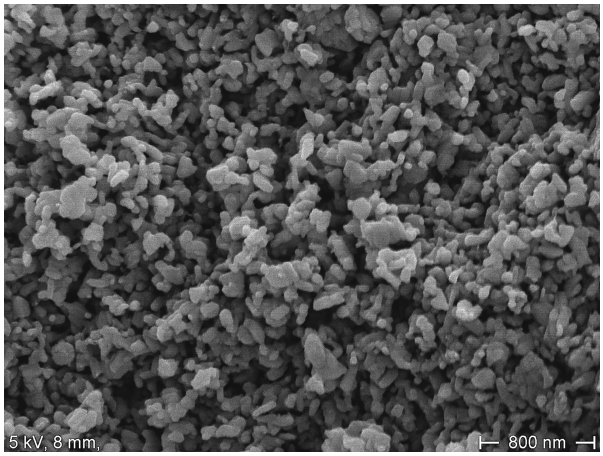
Figure 2.13: Polydisperse Nanorods. (BF TEM.) TEM images of FeF_2 nanorods showing the polydisperse products obtained when large nuclei are formed below the final reaction temperature. Figure (a) shows the result of deliberately holding the reaction temperature at 290 °C before raising the reaction temperature to 310 °C. Figure (b) shows FeF_2 nanorods synthesized at high precursor concentration, which increases reaction rates at lower temperatures.

2.6 Ligand Exchange Techniques

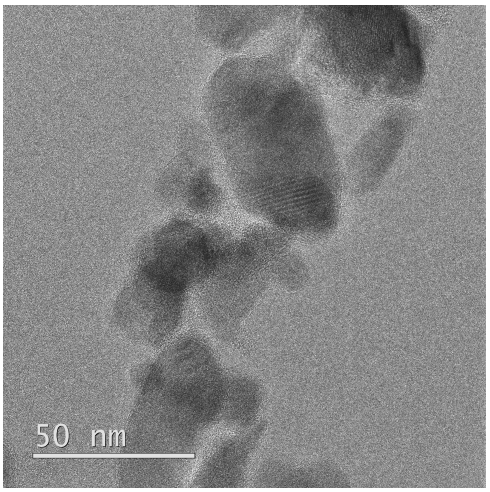
The use of surfactants in the synthesis is essential to stabilizing small, high surface area particles and preventing the growth of irregular morphologies.[77,78] However, because surfactants (i.e. OLAC) are typically covalently bonded to the nanoparticle surface, they cannot be displaced by simple heating or washing procedures. In the next chapter, I examine the electrochemical properties of the FeF_2 nanorods; certain surfactants, if present in high concentrations in the electrode, can lead to detrimental redox reactions and a large irreversible capacity. Fortunately, the reduction potential of carboxylic acids is approximately 0.5 V vs Li^+/Li, while that of carboxylates is greater than 4.0 V vs Li^+/Li, and no OLAC related redox reactions were observed in my cycling experiments.[89]

However, if higher or lower potential ranges are used for cycling, then a means of surfactant removal is required. A commonly employed strategy involves annealing the nanoparticles in an inert atmosphere, which generates a carbon coating in the process.[90,91] However, in the case of FeF_2 nanorods, significant solid state diffusion and near

complete loss of nanorod morphology was observed (Figure 2.14) below the temperature required to achieve complete carbonization (500 °C to 800 °C).[90,91] The most reliable way of completely removing surfactants is through a ligand exchange. Dong *et al.* developed a nearly universal ligand exchange method using a nitrosonium tetrafluoroborate salt ($NO^+BF_4^-$).[92] $NO^+BF_4^-$ added to the colloidal dispersion generates acidic species *in-situ* via decomposition of the NO^+ cation; the resulting protonation of both amines and weak acids facilitates their desorption and replacement with the more abundant BF_4^- anions. We adapted this method using $NO^+PF_6^-$ to match the anion more commonly found in lithium ion battery electrolytes. Figure 2.15 below depicts the ligand exchange process whereby the FeF_2 nanorods are transferred from the nonpolar (top) phase where they are sterically stabilized by the aliphatic ligands to the polar phase (bottom) where they are charge stabilized by the PF_6^- ligands. FTIR before and after this ligand exchange process indicates near complete removal of the OLAC.



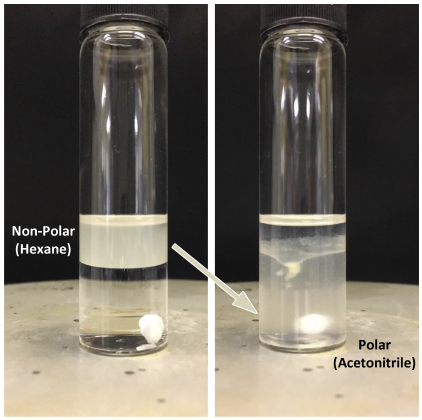
(a) Low mag SE SEM



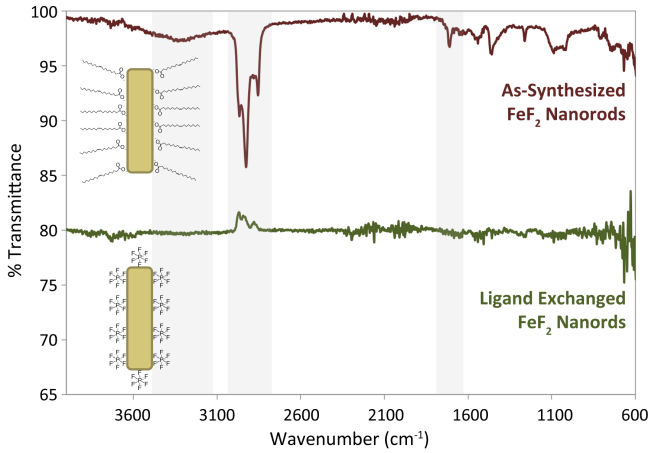
(b) BF TEM micrograph

Figure 2.14: Thermal Annealing. SEM (a) and TEM (b) micrographs showing FeF_2 particles after annealing at 450 °C. The loss of nanorod morphology and the growth of irregular shapes indicates that significant solid state diffusion occurs far below the melting point of FeF_2 (970 °C. However, this annealing temperature is still too low to carbonize the OLAC surfactant.

In the next chapter, I detail the use of an N-methyl-N-propylpyrrolidinium fluorosulfonylimide ($Pyr_{1,3}FSI$) ionic liquid based electrolyte. It was discovered that replacement of the OLAC surfactant with FSI anions could be readily achieved by simply treating the FeF_2 nanorod dispersion with an excess of lithium fluorosulfonylimide dissolved in anhydrous isopropanol (IPA).



(a) Photograph of the phase-transfer ligand exchange process.



(b) FTIR spectra showing removal of OLAC ligands.

Figure 2.15: Ligand Exchange. Treatment of as-synthesized nanorods with nitrosonium hexafluorophosphate ($NO^+PF_6^-$) removes the OLAC ligands and replaces them with PF_6^- ligands. This process is depicted in (a), with the FeF_2 nanorods moving from the non-polar to the polar phase upon completion of the ligand exchange. Removal of OLAC is evident from FTIR spectra post ligand exchange (b).

2.7 Alternative Precursors and Other Transition Metal Fluorides

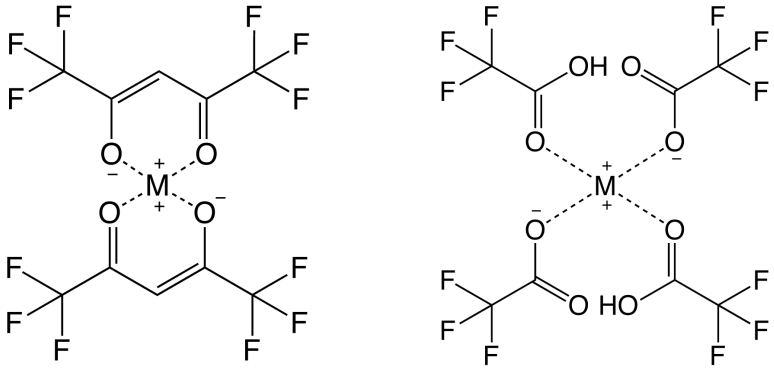
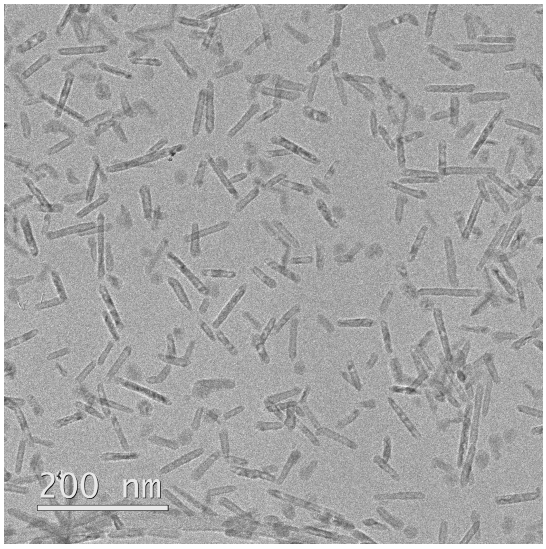


Figure 2.16: Comparison of Precursor Structures. Both transition metal trifluoroacetates and hexafluoroacetylacetonates were used to synthesize transition metal fluoride nanorods. The two compounds share a similar structure and elemental composition.

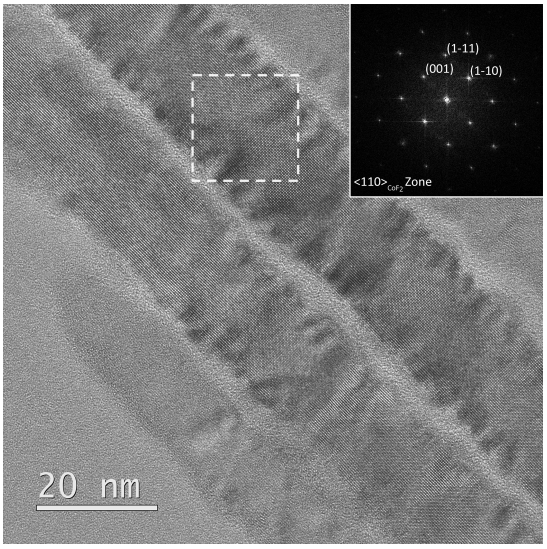
The colloidal synthesis of FeF_2 and its corresponding precursor occurs quite readily. However, the difficulty of generating stoichiometric precursors in the case of Co, Ni, and Cu proved detrimental to the reproducability of the syntheses and the reliabiity of the results. For this reason, further synthetic investigations were conducted using the related hexafluoroacetylacetonate salts of Co, Ni, and Cu, which are commericially available.

These precursors resemble the metal trifluoroacetates in both structure and reactivity

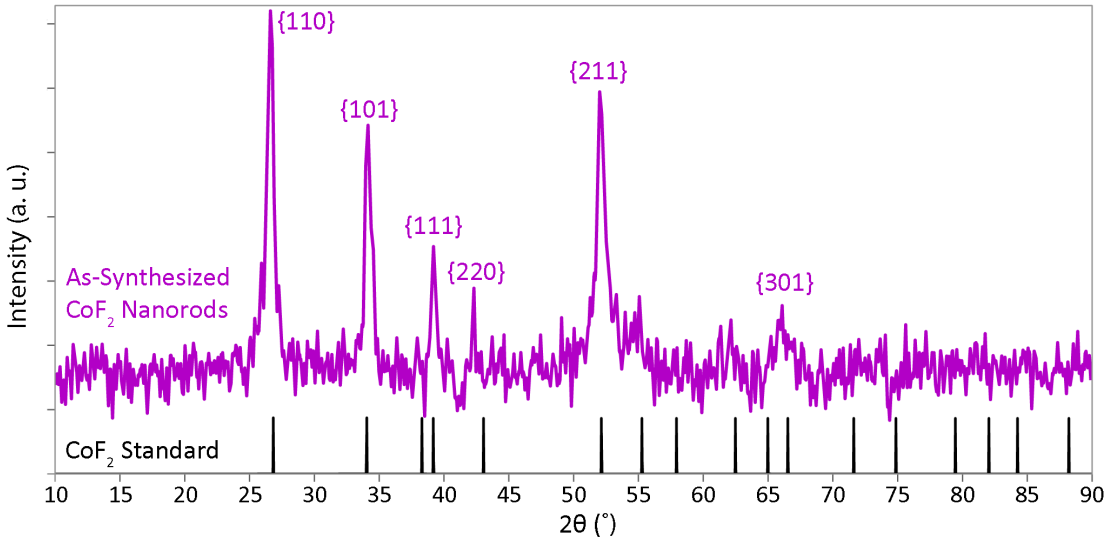
and their non-fluorinated anologues (acetylacetonate salts) are well known precursors for metal oxide nanoparticles (Figure 2.16).[80,93]



(a) Low mag TEM image.



(b) High resolution TEM image, FFT inset.

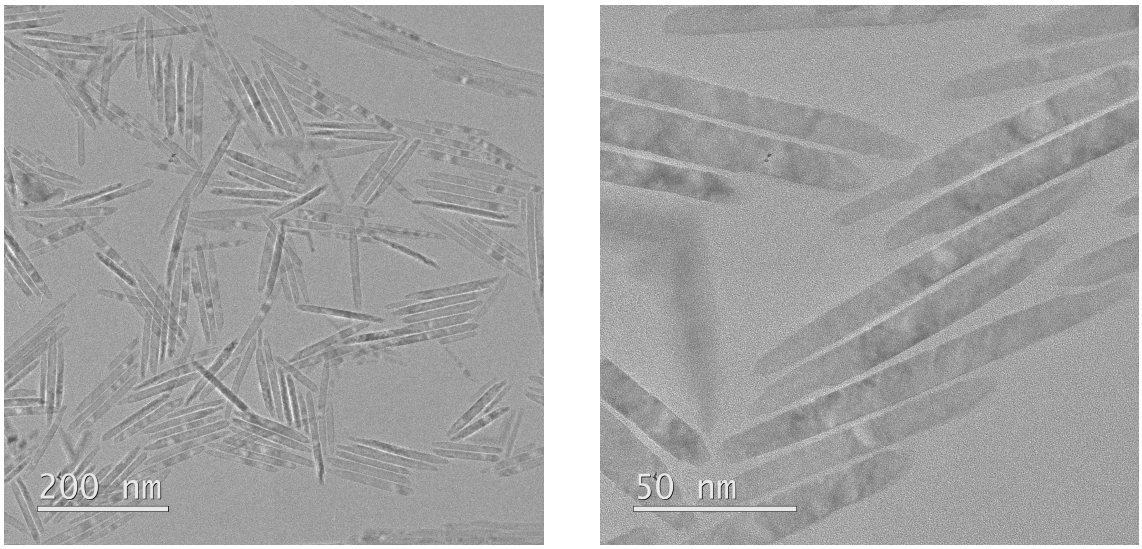


(c) Powder XRD pattern of as-synthesized CoF_2 nanorods.

Figure 2.17: CoF_2 Nanorods (TFA Precursor). (BF TEM.) Cobalt fluoride nanorods synthesized at 320 °C using the $Co(TFA)_4$ precursor. CoF_2 nanorods exhibit a uniform morphology but a more disordered structure than the FeF_2 nanorods. Crystal structure and lattice orientation of the CoF_2 nanorods is analogous to the FeF_2 system. XRD (c) confirms the presence of the tetragonal CoF_2 crystal structure.

The colloidal synthesis of higher energy transition metal fluorides becomes increasingly difficult, because the same high reduction potentials that makes these compounds desirable, also by definition, makes them strong oxidizing agents. CoF_2, with its more modest reduction potential (2.78 V vs Li^+/Li) was synthesized quite readily; however, the

same reaction temperatures (290 °C-310 °C) produced much lower yields (<30%) with a lower degree of crystallinity. At higher temperatures (320 °C-330 °C), both yields and crystallinity were improved. In the case of CoF_2, more uniform and highly crystalline nanoparticles were produced using the commercially available hexafluoroacetylacetonate (HFAC) precursors, suggesting that precursor purity is important to nanorod quality. Despite this success, further improvements in yield are required before these CoF_2 nanorods can be tested in batteries.

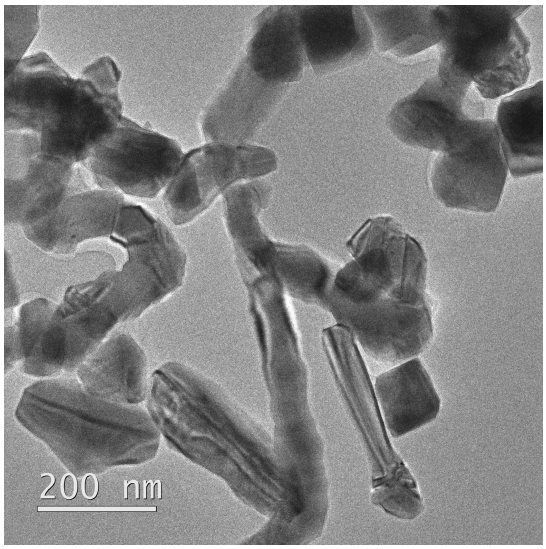


(a) Low Magnification. **(b)** High Magnification.

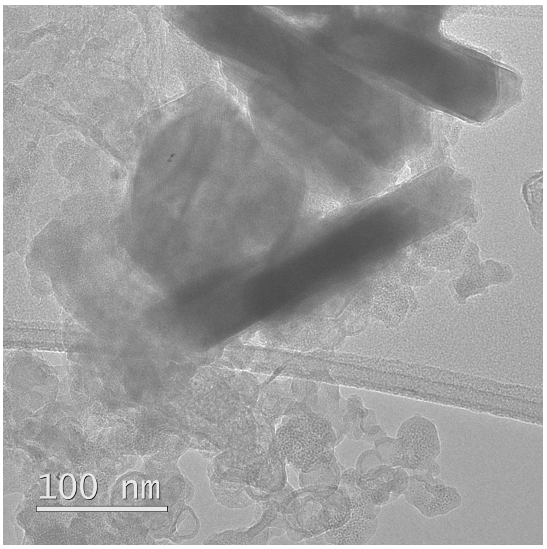
Figure 2.18: CoF_2 Nanorods (HFAC Precursor). (BF TEM.) Cobalt fluoride nanorods synthesized at 320 °C using the commercial $Co(HFAC)_2$ precursor. Both monodispersity and crystallinity are improved over CoF_2 nanorods synthesized with the $Co(TFA)_4$ precursor.

Issues in the colloidal synthesis of transition metal fluorides arise at nickel fluoride (NiF_2) (3.2 V vs Li^+/Li). If the exact synthesis parameters outlined above are applied to the nickel(II) trifluoroaceatate precursor, the major product consists of phase pure metallic nickel as evidenced by the XRD plot. In the case of the HFAC precursor, some large NiF_2 nanoparticles are observed; however, the major product is still metallic nickel suggesting the inherent instability of Ni^{2+} species in the reaction mixture at high temperatures.

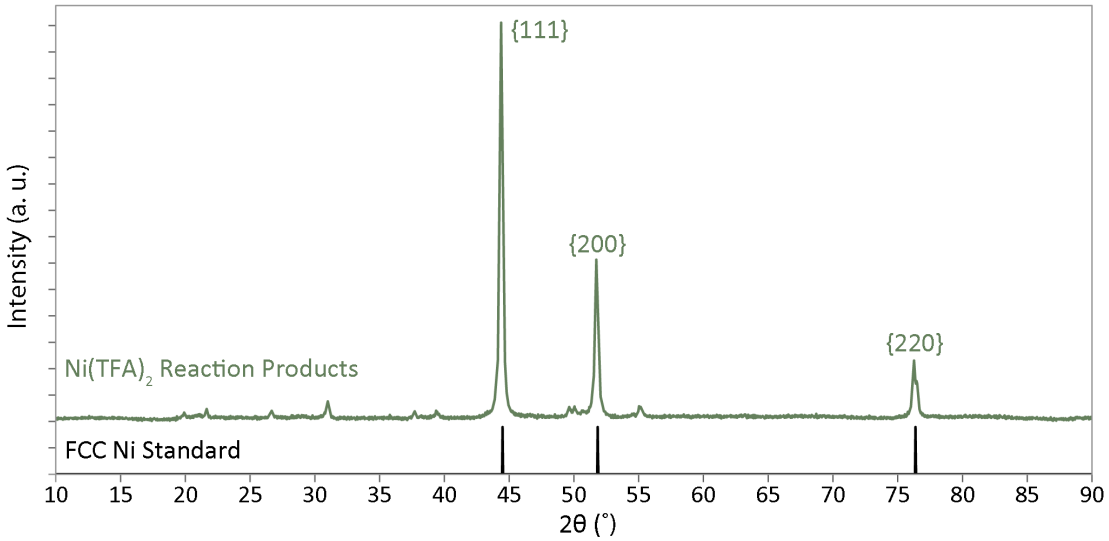
A similar result is observed in the case of copper precursors. This is unsurprising considering the much higher potential (3.38 V vs Li^+/Li) of the $Cu^{2+} \rightarrow Cu^0$ redox couple. To get around this problem, it's necessary to design a solvent/surfactant system that's oxidatively stable. Using the reduction potentials of organic small molecules as a crude approximation, the replacement of oleylamine with oleyl alcohol may enable the synthesis



(a) (BF TEM.) Metallic Ni nanoparticles synthesized from the $Ni(TFA)_2$ precursor.



(b) (BF TEM.) Large NiF_2 rods synthesized using the $Ni(HFAC)_2$ precursor.



(c) Powder XRD pattern of products from $Ni(TFA)_2$ synthesis.

Figure 2.19: NiF_2 Synthesis. The major product obtained from the decomposition of both NiF_2 precursors in the presence of OLAC, OLAM, and ODE is metallic nickel. However, the XRD pattern indicates the presence of minor phases, and very large NiF_2 nanorods are also observed in the reaction mixture.

of NiF_2. The synthesis of CuF_2, however, would only be possible in a system with virtually no species to be oxidized (i.e. saturated aliphatic solvents and surfactants with carboxylic acid head groups).

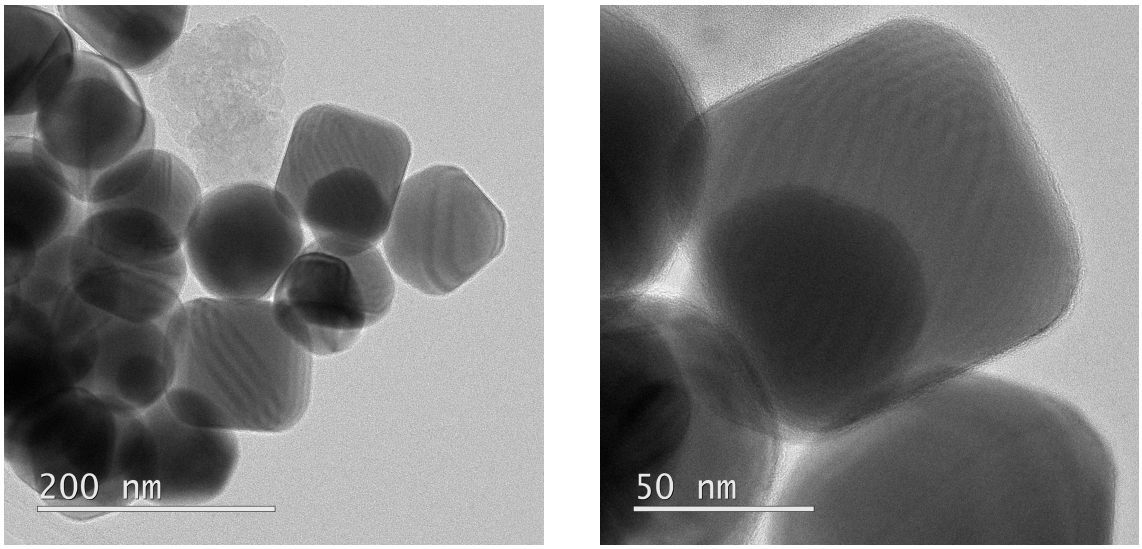


Figure 2.20: CuF_2 Synthesis. (BF TEM.) TEM images of the metallic Cu particles obtained from the thermal decomposition of CuF_2 precursors in the presence of OLAC, OLAM, and ODE.

Chapter 3

Electrochemical Performance

3.1 Electrochemistry Of Transition Metal Fluorides

Redox reactions involve the transfer of charge (electrons) from one molecule (which is oxidized) to another molecule (which is reduced). An electrochemical reaction is simply a redox reaction in which the oxidation and reduction processes are spatially separated and localized to two different electrodes connected by a common electrolyte solution. The requisite transfer of electrons between these two electrodes can be accomplished using a wired connection or some external circuit. The diffusion of ions through the electrolyte along with their generation/consumption at the electrode/electrolyte interface maintains charge neutrality.

In a redox reaction the transfer of charge is spontaneous and occurs because the electrons in the highest occupied molecular orbital (HOMO) of the reducing agent are at a higher energy than the electrons in the lowest unoccupied molecular orbital (LUMO) of the oxidizing agent; in this way electrons move down a chemical potential gradient from the more "electropositive" species to the more "electronegative" species.[94] Analogously, in a spontaneous electrochemical reaction (galvanic cell), electrons diffuse down an (electro)chemical potential gradient from an electrode with a high Fermi level to an electrode with a low Fermi level.[95] The beauty of electrochemistry is that by applying an electrical potential between the two electrodes, one can control the magnitude and direction of the electrochemical potential gradient, causing the spontaneous flow of electrons to stop and even reverse. If the chemical transformations that accompany the flow of electrons can

also be reversed, than the cell can effectively be recharged.

In this chapter I discuss the electrochemical reactions occurring at the FeF_2 cathode, with a particular focus on the phenomena which limit the reversibility of the oxidation and reduction process in a lithium ion battery (LIB) cell. Although we are primarily concerned with the characteristics of the FeF_2 cathode, its electrochemical properties do not exist independently and must be measured with respect to another electrode. This counter electrode or anode is typically chosen to be a piece of metallic lithium foil because the oxidation and reduction of lithium occurs at a relatively constant potential in a non-aqueous Li^+ electrolyte. Furthermore, measurement of the cathode potential against the reduction potential of Li^+ ions themselves indicates the maximum voltage that can be produced, and a Li-metal anode provides a practically infinite and kinetically fast source of Li^+ ions. Altogether, this so-called half cell configuration allows the properties of the FeF_2 electrode to be (approximately) isolated. Rigorously speaking, the identity of the anode and cathode in an electrochemical reaction are dependent on the direction of current flow. However, in LIB studies, these labels are typically fixed to each material based on their intended role in the spontaneous or discharge reaction.

Figure 3.1 shows a typical coin-cell configuration with FeF_2 as the cathode and lithium metal as the anode. When the electrodes are connected externally, a spontaneous discharge reaction occurs. The FeF_2 cathode is reduced with a concomitant insertion of Li^+ according to the half reaction below.

$$FeF_2 + 2Li^+ + 2e^- \rightarrow Fe^0 + 2LiF \tag{3.1}$$

At the anode, lithium metal is oxidized generating Li^+ ions in solution.

$$2Li^0 \rightarrow 2Li^+ + 2e^- \tag{3.2}$$

Summing the two half reactions above yields the net reaction on discharge.

$$FeF_2 + 2Li \leftrightarrow Fe + 2LiF \tag{3.3}$$

The reverse reaction is expected on charging. In the next chapter, I define the intrinsic phase transformations and reaction mechanisms that facilitate the forward and reverse

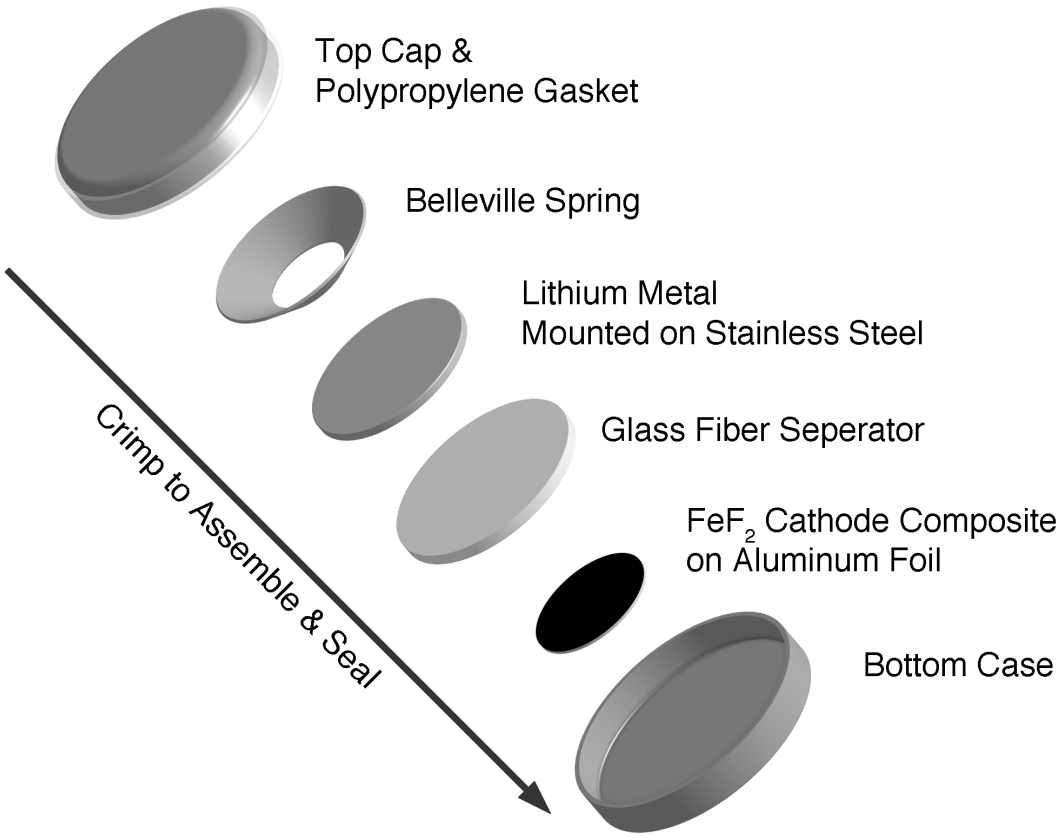


Figure 3.1: Coin Cell Configuration. The coin cell format is frequently used in the testing of battery materials. The FeF_2 cathode and lithium metal anode are arranged opposite each other and pressed into opposite sides of a porous, electrolyte-soaked separator. This is termed a "half-cell" configuration.

reactions. In this chapter, I explore extrinsic factors related to the construction and composition of the electrochemical cell that inhibit this reversibilty. The free energy change for Reaction 3.3, based on standard free energies of formation for Li, FeF_2, Fe, and LiF, is –506.8 kJ mol^{-1}.[17]

$$E = \frac{-\Delta G}{nF}$$
$$n = \#\ of\ electrons\ transferred \tag{3.4}$$
$$F = Faraday's\ Constant$$

Using relation 3.4, the equilibrium cell potential (E^0) is calculated to be 2.62 V. This is the open circuit potential or the electrostatic potential that must be applied across the electrodes to oppose the spontaneous flow of current. If a higher potential is applied the current will flow in the opposite direction. The open circuit potential (E_{OC}) is the theoretical

maximum voltage that the reaction can produce; however, in a real cell the dissipative losses always result in a lower potential on discharge and a higher potential on charge. At a fundamental level there is always a reaction overpotential (ν_{rxn}) required to drive the chemical and structural transformations in the electrode. In addition to this, there are additional overpotentials related to the ohmic resistance through the electrodes and the electrolyte (Φ_{ohm}) as well as the concentration gradients that form within the electrolyte and electrode when a current is flowing (ν_{conc}). Thus the actual cell potential on discharge is given by

$$E_{cell} = E_{OC} - (\nu_{rxn} + \Phi_{ohm} + \nu_{conc}) \tag{3.5}$$

Figure 3.2 below displays a galvanostatic (constant-current) discharge/charge profile for the FeF_2 cathode, where the dotted line represents the equilibrium cell potential. The large difference between the potentials on charge and discharge is known as hysteresis and results from the overpotentials described above. If any of these overpotentials become exceedingly large, than the potential required to pass a current cannot be reached and the reaction can no longer occur.

The presence of large overpotentials can further exacerbate side reactions that degrade the electrode/electrolyte, reducing the amount of electrochemically active material, and resulting in irreversible losses of capacity. For example, on discharge, LiF and Fe form preferentially as the most thermodynamically stable products; however, if a large overpotential is required to drive this reaction forward, then the formation of less stable compounds (i.e. from the decomposition of the electrolyte) are possible. Likewise on charge, an applied potential reverses the direction of current flow; however, if the reverse chemical reaction is thermodynamically or kinetically limited, than the current may be carried in part by alternative, irreversible redox reactions.

Below, I discuss how physical changes in the electrode as well as the thermodynamics of competing chemical processes can lead to cell failure. I further demonstrate how electrode fabrication and electrolyte design can be used to preclude these failure mechanisms. In particular, this work investigates the use of ionic liquid electrolytes in conjunction with transition metal fluoride cathodes. Ionic liquids (IL), as the name suggests, are entirely salt compounds which are liquid at or near room temperature. Their low melting points

result primarily from the use of bulky organic molecules with flexible substituent groups as cationic/anionic species.[96] Accordingly, ionic liquids exhibit properties similar to molten salts as well as organic liquids. In recent years, electrolytes composed of alkali salts in ionic liquid solvents have demonstrated improved performance in a variety alkali ion battery systems.[97–100] In section 3.4, I will briefly highlight the advantages of ionic liquid electrolytes and demonstrate how the lithium bis(fluorosulfonyl)imide (LiFSI)/N-methyl-N-propyl-pyrrolidinium bis(fluorosulfonyl)imide($Pyr_{1,3}FSI$) electrolyte is particularly suited to mitigate the failure mechanism unique to transition metal fluoride cathodes.

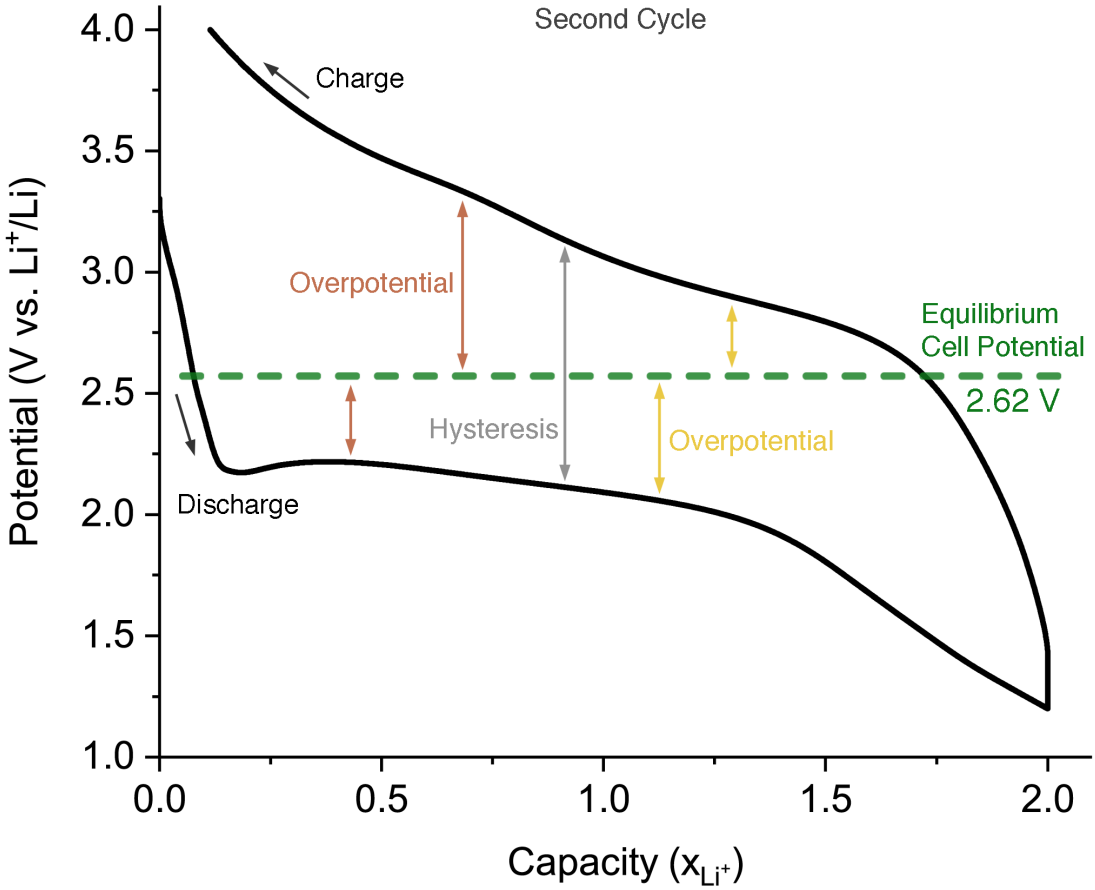


Figure 3.2: Overpotentials and Reaction Hysteresis. In the case of FeF_2, large overpotentials are required to drive both the forward and reverse reactions. This is evident, even for the highly reversible system shown here, as both the experimental charge and discharge potentials deviate significantly from the equilibrium electrode potential. This origin of this large hysteresis is considered in **Chapter 4**.

3.2 Electrode Preparation

In a lithium ion battery, redox reactions happen within the electrode active materials themselves rather than at the electrode surface. As a result, monolithic electrodes are not conducive to ionic and electronic transport within a real battery, and instead the powdered active material (i.e. FeF_2) is finely mixed with a conductive carbon phase (i.e. carbon black) and held together by an inert polymer binder (i.e. polyvinylidene fluoride) as depicted in Figure 3.3 below.

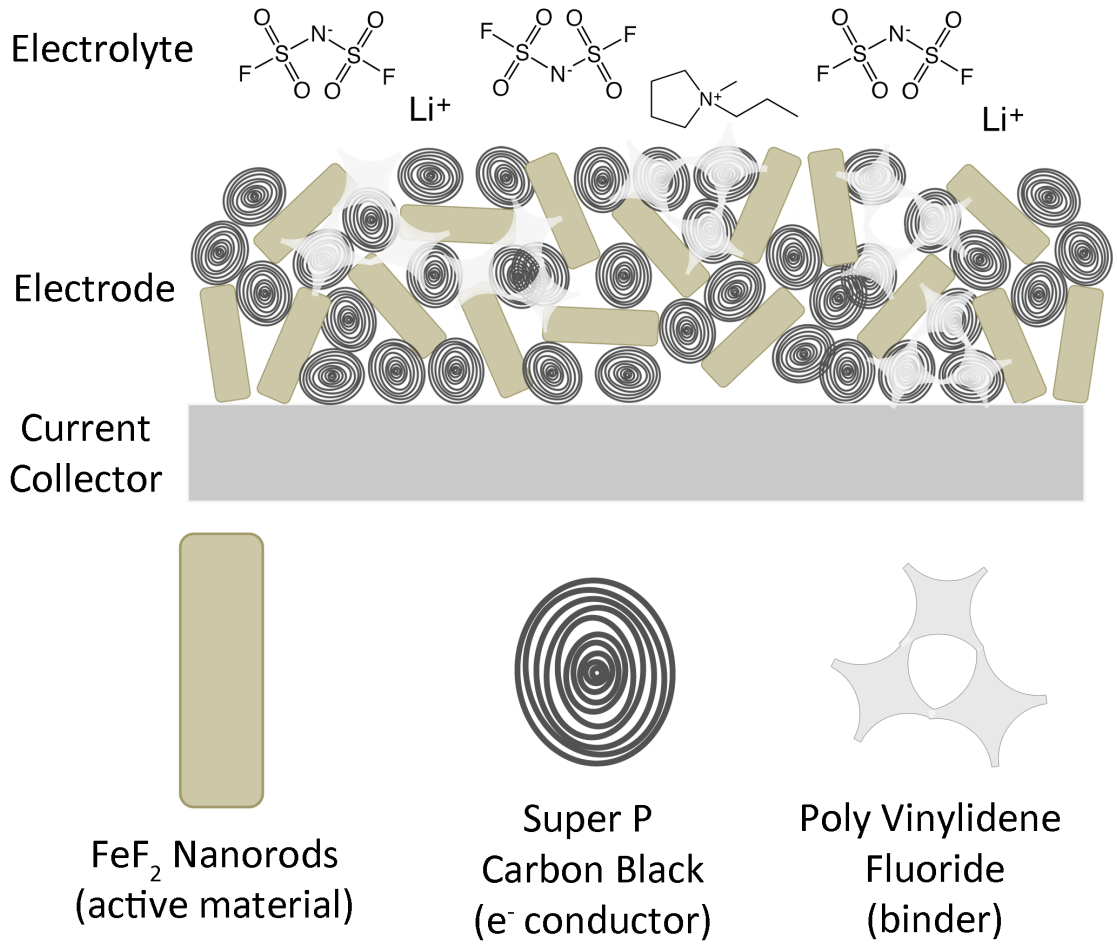


Figure 3.3: Structure of the Electrode Composite. For the test electrodes used in my experiments, FeF_2 nanorods are prepared with Super P and polyvinylidene fluoride (PVDF) in a ratio of 7:2:1 by mass.

If the active material particles are too large, both the ohmic resistance and the reaction overpotentials can increase as a result of long diffusion distances (for Li^+ and e^-). As mentioned in **Chapter 1**, small particle sizes are even more important for metal fluorides because they are electronically insulating and have limited ionic conductivity. The synthesis

developed in **Chapter 2** precisely controls the FeF_2 particle dimensions to meet this stringent size requirement. Below I briefly detail the assembly of these monodisperse FeF_2 nanoparticles into electrodes and explore how electrode structure can also affect the reversibility of the reaction.

3.2.1 Mixing Methods

Typically, the electrode composites depicted above are prepared by the mechanical grinding and mixing of dry carbon and cathode powders. However, to mix the FeF_2 nanorods with carbon at the individual particle level involves the formation of vast interfacial regions that are thermodynamically costly and cannot be produced using conventional mixing techniques. The use of high energy mixing techniques such as ball milling would damage the nanoparticle structure, defeating the entire purpose of producing monodisperse FeF_2 particles.

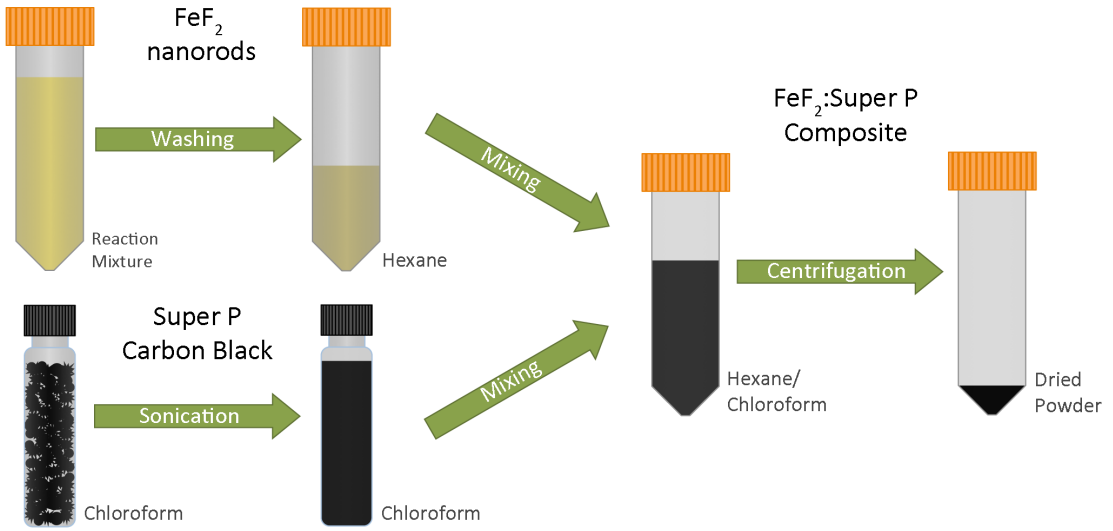
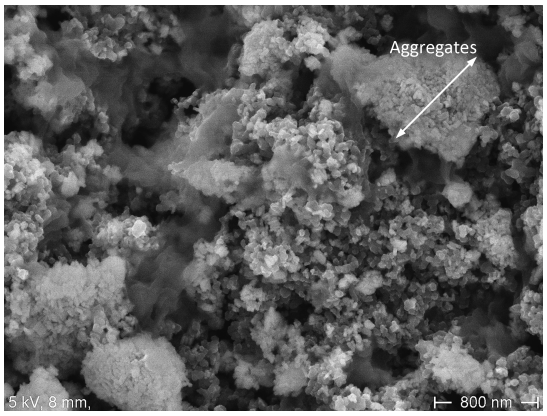


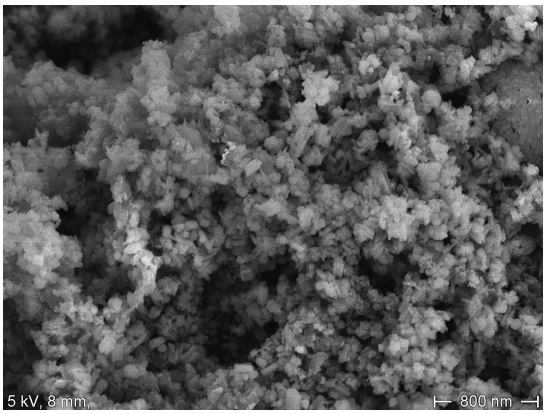
Figure 3.4: Mixing by Co-Dispersion. Schematic explaining the mixing of FeF_2 nanorods with conductive Super P carbon black. The combination of FeF_2 nanorods and Super P in the colloidal phase yields a stable "co-dispersion." Subsequent precipitation, centrifugation and drying yields an intimately mixed composite powder.

Instead, intimate mixing can be achieved by manipulating the energetics of nanoparticle dispersions. The as-synthesized FeF_2 nanorods form stable dispersions in non-polar organic solvents, such as hexane, due to favorable interactions between the solvent and the aliphatic ligands (surfactants) bound to the nanoparticle surface. On the other hand, carbon nanoparticles are notoriously difficult to disperse. Super P (carbon black), forms

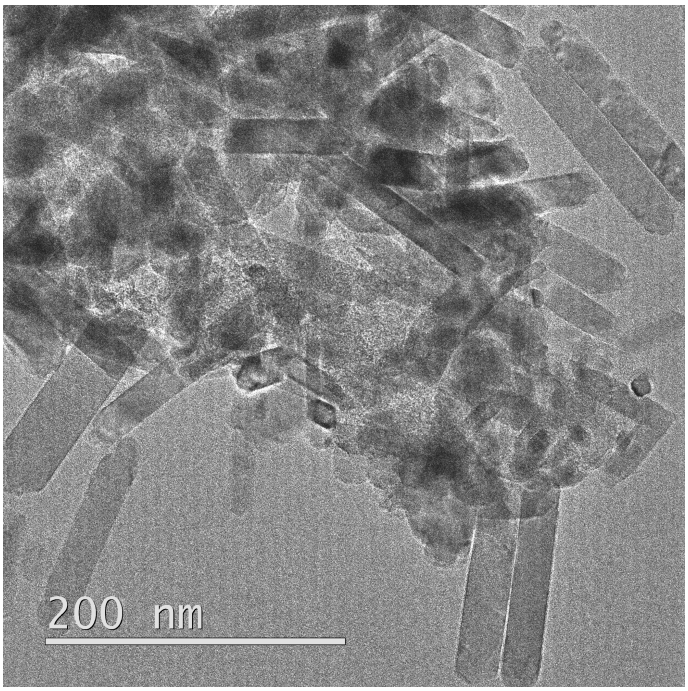
an unstable dispersion (after prolonged ultrasonication) in chloroform or dichloroethane that visibly aggregates after ~5-10 minutes. However if the two dispersions are mixed, the resulting dispersion is stable for many hours. This process is depicted in Figure 3.4.



(a) Secondary electron (SE) SEM image of FeF_2:Super P composite prepared by hand mixing.



(b) SE SEM image of FeF_2:Super P composite prepared by co-dispersion.



(c) Bright field (BF) TEM micrograph of FeF_2 co-dispersed with Super P carbon black.

Figure 3.5: Effect of Mixing Method of Electrode Structure. Conventional low-energy mechanical mixing techniques do not effectively combine the FeF_2 and Super P powders. The SEM micrograph in (a) shows large (>500 µm) aggregates of FeF_2 nanorods left behind by insufficient mixing. In contrast, (b) shows a practically homogeneous mixture of FeF_2 nanorods and Super P nanoparticles. TEM confirms that individual FeF_2 nanorods are interspersed with Super P at the particle level as a result of the co-dispersion technique.

The interfacial free energy (γ) between the Super P and the FeF_2 is lower than the sum of those between Super P, FeF_2 and the solvent ($\gamma_{carbon-FeF_2} < \gamma_{carbon-solvent} + \gamma_{FeF_2-solvent}$). As a result, the FeF_2 nanorods preferentially segregate to the Super P|solvent interface to reduce the overall free energy, forming a co-dispersion. Figure 3.5 compares the nanostructure of electrodes prepared by mechanical grinding and those prepared using the co-dispersion method. Mechanical grinding leaves behind large aggregates containing hundreds of FeF_2 nanorods, while the co-dispersion method produces an intimate mixture of FeF_2 and Super P at the individual particle scale. In theory, this nanostructure should establish electrical contact to each FeF_2 nanorod (reducing ohmic resistance) while also maintaining short diffusion distances within each FeF_2 particle (enabling a complete reaction).

3.2.2 Effects of Calendaring

Discharge-charge cycling of electrodes fabricated using the co-dispersion method above are displayed as galvanostatic profiles in Figure 3.6 below. In these experiments, the FeF_2 electrodes are charged and discharged at constant current; the potential between the two electrodes (FeF_2-Li) is plotted against the amount of charge stored/released by the electrochemical reaction (capacity), normalized by the original mass of FeF_2 in the electrode.

While the full theoretical capacity of FeF_2 is reached on the first discharge, the capacity reached on charge is $\sim$ 40% lower. This suggests a drastic change in the electrode structure during the first discharge, either from volume expansion of the active material or the flow of electrolyte through the electrode. While the active material itself is still present, if the electrical connections within the electrode are damaged, the ohmic resistance would increase and some FeF_2 may even become electrically disconnected from the electrode.

For such physical degradation mechanisms, failure can be readily mitigated by increasing the mechanical strength of the electrode. For carbon nanomaterials, densification using a mechanical press increases both tensile strength and electrical conductivity.[101,102] Figure 3.6 shows the galvanostatic cycling results of electrodes pressed to different degrees in a mechanical rolling press (calender). As the the degree of densification increases, the capacity achieved on the first charge cycle approaches the theoretical limit (571 mA h g^{-1}),

and the amount of capacity lost on each successive cycle (capacity fade) decreases considerably. This indicates that FeF_2 reacts fully on each cycle and no widespread exfoliation of active material is occuring. In addition, the voltage hysteresis also decreases, indicating a reduced ohmic resistance through the cell.

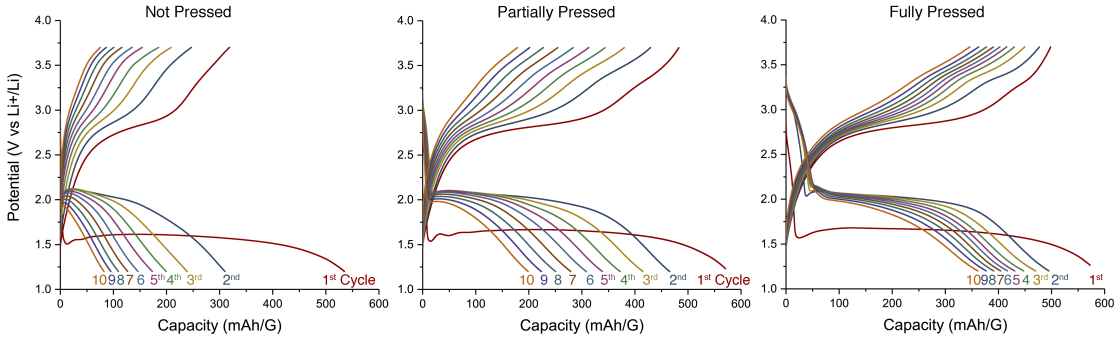


Figure 3.6: The Effect of Densification. The FeF_2 composite electrodes prepared by co-dispersion were rolled in a calendering press with incrementally decreasing thicknesses. Electrodes were cycled in the LP30 electrolyte.

In the fully dense electrodes, the first discharge capacity is actually greater than the theoretical value. This additional capacity arises from the electrochemical decomposition of the electrolyte and significantly affects chemical failure mechanisms in FeF_2 cathodes as discussed below.

3.3 Failure Mechanisms

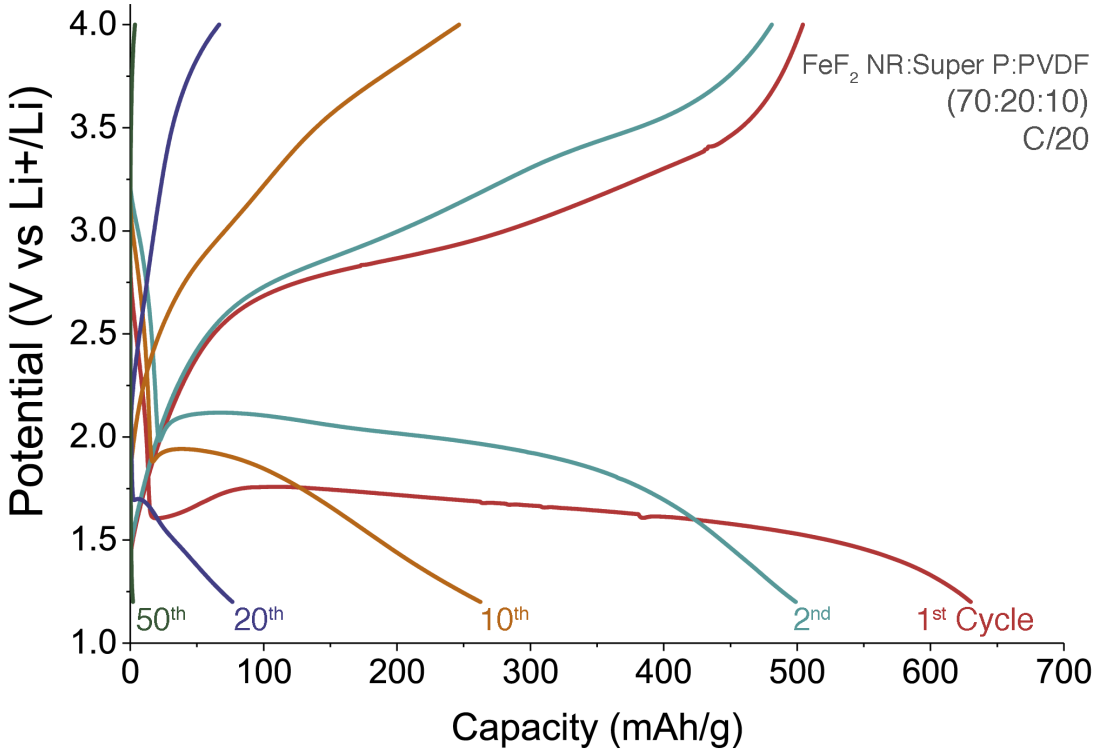


Figure 3.7: Electrode Performance in Conventional Electrolytes. While a catastrophic failure of the FeF_2 electrodes is prevented by electrode fabrication techniques presented above, a near total loss of capacity is observed by the 50th cycle in a conventional lithium ion battery electrolyte (LP30).

Figure 3.7 displays the galvanostatic profiles for a fully densified electrode as prepared above. Although a robust electrode construction results in a vastly improved capacity retention over the first 10 cycles as demonstrated above, a near complete loss of capacity is still observed after 50 discharge/charge cycles. In the case of iron fluoride a number of chemical mechanisms can still cause cell failure even if the electrode structure remains physically intact.

The cycling experiments displayed in the previous section were performed in an electrolyte composed of 1 M $LiPF_6$ in a 1:1 (v/v) mixture of ethylene carbonate (EC) and dimethyl carbonate (DMC) (Figure 3.8). This is a commonly used electrolyte in conventional lithium ion batteries and is sold commercially as LP30. In the following sections, I use this generic electrolyte to introduce the major failure mechanisms associated with FeF_2 and other transition metal fluoride cathodes.

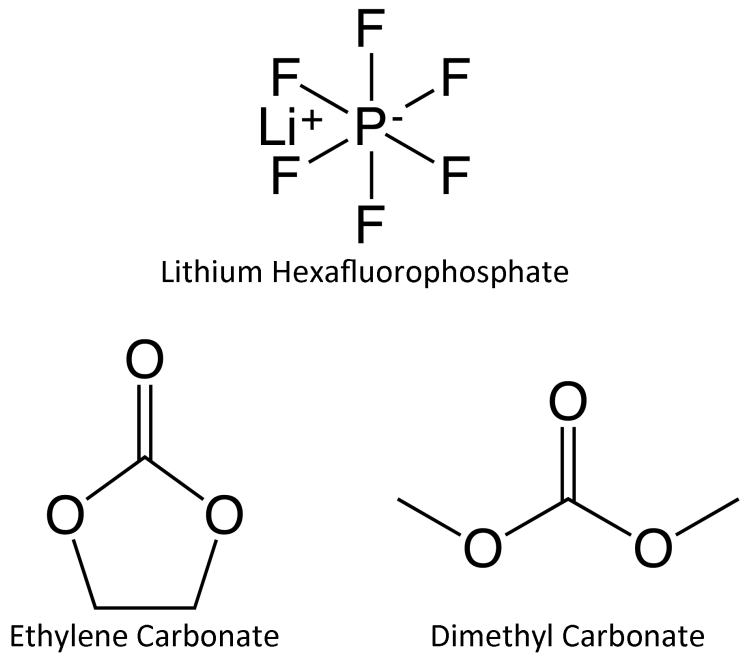


Figure 3.8: Conventional LIB Electrolytes. The chemical structures of lithium hexafluorophosphate ($LiPF_6$), ethylene carbonate (EC), and dimethyl carbonate (DMC). 1 M $LiPF_6$ in EC:DMC (1:1 v/v) is known commercially as LP30.

3.3.1 Cathode Dissolution

Cathode dissolution is perhaps the most well documented failure mechanism.[25,32,36] As the (over)potential applied to charge the battery increases, the reverse reaction (Figure 3.9) competes with the direct oxidation of metallic iron to Fe^{2+} and Fe^{3+} species in solution. The potentials at which these processes occur is shown in Figure 3.9. The next chapter, provides a mechanistic rationale for the prevalence of these side reactions in transition metal fluorides. Presently, I demonstrate how cathode dissolution can be identified and mitigated.

During cycling, if iron dissolves from the cathode as a positive ion on charge, then it would migrate to the lithium anode under the applied potential. Indeed, when the lithium metal anodes are removed from the coin cells (Figure 3.10) after 15 cycles in LP30 and dried under vacuum, XPS analysis demonstrated the unequivocal presence of deposited iron. For comparison, the XPS survey spectra for a lithium metal anode cycled in our ionic liquid (IL) is also shown. In this case no iron signal is observed, indicating that cathode dissolution has not occured. The reason for this difference is presented below.

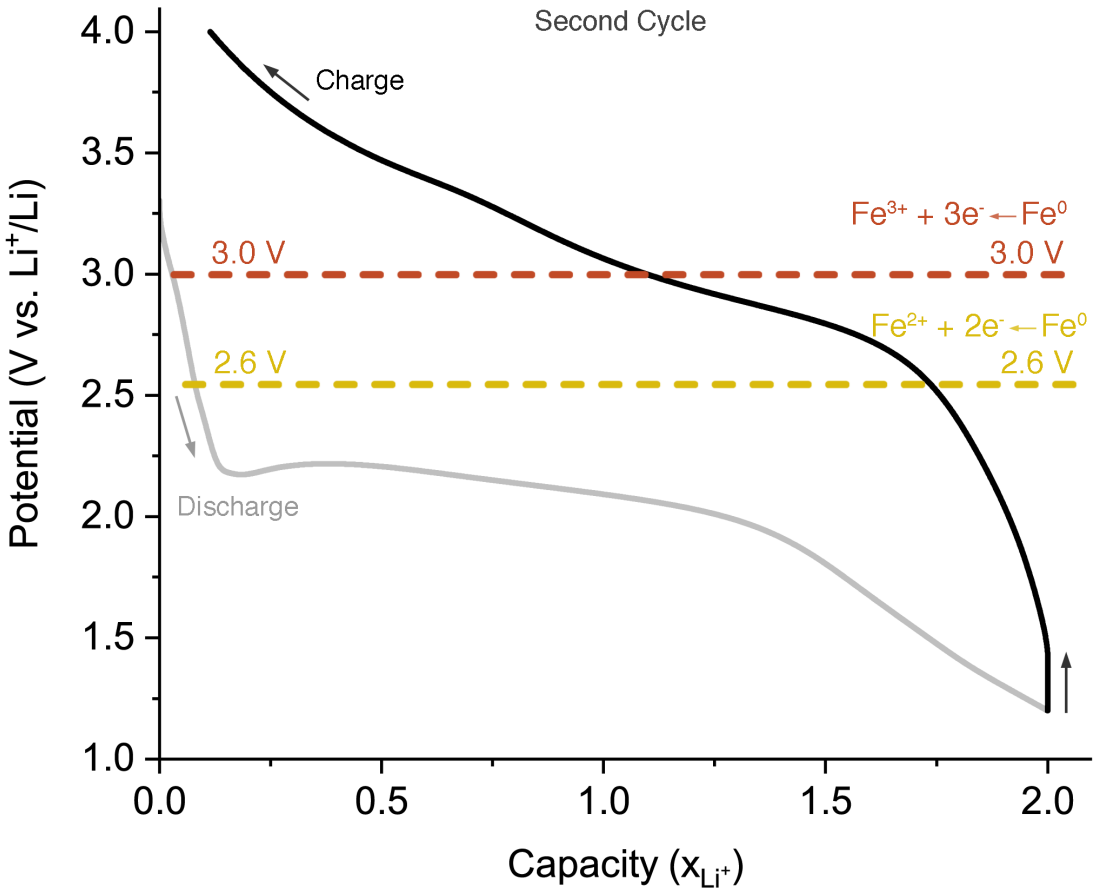
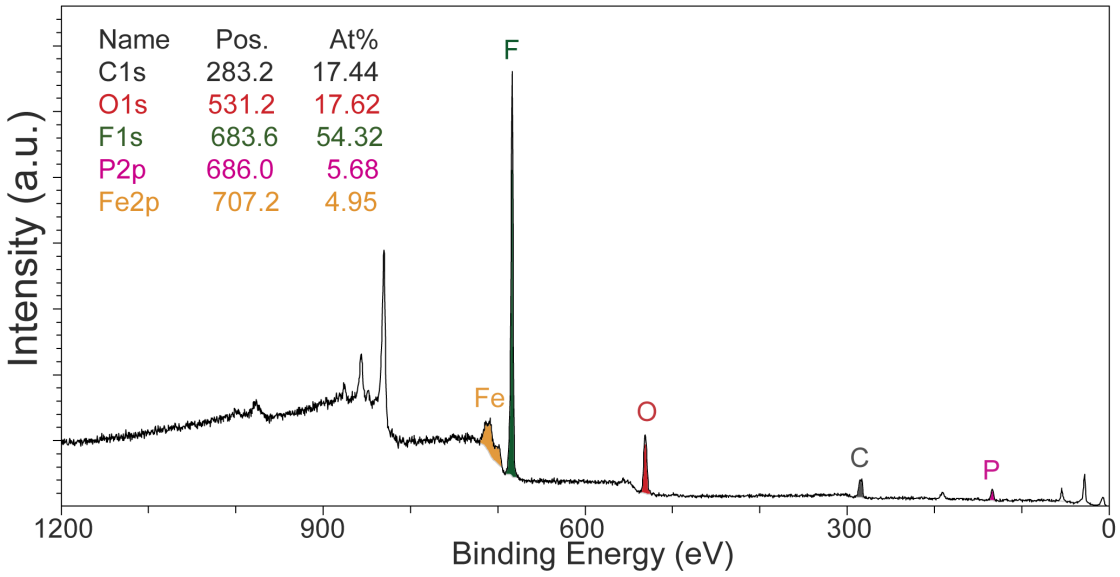
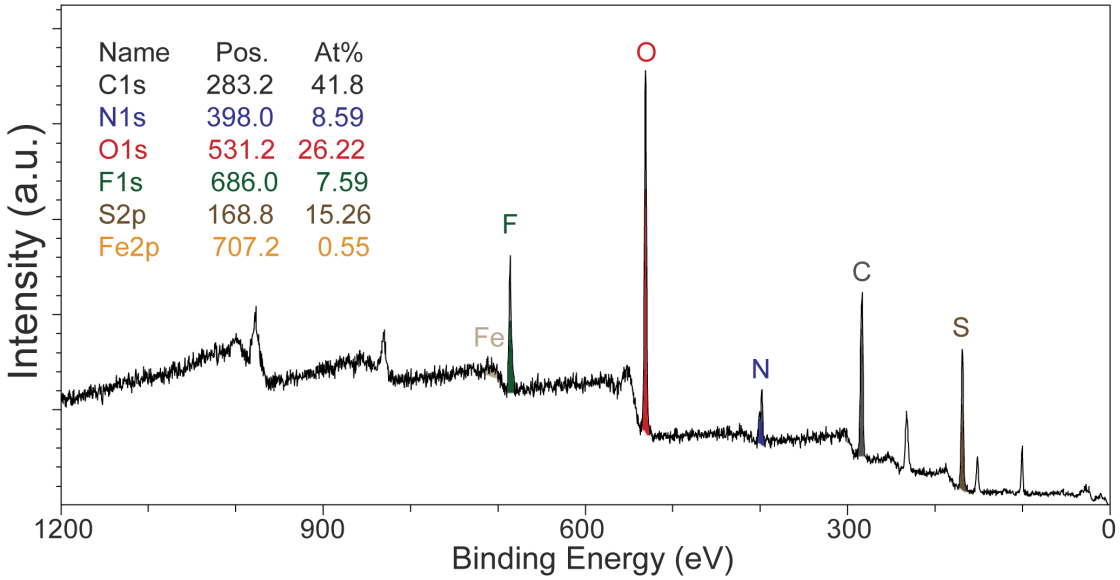


Figure 3.9: Iron Dissolution on Charge. Due to the large overpotential required for the reconversion (charge) reaction, this process competes with the direct oxidation of metallic iron to Fe^{2+} and Fe^{3+} cations in solution. Both plateaus observed on charging occur above the standard potentials for oxidation of metallic Fe.



(a) LP30 ($LiPF_6$/EC:DMC)



(b) Ionic Liquid ($LiFSI/Pyr_{1,3}FSI$

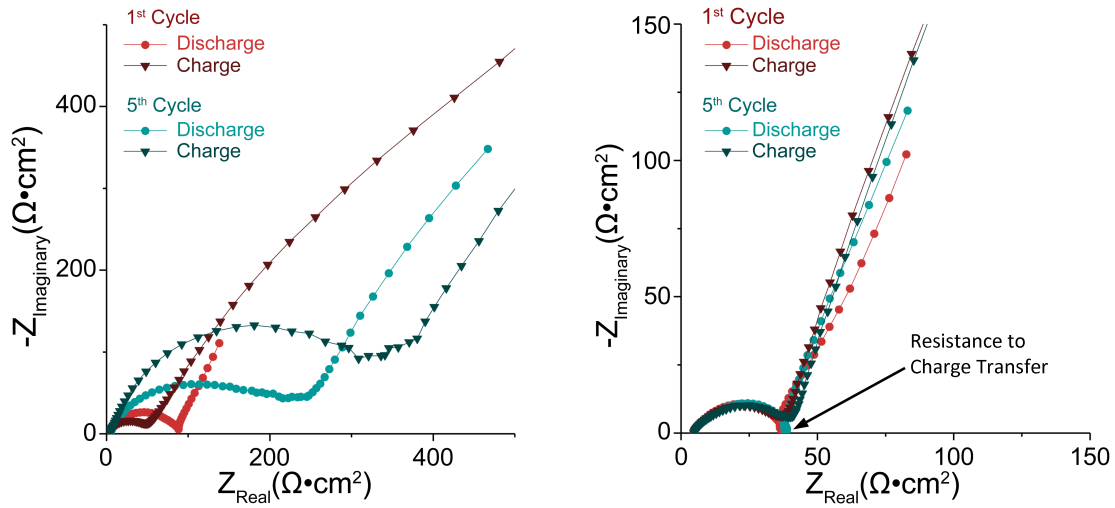
Figure 3.10: Iron Dissolution *Ex-situ* XPS survey spectra of the lithium metal anodes taken after 15 cycles against FeF_2 nanorod cathodes in both the LP30 (a) the ionic liquid (b) electrolytes. The lithium anode taken from the LP30 electrolyte exhibits an Fe 2p peak, meaning that Fe has dissolved from the cathode and deposited on the anode. Cathode dissolution is prevented in the IL electrolyte.

3.3.2 Electrolyte Decomposition

Typically, for a well constructed cathode, the capacity observed on the first discharge (reduction) is higher than the theoretical capacity of FeF_2. Assuming that the other components of the electrode (Super P, PVDF, aluminum) are reductively stable, this additional capacity must result from the electrochemical decomposition of electrolyte species. Most LIB electrolytes are nominally stable in the potential window used for battery cycling (i.e. 1.2 V to 4.0 V vs. Li^+/Li). However, the reactivity of the electrolyte species can be enhanced by high concentrations as well as the local chemical environment at the electrode surface.[76,103] In organic electrolytes, some degree of electrolytsis is always observed at the anode on reduction and at the cathode on oxidation.[104] The resulting layer of decomposition products at the electrode surface is known as the solid-electrolyte interphase (SEI).

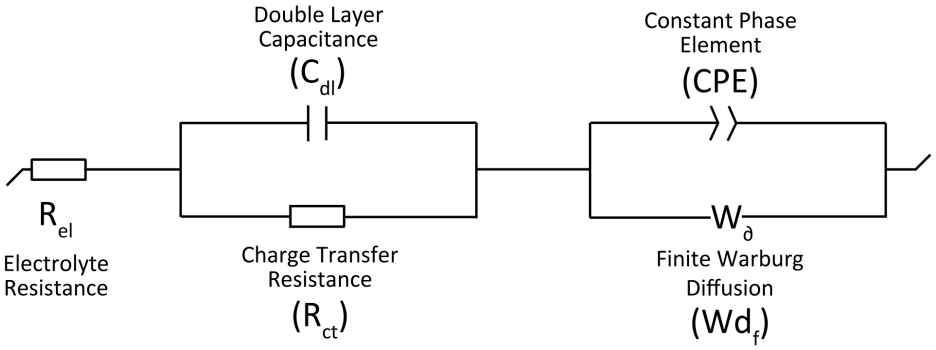
In the case of FeF_2, the surface of the material has been shown to exhibit catalytic activity, resulting in SEI formation on discharge (reduction) as well as charge (oxidation).[25,68,76] In the LP30 electrolyte, the discrepancy between charge and discharge capacity continues past the first cycle; the ratio between charge and discharge capacity is termed the "coulombic efficiency." Low coulombic efficiencies suggest progressive electrolyte decomposition on each cycle. Electrochemical impedance spectroscopy (EIS) can be used to probe charge transfer phenomena between the FeF_2 cathode and the electrolyte.[105] In a typical potentiostatic impedance spectroscopy experiment, a sinusoidally varying (AC) potential (1 mV to 10 mV) is applied between two electrodes of a battery (cell). The corresponding sinusoidal current response is then measured while the AC frequency of the applied potential is varied from high frequencies 10 kHz to 100 kHz to low frequencies 10 mHz to 0.1 mHz. Impedance is the ratio of the applied potential to the current response and, at each frequency (ω), is defined by an amplitude (Z_0) and a phase shift (ϕ) relative to the applied potential.

$$Z(\omega) = Z_0(cos\phi + isin\phi) \tag{3.6}$$



(a) Impedance spectra in LP30 electrolyte.

(b) Impedance spectra in IL electrolyte.

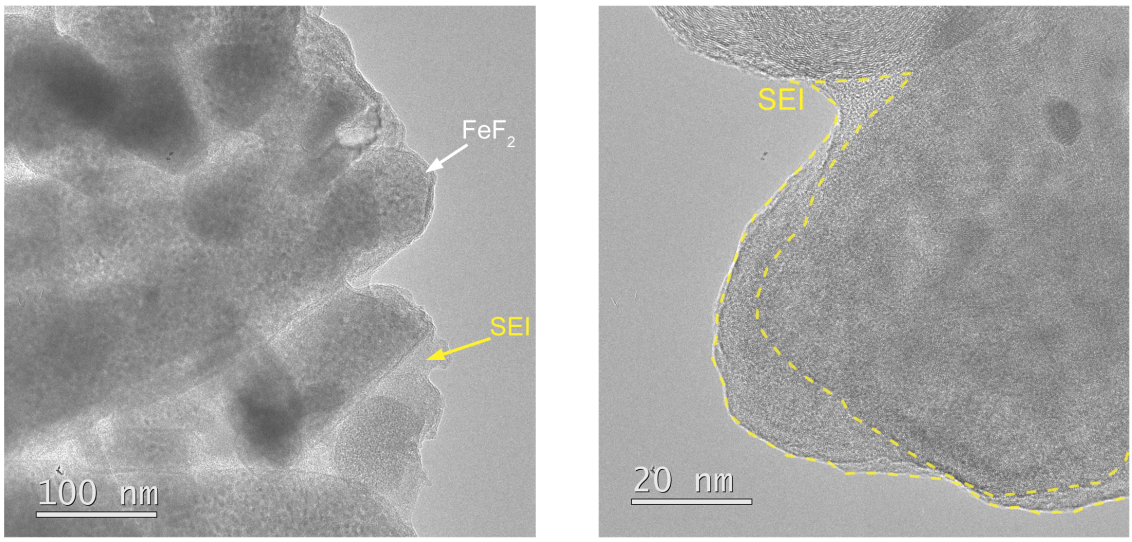


(c) Equivalent circuit used to model the impedance spectra.

Figure 3.11: Electrolyte Stability on Cycling Nyquist impedance plots for the FeF_2 nanorod cathodes highlight the difference in stability between the ionic liquid (IL) electrolyte (b) and the LP30 electrolyte (a). Data from the first (red) and fifth (turquoise) cycles are plotted to demonstrate the long-term effects of cycling. Impedance spectra are collected directly after discharge and charge for each cycle. To determine charge transfer resistance values, the impedance spectra were modeled and fit using the equivalent "Randles" circuit shown in (c). Charge transfer resistance (R_{ct}) and electrochemical double-layer capacitance in parallel represent the electrode-electrolyte interface, while diffusion within the electrode is modeled by Warburg diffusion in parallel with a constant phase element to represent slightly capacitive behavior. Fitted spectra are shown in Appendix I (5.3). Charge transfer resistance values in order of measurement (1st discharge, 1st charge, 5th discharge, 5th charge) are 83.9, 46.2, 201.1 and 322.9 $\Omega\,cm^2$ for LP30 (a) and 32.6, 34.6, 34.1 and 36.7 $\Omega\,cm^2$ for the IL (b). In (a) fluctuations in the charge transfer resistance (second x-intercept) indicate uncontrolled electrolyte decomposition and SEI growth. In contrast the charge transfer resistance in the ionic liquid electrolyte (b) is largely stable.

The impedance is thus a complex value composed of a real ($Z_0 cos\phi$) "in-phase" component related to purely resistive elements, and an imaginary ($Z_0 i sin\phi$) component related to capacitive ($\phi = -90°$) and inductive ($\phi = 90°$) elements. By measuring impedance

at different frequencies, EIS differentiates the resistive contributions of various charge transport phenomena based on the timescale on which they occur.[22] A Nyquist impedance diagram (3.11) plots the imaginary component against the real component at each frequency. Electrochemical cells are often modeled as "equivalent circuits" of resistors and capacitors to assign physical meaning to the shape of the Nyquist plot. Herein, we focus on the first semicircle, which is modeled by a resistor and capacitor in parallel to represent the double-layer capacitance and charge-transfer resistance at the electrode-electrolyte interface 3.11c. At the high frequency intercept (left), charge flow through the capacitor is fast, and the impedance is simply due to the electrolyte resistance. At the low frequency intercept, no current flows through the capacitor and the impedance is the sum of electrolyte resistance and charge-transfer resistance at the interface. The charge transfer resistance is sensitive to the formation of resistive interphases (SEI) at the interface.



(a) FeF_2 nanoparticles encased in SEI. **(b)** Single FeF_2 particle showing SEI layer.

Figure 3.12: Uncontrolled SEI Growth. (BF TEM.) The TEM images of FeF_2 nanorods after 15 cycles in the LP30 electrolyte show a thick and non-uniform SEI layer. This SEI appears to encase and bind together the very large (fused) FeF2 particles and is likely a major contribution to electrode failure.

Figure 3.11 shows the Nyquist impedance plots for the FeF_2 cathode in both the LP30 and IL electrolytes as well as the "Randles" equivalent circuit used to fit the data. In LP30, the charge transfer resistance grows by nearly a factor of four over the first five cycles and further fluctuates between charge and discharge. This indicates the formation of a thick SEI layer that is electrochemically unstable. For comparison, the charge transfer

resistance in our IL electrolyte is extremely stable (~34 $\Omega\,cm^2$), remaining constant over many cycles.

Excessive SEI growth increases the ohmic resistance of the cell, resulting in large overpotentials on charge and discharge. The plot of differential capacity ($\frac{dQ}{dV}$) vs cell potential in Figure 3.18 exhibits peaks showing the potentials of different redox reactions. In LP30, the voltage difference between corresponding oxidation and reduction processes grows upon cycling (Figure 3.18b). This increasing hysteresis produces less current for a given applied voltage and a corresponding reduction in capacity. The effect of this uncontrolled SEI growth and electrolyte decomposition is illustrated in the *ex-situ* TEM image above. After only 15 cycles in the LP30 electrolyte, the FeF_2 particles are completely in encased in a pervasive SEI that appears to block even the pores between particles.

3.3.3 In-Situ TEM Technique and Limitations

In Chapter 1, I discussed how *in-situ* TEM lithiation experiments informed previous understanding of the conversion mechanism in transition metal fluorides. *In-situ* TEM data is also used to illustrate concepts herein, such as the long-range diffusion of lithium (Chapter 1), the fusing of adjacent nanorods (Section 3.3.4 below), and the nucleation of metallic iron during the discharge process (Chapter 4). Before proceeding, I will briefly discuss the setup of these experiments and their inherent limitations.

The *in-situ* experiment is presented in the schematic diagram above (Figure 3.13). The FeF_2 nanorods were loaded onto a thin copper wire composing one electrode of a biasing STM-TEM sample holder; the other electrode consists of a small piece of lithium metal loaded onto a tungsten (W) probe. Electrically insulating oxides and nitrides are formed over the surface of this lithium during a brief exposure to air and act as a solid electrolyte between the lithium and the active material specimen. This fully solid-state configuration avoids contamination and is compatible with the high vacuum of the TEM column. Inside the TEM, this lithium probe can be placed in contact with the active material at any region of interest using a piezo electric motor. The Upon contact between the lithium probe and the FeF_2, a large reverse bias is applied to drive lithiation. While this lithiation can be performed in conjunction with any imaging/analytical technique (TEM, STEM, Diffraction, EDX, etc.), the dynamic nature of the lithiation process requires very short exposure

times/scan rates and limits the resolution and signal-to-noise ratio of the experiment. TEM/STEM imaging are the easiest techniques to perform under these conditions.

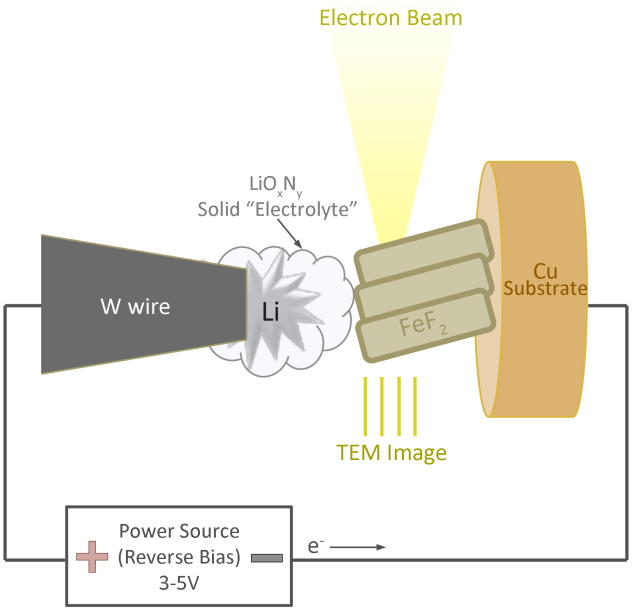


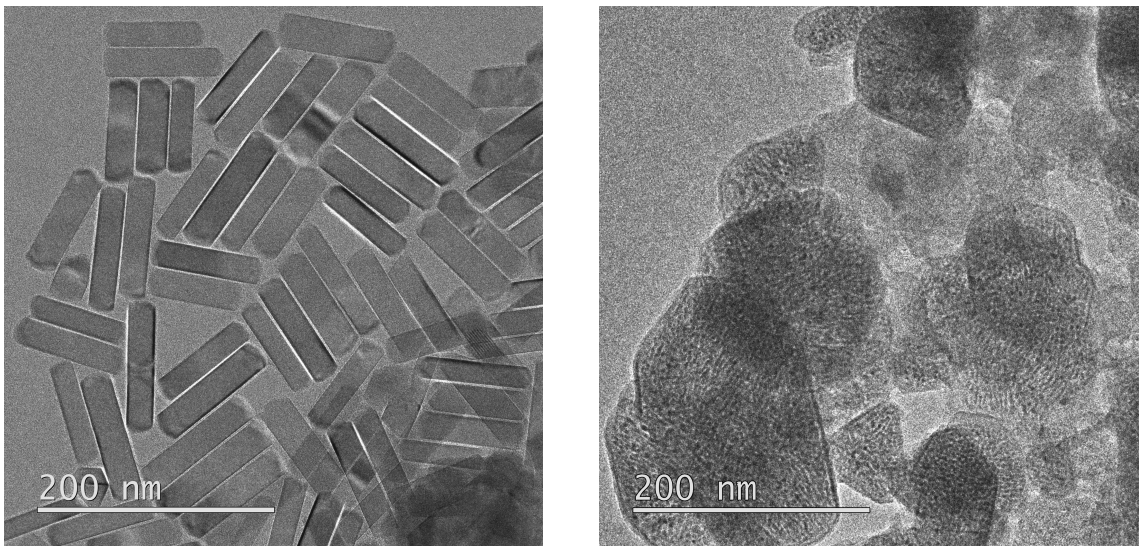
Figure 3.13: The *In-Situ* TEM Lithiation Technique. As described in **Chapter 1**, *In-situ* TEM experiments were performed using a biasing sample holder. Experiments were performed with our collaborator Prof. Hyun-wook Lee (Ulsan National Institute of Science and Technology. Ulsan, South Korea).

While the ability to visualize real-time lithiation at the nanoscale makes this technique very attractive, there are several constraints which limit the conclusions that can be drawn from this data. First of all, because of the high resistance between the Li-probe and the active material, a large reverse bias is required to pass a current (in a real battery, current flows spontaneously). Consequently, any material in contact with the Li-probe is quickly lowered to a negative potential (–1.5 V to –5 V vs. Li^+/Li) and phase evolution follows a kinetically limited, rather than the equilibrium thermodynamic, pathway. For this reason, *in-situ* TEM techniques are not useful for understanding the formation of equilibrium phases; however, they can be used to observe structural/morphological transformations. Additionally, because only the bias (voltage) can be controlled, this *in-situ* technique offers no way to correlate images with a particular state of charge (e.g. position in the galvanostatic profile). In theory, the STM-TEM biasing holder is capable of providing both forward and reverse bias; however, in practice, the resistance observed on charging is often larger, and the delithiation process may indeed require larger overpotential. For transition metal fluorides, charging has never been achieved *in-situ* because the potential

required exceeds the capabilities of most biasing holders.

3.3.4 Particle Fusing

The well-defined morphology of my FeF_2 nanorod cathodes clearly reveals the fusing of adjacent particles on discharge. This third failure mechanism has not previously been demonstrated for transition metal fluorides. *Ex-situ* TEM images taken directly after the first discharge (Figure 3.14), show the formation of large irregular particles. The volume change associated with the full conversion of FeF_2 to LiF and Fe is only 16.6%, suggesting that these large irregular particles consist of many individual nanorods fused together. Small particle sizes are crucial for reducing diffusion lengths in the material. The fusing of particles rapidly increases the particle size beyond the length-scale of the reconversion (charge) reaction, leaving effectively dead material at the center.[15,22]



(a) Pristine FeF_2 nanorods. **(b)** FeF_2 nanorods discharged in LP30.

Figure 3.14: Particle Fusing. (BF TEM.) An *Ex-situ* TEM micrograph of FeF_2 nanorods after a single discharge in LP30 shows the exclusive presence of large irregular particles formed through the fusing of adjacent nanorods. The fused particles are the size of many pristine FeF_2 nanorods joined together. The fused particles in (b) were discharged according to the net reaction $FeF_2 + 2Li \rightarrow Fe^0 + 2LiF$ with a capacity of 740 mA h g^{-1}. This capacity is higher than the theoretical (571 mA h g^{-1}), indicating a complete reaction and that the fused particles are composed entirely of LiF and Fe^0.

To further illustrate this fusing process, an *in-situ* TEM experiment was performed on the FeF_2 nanorod samples. The images in Figure 3.15 show that in the absence of electrolyte, the reaction (lithiation) front propagates readily across interparticle boundaries such that two nanorods appear to react as one. In the fully discharged state, the interface

between the adjacent nanorods is completely obscured. The discussion to this point has laid out the major failure mechanisms present in transition metal fluoride systems. Next, I discuss how our IL electrolyte precludes all three of these failure mechanisms.

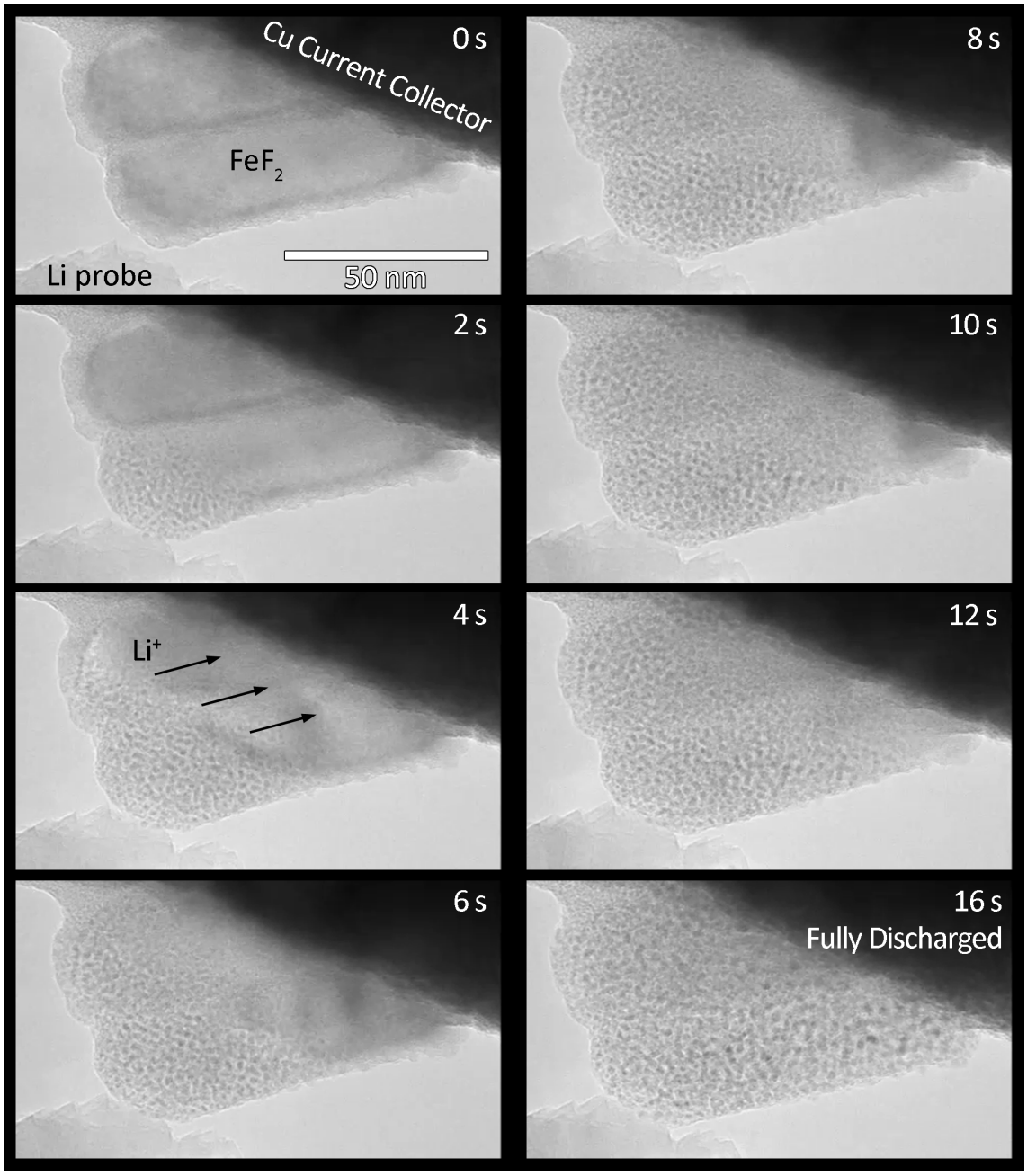
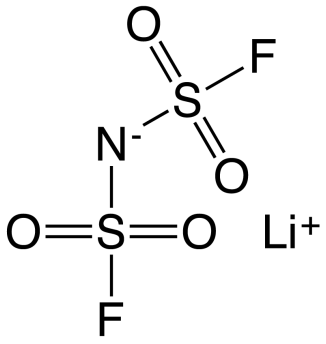
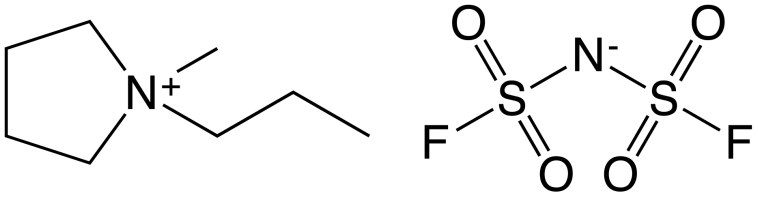


Figure 3.15: Particle Fusing *In-Situ*. (BF TEM from live view video.) TEM micrographs extracted from an *in-situ* lithiation (discharge) experiment, illustrating the fusing of adjacent FeF_2 particles. Prior to lithiation, a distinct boundary is apparent between the two nanorods. During the lithiation, propagation of the reaction front from one rod to the next obscures the boundary. In the fully discharged state, the boundary is no longer apparent.

3.4 Ionic Liquid Electrolytes



Lithium bis(fluorosulfonyl)imide



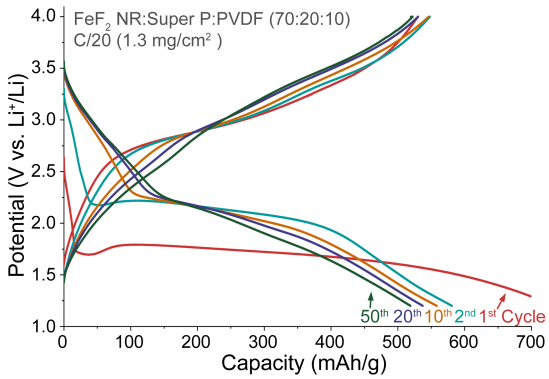
N-methyl-N-propylpyrrolidinium bis(fluorosulfonyl)imide

Figure 3.16: The Ionic Liquid Electrolyte. The chemical structures of lithium bis(fluorosulfonyl)imide (LiFSI) and N-methyl-N-propyl-pyrrolidinium bis(fluorosulfonyl)imide ($Pyr_{1,3}FSI$). The ionic liquid electrolyte used in this study consists of 1 M LiFSI in $Pyr_{1,3}FSI$.

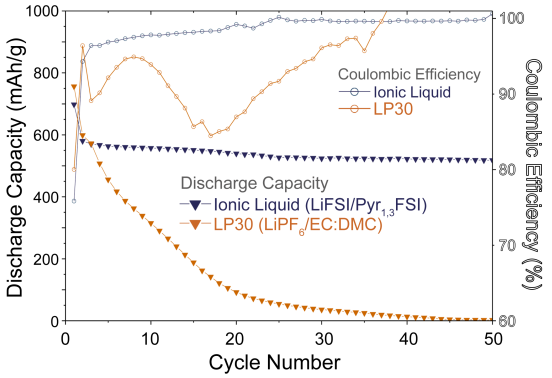
The next chapter assesses the mechanism of the conversion reaction in transition metal fluorides. To ensure that this analysis yields relevant conclusions about reversibility, I first demonstrate a high degree of reversibility within the system in question. As previously mentioned, this is achieved through the use of an ionic liquid electrolyte. Ionic liquids are typically organic salts containing bulky substituent groups that shield and sterically seperate the positive and negative charges on adjacent ions (Figure 3.16) and also increase the entropy of the liquid state. As a result, ionic liquids are molten at or below room temperature.

Their ionic nature makes them excellent solvents for a variety of salts, while their organic nature results in electrochemical stability over a wide potential range.[97,106] In the context of lithium ion batteries, ionic liquid electrolytes are often based on quaternary pyrrolinidium cations and bis(fluorosulfonyl)imide (FSI) or bis(trifluoromethylsulfonyl)imide (TFSI) anions.[99,100,107] $Pyr_{1,3}TFSI$ electrolytes exhibit an exceptional electrochemical stability range (0.0 V to 5.5 V vs. Li^+/Li) and is further able to withstand temperatures in

excess of 400 °C without decomposition or significant increase in vapor pressure, making them highly desirable for safe battery operation at high temperatures.[97,100] While $Pyr_{1,3}FSI$ electrolytes, exhibit slightly lower thermal and electrochemical stability, the FSI anion has been shown to enable improved cycling of various electrode systems via the formation of a stable, passivating SEI layer.[99] Very recently, it was demonstrated that $Pyr_{1,3}FSI$ based electrolytes enabled long-term (>1500 cycles), moderate rate (1.0 mA cm^{-2}) cycling of both lithium and sodium metal anodes without significant dendrite growth.[98,107] As the commercial development of transition metal fluoride cathodes will likely rely on the use of lithium metal anodes, this section focuses on use of LiFSI/$Pyr_{1,3}FSI$ based electrolytes in conjunction with my FeF_2 nanorod cathodes. In some ways, ionic liquid electrolytes approximate conventional organic electrolytes in the limit of extremely salt high concentration. Recall that Huang *et al.* demonstrated improved cycling stability with 3 M LiFSI in dimethoxyethane.[25] Herein, I detail how our ionic liquid electrolyte outperforms even the best reported electrolytes for transition metal fluorides.



(a) Galvanostatic profiles of FeF_2 nanorod cathodes cycled in ionic liquid electrolyte.

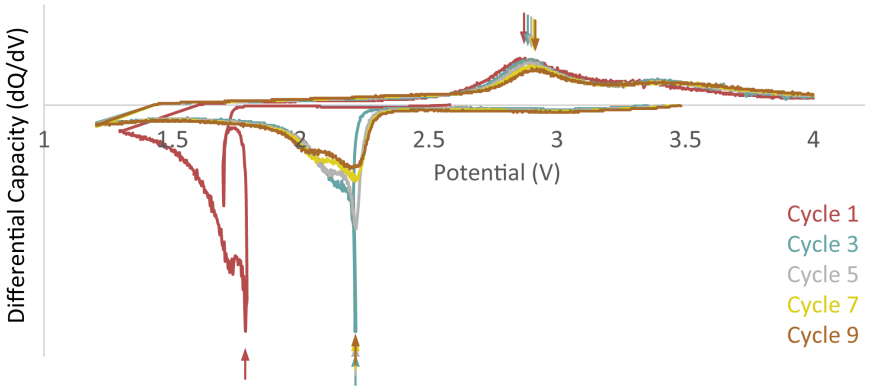


(b) Capacity vs. Cycle Number plot comparing the performance of ionic liquid and LP30 electrolytes.

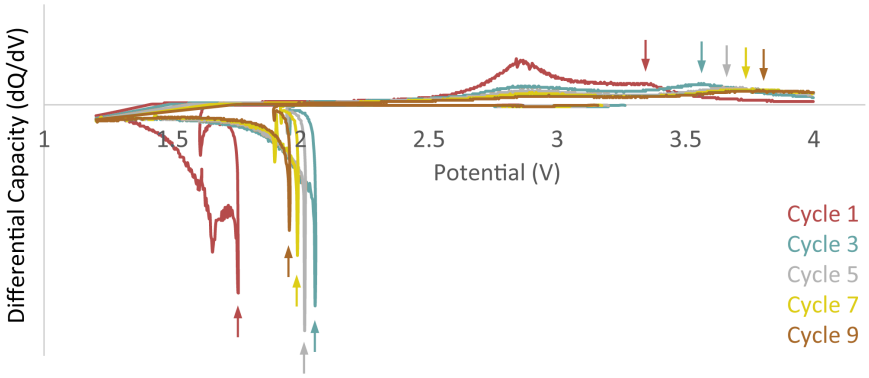
Figure 3.17: Superior Cycling Stability. The first discharge profile (a) shows a large irreversible capacity due to initial SEI formation. Stable cycling with minimal capacity loss is observed from the second cycle onward. Discharge and charge profiles become increasingly symmetric as cycle number increases. In the conventional LP30 electrolyte (orange) rapid and complete capacity loss is observed. In the ionic liquid (purple), more than 90% of the theoretical capacity is maintained after 50 cycles.

Figure 3.17 above shows galvanostatic profiles and a capacity vs. cycle life plot for a fully dense FeF_2 nanorod electrode. The electrolyte used is composed of 1 M lithium fluorosulfonyl imide (LiFSI) dissolved in N-methyl-N-propyl-pyrrolidinium fluorosulfonyl imide ($Pyr_{1,3}FSI$) (Figure 3.16). The galvanostatic profile (Figure 3.17a) shows 24%

irreversible capacity on the first discharge due to initial formation of the SEI layer. The coulombic efficiency increases immediately on the second cycle (Figure 3.17b), exceeding 99% within the first 20 cycles, and a stable hysteresis of 0.6 V is observed (figure 3.18a). This stands in stark contrast to the electrodes cycled in the LP30 electrolyte, which exhibit low coulombic efficiency, increasing hysteresis (Figure 3.18b), and a total loss of capacity within the first 40 cycles.



(a) Stable hysteresis in the IL electrolyte.



(b) Increasing hysteresis in the LP30 electrolyte.

Figure 3.18: Effect of Electrolyte on Overpotentials. The plots of differential capacity (dQ/dV) vs. cell potential show the potentials at which reduction (discharge) and oxidation (charge) reactions occur. The first nine cycles are shown for FeF_2 nanorod electrodes cycled in the 1 M LiFSI/$Pyr_{1,3}$FSI ionic liquid (IL) electrolyte (a) and the 1 M $LiPF_6$/EC:DMC organic (LP30) electrolyte (b). Arrows indicate the position of reduction and oxidation peaks on each cycle. In the LP30 electrolyte, the difference between reduction peak potentials widens with each cycle. This increasing hysteresis indicates growing overpotentials that lead to cell failure. In contrast, a stable hysteresis is observed the IL electrolyte.

Similarly stable capacities are observed in long term cycling experiments at higher current densities (Figure 3.19). In the 1 m LiFSI/$Pyr_{1,3}$FSI ionic liquid (IL) electrolyte, the FeF_2 electrodes retain over 90% of the theoretical capacity after 100 cycles. This solely

electrolyte based approach eliminates the need for excessive carbon content or special processing techniques. This is not only valuable for the mechanistic study presented in **Chapter 4**, but also for preserving the innately high energy density of metal fluoride cathodes in general. In the following sections, I elucidate why this IL electrolyte results in exceptional electrochemical performance.

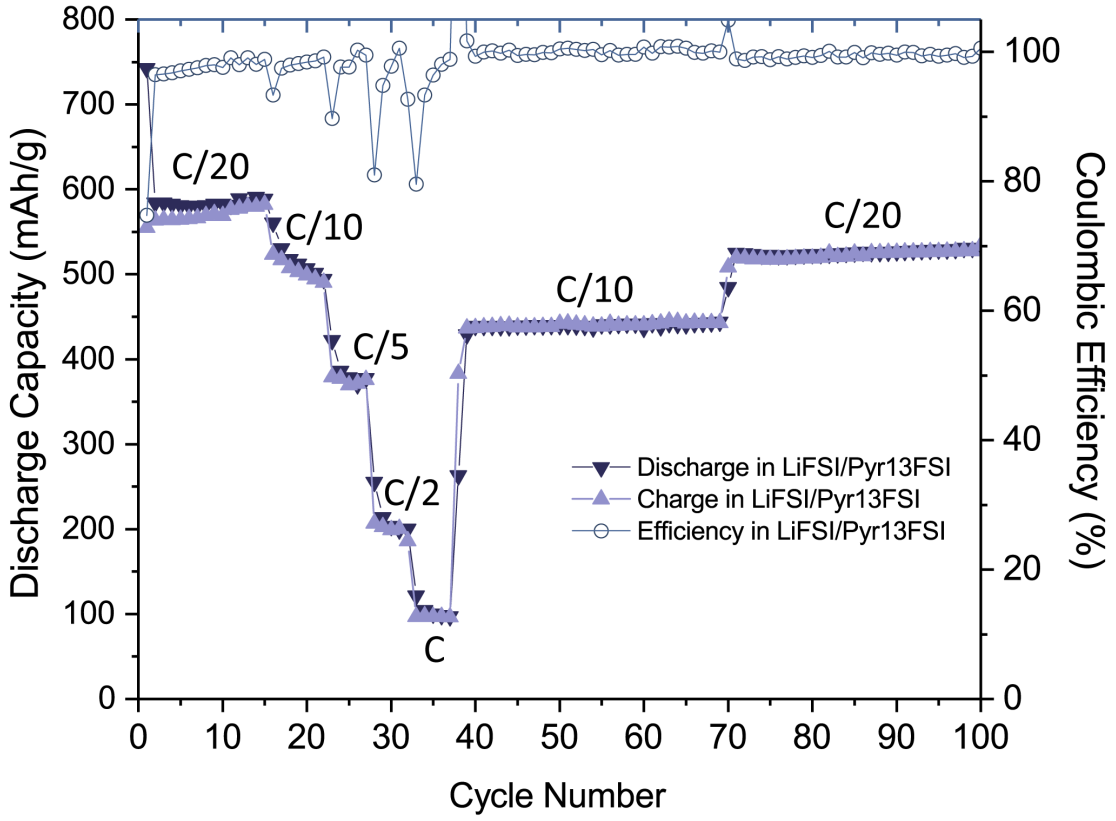


Figure 3.19: IL Electrolyte Stability at Increased Cycling Rate. Gravimetric capacity and coulombic efficiency are plotted over 100 cycles for FeF_2 nanorod cathodes cycled in ionic liquid electrolytes. The discharge/charge current density (cycling rate) is varied between C/20 and 1C as indicated in the plot. 92.8% of the theoretical capacity is retained after 100 cycles with a cumulative experiment time of 111 days. The outstanding cycling stability enabled by the IL electrolyte is maintained at higher cycling rates and over long periods of time, indicating it's suitability for commercial applications.

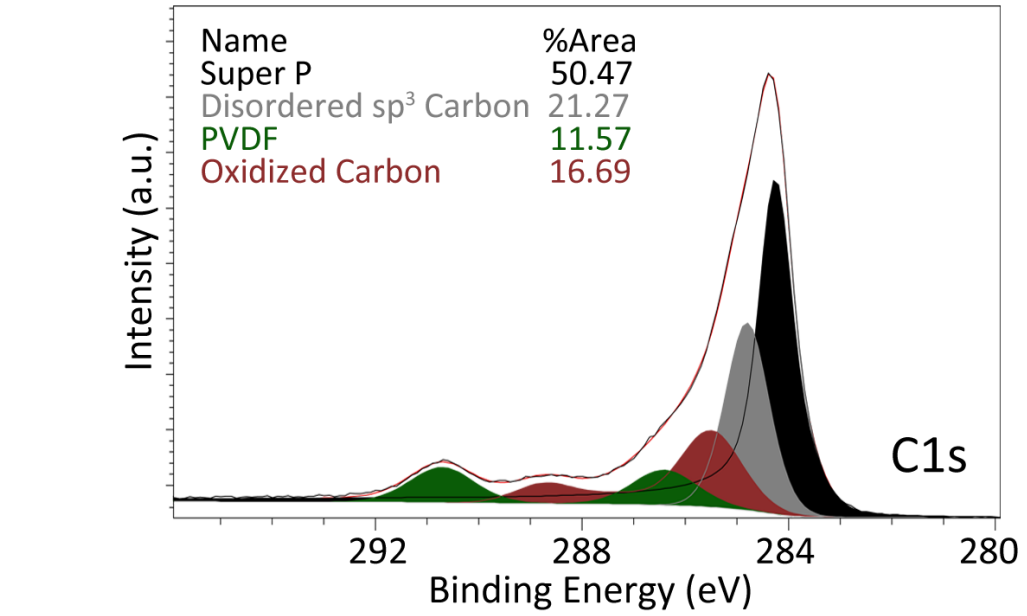
3.4.1 SEI Composition and Stability

An excessive or progressively growing SEI results in increased ohmic resistance and irreversible capacity loss (as in the case of LP30 above); on the other hand, the formation of the stable SEI layer is actually critical to stable cycling in LIBs. Electrochemical impedance spectra for the IL system show an increase in charge transfer resistance

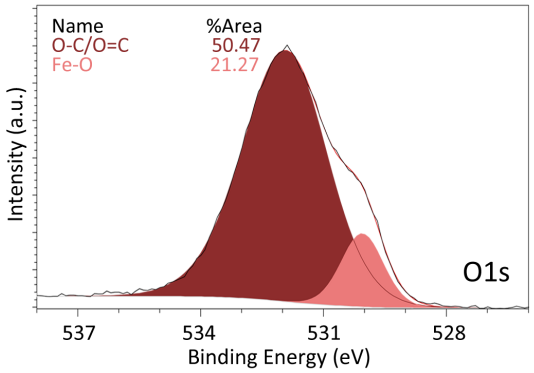
following the first discharge. After this initial SEI layer formation, EIS spectra show virtually no increase in charge transfer resistance for the first five cycles and only minimal increases thereafter (3.11b). This is consistent with the stable cycling observed immediately after the first discharge. In contrast, the charge transfer resistance is higher in the LP30 system and increases by a factor of three over the first five cycles.

X-ray photoelectron spectroscopy (XPS) can be used to understand chemical transformations within the SEI layer. Before *ex-situ* measurement, electrodes cycled in the LP30 and IL electrolytes were repeatedly washed in dimethyl carbonate to allow for removal of any readily soluble species. XPS spectra of the pristine (uncycled) electrodes are shown in Figure 3.20 below. The peaks observed in this case result only from the as-synthesized FeF_2, carbon black, and PVDF. Components corresponding to these materials were also observed in the XPS spectra of the cycled electrodes, albeit with a much lower intensity due to the widespread SEI formation over the electrode surface. The graphitic (sp^2) component of the C1s peak at 284.0 eV was used for charge correction of each spectra as this component can be attributed entirely to the Super P carbon black, which is chemically inert and redox stable within the potential range of the experiment (4.0 V to 1.2 V vs. Li^+/Li). Charge correction in this way produced the best fit (lowest residual standard deviation) between the spectrum and synthetic components and further placed the two PVDF C1s peaks at or near the characteristic values (290.8 eV and 286.3 eV), suggesting a successful calibration.[108]

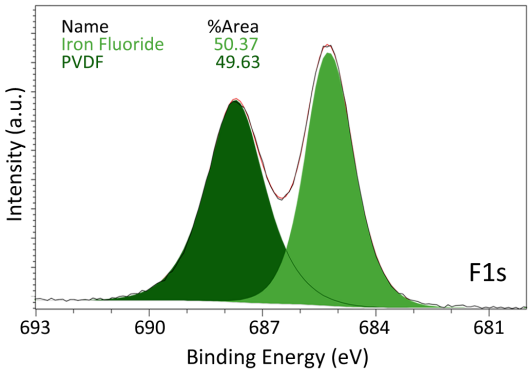
In both electrolytes, the first discharge deposits of large amounts of aliphatic carbon with some oxygen functionalities, presumably from the breakdown of carbonate solvents in the LP30 and pyrrolidinium in the IL. This phenomenon is indicated by the intense sp^3 signal in the C1s spectra and the diminishing of peaks related to Super P and PVDF. This change is more pronounced in LP30, implying a thicker SEI in line with the higher charge transfer resistance observed. In LP30, Li_2CO_3 is formed on discharge but is not present after charge (Figure 3.21,3.23); a significant portion of the organic component is also dissolved, while the concentration of $Li_4P_2O_7$ nearly doubles (Figure 3.23). This uncontrolled redox behavior explains the large fluctuations in charge transfer resistance observed in the EIS spectra between charge and discharge and likely contributes to the low coulombic efficiency (Figure 3.17b).



(a) Carbon 1s Spectra.



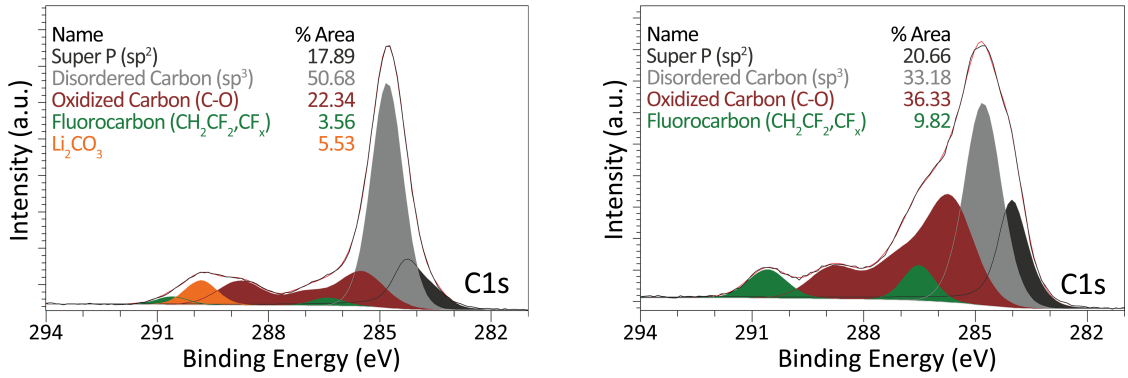
(b) Oxygen 1s Spectra



(c) Fluorine 1s Spectra

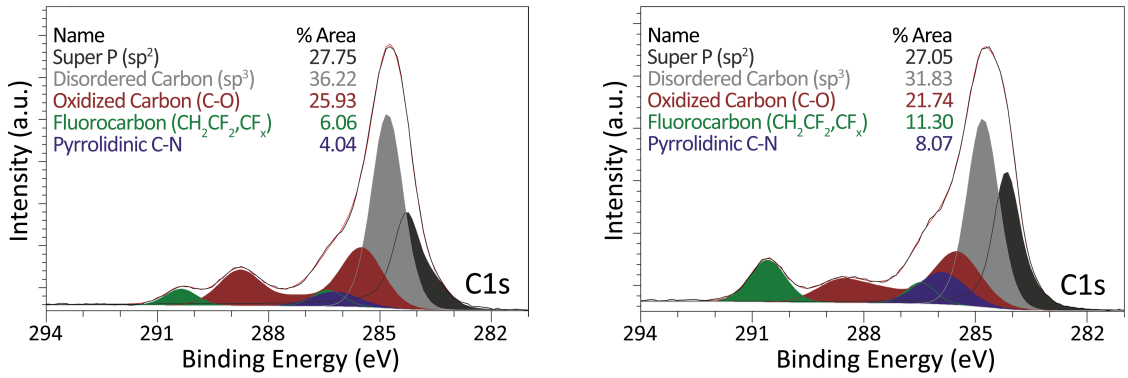
Figure 3.20: Chemistry of the Uncycled Electrode Surface. C1s, O1s, and F1s XPS spectra are shown for the pristine FeF_2 nanorod electrodes. These spectra provide a reference for the analysis of SEI formation at the electrode surface. An asymmetric line shape was used to fit the sp^2 component of the C1s spectra as described by Blume *et al.*[109] The C1s spectra exhibits significant changes on cycling due to the organic nature of the electrolytes as well as the SEI layer itself. Oxidized carbon and fluorocarbon peak areas are fit using the deconvoluted high-resolution O1s and F1s spectra to produce a self-consistent peak model.

No such fluctuations are observed in the EIS spectra for the ionic liquid electrolyte; XPS also demonstrates a greater degree of electrochemical stability. The SEI formed from the ionic liquid contains significantly more inorganic components derived from the FSI (Figure 3.22, 3.23). These phases include lithium oxides, lithium sulfides, and sulfonimide derivatives (Figure 3.23b). On charging, this inorganic component is increased, while the organic material becomes increasingly functionalized with nitrogen and fluorine.



(a) LP30-Discharged State **(b)** LP30-Recharged State

Figure 3.21: LP30 Derived SEI. Carbon 1s XPS spectra of FeF_2 nanorod electrodes cycled in the LP30 electrolyte. Comparison with the pristine electrode indicates the formation of a significant aliphatic layer on discharge (a) and its dissolution on charge (b). This is apparent from the prevalence of the sp^3 peak as well as the diminishing of the PVDF and graphitic carbon peaks related to the underlying electrode. Large fluctuations in the C1s envelope are observed between charge and discharge.

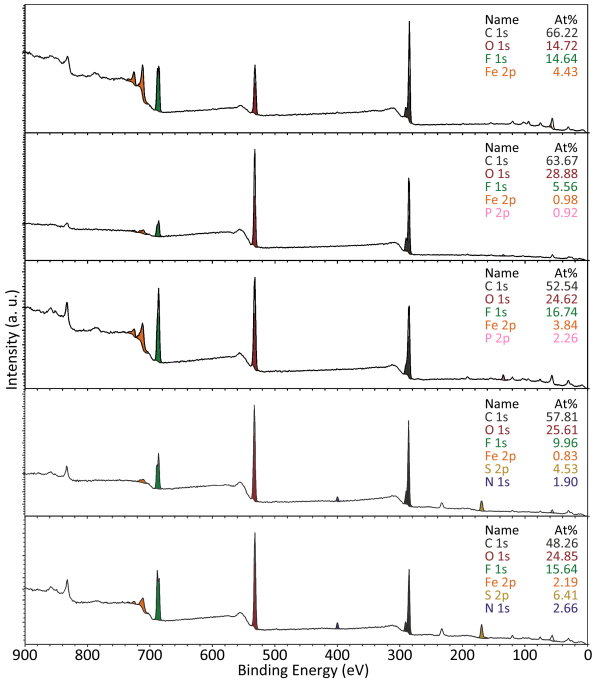


(a) IL-Discharged State **(b)** IL-Recharged State

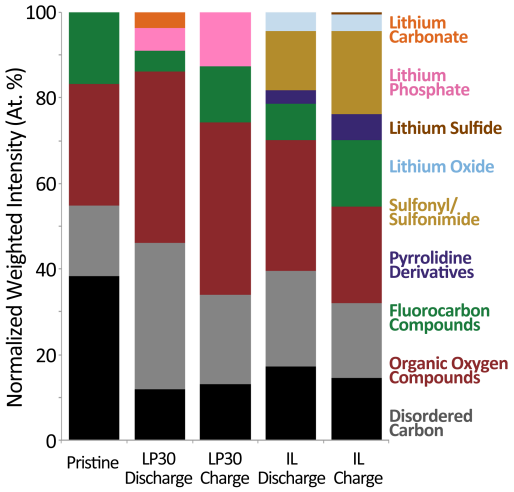
Figure 3.22: IL Derived SEI. Carbon 1s XPS spectra of electrodes cycled in the IL electrolyte. Compared to the LP30 system, a less massive aliphatic component is observed on discharge (a), and significantly less fluctuation in the relative intensities of all peaks is observed between discharge and charge. An increase in N and F functionalities is apparent on charge.

These additional elements may contribute to the SEI stability by preventing it from redissolving.[110,111] The chemical composition of the SEI layers is summarized in the chart below. The quantification was based on the XPS survey spectra and components from deconvoluted high resolution elemental scans. The IL electrolyte consists of 50 mol.% FSI anions; these anions serve as inorganic precursors, which travel with the Li^+ ions to the cathode surface on discharge.

The IL-derived SEI is manifest in the *ex-situ* TEM images (Figure 3.24) as a uniform and continuous surface coating. In both TEM images below the SEI layer is about



(a) Comparison of XPS Survey Spectra.

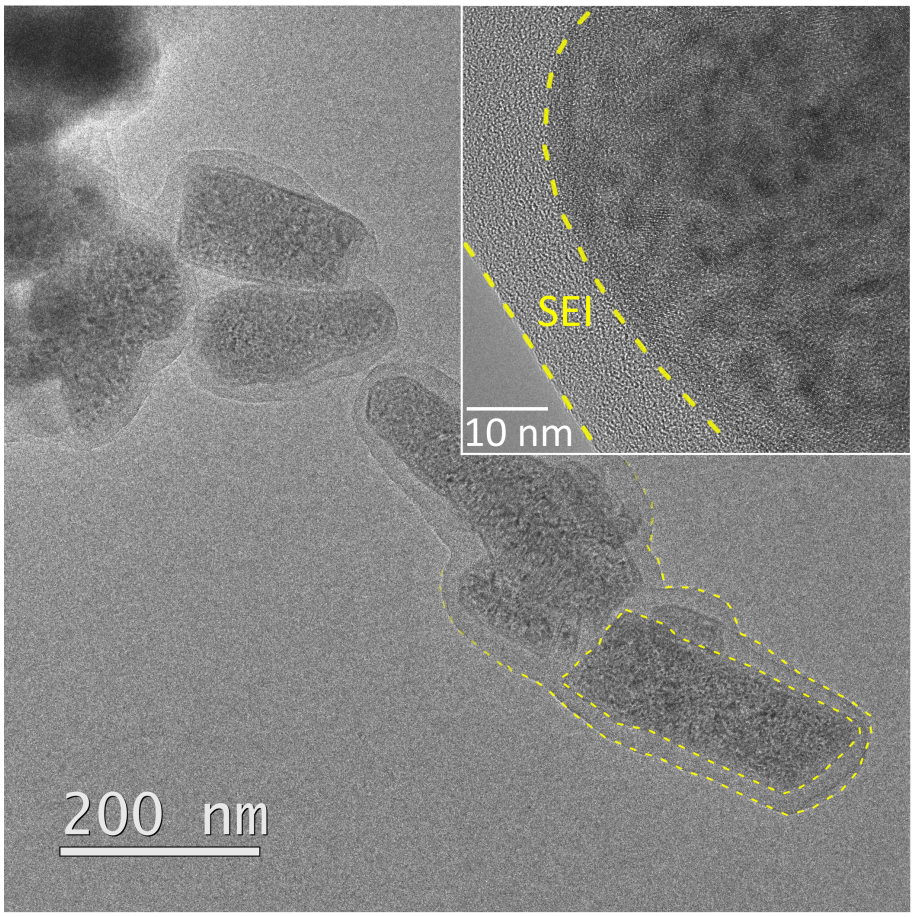


(b) Changes in Chemical Composition Over all Elemental Windows.

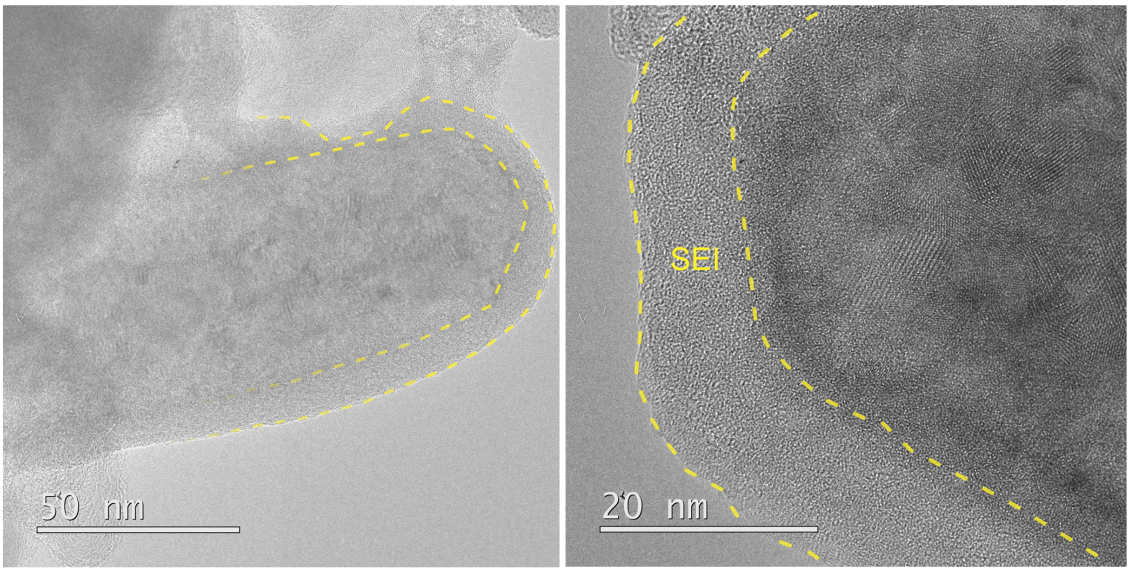
Figure 3.23: Chemical Composition of SEI Layers. The XPS survey spectra (a) also show large differences in chemical composition at the electrode surface between the two electrolytes. Again significant fluctuation between charge and discharge is apparent in the LP30 electrolyte, while more inorganic elements are observed in the IL electrolytes. Combining the survey spectra with the deconvoluted high-resolution spectra for each elemental window provides a more complete description of the SEI composition. This is summarized in (b) FeF_2, Fe and LiF are excluded for clarity. An explanation of how the chemical composition was quantified is given in Appendix I (Figure 5.4). The intensities shown in (b) are normalized by the total integrated intensity of the corresponding survey spectra with each component weighted by the relevant relative sensitivity factors. (b) shows relative rather than absolute surface composition.

10 nm thick, again indicating that no significant SEI growth occurs. After 15 cycles, the SEI appears darker; this may suggest an increased density resulting from increasingly inorganic composition (Figure 3.24b).

Once formed, this robust SEI layer acts as an electrically insulating passivation layer that provides stability against additional electrolysis of the electrolyte. The inorganic components of the IL-derived SEI exhibit a low solubility and conductivity for Fe^{2+} and Fe^{3+} cations. Thus the IL-derived SEI forms an effective barrier between the FeF_2 particle and the electrolyte preventing solubilization and dissolution of iron from the cathode on charging. The SEI formed from the LP30 electrolyte is mostly aliphatic and contains a number of oxygen functionalities. The fact that it redissolves into the electrolyte suggests that it has a similar chemistry and may actually behave like an solvent at the FeF_2 particle surface, facilitating the dissolution of iron from the cathode.



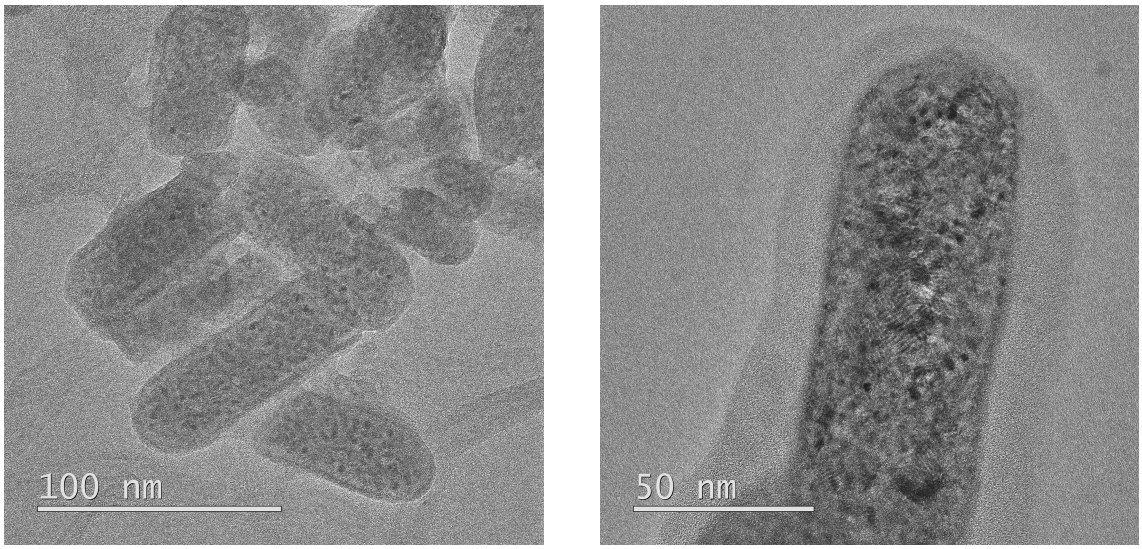
(a) TEM image of the SEI after the 1st Discharge.



(b) SEI after 15 Discharge and Charge Cycles

Figure 3.24: SEI Formation and Evolution in the IL Electrolyte. (BF TEM.) The first discharge in the IL electrolyte produces a uniform solid-electrolyte interphase that passivates the surface of each FeF_2 nanorods and prevents further electrolyte decomposition. This SEI is robust and remains unchanged after 15 cycles.

3.4.2 Morphology Preservation



(a) A cluster of discharge FeF_2 nanorods. **(b)** A single FeF_2 nanorod with intact SEI layer.

Figure 3.25: Preservation of Nanorod Morphology. (BF TEM.) The IL electrolyte exhibits the unique ability to prevent the fusing of adjacent nanorods on discharge. The majority of FeF_2 particles retain their nanorod morphology on cycling and adjacent particles remain seperated, enabling the mechanistic characterization in **Chapter 4**

The robust SEI layer formed from the IL prevents both cathode dissolution and electrolyte decomposition at the FeF_2 surface. The IL electrolyte demonstrates the unique ability to prevent the fusing of FeF_2 particles as well. The TEM images of FeF_2 particles cycled in LP30 all exhibit large irregular particles and a near complete loss of the nanorod morphology. However, this fusing phenomenon is not apparent in the IL electrolyte.

Figure 3.25 above shows an image of the FeF_2 nanorods after the first discharge; other TEM images presented in this chapter demonstrate that the nanorod morphology is still preserved after many cycles. The mechanistic reasoning for this will be flushed out in the next chapter; however, it is important to note that the ability to prevent particle fusing is what enabled this mechanistic investigation in the first place. This phenomenon cannot be a result of the SEI Layer seperating particles because fusing is still apparent even when an SEI has formed (i.e. in LP30), and because the SEI forms concurrently with the fusing of particle on the first discharge.

In the introductory chapter; I discussed how ionic liquid mediated synthesis methods were able to stabilize small particle sizes during the growth of metal fluorides. This is thought to be a result of electrostatic interactions between the liquid ions and nanoparticle

surface. It's possible that a similar electrostatic interaction in the electrolyte creates a strongly bound solvation layer that maintains the seperation of particles during cycling.

3.5 Differential Rate Capability on Charge and Discharge

The reaction overpotential is strongly dependent on the current density applied to the electrode (discharge/charge rate). If mass transport within the electrode cannot maintain concentrations of the electrochemically reactive species at the relevant interfaces, than a large increase in reaction overpotential is observed. As a result, the capacity observed during cycling decreases if the charge/discharge rate becomes too high. The "rate capability" of an electrode refers to the amount of capacity that can be retained at relatively high cycling current densities.

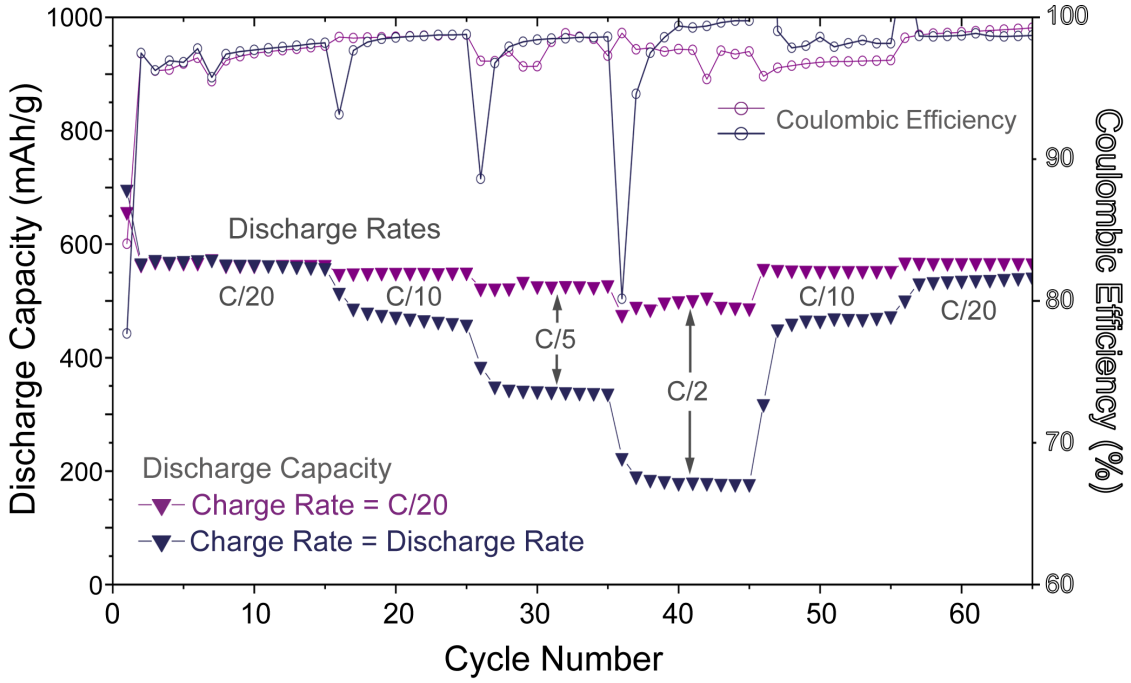


Figure 3.26: High Discharge Rate Capability. When the FeF_2 nanorod cathodes are charged to their full capacity, a high discharge rate capability is observed, even at relatively high active material loading (70 wt%). This property is inherent to transition metal fluorides and can be seen from 1.9.

As mentioned previously, transition metal fluorides are electronic insulators with low ionic conductivities and are typically classed as "sluggish" electrode materials. Indeed the rate capability appears quite poor as indicated by the light purple plot of capacity vs. cycle # in Figure 3.26. For a 2 h discharge or charge (C/2 rate), only 200 mA h g^{-1} can

be accessed. However, if the material is always charged at a slow (C/20) rate to the full capacity, and only the discharge rate is varied, than ~500 mA h g^{-1} can be delivered at a C/2 rate. In other words, the discharge rate capability of FeF_2 is actually quite high, and the cycling rate is primarily limited by the charging kinetics. In the next chapter, I demonstrate that this differential rate capability is fundamentally tied to the reaction mechanism.

3.6 High Temperature Performance

A comparison between the IL electrolyte and a conventional 1 M $LiPF_6$ in 1:1 ethylene carbonate:dimethyl carbonate (LP30) electrolyte is made with a slow cyling rate (C/20) at room temperature (Figure 3.17b).

The cycling comparisons between the LP30 and IL electrolytes shown above were made at slow cycling rates (C/20) at room temperature. However, in real life applications, LIBs can become considerably hot due to resistive (Joule) heating. While conventional LIBs are stable to between 50 °C-60 °C, transition metal fluorides typically show vastly diminished stability even 10 °C-20 °C above room temperature.[25] The same failure mechanisms that plague transition metal fluorides at room temperature are only exacerbated at elevated temperatures. Higher temperatures may thermally activate the decomposition of electrolytes, and would certainly increase the solubility of Fe cations in the solvent.

In our IL electrolyte, however, stable cycling is observed for over 200 cycles at 50 °C and rates as high as C/2 (300 µA cm^{-2}). This high temperature performance is comparable to that recently demonstrated using a solid polymer electrolyte, but is achieved at much higher active material loading (70 wt.%).[25] Furthermore, the rate capability of FeF_2 was actually increased upon raising the cycling temperature. In Figure 3.27 below, initial cycles were performed at C/10 to demonstrate the full capacity of the electrodes, which is close to the theoretical value (571 mAh/g). As the cycling rate is increased by a factor of 5, the capacity decreases gradually to 350 mAh/g at 40 °C and 400 mAh/g at 50 °C. This represents a large improvement in rate capability compared to room temperature (200 mAh/g). This phenomenon can also be explained in terms of the mechanism defined in the next chapter.

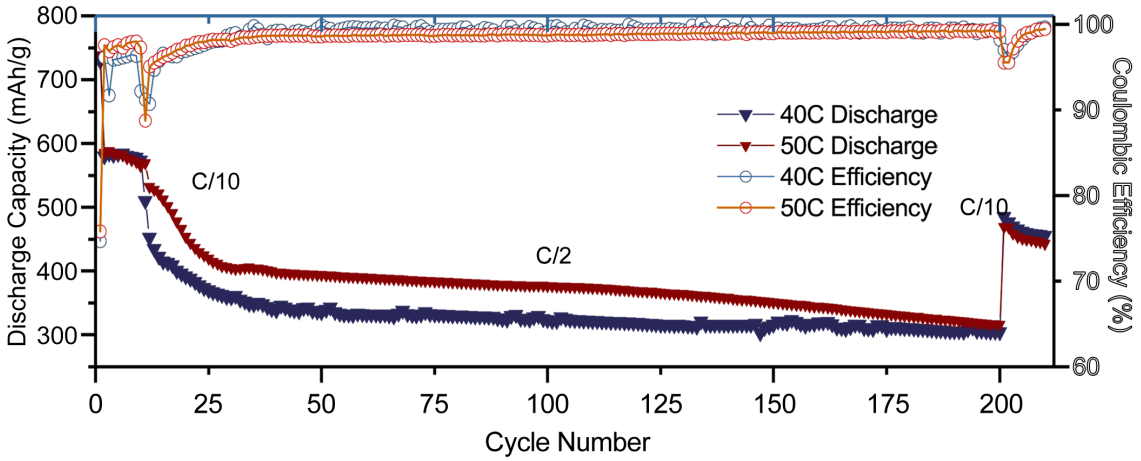


Figure 3.27: High Temperature Cycling Stability. The ionic liquid electrolyte developed herein allows for superior cycling stability at the highest active material loading in the literature.[1] This stability is retained at elevated temperatures and the rate capability of FeF_2 nanorod cathodes is improved by the additional thermal energy.

Chapter 4

The Conversion Mechanism

4.1 *Ex-Situ* Mechanistic Characterization

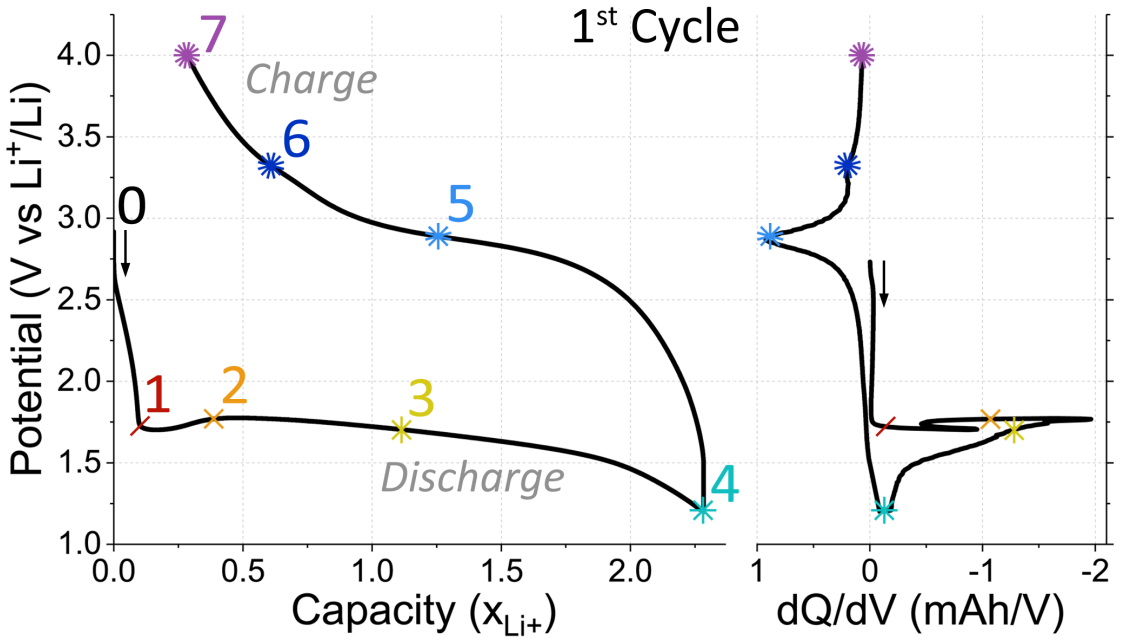


Figure 4.1: *Ex-Situ* Data Points. One of the major advantages of my approach to mechanistic study is the ability to correlate structural and chemical data to their state of charge. Seven reaction stages were investigated and are denoted by the points in the galvanostat and the corresponding differential capacity plot. Capacity is displayed as x_{Li^+} in the reaction $\frac{x}{2}\mathrm{FeF_2} + x\mathrm{Li}^+ + xe^- \rightarrow \frac{x}{2}\mathrm{Fe} + x\mathrm{LiF}$. The full theoretical capacity corresponds to $x_{Li^+} = 2$.

In this chapter we present a detailed and comprehensive study of the full discharge/charge (conversion/reconversion) mechanism in the prototypical FeF_2 system. Most measurements were performed *ex-situ* using FeF_2 nanorod electrodes cycled in the coin cell format described in **Chapter 3**. Non-destructive and air-free sample preparation is described in

Appendix I. The galvanostatic profile displayed above (Figure 4.1) indicates the different stages of the reaction from which *ex-situ* samples were extracted. The *ex-situ* XRD and TEM data below are labeled with numbers 0-7, referring to the corresponding reaction stages marked in the galvanostatic profile.

Chapter 1 described how *in-situ* TEM measurements formed the basis for the common understanding of the conversion mechanism. *In-situ* TEM measurements require a large negative bias between the lithium probe and the sample, which promotes kinetic reaction pathways, making it difficult or impossible to observe transient intermediates that are stable in a real battery.[72,73] Nevertheless, *in-situ* TEM is employed to help visualize and corroborate larger scale observations from the *ex-situ* data.

4.1.1 *Ex-Situ* XRD

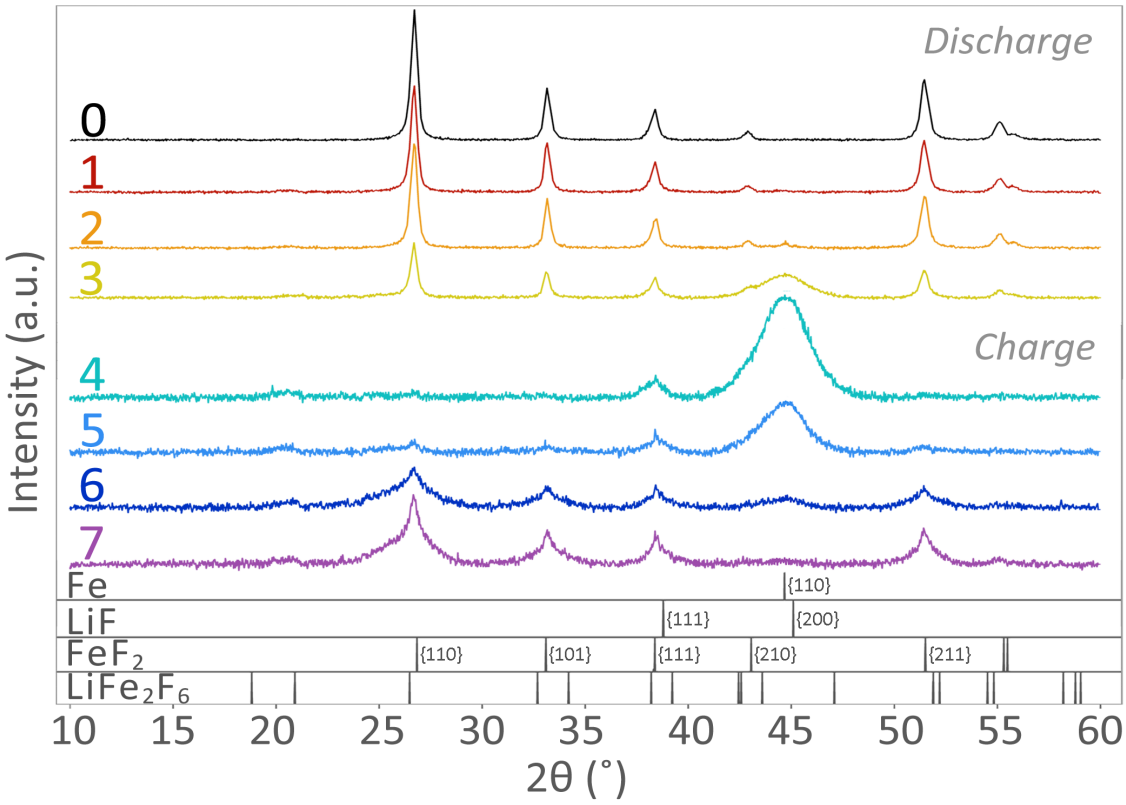


Figure 4.2: Conventional Characterization by XRD. Powder XRD patterns obtained from the pristine electrode and the seven *ex-situ* samples defined in Figure 4.1.

To understand the significance of the results presented herein, we first consider the limitations of conventional characterization techniques. Figure 4.1 above displays *ex-situ* XRD data of the FeF_2 nanorod cathodes at different states of charge and discharge. On

discharge, the intensity of the rutile FeF_2 peaks gradually decreases, and as the reaction progresses, a small LiF peak is observed, followed by the formation of a very broad peak indicating the presence of extremely small iron nanoparticles. On charge, the Fe and LiF phases are consumed with the concomitant formation of a noticeably more disordered rutile phase. The only conclusions that can be made from this data are that the conversion reaction appears to follow the equation $\mathrm{FeF_2 + 2Li^+ + 2e^- \rightarrow Fe^0 + 2LiF}$, which has been well established.[15] While more advanced spectroscopic and X-ray diffraction techniques are sensitive enough to measure more nuanced changes in phase composition and structure, they still lack the spatial resolution to make definitive conclusions about the mechanism. That is they can explain what the conversion reaction does, but not how or why this reaction works.

Typically, high-resolution transmission electron microscopy (HRTEM) offers little information due to the difficulty of isolating single crystals from a battery and the impossibility of correlating structure and morphology between disparate particles. The purpose of the work presented up to this point has been to overcome these challenges. In **Chapter 2** we designed a material system where all particles of the FeF_2 cathode are single crystalline and share the same size, morphology, lattice orientation, and exposed facets. In **Chapter 3**, we developed an electrolyte system that enabled fully reversible cycling, while preserving the nanorod morphology throughout discharge and charge. HRTEM investigation from this unparalleled vantage point redefines the understanding of the conversion reaction. I first introduce the concept of surface-specific reaction mechanisms and delineate their role in controlling morphology and phase evolution.[19,20] Subsequent sections detail the large-scale lithiation prior to nucleation of metallic iron and complex phase equilibria involving intermediate phases; these results provide long-awaited experimental verification of theoretical predictions.[24,74] I expand on the recent report from Karki *et al.* to decisively establish the conversion reaction as a topotactic transformation between fluoride phases.[23] An unprecedented view of the reconversion (delithiation) reaction uncovers considerable chemical and structural symmetry in the reaction pathways. This discussion will provide a new rationale for the reversibility of the conversion reaction, based on interfacial coherence and the persistence of the fluoride lattice.

4.1.2 Interpretation of TEM Data

The reaction mechanism presented herein relies heavily on high resolution transmission electron microscopy (HRTEM) data. An HRTEM image is formed from a combination of mass-thickness contrast, atomic number (Z) contrast, diffraction contrast, and phase contrast. When interpreted accurately, these features can yield a wealth of information about the morphology, composition, and structure of complex nanoparticles. Mass-thickness contrast and Z contrast are primarily useful for resolving morphological features. In a particle of uniform thickness (such as an FeF_2 nanorod) differences in observed pixel intensity at lower magnifications result from differences in density or atomic number. For example, distinguishing between the Fe and LiF discharge products is straight forward as metallic Fe is both more dense and contains heavier atoms than LiF and thus appears as darker regions in the bright-field image.

Ultimately, however, diffraction contrast in HRTEM is the key to understanding the mechanism of the conversion reaction. As the electron beam in a TEM interacts with a crystalline sample, most of the beam is directly transmitted, forming a 2D projection of the sample morphology. However, a portion of the beam is diffracted at Bragg angles due to the periodic arrangement of atoms in the lattice. In an HRTEM, both the directly transmitted beam as well as the diffracted beam are focused into a diffraction pattern on the back focal plane of the objective lens (Figure 4.3). Inherent in this is a Fourier transform of the 2D structure of the sample from real-space to reciprocal space. Likewise, an inverse Fourier transform occurs as the electron beam is resolved on the imaging plane. In real space, the diffraction spots appear as lattice fringes superimposed on the image; if all of the lattice fringes can be resolved by the microscope, than the diffraction pattern at the back focal plane can be recovered using a digital fast Fourier transform (FFT). As a result of interference between the directly transmitted and diffracted beams, along with phase shifts induced by lens abberations, the final HRTEM image does not reproduce the actual positions of atomic columns. However, the periodicity and orientation of lattice planes is preserved, and this spatially resolved diffraction data allows for the determination of the different crystallographic phases in an image and even the orientation relationships between them.

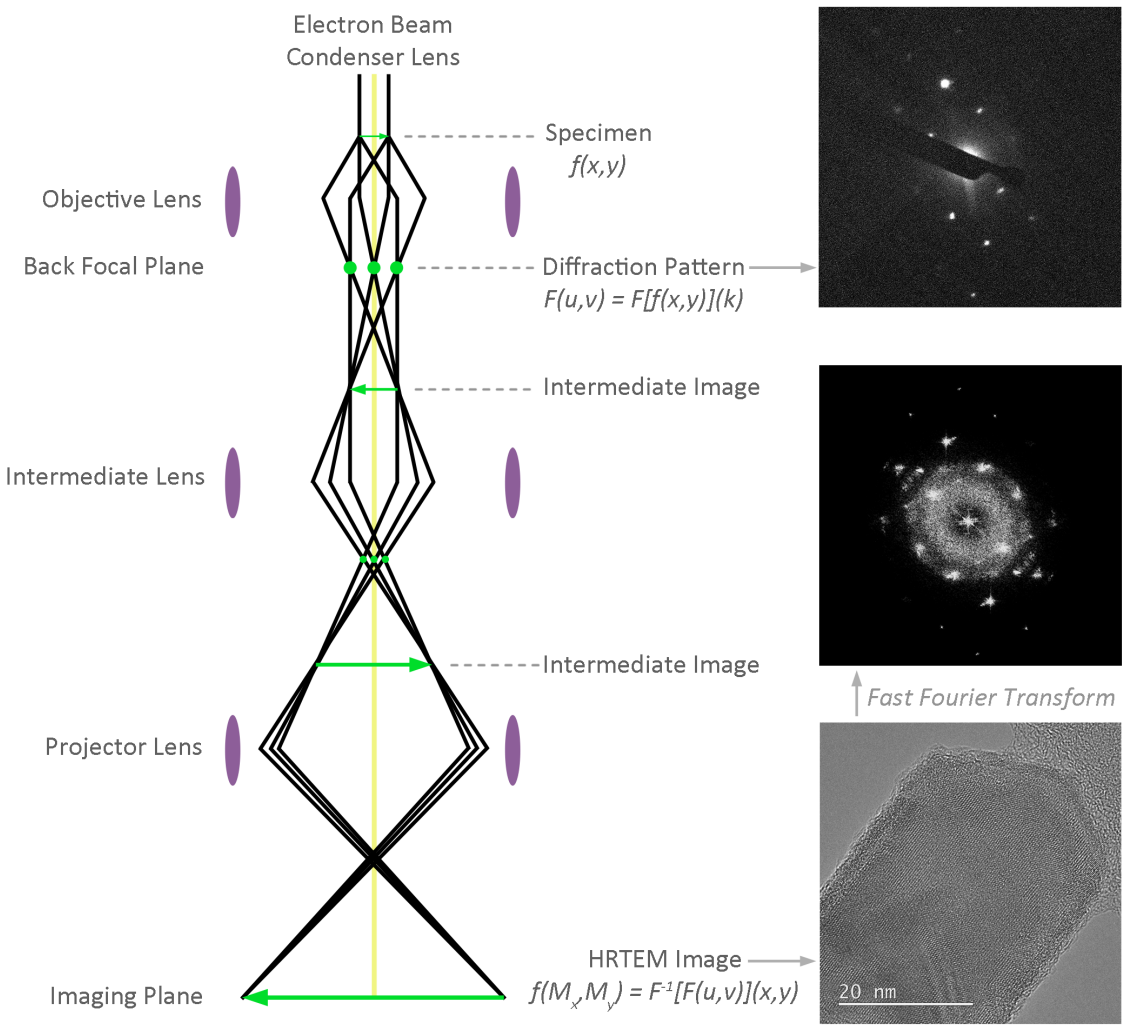


Figure 4.3: Structural Data from HRTEM. Electron diffraction data is contained within an HRTEM image. Localized crystallographic information can be obtained by applying a fast Fourier Transform to a HRTEM image. For small individual nanoparticles, diffraction patterns obtained via FFT are of higher quality than those obtained by direct electron diffraction.

In addition to bright field (BF) HRTEM, high angle annular dark field (HAADF) scanning transmission electron microscopy (STEM) coupled with electron energy loss spectroscopy (EELS) was used to measure chemical changes in FeF_2 nanorods during discharge and charge. EELS measures core-level electronic transitions in the atoms of a sample and is highly sensitive to oxidation state changes. For 3d transition metals, the major feature in the energy loss spectrum is the $L_{2,3}$ edge, which corresponds to transitions originating in the $2p_{3/2}$ (L_3) and $2p_{1/2}$ (L_2) core energy levels. In addition to the continuum "saw-tooth" edge resulting from the ejection of 2p core electrons to vacuum energy levels (i.e. complete ionization), transition metal L edges also contain a pair of sharp peaks or

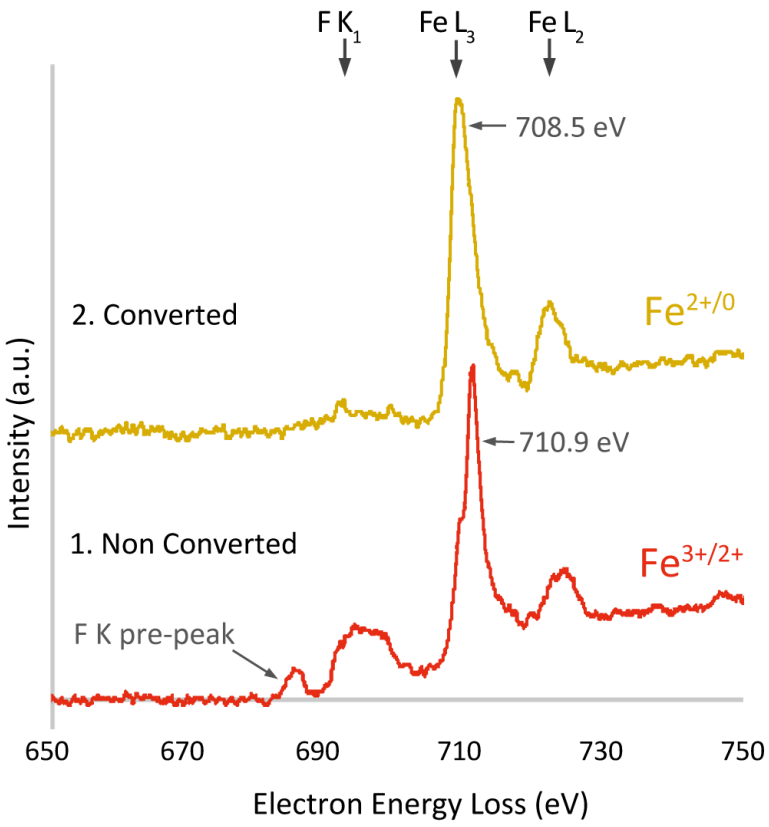


Figure 4.4: EELS Analysis. Sample EELS spectra obtained from an *ex-situ* TEM experiment showing the difference between characteristic Fe^{2+} and Fe^{3+} electron energy loss peaks. The spectra were taken from a single FeF_2 nanorod lithiated (converted) to half the theoretical capacity. There are two distinct regions within each particle at this stage. The unconverted region contains $Fe^{II}F_2$, $LiFe_2^{II,III}F_6$, and LiF, and exhibits a higher L_3 peak position. The converted region contains $FeF^{II}F_2$, LiF, and Fe^0, and exhibits a lower L_3 peak position. A detailed description of these two regions and their corresponding phase equilibria is presented in Section 4.4.

"white lines" in the near-edge structure resulting from the excitation of electrons to empty states just above the Fermi energy (i.e. the transition metal d band). The L_3 peak position coincides with the onset of the $L_{2,3}$ edge, and this onset energy is strongly dependent on the binding energy of the p orbitals. The effective nuclear charge and consequently binding energy, increase with increasing oxidation state, and thus the L_3 peak position (chemical shift) shifts to higher energy loss values as the oxidation state of the transition metal increases. Because the L_3 and L_2 peaks result from transitions between the filled 2p orbitals and empty states in the 3d bands, their relative intensity is a function of the probability with which either transition occurs; this is ultimately related to the d-orbital occupation. For 3d transition metals, it has been shown that the L_3/L_2 peak intensity ratio increases with d-orbital occupation from d^1 to d^5 and then decreases from d^5 to d^9.[112]

Thus, for Fe, the L_3/L_2 ratio is highest for Fe^{3+} (d^5), lower for Fe^{2+} (d^6) and lowest for Fe^0 ($d^{>6}$).

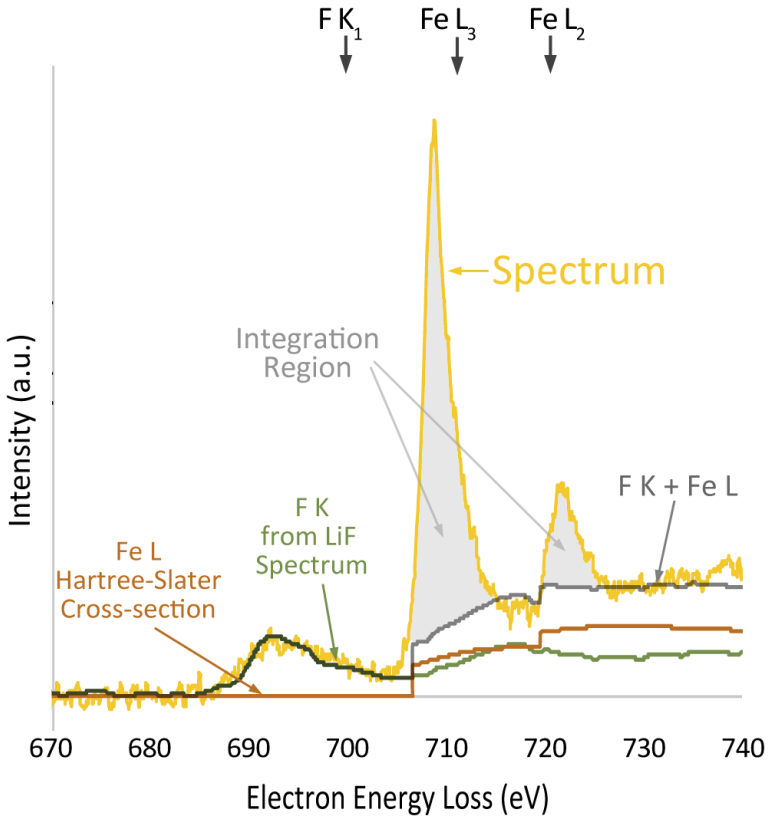


Figure 4.5: L_3/L_2 Quantification. An example EELS spectrum demonstrating the removal of F K-edge and Fe L-edge continuum energy loss signal for the accurate quantification of L_3/L_2 peak intensity ratios. The orange line represents the Fe L-edge continuum energy loss calculated using a Hartree-Slater cross section. The green plot is the estimated F K-edge contribution obtained from a background subtracted LiF spectra. The grey line represents the sum of these two contributions and the intensity that was subtracted from the spectrum before peak integration. Peaks were integrated over 4 eV windows centered on the peak maxima.

While a general trend can be predicted, the exact values of the chemical shifts and L_3/L_2 peak ratios depends on the material in question. For iron fluorides (FeF_2, FeF_3), Cosandey *et al.* experimentally demonstrated an L_3 peak shift of nearly 2 eV between Fe^{3+} (710.8±0.5 eV) and Fe^{2+} (708.9±0.5 eV) states, but only a modest shift with further reduction to the Fe^0 oxidation state (708.5±0.5 eV).[113] The L_3/L_2 peak ratios exhibit only a small decrease from Fe^{3+} (4.8±0.4) to Fe^{2+} (4.4±0.4) but, fortuitously, provide a clear distinction between these higher oxidation states and Fe^0 (2.9±0.4). The differences between Fe^{3+} and Fe^{2+} EELS spectra are shown in Figure 4.4. The F K-edge in these compounds is characterized by a primary (K_1) peak at a ~694 eV corresponding to

transitions between the F 1s orbital and empty 2p states. A "pre-peak" in the F K-edge at ~685 eV is observed only in the Fe^{3+} fluorides and can be used to further identify Fe^{3+} oxidation states. Determination of L_3/L_2 ratios in iron fluorides is particularly difficult because the tail of the F K-edge overlaps with the onset of the Fe L-edge, and it is suggested that a second F K_2 peak is buried in the Fe $L_{2,3}$ region.[113] Herein, we measure the Fe L_3/L_2 ratio following the precedent of Cosandey *et al.* by first subtracting a power-law background, followed by a F K-edge reference spectra from a LiF standard, and finally a Hartree-Slater cross-section (to account for the continuum portion of the Fe L-edge), before integrating over the peak area. This process is demonstrated in Figure 4.5.

4.1.3 FeF_2 Nanorod Structure and Morphology

In **Chapter 1** I briefly examined the FeF_2 nanorod morphology during nucleation and growth. Before examining the *ex-situ* data, it is helpful to define the lattice orientation of the FeF_2 nanorods in the pristine state (Stage 0). Figure 4.6 below shows the FeF_2 nanorod as viewed from the end as well as from the side. The ⟨001⟩ zone can be seen from the end-on view (Figure 4.6) and is distinguished from the ⟨110⟩ zone (side-on view) by the greater number of reflections. The two perspectives unequivocally show that the lattice is oriented with the ⟨001⟩ along the length of the rod, and the ⟨110⟩ normal to the sides.

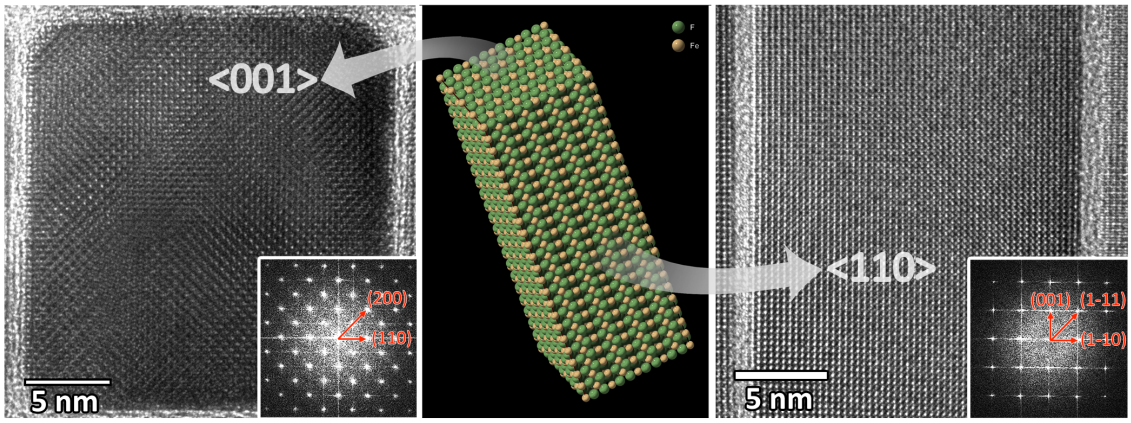


Figure 4.6: FeF_2 Nanorod Crystal Structure and Lattice Orientation. (BF TEM, FFT inset.) In the pristine state, the lattice orientation of FeF_2 nanorods is clearly displayed. The ⟨001⟩ direction runs parallel to the long axis of the nanorod, and the ⟨110⟩ directions are normal to the surface facets.

The tetragonal symmetry of the FeF_2 crystal system is reflected in the square prismatic

geometry of the nanorods. The angular position of the reflections in the FFTs (Figure 4.6 insets) indicates the direction of the plane normals, confirming that the nanorods exhibit facets dominated by the $\{1\,1\,0\}$ planes on the sides and bounded by a curved surface tangent to the $\{0\,0\,1\}$ planes on the end. This faceting causes the rods to naturally fall on their side in the $\langle 1\,1\,0\rangle$ zone axis orientation (Figure 4.6), which is used as a common reference frame to image the conversion reaction.

This high-symmetry zone-axis orientation allows for the facile derivation of lattice orientation relationships between phases. A fully defined lattice orientation relationship can be specified by a set of parallel planes ($(h\,k\,l)_A//(h\,k\,l)_B$) and set of parallel directions ($[u\,v\,w]_A//[u\,v\,w]_B$) within said planes. If the zones of two different lattices appear in the same diffraction pattern (FFT) then parallel planes are already apparent, and parallel directions can be determined by relative position of lattice reflections.

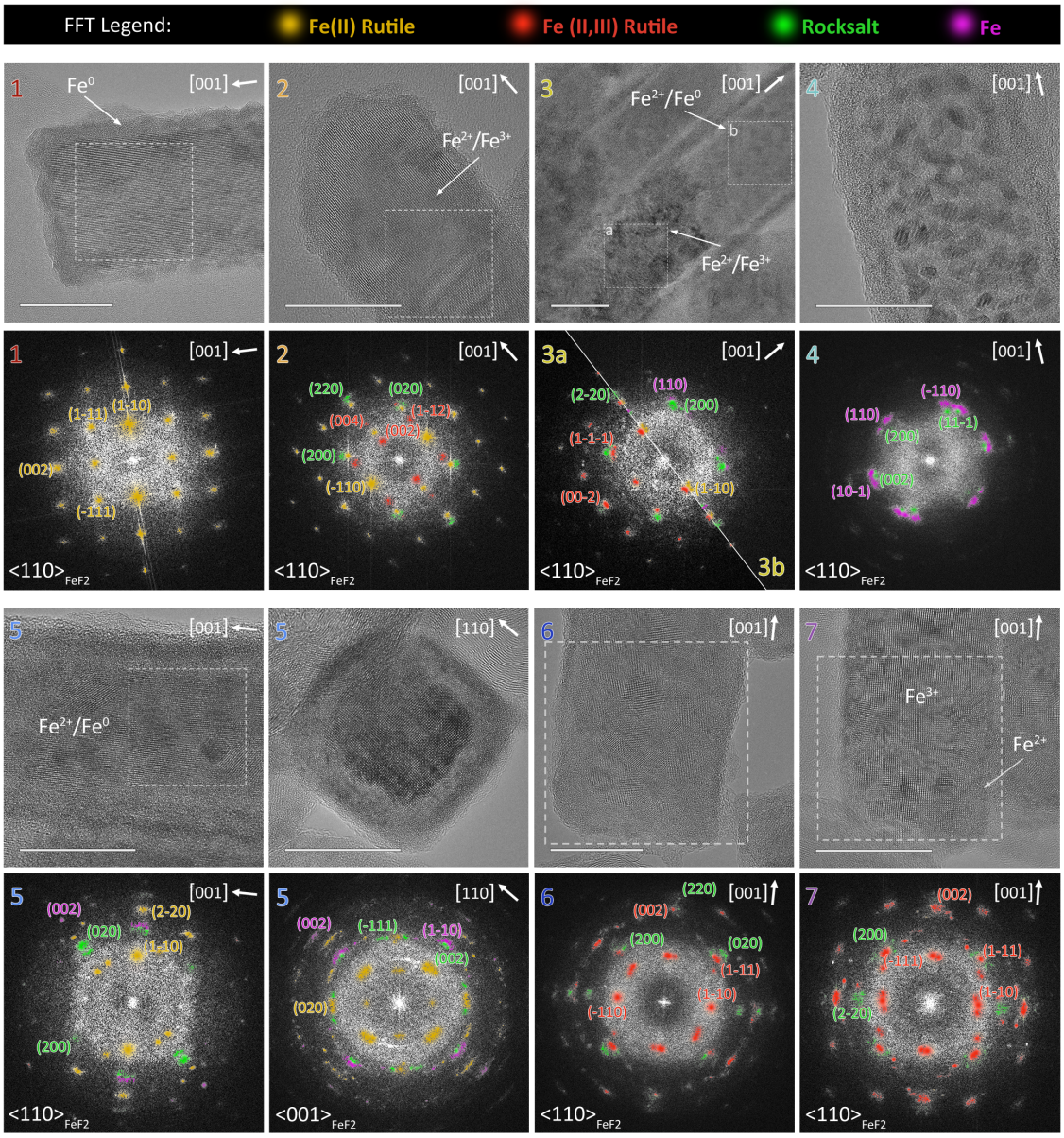
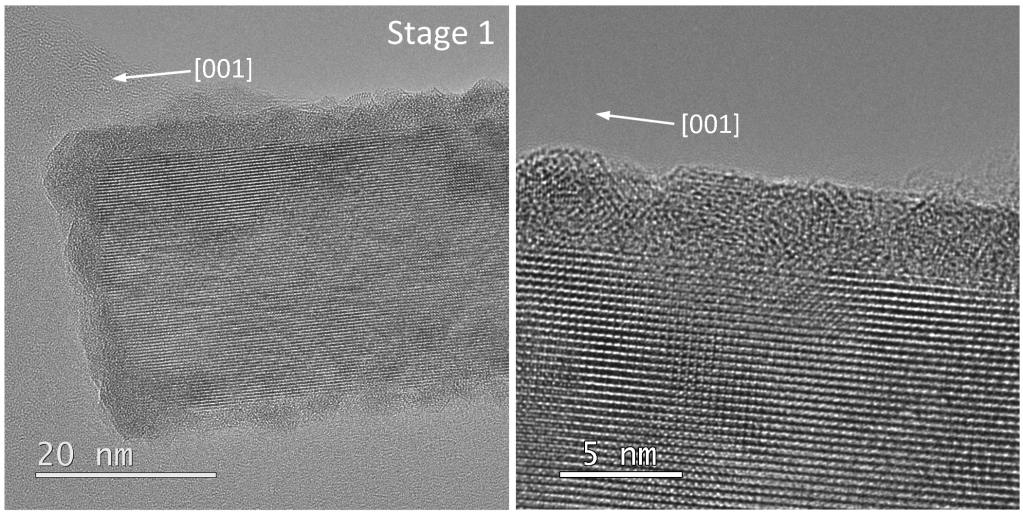


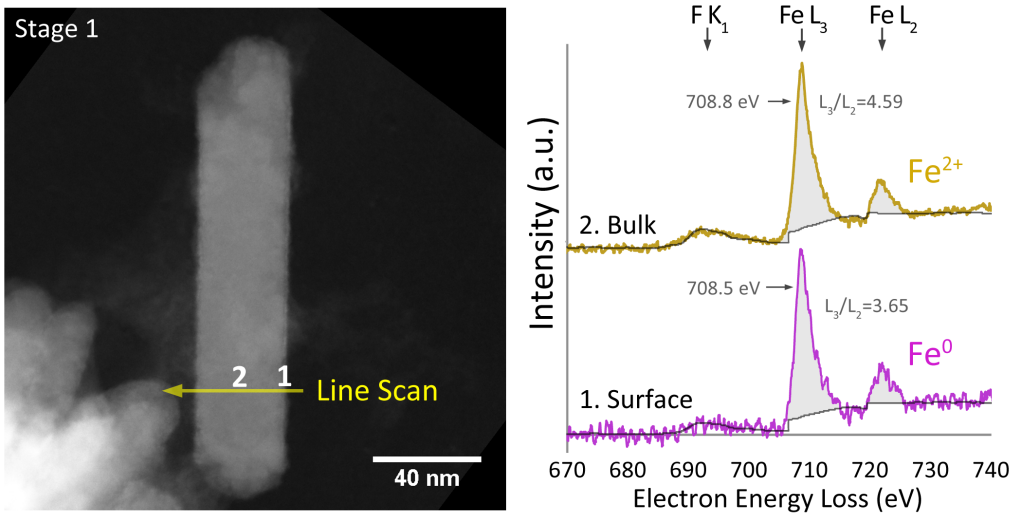
Figure 4.7: The Complete Conversion Reaction. (BF HRTEM and FFT.) TEM images and FFT diffraction patterns are displayed for each *ex-situ* data point in the discharge/charge pathway. FFT patterns are selectively colored based on their white pixel intensity to show the presence of different coexisting phases. For the sake of brevity and clarity, I will not detail the step by step progress of the reaction, but simply provide this figure as a guide to the conversion and reconversion process.

4.2 Surface Reactions

Reversible metal fluoride systems are invariably defined by particle sizes in the tens of nanometers and correspondingly high surface areas.[15,28,39,40] Despite being necessarily substantial, reactions specific to the surface have been largely ignored in the investigation of transition metal fluorides.



(a) BF HRTEM image of the amorphous surface layer.



(b) EELS spectra from the nanorod surface and core.

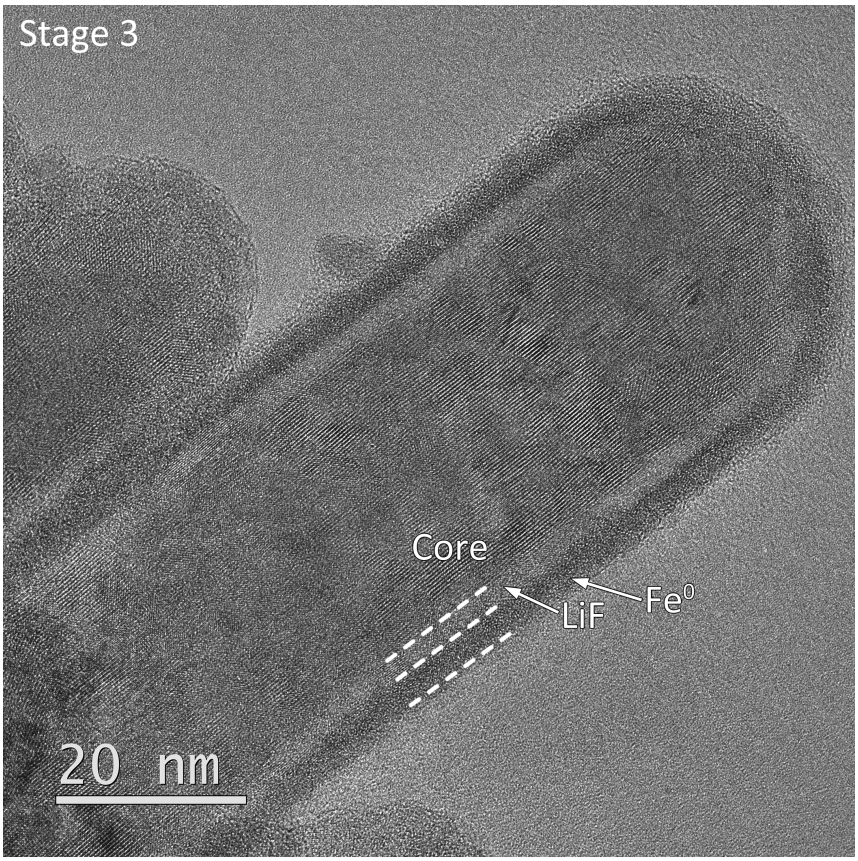
Figure 4.8: Stage 1—Discharge (1.7 V, x_{Li^+} = 0.05). An amorphous layer is readily apparent at the nanorod surface. The corresponding EELS line scane shows an Fe^0 signal localized to the nanorod surface and an Fe^{2+} signal from the core. Fe^0 can be distinguished from Fe^{2+} by its lower L_3/L_2 peak ratio and slightly lower L_3 peak position. The black plots shows the total contribution of the F K and continuum Fe L edges to better emphasize the difference in L_3/L_2 ratios between the two spectra. The reaction begins with a direct conversion of surface material to a disordered and finely divided mixture of Fe^0 and LiF.

The FeF_2 surface exhibits a distinct direct conversion reaction that plays a critical role in defining the reaction mechanism of the bulk. The reaction begins at the equilibrium discharge potential for FeF_2, 2.6 V vs. Li^+/Li, (Stage 0, Figure 4.1) with a small capacity (<5%) observed directly before the activation overpotential. This corresponds to the formation of a disordered surface layer (2 to 4 nm) of finely divided reaction products (Figure 4.8a). This layer is distinguished from the SEI by short-range (<2 nm) lattice fringes and strong Fe^0 EELS signal (Figure 4.8b). The structure of this layer is reminiscent of that predicted by Ma and Garofalini using a molecular dynamics approach.[19] The mechanism for its formation may indeed follow a similar pathway, whereby the insertion of lithium within the first few atomic layers causes a disordering of the lattice and the rapid formation of exceedingly small iron clusters. The prediction of anisotropic behavior along different crystallographic directions is also confirmed.[19] Along the $[0\,0\,1]$ direction, the interface between the amorphous layer and the single crystal is diffuse, suggesting short-range intercalation quickly followed by conversion; conversely, along the $[1\,1\,0]$ direction, the interface appears sharp, suggesting a layer by layer process (Figure 4.8a).

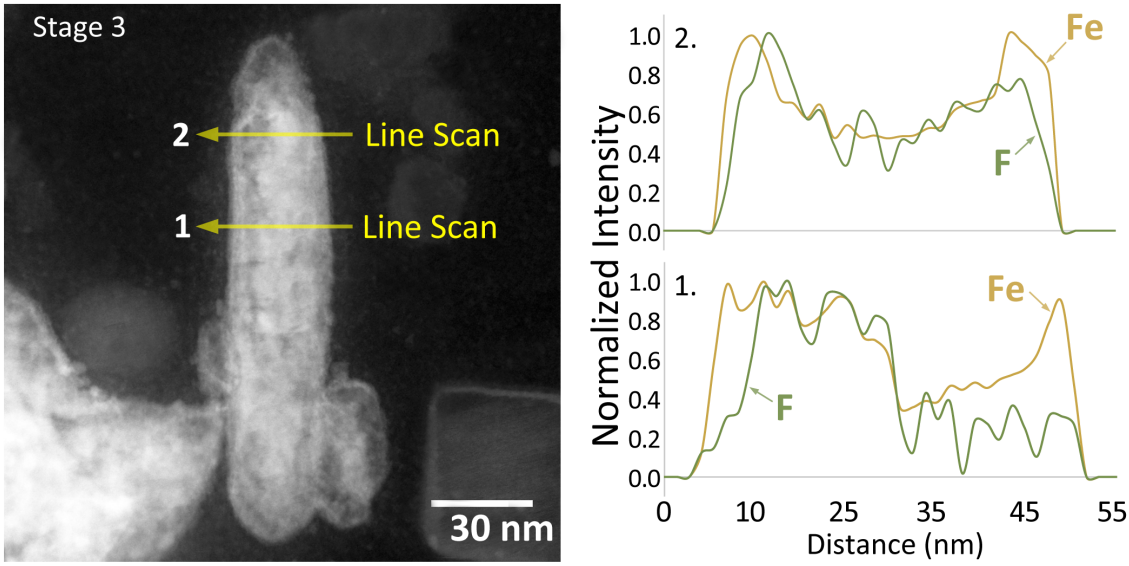
This direct conversion is limited to the first few nanometers of material, as the reaction model requires an uninhibited supply of electrons to the reaction front.[19] This assumption breaks down a small distance away from points of electrical contact at the nanorod surface. Lithium diffusion kinetics also decrease considerably as the converted layer grows to even a few nanometers.[19] This is reflected in the rapid drop in cell potential observed in the galvanostatic profile (Figure 4.1).[95] Ultimately, it is the diminished electron transport beyond the surface that necessitates a different reaction mechanism within the bulk. However, lithium diffusion within the bulk is defined by the formation and growth of this surface layer.

The initial finely divided surface layer is energetically unfavorable, and as discharge progresses, the crystallinity of this layer increases with the phase segregation of Fe and LiF (Figure 4.9a). By Stage 3, a strikingly epitaxial, crystalline double-layered shell has formed with a light layer of LiF around the core of the particle, further encapsulated by a dark layer of metallic iron (Figure 4.9a). Accordingly, EELS measurements show that iron signal is spatially offset toward the surface from the fluorine signal (Figure 4.9b). The $LiF|FeF_2$ interface is fully coherent and the arrangement of layers $Fe|LiF|FeF_2$ minimizes

the total interfacial free energy.



(a) BF HRTEM image from Stage 3 showing distinct double-layered shell.



(b) EELS line scan indicating relative Fe and Fe location.

Figure 4.9: Formation of the Double-Layered Shell. As the reaction progresses, the finely divided surface layer phase segregates into a double layered shell composed of crystalline LiF and Fe. EELS line scan across the width of the nanorod confirms that the outermost layer is Fe^0.

The insertion of Li^+ into a crystalline LiF or Fe surface is energetically and mechanistically not possible.[20] As the double-layered shell forms primarily on the $\{1\,1\,0\}_{FeF_2}$ facets, the sides of the nanorod are rendered impermeable to lithium at an early stage in the reaction. This phenomenon, combined with the low energy barrier for diffusion along the $\langle 0\,0\,1\rangle_{FeF_2}$ direction forces lithiation to proceed in a unidirectional fashion along the length of the nanorod (Figure 4.9a, Figure 4.13, Figure 4.14).[19] The Fe|LiF double-layered shell remains largely unchanged throughout the discharge.

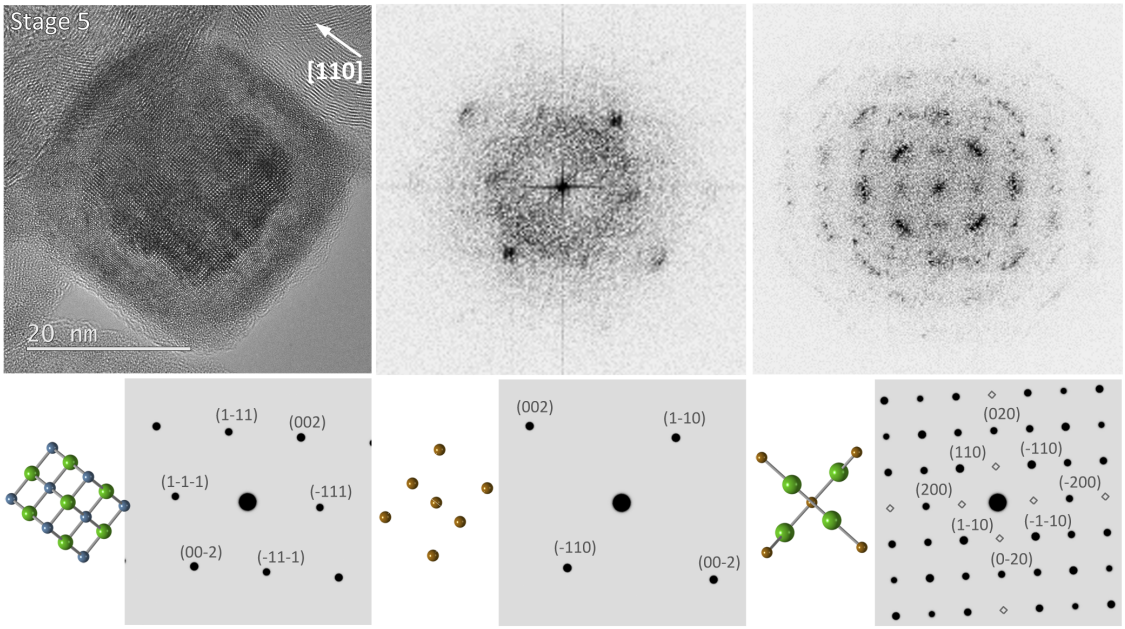


Figure 4.10: Crystal Structure of the Double-Layered Shell. (BF TEM, FFT and simulated diffraction.) The double layered shell that forms early on in the discharge reaction and persists throughout much of the charge reaction exhibits a well defined crystal structure and lattice orientation between the Fe and LiF. This lattice matching is also observed in the core of the particle.

The delithiation (charge) reaction requires the diffusion of lithium out of the nanorod and the concomitant insertion of iron into the LiF lattice. Lithium in the double-layered shell cannot diffuse outward through the iron, and the iron cannot easily migrate across the semi-coherent interface into the LiF (Figure 4.10).[81] It is only at a nearly fully charged state that the double-layered shell disappears (Figure 4.17). Coincidentally, the shell becomes amorphous once again, eliminating the semi-coherent LiF|Fe interface. However a large overpotential is required for this amorphization, and this reconversion of the double-layered shell does not occur until 3.3 V vs. Li^+/Li (Figure 4.1), which is above the reduction potential for $Fe^{3+} \rightarrow Fe^0$ (3.0 V vs. Li^+/Li).[17] The dissolution of Fe from the cathode was demonstrated in **Chapter 3**. The segregation of metalic Fe to the particle surface and the

large overpotential required for its reconversion explains why cathode dissolution is so prevalent in transition metal fluoride systems.

4.3 Pseudo-Intercalation and the Activation Overpotential

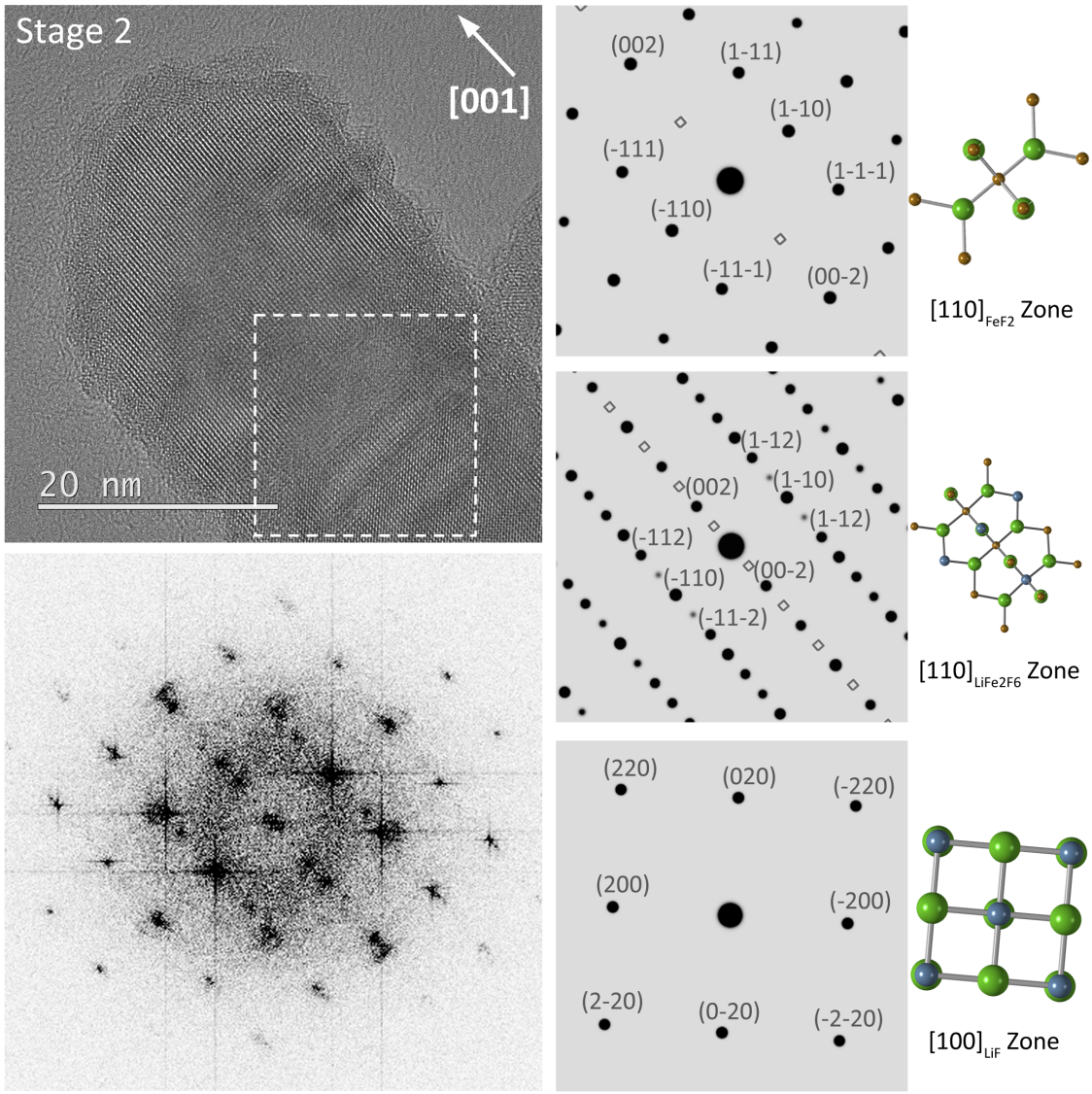


Figure 4.11: Stage 2—Discharge (1.75 V, x_{Li^+} = 0.3). (BF TEM, FFT, and simulated diffraction.) The HRTEM image and corresponding FFT are presented with simulated diffraction patterns and crystal models depicting the observed lattice orientations. FFT of the interior portion of the nanorod reveals the widespread formation of two additional phases within the FeF_2 framework, one related to a rocksalt ($Fe_zLi_{2-z}F_2$) structure and another corresponding to the trirutile $LiFe_2F_6$ structure. The corresponding EELS spectra shown in Figure 4.12 shows a splitting of the Fe L_3 peak, indicating the presence of both Fe(II) and Fe(III) species.

In the literature, the activation overpotential observed on the first discharge (Stage 1, Figure 4.1) is often attributed to the initial nucleation and growth of Fe^0 and LiF grains,

in other words, the onset of a direct conversion described in **Chapter 1**.[14,22,32,70] This is actually a misconception; the true origin of the activation overpotential is the formation of a second phase via the disproportionation of iron and pseudo-intercalation of lithium within the nanorod interior.

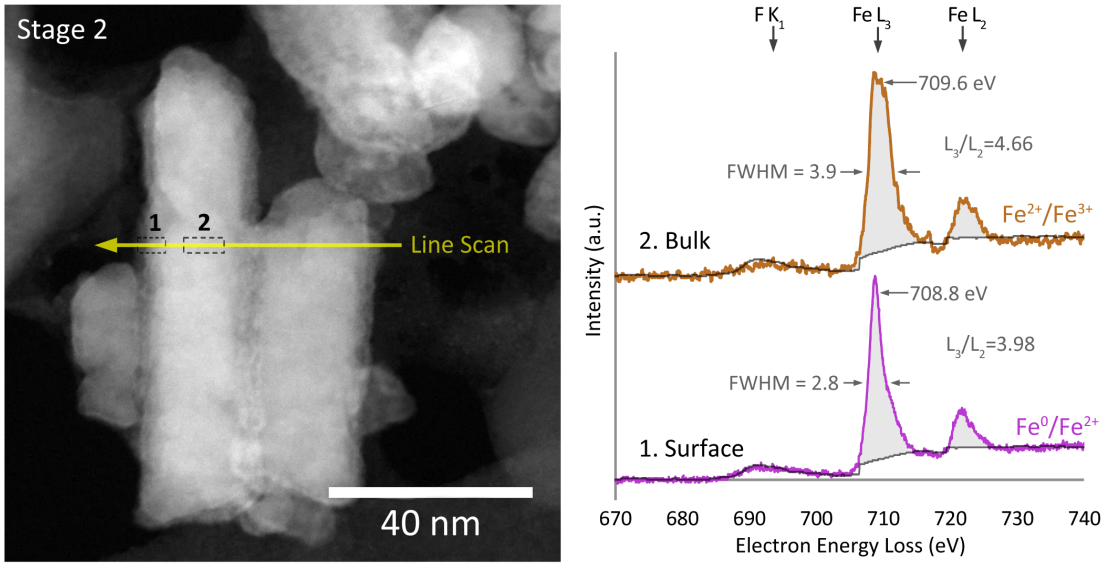


Figure 4.12: Discharge Disproportionation and Fe^{3+} Formation. (HAADF STEM and EELS). EELS spectra from the core of the nanrod exhibit a splitting of the Fe L_3 peak, specifically broadening toward higher energy loss values indicative of Fe^{3+}. The greater full-width at half maximum of this peak is evident when compared to the EELS spectra acquired from the surface. This increase in Fe oxidation state indicates that a disproportionation to form the trirutile phase has occurred. This oxidation is not a result of air exposure as this would oxidize material at the surface first. Instead, the EELS spectra near the nanorod surface are still indicative of Fe^0 or Fe^{2+} as evidenced both by the lower L_3 peak position and lower L_3/L_2 ratio.

After the dip in potential (Figure 4.11) the nanorods appear morphologically unchanged from the previous stage (Figure 4.8). However, a FFT derived from the interior of the nanorods exhibits several sets of reflections: one from the $\langle 1\,1\,0 \rangle$ zone of FeF_2 and a second set with larger d-spacings that is unambiguously indexed to the $\langle 1\,1\,0 \rangle$ zone of the trirutile $LiFe_2F_6$.[18,74] The trirutile reflections share the same symmetry and $\langle 0\,0\,1 \rangle$ direction as those of the FeF_2, indicating an identical lattice orientation. This is consistent with the fully coherent structure observed in the TEM (Figure 4.11). The structure of the trirutile phase is practically identical to that of FeF_2 with lithium periodically substituted for iron (Figure 4.19). The formation of this phase can be visualized as the Li^+ diffusing through the channels in the $[0\,0\,1]_{FeF_2}$ direction before knocking an iron cation out of a lattice site. As mentioned in **Chapter 1**, an electrochemical disproportionation ($Li^+ + 3Fe^{II}F_2 + e^- \rightarrow LiFe^{II}Fe^{III}F_6 + Fe^0$)

is required to accommodate Li^+ in the rutile lattice.[74] Disproportionation must also produce Fe^{3+} cations;[71,74] indeed, EELS measurements at this stage reveal a splitting of the Fe L_3 peak toward higher energy loss values indicative of Fe^{3+} species (Figure 4.12).[113] This trirutile phase is the same equilibrium intermediate predicted by Doe *et al.* for the conversion of iron fluorides over a decade ago.[74] Experimental validation is finally achieved through the pairing of real battery conditions with the high resolution structural data afforded by monodisperse, single-crystalline nanoparticles.

A true intercalation via wholesale reduction of Fe^{2+} to Fe^+ is not allowed; however, the lithium diffusion barrier in the $\langle 0\,0\,1\rangle_{FeF_2}$ is low.[19,71,74] Thus a pseudo-intercalation occurs with an activation overpotential required to initiate disproportionation (Figure 4.1). The conventional description of discharge as a three-phase reaction between FeF_2, LiF, and Fe is clearly incorrect and fails to capture the complex phase equilibria present in a reversible metal fluoride system.

4.4 Phase-Equilibria and Reaction Symmetry

Several studies have suggested that phase evolution in transition metal difluorides follows different chemical pathways for discharge and charge.[14,22,32] However, the previous sections have demonstrated the presence of reaction intermediates as well as different mechanisms between the surface and the bulk which would confound the interpretation of even the highest quality spectroscopic data. With a high degree of spatial resolution, I show the local evolution of phases is remarkably symmetric between charge and discharge, differing not in the spatial distribution of phases, but in the temporal separation of different reaction steps.

In addition to reflections from FeF_2 and trirutile phases, nanorods during Stage 2 of discharge exhibit a set of reflections from the $\langle 0\,0\,1\rangle$ zone of a rocksalt phase (Figure 4.12). The intensity of these reflections is higher than expected for LiF and are even apparent in the powder XRD (Figure 4.2). This seems to suggests an Fe substituted rocksalt phase with an increased structure factor similar to that proposed by both Ko *et al.* and Yamakawa *et al.*[14,22,32] The rocksalt arises from the decomposition of unstable phases formed from Li^+ intercalation beyond the $LiFe_2F_6$ stoichiometry.[18,74] An initial "unconverted" equilibrium

exists between FeF_2, rutile $Li_yFe_{3-y}F_6$, and rocksalt $Fe_zLi_{2-2z}F_2$.

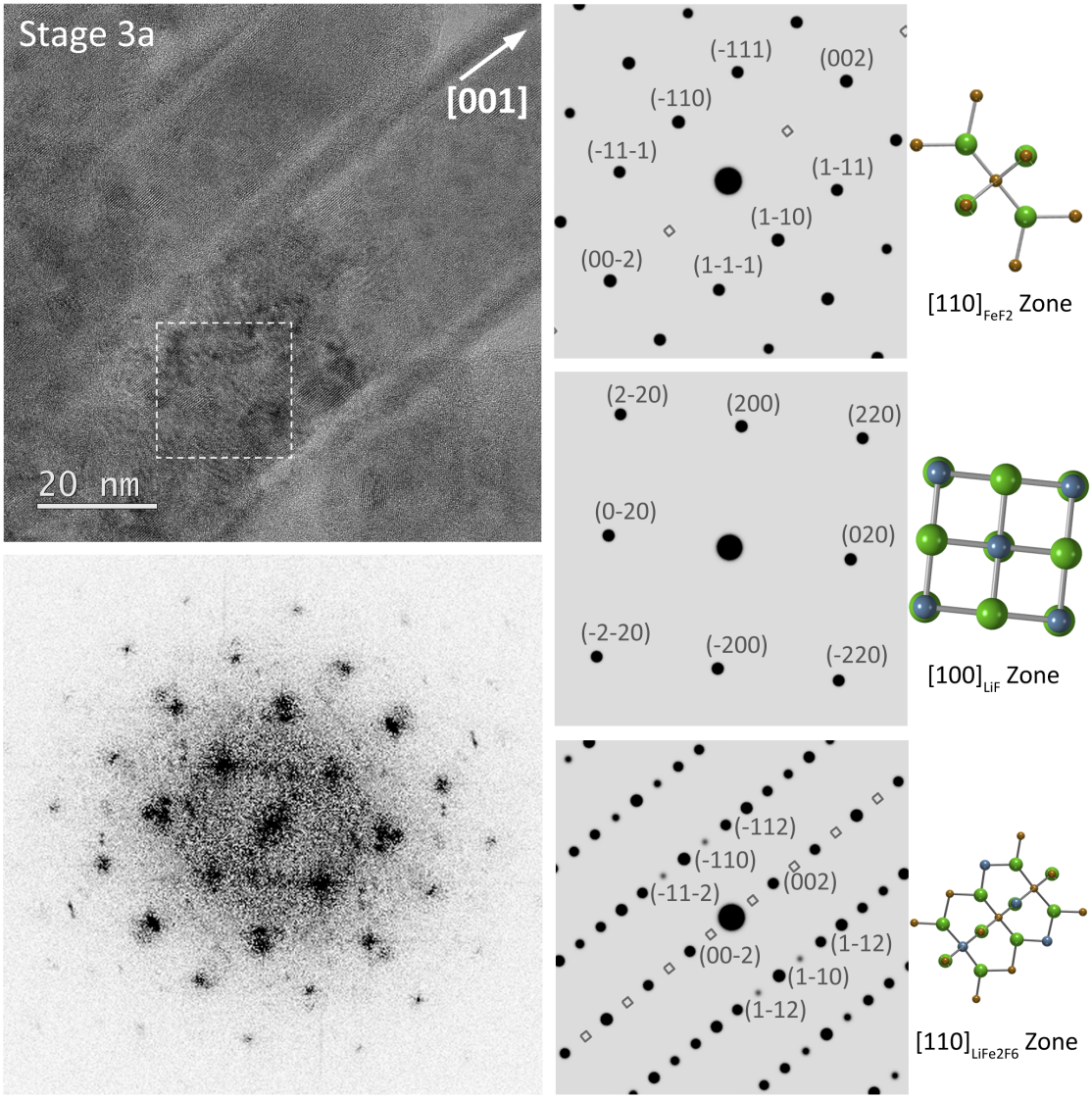


Figure 4.13: Stage 3a—Discharge (1.7 V, x_{Li^+} = 1.0). (BF TEM, FFT, and simulated diffraction.) Two different regions are apparent within the interior of the nanorod. The FFT of the unconverted region is shown here as Stage 3a, while that of the converted region is shown in Figure 4.14 below as Stage 3b. The unconverted region is marked by the presence of high index rutile reflections, while the converted region exhibits reflections indicative of metallic Fe. A rocksalt phase and a rutile phase reminiscent of FeF_2 are clearly evident from the FFT. However, the EELS spectra of the unconverted region, shown in Figure 4.15, reveal the clear presence of Fe^{3+} which is indicative of the trirutile $LiFe_2F_6$.

Due to the higher oxidation state of Fe^{2+} with respect to Li^+, the presence of an iron cation within the rocksalt LiF lattice requires a corresponding vacancy at a lithium lattice site. Indeed Ma and Garofalini showed that cation diffusion within a rocksalt structure occurs with periodic lattice substitution and that a lithium-deficient (vacancy-rich) rocksalt structure is actually conducive to ion transport.[20] In Section 4.5 below, we demonstrate

that conversion between FeF_2 and LiF occurs via the diffusion and substitution of Li^+ and Fe^{2+} cations within a stable lattice of fluoride anions. From this viewpoint, the formation of cation vacancies at stoichiometries between FeF_2 and LiF appears quite likely.

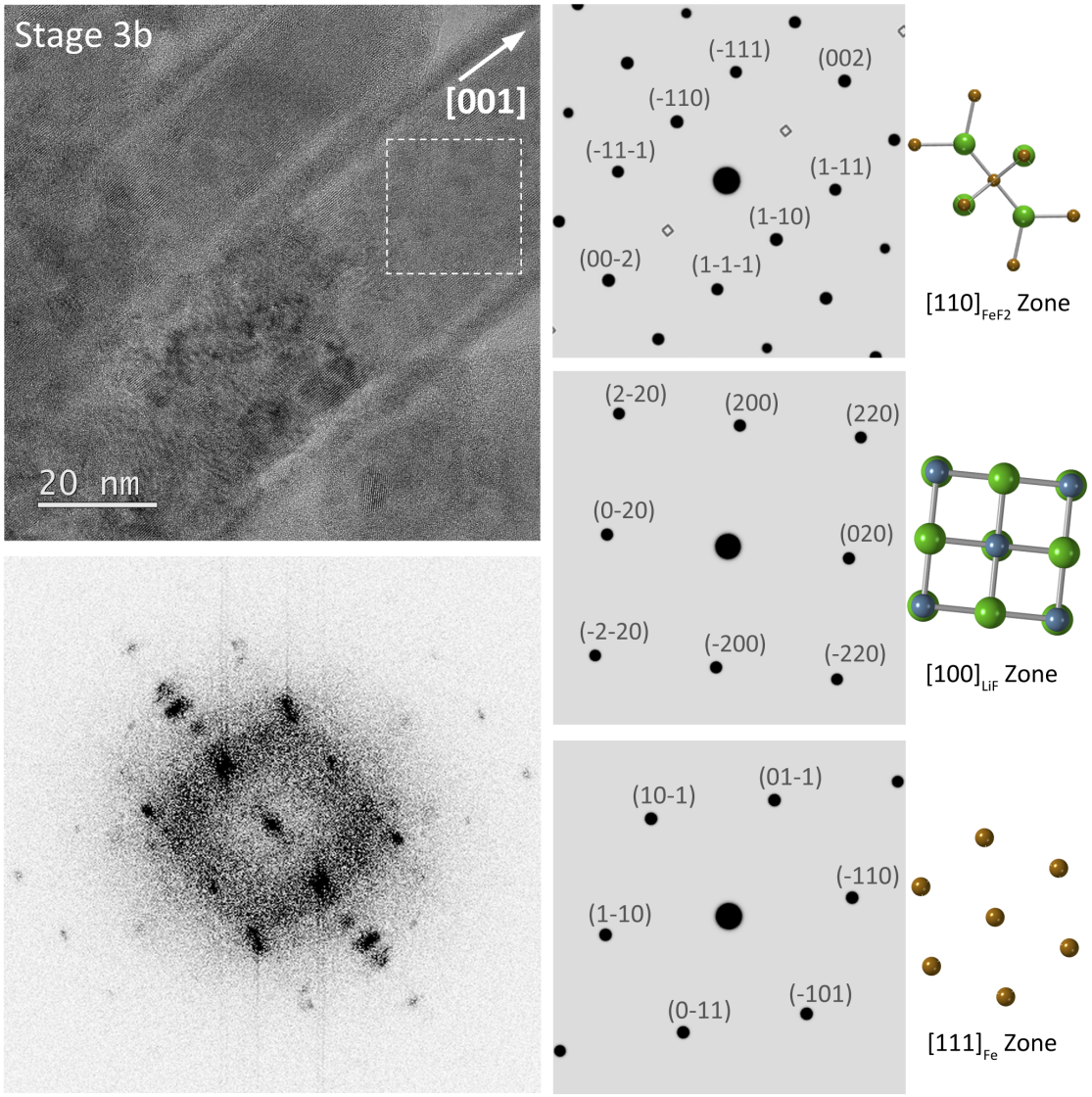


Figure 4.14: Stage 3b—Discharge (1.7 V, x_{Li^+} = 1.0). (BF TEM, FFT, and simulated diffraction.) The uncanny disappearance of the higher index FeF_2 reflections at this stage indicate consumption of the native FeF_2 and increased disorder in line with the onset of the conversion reaction. Additionally, reflections indexed to metallic iron are now present. Equilibrium exists between this metallic iron, the rocksalt phase, and the residual rutile phase.

Inevitably, a second "converted" equilibrium emerges as further lithiation consumes native FeF_2 and increasing Fe^0 concentration nucleates metallic Fe particles. Astonishingly, in the 50% discharged state, both the unconverted (Figure 4.13) and converted (Figure 4.14) regimes exist simultaneously in each nanorod with a distinct boundary perpendicular to the $[0\,0\,1]_{FeF_2}$ direction. The converted section is marked by the appearance of discreet

Fe nanoparticles, while the unconverted section is defined by presence of higher index FeF_2 reflections. Equivalently, an EELS line scan along the $[001]_{FeF_2}$ direction (Figure 4.15) shows a sharp transition from a converted area of Fe^{2+} and Fe^0 to an unconverted area containing Fe^{2+} and Fe^{3+}. FFT of the converted region indicates a three-phase equilibrium with clear Fe^0 and rocksalt $Fe_zLi_{2-z}F_2$ reflections and weak rutile $Li_yFe_{3-y}F_6$ reflections (Figure 4.14).

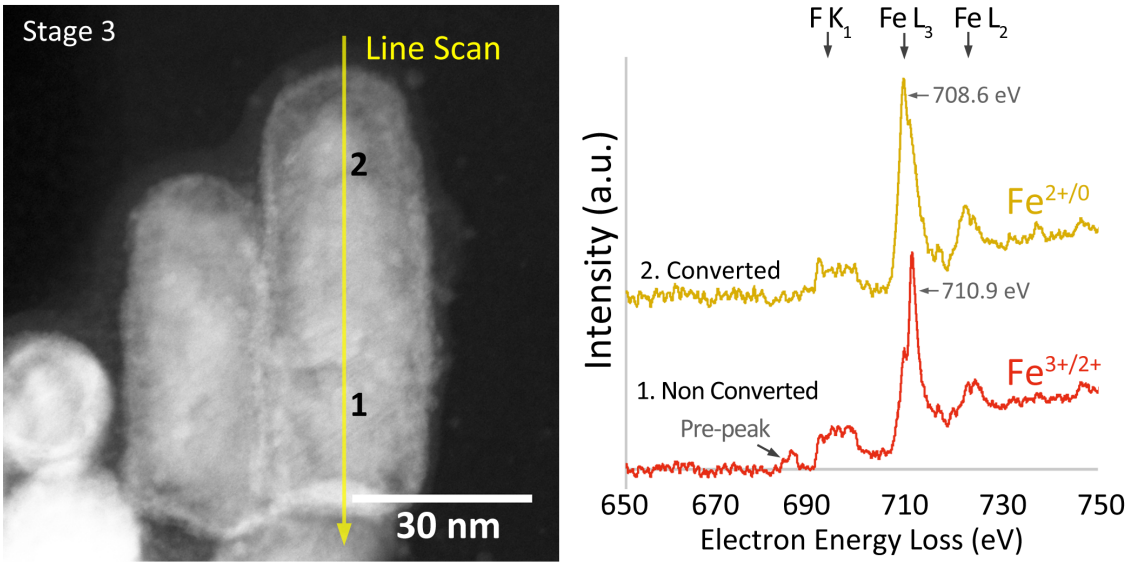


Figure 4.15: The Converted and Unconverted Regimes. (HAADF STEM and EELS.) Dark field STEM image of an FeF_2 nanorod from stage 3 of discharge (Top Left). The overlay shows the path of the EELS line scan and the numbers indicate the approximate position at which the EELS spectra (top right) were obtained. EELS spectra of the unconverted region exhibit a characteristic "pre-peak" and an L_3 peak position at higher energy loss values indicative of Fe^{3+} fluoride compounds.[113] EELS spectra show a transition from primarily Fe^{3+} to primarily Fe^{2+} going from the unconverted region to the converted region.

These "converted" and "unconverted" phase equilibria are observed again on charging; however, they occur separately over two distinct plateaus in the galvanostatic profile (Stage 5 and 6, Figure 4.1). The first plateau at 2.9 V vs. Li^+/Li occurs close to the 50% charged state; however, no distinct conversion boundary is observed (Figure 4.16). The FFT in Figure 4.16 reveals that high intensity rocksalt reflections are again apparent at this stage. This rocksalt $Fe_zLi_{2-z}F_2$ phase is stable up to a composition of z = 0.5.[22] Accordingly, at x_{Li^+} = 1.0 the reappearance of a rutile $Li_yFe_{3-y}F_6$ phase is also observed in the FFT. Distinct iron particles are visible and EELS spectra indicate the presence of Fe^{2+}/Fe^0 species (Figure 4.16). As such Stage 5 of charge recovers the phase relationship and appearance of the converted section of the nanorod from Stage 3 of discharge (Figure

4.14).

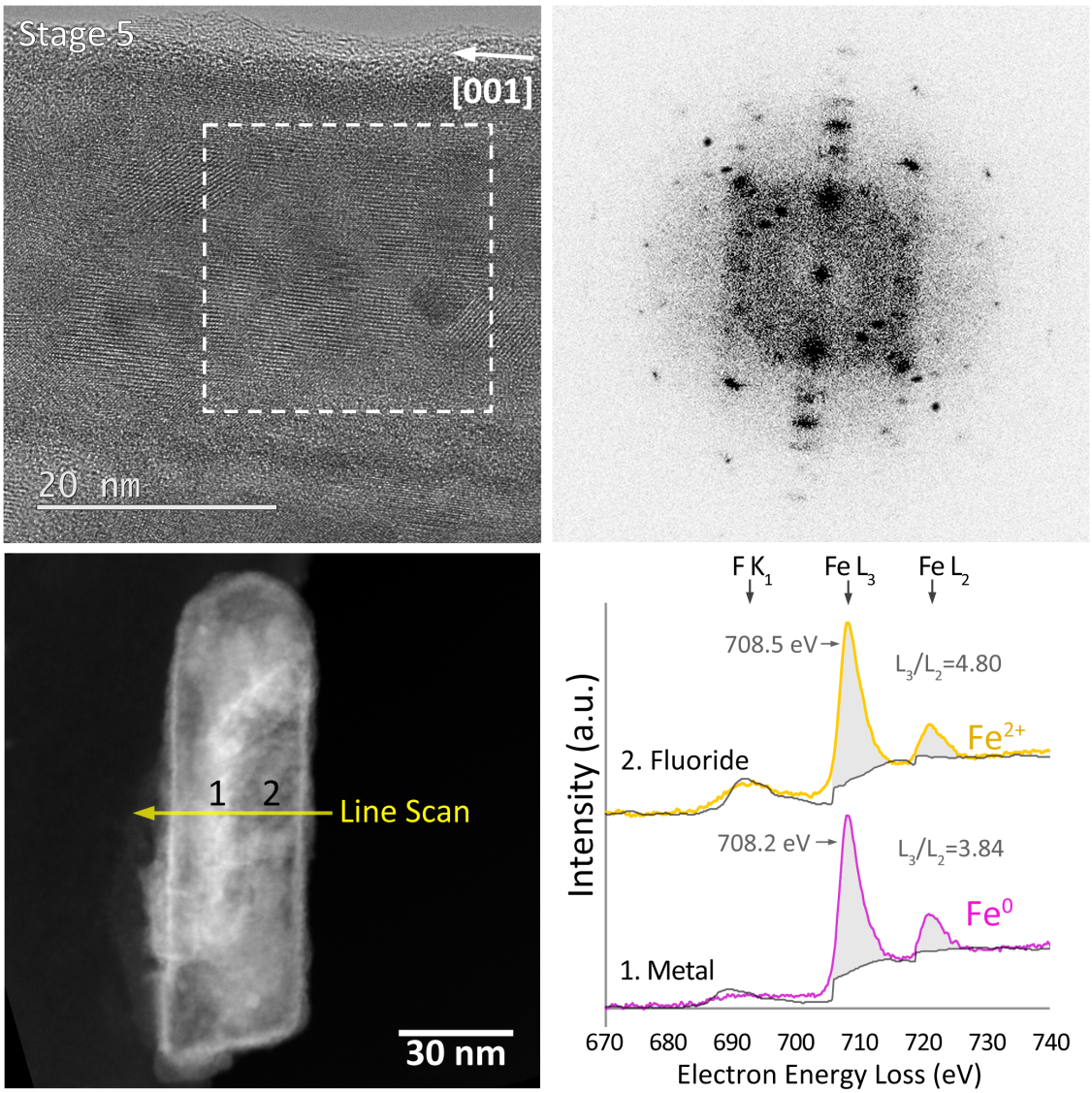


Figure 4.16: Stage 5—Charge (2.9 V, x_{Li^+} = 1.0). (BF TEM, FFT, HAADF STEM, and EELS.) The image shows few metallic iron particles and FFT shows diminished iron reflections indicating that metallic iron at the interior of the rod is quickly consumed during charge. Remaining iron particles are highly faceted, corroborating the presence of immobile, low-energy interfaces. FFT resembles that of 3b and indicates the reformation of a rutile phase. THe EELS spectra show that different regions within the nanorod exhibit large differences in L_3/L_2 ratio and slight differences in L_3 peak position that indicates the presence of both Fe^{2+} and Fe^0.

After the complete consumption of Fe particles in the interior of the nanorod (disappearance of the broad Fe XRD peak in Figure 4.1), a second plateau occurs at 3.3 V vs. Li^+/Li. FFT of HRTEM images from this plateau show decreased intensity of rocksalt reflections and the reappearance of higher index rutile reflections (Figure 4.17). Interestingly, this second plateau also corresponds to the further oxidation of Fe^{2+} species. EELS spectra of

the fully recharged state (Figure 4.18) show an additional peak and the higher L_3 position characteristic of Fe^{3+}. This Fe^{3+} formation on charge explains why a potential plateau around 3.3 V appears on and after the second discharge cycle. The phase equilibria present during this second plateau mirrors that of the unconverted portion of the nanorod during Stage 3 of discharge (Figure 4.17) in both crystal structure and oxidation state.

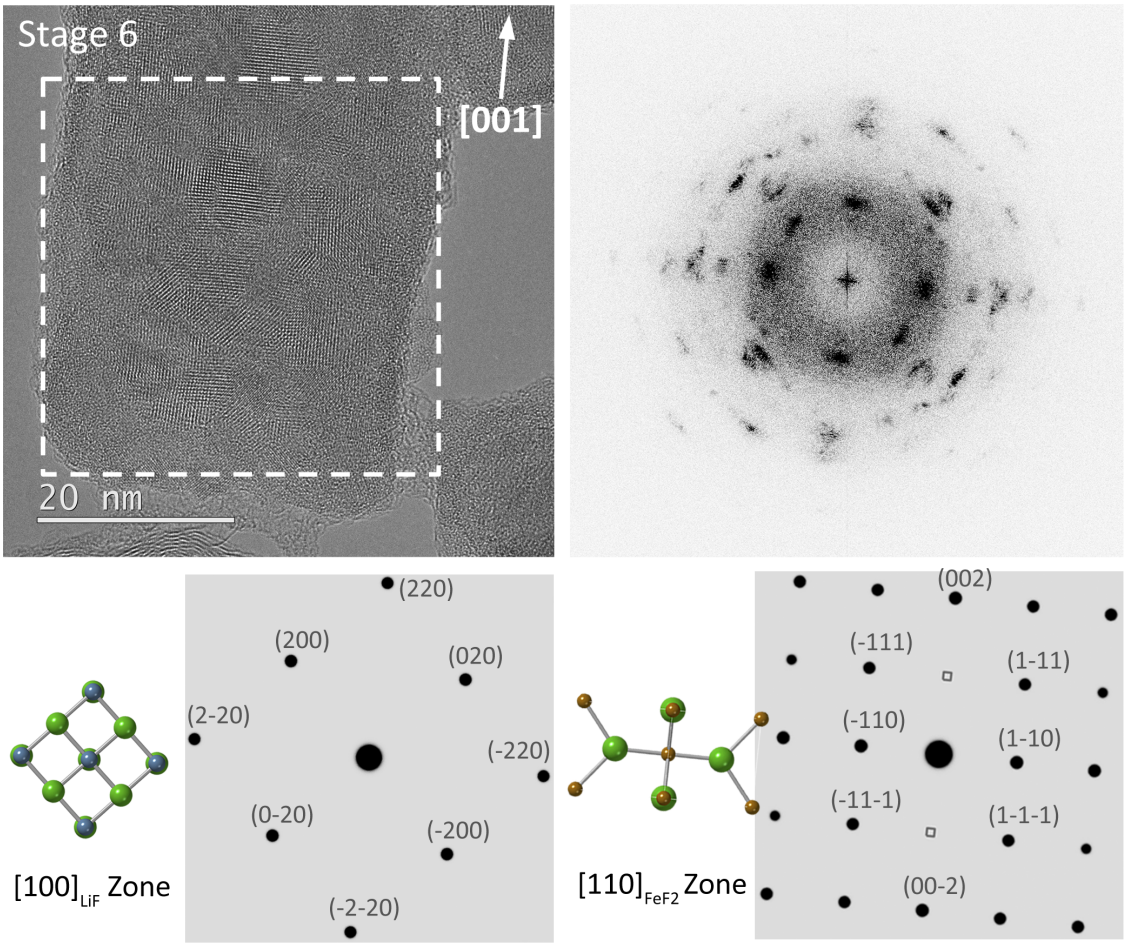


Figure 4.17: Stage 6—Charge (3.3 V, x_{Li^+} = 0.3). (BF HRTEM, FFT, and simulated diffraction.) The FFT resembles that of Stage 3a and indicates the presence of strong rutile and rocksalt reflections. Metallic iron particles are no longer visible and smorphous material is visible toward the edge of the nanorod, indicating partial reconversion of the double-layered shell.

The reaction pathways are chemically symmetric to a large extent; the discharge and charge profiles also become increasingly symmetric with each successive cycle (Figure 3.17a). A disparate arrangement of electrochemically active species on discharge and charge is thought to contribute to voltage hysteresis.[70] However, this "compositional inhomogeneity" is not apparent for FeF_2 as the spatial distribution of phases on charge and discharge is also largely symmetric. The large hysteresis observed in metal fluorides

may primarily be a result of the internal resistance and the reaction overpotential, which are more easily mitigated by rational electrode/materials design.

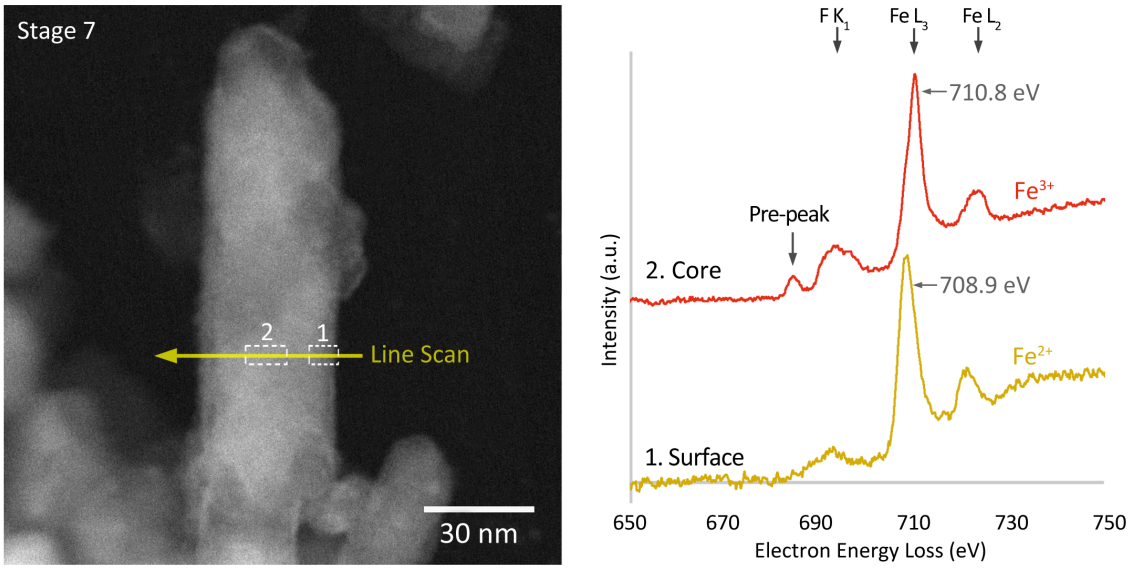


Figure 4.18: Oxidation to Fe^{3+}. (HAADF STEM and EELS.) Upon charging to the full capacity at 4.0 V vs. Li^+/Li, the widespread presence of Fe^{3+} is observed at the interior of the nanorod. Indeed, this potential is higher than the standard reduction potential of $Fe^{3+} + e^- \rightarrow Fe^{2+}$ (3.8 V vs. Li^+/Li). The kinetically limited reinsertion of Fe from the double layer shell which causes the core of the nanorod to reconvert with a stoichiometry closer to FeF_3. EELS spectra from the nanorod surface show the distinct presence of Fe^{2+} in line with the its delayed reconversion.

The over-oxidation of Fe on charging has not been previously explained in the literature. In Section 4.2, I demonstrated that the insertion of Fe from the outer shell (on charge) into the nanorod core is kinetically limited. Indeed, EELS spectra from the reconverted shell indicate the presence of Fe^{2+} (Figure 4.18), with residual metallic Fe visible in the bright field TEM (Figure 4.21. This kinetic "trapping" of Fe at the nanorod surface, actually relegates the the coherent LiF/rutile core to reconvert with a stoichiometry closer to FeF_3; thus the charge capacity is maintained in part by the oxidation of Fe^{2+} to Fe^{3+}. Ultimately, this incomplete reaction and the prevalence of Fe dissolution both result from the same phenomenon as alluded to in **Chapter 1**.

4.5 Lattice Orientation Relationships

4.5.1 The Invariant Fluoride Lattice

The lattice orientation relationship (O.R.) between FeF_2, rutile, rocksalt and LiF reveals that conversion proceeds with nearly universal coherency between fluoride phases, resulting from invariant lattice of fluoride anions (Figure 4.19, 4.20). This new discovery may present the single greatest rationale for the reversibility of the conversion reaction in iron fluoride and similar transition metal difluorides. Lattice orientation is naturally maintained in transformations between phases with the same crystal structure (i.e. $\mathrm{FeF_2} \leftrightarrow \mathrm{rutile}$ or $\mathrm{LiF} \leftrightarrow \mathrm{rocksalt}$). Interestingly, the HRTEM data shows a common lattice orientation for all transitions between rocksalt and rutile phases as well (Figure 4.7). This ubiquitous alignment between the $\{200\}$ reflections from the $\langle 001 \rangle_{rocksalt/LiF}$ zone and the $\{1\bar{1}\bar{1}\}$ reflections from the $\langle 110 \rangle_{rutile|FeF_2}$ zone defines the orientation relationship $(110)_{rutile}//(001)_{rocksalt}$, $[1\bar{1}0]_{rutile}//[1\bar{1}0]_{rocksalt}$ (Figure 4.19, Table 4.1). This relationship is visible at the periphery of the nanorod (Figure 4.20).

The $(110)_{rutile}$//(1-10)$_{rocksalt}$, $[1\bar{1}0]_{rutile}//[00\bar{1}]_{rocksalt}$ relationship—symmetrically equivalent by 90° rotation about the $[001]_{FeF_2}$ nanorod axis—is also present. Superposition of the two lattices with this relationship reveals that the arrangement of fluoride ions is nearly identical (Figure 4.19). The decomposition of the rutile to form rocksalt involves the insertion lithium at interstitial sites within the $[001]_{rutile}$ channels, followed by the shifting of cations at the body center. The transformation $FeF_2 \rightarrow rutile \rightarrow rocksalt \rightarrow LiF$ is an entirely topotactic transformation involving intercalation and diffusion of cations within a stable host of fluoride anions.

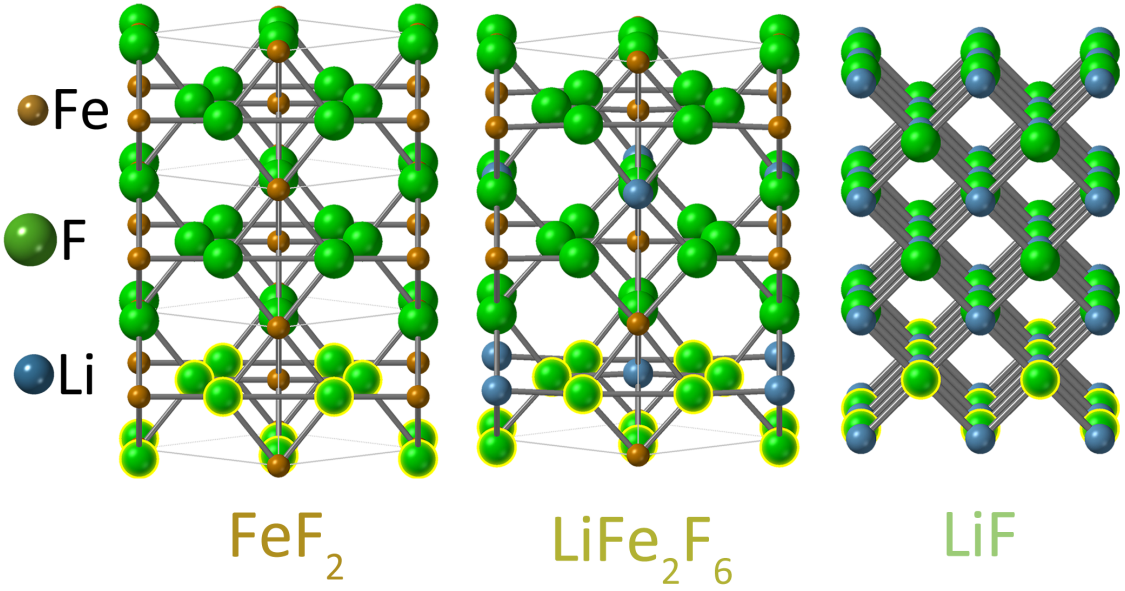


Figure 4.19: The Fluoride Anion Lattice. When arranged with the empirically observed orientation relationships, crystal models of FeF_2, $LiFe_2F_6$ and LiF illustrate the invariant fluoride lattice. Equivalent fluorine atoms are highlighted in yellow.

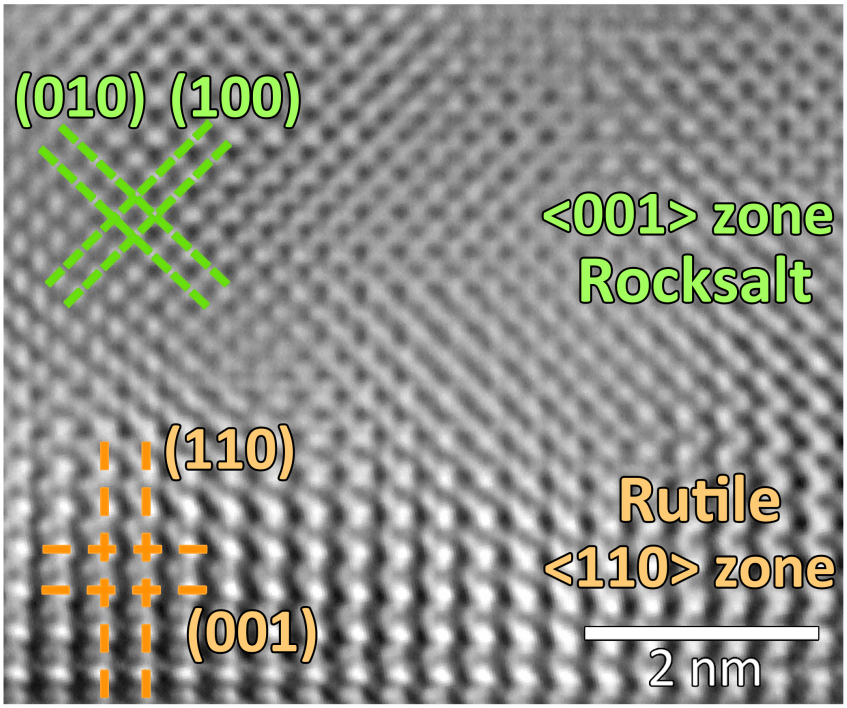


Figure 4.20: Fully Coherent Fluoride Phases. (FFT/IFFT of BF HRTEM.) The transition between rocksalt and rutile phases occurs in a fully coherent manner as a result of the invariant fluoride anion positions. This phase transition is visible at phase boundaries in the HRTEM images.

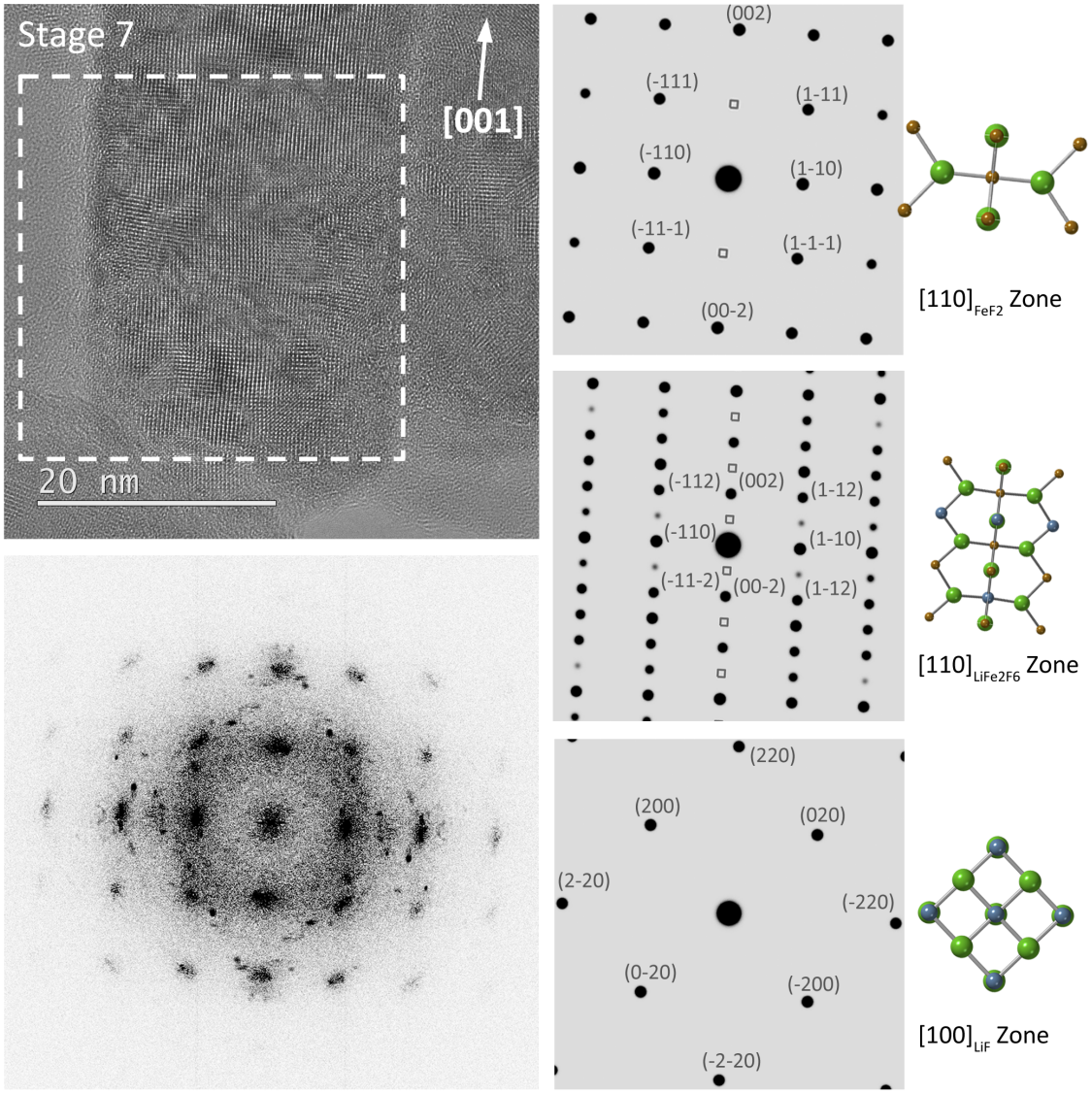


Figure 4.21: Stage 7—Fully Charged (4.0 V, x_{Li^+} = 0.0). (BF HRTEM, FFT, and simulated diffraction.) TEM image shows uniform 110 lattice fringes present throughout the crystal structure, highlighting the reformation of a pseudo-single crystalline structure. Dark areas at the edge of the nanorod suggest incomplete consumption of iron and faint rocksalt reflections are apparent from the FFT. EELS measurements (Figure 4.18) indicate the presence of Fe^{2+} at the edge of the particle and Fe^{3+} at the core.

The reverse topotactic transformation is observed on charge with the exact same orientation relationship. However, delithiation requires migration of the fluoride interface into regions of iron and amorphous material. The formation of this new fluoride material occasionally results in FeF_2 grains rotated from the original lattice orientation (Figure 4.16, 4.17, 4.21)). In the fully recharged state the crystal structure and lattice orientation of the original nanorod are almost entirely restored, resulting in the reformation of a pseudo-single crystalline nanorod morphology (Figure 4.21). This stunning manifestation

of reversibility is further displayed as the nanorod morphology is actually maintained for over 50 discharge/charge cycles (Figure 4.26). The shared orientation of the metallic iron particles on discharge is a secondary effect of the invariant fluoride lattice. The orientation relationships between all the phases present are summarized in Table 4.1.

Phase Name	Parallel Lattice Plane (hkl) and Direction [uvw]		
FeF_2 (rutile)	Side View: $(1\,1\,0),[1\,\bar{1}\,0]$		Top View: $(0\,0\,1),[1\,1\,0]$
LiF (rocksalt)	$(1\,0\,0),[0\,0\,\bar{1}]$	$(0\,0\,1),[0\,1\,0]$	$(1\,1\,0),[0\,0\,1]$
Fe	$(1\,1\,1),[1\,0\,1]$	$(\overline{0.174}\,\overline{0.174}\,\overline{0.147}),[1\,1\,0]$	$(1\,1\,0),[1\,\bar{1}\,0]$
Label	Type I	Type II	

Table 4.1: Orientation Relationships Columns of parallel planes and directions that summarize the full extent of empirically observed lattice orientation relationships in the FeF_2/LiF/Fe system.

4.5.2 Iron Particle Nucleation

On discharge, distinct iron particles are not observed until lithium insertion to half the theoretical capacity, and even at this stage they are sparsely distributed within the converted section of the nanorod (Figure 4.14). Likewise XRD, shows a low-intensity, broad $\{1\,1\,0\}_{Fe}$ reflection (Figure 4.2). In **Chapter 2**, I introduced the concept of a critical radius for nucleation (2.1). The delayed nucleation of iron particles likely results from the interfacial free energy cost between the iron and the fluoride lattice. This activation energy barrier results in a corresponding critical radius and Fe^0 concentration below which nucleation of iron particles cannot occur.[81] Indeed, *in-situ* measurements depict iron particles forming with an initial diameter of 2 to 3 nm (Figure 4.22). The first particles to form on discharge appear to be discrete rather than well connected (or continuous), suggesting they are not crucial for electron conduction as previously thought. Similarly, the iron particles are one of the first features to disappear on charging (Figure 4.16). Nevertheless, the orientation of these metallic nanoparticles with respect to the fluoride lattice is well defined and has large implications for the kinetics and reversibility of the reaction.

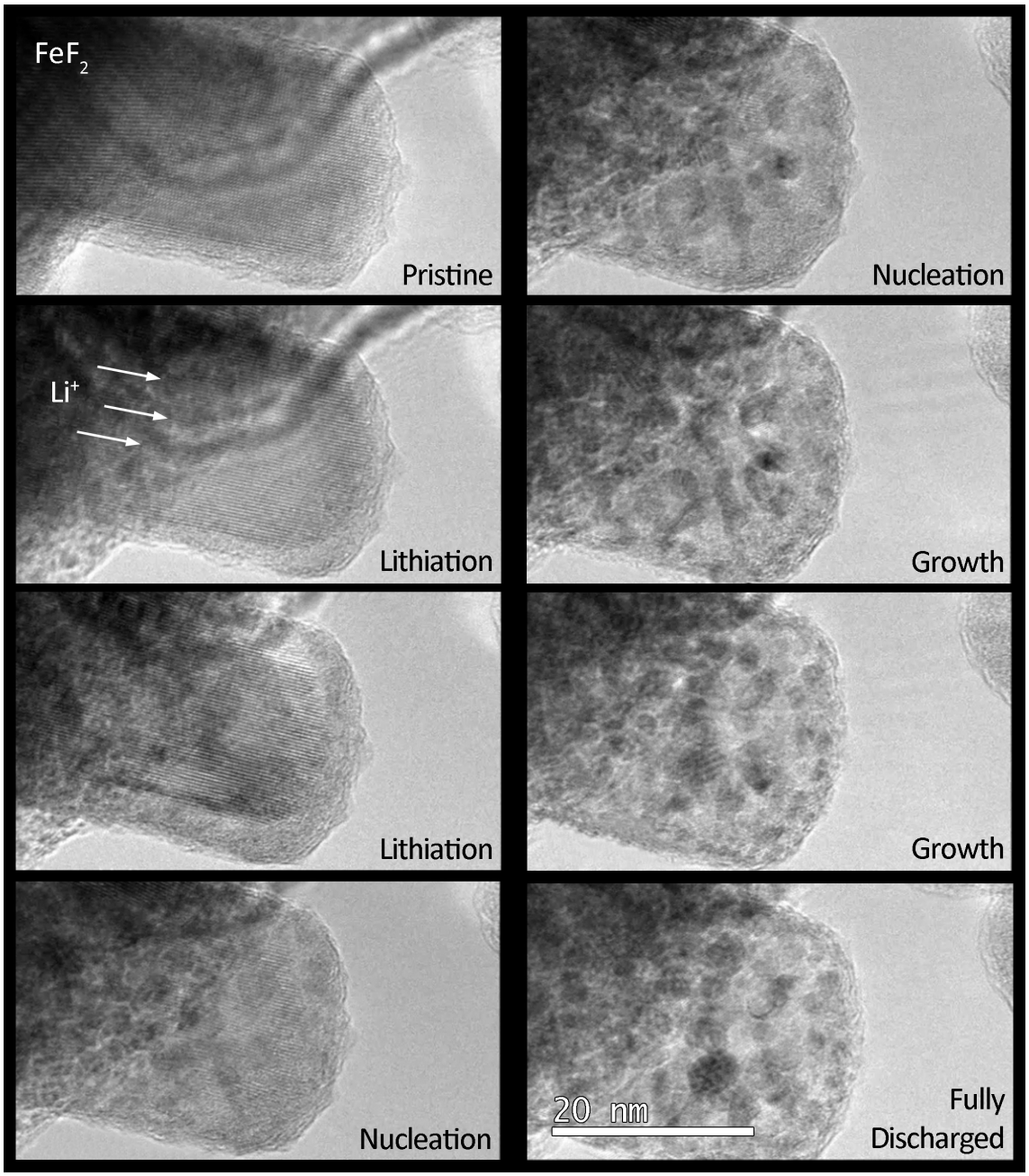


Figure 4.22: Nucleation of Metallic Iron. (BF TEM from live view video.) In this *in-situ* lithiation experiement, contact with the lithium probe occurs out of frame and slow transfer of Li^+ from rod to rod enables a more gradual progression of the conversion reaction. Iron nanoparticles appear to form with an initial diameter of ~3 nm (Supplementary Video 3) and do not appear to be interconnected as previously thought.

In the fully discharged state (Figure 4.23), the original $\langle 1\,1\,0\rangle_{FeF_2}$ zone axis orientation can still be identified by the symmetry of the LiF reflections based on the invariant fluoride lattice described in the previous subsection. Despite the two-phase polycrystalline nature of this fully discharged stage, the FFT along this zone axis is astonishingly symmetric, displaying only a handful of reflections corresponding to the $\langle 1\,0\,0\rangle_{LiF}$ and $\langle 1\,1\,0\rangle_{LiF}$ zones

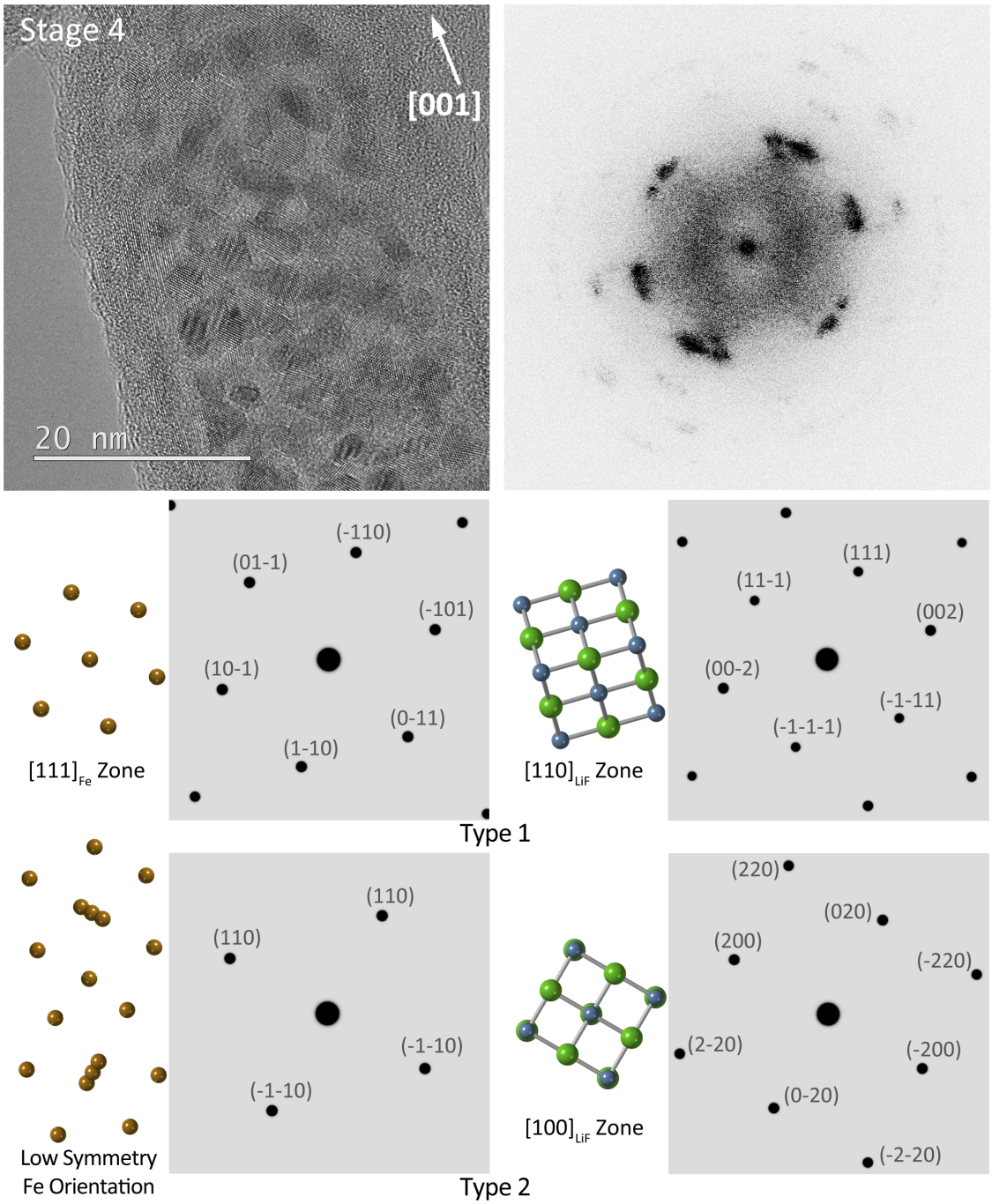
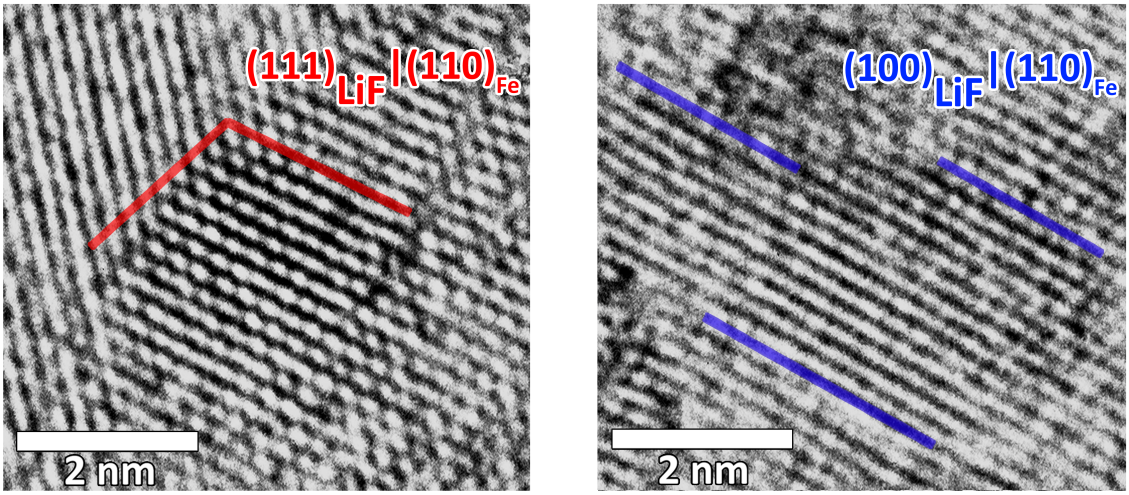


Figure 4.23: Stage 4—Fully Discharged (1.2 V, x_{Li^+} = 2.0). (BF HRTEM, FFT, and simulated diffraction.) The polycrystalline nature of the fully discharged state is evident from the TEM image, however the FFT exhibits exceedingly few reflections indicating a shared orientation relationship. The Fe reflections are coincident with the rocksalt reflections defining parallel crystallographic directions between the two systems. Planar boundaries between metallic iron particles (dark) and LiF (bright) are indicative of low energy semi-coherent interfaces.

and several different iron zones, predominantly the $\langle 1\,1\,1\rangle_{Fe}$ (Figure 4.23). The $\{0\,0\,2\}_{LiF}$ reflections of the $\langle 1\,1\,0\rangle_{LiF}$ zone are entirely coincident with the $\{1\,\bar{1}\,0\}_{Fe}$ reflections from the $\langle 1\,1\,1\rangle_{Fe}$ zone, resulting in the orientation relationship $(1\,1\,0)_{LiF}//(1\,1\,1)_{Fe}$, $[0\,0\,1]_{LiF}//[\bar{1}\,0\,1]_{Fe}$

(type I – Table 4.1, Figure 4.24a, 4.25a). Reflections from the $\langle 1\,1\,0\rangle_{Fe}$ zone are also present as dictated by the four-fold rotational symmetry of the nanorod.

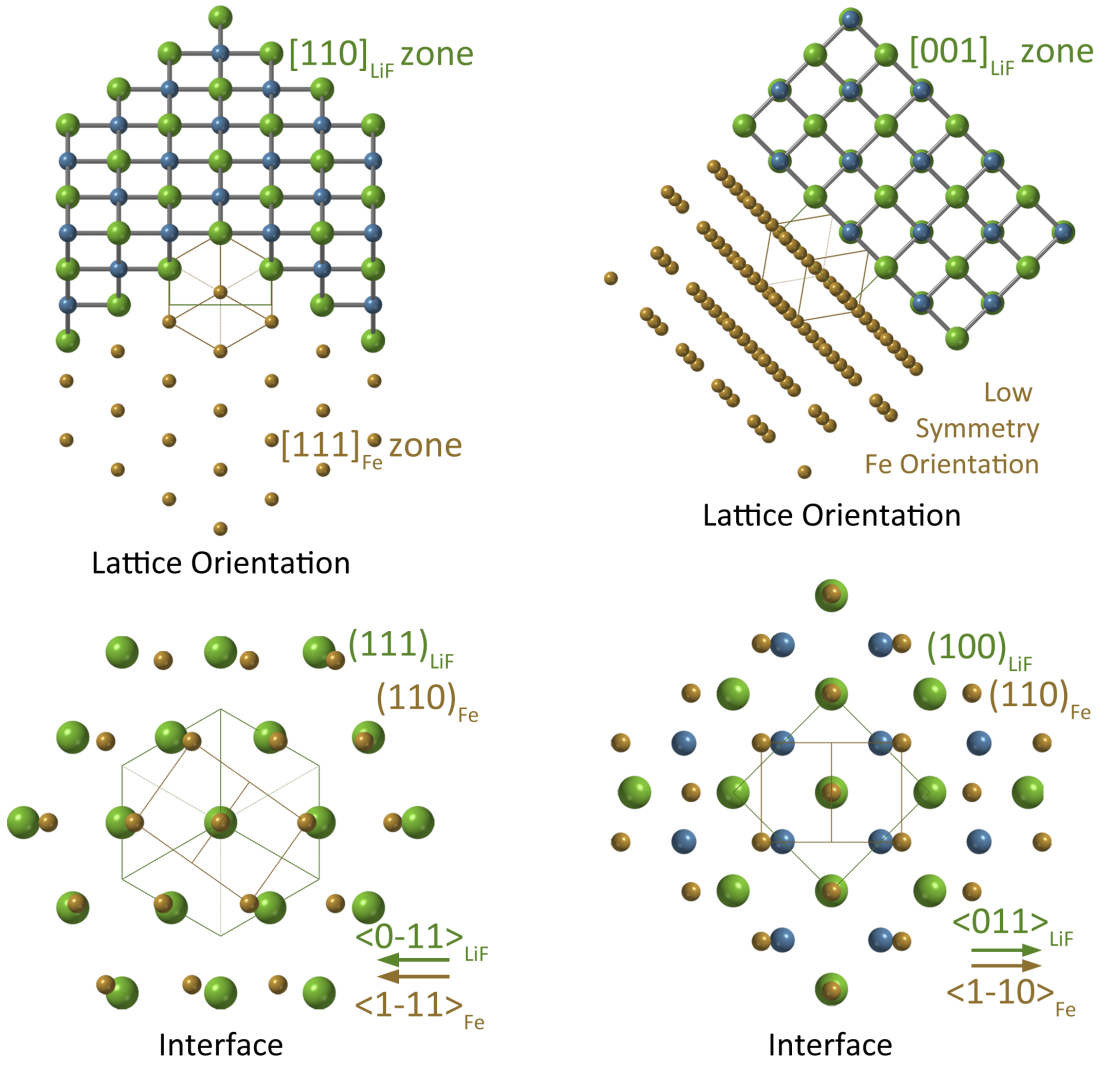


(a) Type 1 Orientation Relationship **(b)** Type 2 Orientation Relationship

Figure 4.24: Lattice Matching at the Fe|LiF Interface. (BF HRTEM.) Magnified TEM images of single Fe nanoparticles and surrounding LiF exemplify the two types of lattice orientation relationships observed between metallic Fe particles and the surrounding LiF. Colored lines demarcate the planar, semi-coherent interfaces that facilitate the Fe particle nucleation. Lattice matching at these interfaces defines the orientation relationships observed.

A second orientation relationship is apparent as the $\{2\,0\,0\}$ and $\{0\,2\,0\}$ reflections from the $\langle 1\,0\,0\rangle_{LiF}$ zone are entirely coincident with the $\{1\,1\,0\}_{Fe}$ reflections from a lower symmetry orientation (Figure4.23). Comparison with the relative orientation of Fe and LiF in the double-layered shell (Figure 4.10) reveals the relationship $(1\,1\,0)_{LiF}//(1\,1\,0)_{Fe}$, $[0\,0\,1]_{LiF}//[-1\,1\,0]_{Fe}$ (type II – Table 4.1, Figure 4.24b, 4.25b). Closer examination of the iron nanoparticles reveals that they are truncated ellipsoids with exposed facets that share a planar interface with the LiF matrix (Figure 4.24a, 4.24b). Thus, iron nanoparticles are preferentially nucleated on low energy interfaces within the coherent fluoride matrix, corroborating the presence a significant interfacial free energy barrier to nucleation. It is actually the lattice matching at these interfaces that defines the orientation of the iron nanoparticles with respect to the nanorod.

For type I particles, the $\{1\,1\,1\}_{LiF}|\{1\,1\,0\}_{Fe}$ interface is dominant. Based on type I the orientation relationship (Table 4.1), lattice matching between the $\{1\,1\,1\}_{LiF}$ and $\{1\,1\,0\}_{Fe}$ occurs such that $\langle 0\,\bar{1}\,1\rangle_{LiF}//\langle 1\,\bar{1}\,1\rangle_{Fe}$ (Figure 4.25a). This is exactly the Kurdjumov-Sachs interface that occurs in many FCC|BCC crystal systems.[81,114] Figure 4.25 illustrates how orientation relationships are used to derive interfacial structure. In the case of type II



(a) Crystal Models of the Type 1 Interface

(b) Crystal Models of the Type 2 Interface

Figure 4.25: Semicoherent Fe|LiF Interfaces. Crystal models recreating the two orientation relationships offer a clear picture of the atoms at the Fe|LiF interface. The Type 1 interface is the canonical Kurdjumov-Sachs semicoherent interface. The Type 2 interface exhibits a difference in lattice spacing of only 2.6 pm.

particles, the $\{100\}_{LiF}|\{110\}_{Fe}$ interface is dominant and the type II orientation relationship dictates that $\langle 110\rangle_{LiF}//\langle 011\rangle_{Fe}$ (Figure 4.25b). At this interface, the $\{011\}_{LiF}$ spacings are matched to the $\{011\}_{Fe}$ spacings with a difference of only 2.6 pm; this particular interface was actually calculated to be the lowest energy interface involving the $\{001\}_{LiF}$ plane.[20] While these low energy semi-coherent interfaces are crucial for the nucleation of small iron nuclei on discharge, it is the higher energy curved interfaces, which enable the consumption of iron particles on charge. The transfer of an Fe atom across a coherent interface requires a statistically unlikely vacancy on the opposite side.[81] The transfer of

atoms across high-energy interfaces is far more probable and facilitates diffusion of iron back into the fluoride lattice. Accordingly, the only iron particles that remain at stage 5 of charge exhibit large areas of coherent interface (Figure 4.16).

In a reversible system, the removal of lithium without replacement by another cation would leave an uncompensated F^-, which is energetically unfavorable. Thus lithium can only be extracted as fast as it can be replaced by iron. The delithiation is thus limited by the rate at which iron atoms can be transported across the Fe|LiF interface, that is, charging is interface controlled. In contrast, insertion of lithium from the electrolyte is fast and the discharge reaction is diffusion controlled. This concept is partially responsible for the disparity in discharge and charge kinetics demonstrated in Figure 3.26. Furthermore, as thermal energy increases, a greater proportion of iron atoms are able to jump accross the Fe|LiF interface, resulting in the improved rate capability observed at higher temperatures in **Chapter 3**.

4.5.3 Long Term Phase Evolution

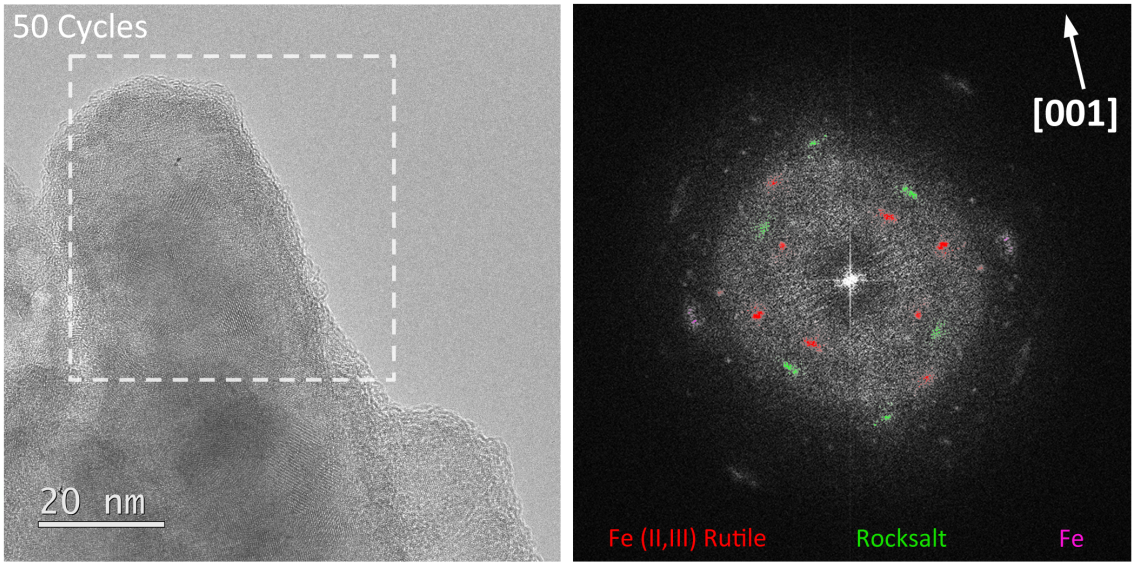


Figure 4.26: Nanorod Morphology After 50 Cycles. (BF TEM and FFT.) The nanorod structure is preserved, even after 50 cycles in the IL electrolyte. The FFT is colored to differentiate between multiple phases present.

To investigate how the mechanism presented above evolves after many cycles, further *ex-situ* TEM measurements were performed on the FeF_2 nanorods in both IL and LP30 electrolytes. In the IL electrolyte, particles after both 15 and 50 cycles exhibit the clear

presence of surface iron as well as a thick rocksalt region near the surface even in the fully charged state. The formation of this double-layer shell happens readily on discharge, but its reconversion is kinetically limited by the semicoherent Fe|LiF interface and competes with the oxidation of $Fe^{2+} \rightarrow Fe^{3+}$ as I have described. Accumulation of this incomplete surface reconversion over many cycles would result in a thickening of the double layer shell and a consequent growth in charge transfer resistance. This increased trapping of iron at the surface may also contribute to the very gradual capacity fade observed. In the IL the nanorod morphology is completely preserved even up to 50 cycles, which is a rather astonishing manifestation of the reversibility of this conversion reaction. A closer look at the interior of the FeF_2 nanorods after 15 cycles shows that pseudo-single crystallinity observed after the first recharge is also largely retained. Although, as evident from the FFT, the proportion of rocksalt to rutile has increased. As the nanorod core becomes more iron deficient and more capacity is directed to the *in-situ* formation of Fe^{3+} species, the iron content required to stabilize the rutile structure cannot be reached and more of the nanorod is left in the intermediate rocksalt structure. After 50 cycles, the interior structure becomes noticeably more disordered with the presence of many misaligned grains; however, the nanorod morphology is still maintained, suggesting some level of coherency between these grains.

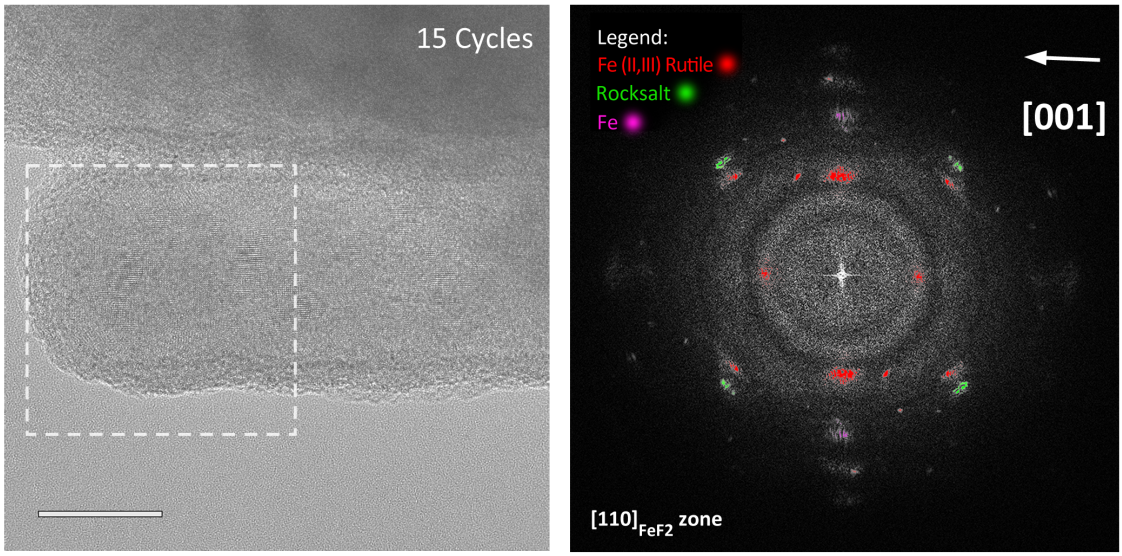


Figure 4.27: Structural Evolution in IL Electrolyte. (BF TEM and FFT.) After 15 cycles, the intensity of rocksalt reflections in the fully charge state is greater than after the first cycle. The double layered shell is readily visible, indicating that incomplete reconversion of surface iron on each cycle.

In contrast, in the LP30, any particles that did not fail by fusing, exhibited almost entirely the rocksalt structure. Again this is related to iron deficiency in the lattice. However, in this case the surface Fe appears to have been completely removed as well. In light of the XPS data presented in **Chapter 3**, iron deficiency in this case probably stems from the dissolution of Fe into the electrolye. This corroborates the original hypothesis that the segregation of Fe to the surface facilitates the dissolution of iron in systems where a robust SEI is not present.

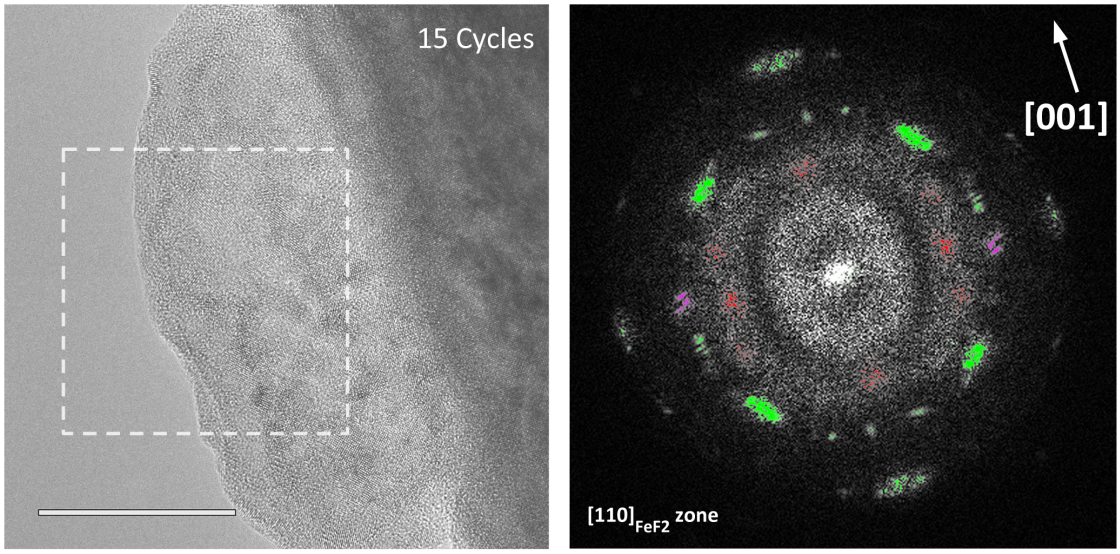


Figure 4.28: Structural Evolution in LP30 Electrolyte. (BF TEM and FFT.) Most FeF_2 nanoparticles do not exhibit the nanorod morphology after 15 cycles in the LP30 electrolyte. However, the few that do exhibit an almost entired rocksalt structure showing very limited reformation of the FeF_2. This results from loss of iron due to dissolution.

4.6 Performance Implications

The purpose of the mechanistic study presented above is to define the capabilities and limitations of transition metal fluorides as cathode materials to inform their application and develop strategies to improve their performance. One of the most important revelations of this work is the differential rate capabilities for the charge and discharge reactions. The charge reaction is interface controlled, accompanied by the slow diffusion of Fe^{2+} through a rocksalt lattice and is thus inherently sluggish. In contrast, the discharge reaction is diffusion controlled and accompanied by the fast diffusion of Fe^0 through open channels in the $\langle 0\,0\,1 \rangle_{FeF_2}$ direction.[23] In the previous chapter, I demonstrated empirically that an

excellent discharge rate capability can be achieved as long as the rate of charge is slow enough to recover the full capacity (Figure 3.26). This suggests the suitability of transition metal fluoride cathodes for applications such as electric aircraft, where recharge rates can be slow, but high energy density and moderate discharge rates are crucial.[2] If IL electrolytes are used, charging time can further be reduced by increasing the temperature by 10 °C to 20 °C.

The voltage hysteresis, one of the largest drawbacks of metal fluorides, is primarily of result of the reaction overpotential, rather than asymmetry in the evolution or distribution of phases. Thus, there is potential to mitigate the reaction hysteresis through materials design, for example doping or structural control. In tetragonal systems, surface metal, which is the main enabler of cathode dissolution, forms primarily on the $\{1\,1\,0\}_{rutile}$ surface. On the other hand, net Li^+ diffusion is limited to the $\langle 0\,0\,1\rangle_{rutile}$ direction. As such, minimization of the $\{1\,1\,0\}$ surface should improve both reversibility and reaction kinetics. The ability to control the $\{1\,1\,0\}/\{0\,0\,1\}$ surface ratio was demonstrated in **Chapter 2** via the temperature dependence of nanorod aspect ratios.

Finally, the nucleation and growth of small metal particles on semi-coherent interfaces has large implications for selecting reversible systems. For example, the CuF_2 system is notoriously irreversible, and, on discharge, forms very large metallic copper particles on the surface of LiF. CuF_2 exhibits Jahn-Teller distortion, and lattice matching between the monoclinic fluoride phase and a cubic or hexagonal metallic phase is likely prohibited. On the bases of lattice matching, high symmetry crystal systems are likely to be more reversible than low symmetry crystal systems.

Chapter 5

Conclusions

5.1 Key Findings

The purpose of this thesis is to form a comprehensive understanding of transition metal fluorides as cathode materials for lithium ion batteries. The major goals of this project were to enable reversible, high-capacity cycling without sacrificing electrode energy density and also to develop a more detailed and useful fundamental understanding of the discharge/charge mechanism. In doing so, I sought to reconcile performance and mechanistic understanding in a single consistent electrode/electrolyte system. My work began with the development of a new method for the colloidal synthesis of single crystalline, monodisperse FeF_2 nanorods. Such a uniform and well-defined system, holds immense value, not only for electrochemical performance, but also the mechanistic study of electrochemical reactions. The full potential of this system is achieved when combined with the LiFSI/$Pyr_{1,3}$FSI ionic liquid electrolyte, which prevents the fusing of particles during cycling, allowing for accurate assessment of morphological and structural transformations. The ability of this IL electrolyte to enable reversible cycling without the use of impractical carbon scaffolds or the introduction of otherwise inactive material is paramount to the realization of high energy density transition metal fluoride LIBs.

From the vantage point of this electrode/electrolyte system, HRTEM unearths new concepts governing the conversion reaction in transition metal fluorides, namely the direct conversion and phase segregation localized to the surface, the topotactic evolution of coherent phases based an invariant fluoride lattice, and the nucleation and lattice

matching of metallic particles on semi-coherent interfaces (Figure 5.1). In developing this new understanding, I have answered long-standing questions regarding the possibility of intercalation, role of metallic iron, the asymmetry of the reaction pathway, and the validity of computed reaction intermediates and mechanistic models. Most importantly, this new mechanistic understanding contains the detail required to inform the rational design and application of transition metal fluoride cathodes. The inherently high discharge rate capability of FeF_2 is demonstrated as a direct result of my proposed mechanism. The abundance and specificity of these results highlights the utility of monodisperse, single crystalline nanoparticle methods for the mechanistic study of electrode systems in general. In this final chapter, I briefly detail specific implications my work has for the field of battery electrode materials as well as interesting topics for future work.

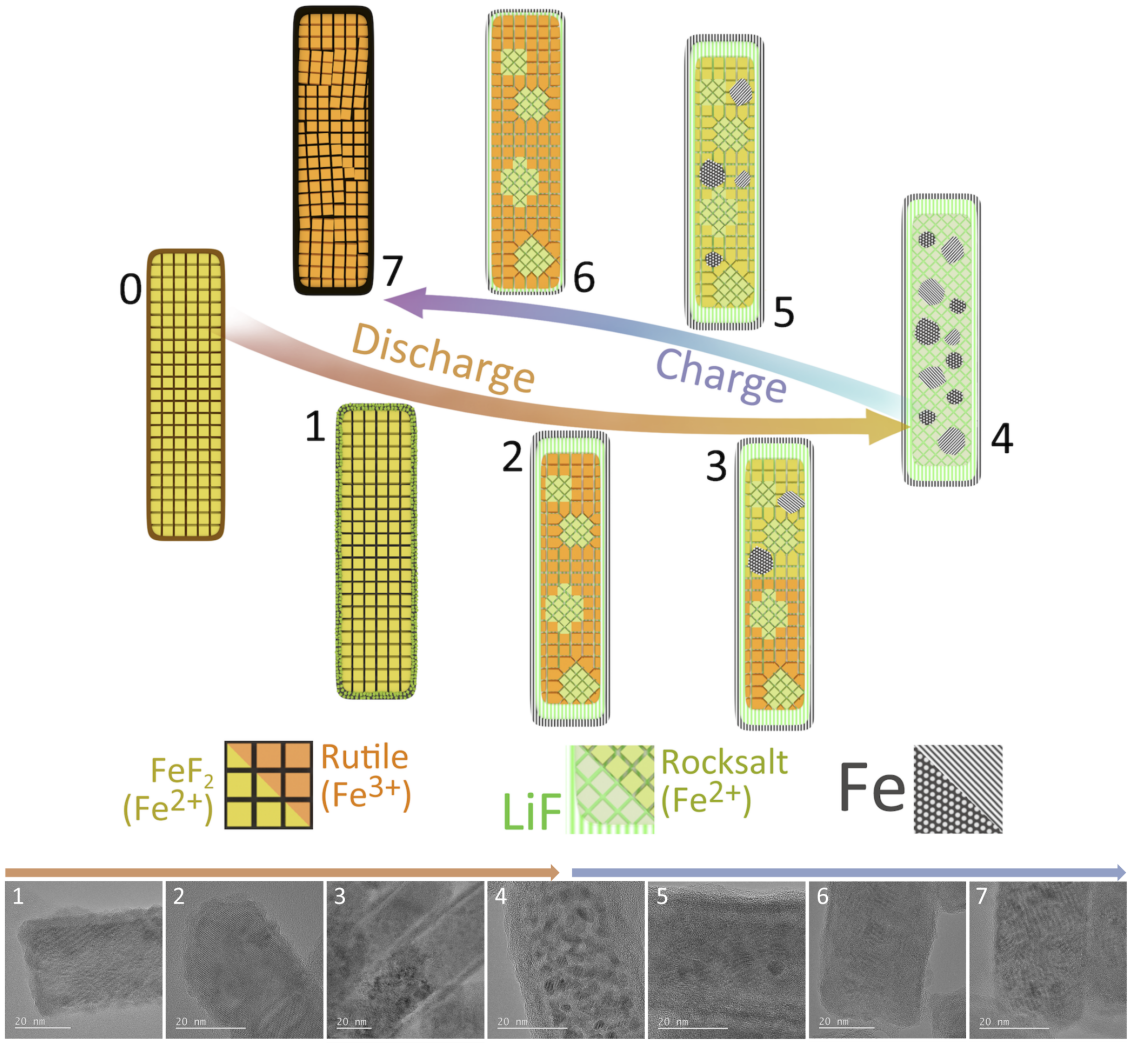


Figure 5.1: The New Conversion Mechanism. This schematic summarizes the comprehensive conversion mechanism presented in this work.

5.2 Implications for the Field

In **Chapter 2**, I examined the reactivity of transition metal trifluoroacetates and hexafluoroacetyl acetonates for the colloidal synthesis of transition metal fluorides. It was hypothesized that the combination of a metal oxide forming reaction with a HF releasing reaction was responsible for the high-yield colloidal synthesis of FeF_2. Based on this framework, more scalable syntheses could be achieved using separate source but more readily available oxide forming reagents (e.g. transition metal nitrates and carbonates) and HF releasing reagents (e.g. ammonium fluoride derivatives). This could potentially allow for the facile colloidal synthesis of more complex fluorides containing multiple transition metals. The successful colloidal synthesis of NiF_2 and CuF_2 has not yet been demonstrated. It is likely that the solution phase synthesis of these and other higher voltage compounds will require more oxidatively stable (high redox potential) molecules as reaction media.

In **Chapter 3** I demonstrated that the inorganic nature of the FSI anion was responsible for the formation a stable SEI layer and the resulting stable cycling behavior. The formulation of electrolytes with anions and cations containing more inorganic functional groups may further enhance this inorganic SEI forming ability. Concentrated FSI based electrolytes should improve cycling stability in electrode systems where metal dissolution leads to cell failure. The fusing of particles was introduced as a major failure mechanism in transition metal fluorides. In the past, this was likely prevented by anchoring active material particles to carbon scaffolds or physicaly seperating particles with large amounts of carbon. In the case of the IL electrolyte presented here, the absence of particle fusing was attributed to electrostatic interactions between the liquid ions and the particle surface. If IL electrolytes are not used, than alternative strategies such as thing surface coatings using conductive carbon or metal oxides would be required to enable stable cycling behavior.

The use of HRTEM and monodisperse, single crystalline nanoparticles in conjunction produced a greater wealth of more accurate mechanistic information than was possible with even the most advanced spectroscopic or diffraction techniques. This single-crystalline nanoparticle technique could be applied to a variety of electrode materials beyond transition metal fluorides. For example, colloidal synthesis techniques already exist for transition

metal sulfides and oxides, and methods for controlling faceting and shape control are well known. The idea of an invariant lattice of fluoride ions, which forms a mechanistic basis for reversibility, blurs the line between intercalation and conversion type electrode materials. It may be that other conversion systems that cycle reversibly also exhibit a stable lattice of anions.

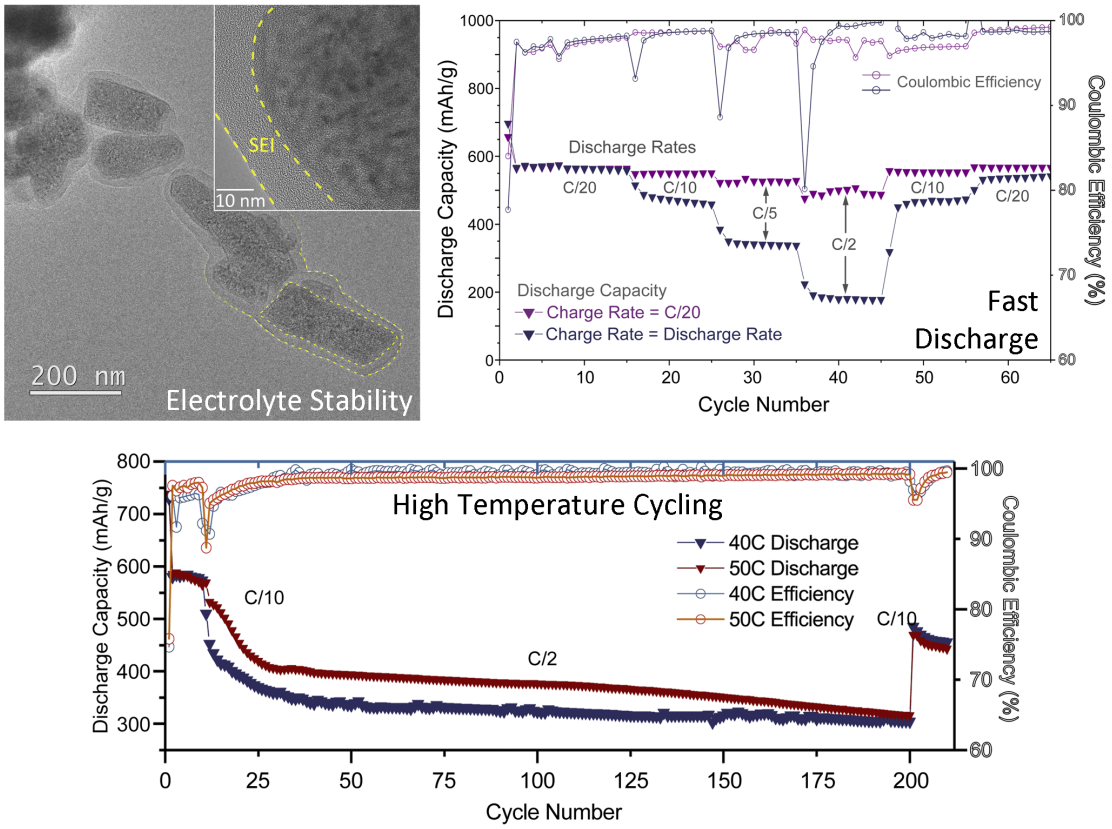


Figure 5.2: Results and Next Steps. The stable SEI forming ability of IL electrolytes, inherently fast discharge rates in transition metal fluorides, and the high temperature stability of this cathode-electrolyte system have all been demonstrated in this work. Future projects will focus on further optimization of electrolyte composition, cycling at higher temperatures, and potential commercialization of transition metal fluoride batteries.

5.3 Future Work

Perhaps the most promising application of the research we have presented is the development of a safe, high temperature, high energy rechargeable battery. As mentioned in **Chapter 3**, the FeF_2 IL electrolyte system exhibits stable cycling for over 200 cycles at temperatures as high as 50 °C. However, the thermally stable cycling at even higher temperatures may be achieved by further tailoring the electrolyte composition. As mentioned

in **Chapter 1**, transition metal fluorides are less prone to thermal decomposition than even the most thermally stable conventional cathode materials. Additionally, ionic liquids have negigible vapor pressures and are practically non-flammable. This electrode-electrolyte system would provide the utmost high temperature safety in addition to the high energy density we have already demonstrated.

The IL electrolyte presented in **Chapter 3** removed the need for large quantities of carbon and enabled the cycling of transition metal fluorides in a more energy dense format. However, to build a battery with a truly competitive specific energy, it is necessary to develop a more scalable synthesis and further increase the loading of active material on the electrodes. Future work will focus on the optimization transition metal fluoride cathodes produced by more scalable methods (e.g. ball milling) and the electrochemical cycling of these cathodes with IL electrolytes.

The development of more scalable synthesis methods would further provide the opportunity to explore higher voltage materials systems. NiF_2 and CuF_2 are interesting from a sheer energy density standpoint; however ternary or quaternary systems containing Fe, Ni, and Cu may enable higher voltages while retaining lower materials cost. Ternary and quaternary transition metal fluorides also exhibit more interesting dicharge/charge mechanisms, and their study would be instrumental in extending the mechanism presented in this work to a more generalized case. I hope that the results presented herein provide a useful reference for future research and engineering as well as an effective methodology for conducting further mechanistic studies.

Bibliography

1. Xiao, A. W. *et al.* cathodes. *Nature Materials* (2020). URL http://dx.doi.org/10.1038/s41563-020-0621-z.

2. Schäfer, A. W. *et al.* Technological, economic and environmental prospects of all-electric aircraft. *Nature Energy* **4**, 160–166 (2019).

3. PNNL. Battery500 Consortium to Spark EV Innovations (2016). URL www.energy.gov/technologytransitions/articles/battery500.

4. Janek, J. & Zeier, W. G. A solid future for battery development. *Nature Energy* **1**, 16141 (2016).

5. Choi, J. W. & Aurbach, D. Promise and reality of post-lithium-ion batteries with high energy densities. *Nature Reviews Materials* **1** (2016).

6. Bruce, P. G., Scrosati, B. & Tarascon, J.-M. Nanomaterials for rechargeable lithium batteries. *Angew. Chem. Int. Ed.* **47**, 2930–2946 (2008).

7. Choi, N. S. *et al.* Challenges facing lithium batteries and electrical double-layer capacitors. *Angewandte Chemie - International Edition* **51**, 9994–10024 (2012). 9809069v1.

8. Dos Santos, M. C., Kesler, O. & Reddy, A. L. M. Nanomaterials for energy conversion and storage. *Journal of Nanomaterials* **2012**, 3127–3171 (2012).

9. Nakajima, T. & Groult, H. (eds.) *Advanced Fluoride-Based Materials for Energy Conversion* (Elsevier Inc., Amsterdam, The Netherlands, 2015), 1 edn.

10. Conte, D. E. & Pinna, N. A review on the application of iron(III) fluorides as positive electrodes for secondary cells. *Materials for Renewable and Sustainable Energy* **3** (2014).

11. Amatucci, G. G. & Pereira, N. Fluoride based electrode materials for advanced energy storage devices. *Journal of Fluorine Chemistry* **128**, 243–262 (2007).

12. Liu, C., Neale, Z. G. & Cao, G. Understanding electrochemical potentials of cathode materials in rechargeable batteries. *Materials Today* **19**, 109–123 (2016).

13. Li, H., Balaya, P. & Maier, J. Li-Storage via Heterogeneous Reaction in Selected Binary Metal Fluorides and Oxides. *Journal of The Electrochemical Society* **151**, A1878 (2004).

14. Li, C., Chen, K., Zhou, X. & Maier, J. Electrochemically driven conversion reaction in fluoride electrodes for energy storage devices. *npj Computational Materials* **4** (2018).

15. Badway, F., Cosandey, F., Pereira, N. & Amatucci, G. G. Carbon Metal Fluoride Nanocomposites. *Journal of The Electrochemical Society* **150**, A1318 (2003).

16. Zhang, N., Xiao, X. & Pang, H. Transition metal (Fe, Co, Ni) fluoride-based materials for electrochemical energy storage. *Nanoscale Horizons* **4**, 99–116 (2019).

17. Haynes, W. M., Lide, D. R. & Bruno, T. J. (eds.) *CRC Handbook of Chemistry and Physics* (CRC Press, Boca Raton, FL, 2017), 97 edn.

18. Jain, A. *et al.* The Materials Project: A materials genome approach to accelerating materials innovation. *APL Materials* **1**, 11002 (2013).

19. Ma, Y. & Garofalini, S. H. Atomistic insights into the conversion reaction in iron fluoride: A dynamically adaptive force field approach. *Journal of the American Chemical Society* **134**, 8205–8211 (2012).

20. Ma, Y. & Garofalini, S. H. Interplay between the ionic and electronic transport and its effects on the reaction pattern during the electrochemical conversion in an FeF2 nanoparticle. *Physical Chemistry Chemical Physics* **16**, 11690–11697 (2014).

21. Wang, F. *et al.* Ionic and electronic transport in metal fluoride conversion electrodes Feng. *ECS Transactions* **50**, 19–25 (2012).

22. Ko, J. K. *et al.* Transport, phase reactions, and hysteresis of iron fluoride and oxyfluoride conversion electrode materials for lithium batteries. *ACS Applied Materials and Interfaces* **6**, 10858–10869 (2014).

23. Karki, K. *et al.* Revisiting Conversion Reaction Mechanisms in Lithium Batteries: Lithiation-Driven Topotactic Transformation in FeF 2. *Journal of the American Chemical Society* **140**, 17915–17922 (2018).

24. Wang, F. *et al.* Tracking lithium transport and electrochemical reactions in nanoparticles. *Nature Communications* **3**, 1201–1208 (2012).

25. Huang, Q. *et al.* Insights into the Effects of Electrolyte Composition on the Performance and Stability of FeF 2 Conversion-Type Cathodes. *Advanced Energy Materials* **9**, 1–11 (2019).

26. Wang, X. *et al.* Carbon Nanotube-CoF2 Multifunctional Cathode for Lithium Ion Batteries: Effect of Electrolyte on Cycle Stability. *Small* **11**, 5164–5173 (2015).

27. Miessler, G. L., Fischer, P. J. & Tarr, D. A. *Inorganic Chemistry* (Pearson Education, Inc., Boston, MA, USA, 2014), fifth edn.

28. Song, H., Cui, H. & Wang, C. Extremely high-rate capacity and stable cycling of a highly ordered nanostructured carbonâĂŞFeF2 battery cathode. *J. Mater. Chem. A* **3**, 22377–22384 (2015).

29. Li, C., Yin, C., Mu, X. & Maier, J. Top-down synthesis of open framework fluoride for lithium and sodium batteries. *Chemistry of Materials* **25**, 962–969 (2013).

30. Gocheva, I. D. *et al.* Mechanochemical synthesis of NaMF3 (M = Fe, Mn, Ni) and their electrochemical properties as positive electrode materials for sodium batteries. *Journal of Power Sources* **187**, 247–252 (2009).

31. Baaz, P. Mechanochemistry in Nanoscience and Minerals Engineering. In *Mechanochemistry in Nanoscience and Minerals Engineerin*, chap. High-Energ, 123–129 (Springer-Verlag Berlin Heidelberg 2008, 2008). 9809069v1.

32. Wang, F. *et al.* Conversion Reaction Mechanisms in Lithium Ion Batteries: Study of the Binary Metal Fluoride Electrodes Conversion Reaction Mechanisms in Lithium Ion Batteries : Study of the Binary Metal Fluoride Electrodes. *J. Am. Chem.Soc* **133**, 18828–18836 (2011).

33. Badway, F. *et al.* Structure and electrochemistry of copper fluoride nanocomposites utilizing mixed conducting matrices. *Chemistry of Materials* **19**, 4129–4141 (2007).

34. Tan, H. J. *et al.* Electrochemical Cycling and Lithium Insertion in Nanostructured FeF3 Cathodes. *Journal of The Electrochemical Society* **161**, A445–A449 (2014).

35. Nishijima, M. *et al.* Cathode properties of metal trifluorides in Li and Na secondary batteries. *Journal of Power Sources* **190**, 558–562 (2009).

36. Wang, F. *et al.* Ternary metal fluorides as high-energy cathodes with low cycling hysteresis. *Nature Communications* **6**, 6668 (2015). arXiv:1507.02142v2.

37. Fan, X. *et al.* Pomegranate-Structured Conversion-Reaction Cathode with a Built-in Li Source for High-Energy Li-Ion Batteries. *ACS Nano* **10**, 5567–5577 (2016).

38. Dimov, N. *et al.* Transition metal NaMF3 compounds as model systems for studying the feasibility of ternary Li-M-F and Na-M-F single phases as cathodes for lithium-ion and sodium-ion batteries. *Electrochimica Acta* **110**, 214–220 (2013).

39. Gordon, D. *et al.* Mixed Metal Difluorides as High Capacity Conversion-Type Cathodes: Impact of Composition on Stability and Performance. *Advanced Energy Materials* **8**, 1–10 (2018).

40. Gu, W., Magasinski, A., Zdyrko, B. & Yushin, G. Metal fluorides nanoconfined in carbon nanopores as reversible high capacity cathodes for Li and Li-Ion rechargeable batteries: FeF2 as an example. *Advanced Energy Materials* **5**, 1–7 (2015).

41. Guntlin, C. P., Tanja, Z. & Kravchyk, K. V. Nanocrystalline FeF3 and MF2 (M 1âĄĎ4 Fe, Co, and Mn) from metal trifluoroacetates and their Li(Na)-ion storage properties. *Journal of Materials Chemistry A* **5**, 7383–7393 (2017).

42. Pereira, N., Badway, F., Wartelsky, M., Gunn, S. & Amatucci, G. G. Iron Oxyfluorides as High Capacity Cathode Materials for Lithium Batteries. *Journal of The Electrochemical Society* **156**, A407 (2009).

43. Chun, J. *et al.* Ammonium Fluoride Mediated Synthesis of Anhydrous Metal Fluoride-Mesoporous Carbon Nanocomposites for High-Performance Lithium Ion Battery Cathodes. *ACS Applied Materials and Interfaces* **8**, 35180–35190 (2016).

44. Rui, K., Wen, Z., Lu, Y., Jin, J. & Shen, C. One-Step solvothermal synthesis of nanostructured manganese fluoride as an anode for rechargeable lithium-ion batteries and insights into the conversion mechanism. *Advanced Energy Materials* **5**, 1–11 (2015).

45. Lu, Y., Wen, Z.-y., Jin, J., Wu, X.-w. & Rui, K. Size-controlled synthesis of hierarchical nanoporous iron based fluorides and their high performances in rechargeable lithium ion batteries. *Chemical Communications* **50**, 6487 (2014).

46. Yamada, Y., Doi, T., Tanaka, I., Okada, S. & Yamaki, J. I. Liquid-phase synthesis of highly dispersed NaFeF3 particles and their electrochemical properties for sodium-ion batteries. *Journal of Power Sources* **196**, 4837–4841 (2011).

47. Li, C., Gu, L., Tsukimoto, S., Van Aken, P. A. & Maier, J. Low-temperature ionic-liquid-based synthesis of nanostructured iron-based fluoride cathodes for lithium batteries. *Advanced Materials* **22**, 3650–3654 (2010).

48. Schütte, K. *et al.* Synthesis of Metal Nanoparticles and Metal Fluoride Nanoparticles from Metal Amidinate Precursors in 1-Butyl-3-Methylimidazolium Ionic Liquids and Propylene Carbonate. *ChemistryOpen* **6**, 137–148 (2017).

49. Li, L., Meng, F. & Jin, S. High-capacity lithium-ion battery conversion cathodes based on iron fluoride nanowires and insights into the conversion mechanism. *Nano Letters* **12**, 6030–6037 (2012). `arXiv:1011.1669v3`.

50. Zhao, X., Hayner, C. M., Kung, M. C. & Kung, H. H. Photothermal-assisted fabrication of iron fluorideâĂŞgraphene composite paper cathodes for high-energy lithium-ion batteries. *Chemical Communications* **48**, 9909 (2012).

51. Zhou, J., Zhang, D., Zhang, X., Song, H. & Chen, X. Carbon-nanotube-encapsulated FeF2 nanorods for high-performance lithium-ion cathode materials. *ACS Applied Materials and Interfaces* **6**, 21223–21229 (2014).

52. Jia, L. P., Yan, B. & Zhang, Q. Barium rare earth fluoride nanocrystals: High temperature solution synthesis, characterization and luminescence. *Journal of Nanoparticle Research* **15** (2013).

53. Chun, J., Jo, C., Lim, E., Roh, K. C. & Lee, J. Solvothermal synthesis of sodium cobalt fluoride (NaCoF 3) nanoparticle clusters. *Materials Letters* **207**, 89–92 (2017).

54. Huang, Q. *et al.* Cycle stability of conversion-type iron fluoride lithium battery cathode at elevated temperatures in polymer electrolyte composites. *Nature Materials* (2019).

55. Jacob, D. S. *et al.* Are ionic liquids really a boon for the synthesis of inorganic materials? A general method for the fabrication of nanosized metal fluorides. *Chemistry of Materials* **18**, 3162–3168 (2006).

56. Maton, C., De Vos, N. & Stevens, C. V. Ionic liquid thermal stabilities: Decomposition mechanisms and analysis tools. *Chemical Society Reviews* **42**, 5963–5977 (2013).

57. Rüssel, C. A pyrolytic route to fluoride glasses. I. Preparation and thermal decomposition of metal trifluoroacetates. *Journal of Non-Crystalline Solids* **152**, 161–166 (1993).

58. Blake, B. P. G. & Pritchard, H. The Thermal Decomposition of Trif luoroacetic Acid. *Journal of Chemical Society B* **1**, 282–286 (1967).

59. Francisco, J. S. Decomposition Pathways for Trifluoroacetic Acid, CF,C(O)OH. *Journal of the Chemical Society, Faraday Transactions* **88**, 3521–3525 (1992).

60. Li, T., Li, L., Cao, Y. L., Ai, X. P. & Yang, H. X. Reversible three-electron redox behaviors of FeF3 nanocrystals as high-capacity cathode-active materials for Li-Ion batteries. *Journal of Physical Chemistry C* **114**, 3190–3195 (2010).

61. Wang, H. & Dai, H. Strongly coupled inorganic-nano-carbon hybrid materials for energy storage. *Chem. Soc. Rev.* DOI:10.1039/c2cs35307e (2012).

62. Gu, W., Magasinski, A., Zdyrko, B. & Yushin, G. Metal fluorides nanoconfined in carbon nanopores as reversible high capacity cathodes for Li and Li-Ion rechargeable batteries: FeF2 as an example. *Advanced Energy Materials* **5**, 1–7 (2015).

63. Li, H., Richter, G. & Maier, J. Reversible formation and decomposition of LiF clusters using transition metal fluorides as precursors and their application in rechargeable Li batteries. *Advanced Materials* **15**, 736–739 (2003).

64. Zhou, M., Zhao, L., Doi, T., Okada, S. & ichi Yamaki, J. Thermal stability of FeF3 cathode for Li-ion batteries. *Journal of Power Sources* **195**, 4952–4956 (2010).

65. Zhou, M., Zhao, L., Okada, S. & Yamaki, J. I. Thermal characteristics of a FeF3 cathode via conversion reaction in comparison with LiFePO4. *Journal of Power Sources* **196**, 8110–8115 (2011).

66. Teng, Y. T., Wei, F. & Yazami, R. Synthesis of NixCo(1-x)F2 (x = 0, 0.25, 0.50, 0.75, 1.0) and application in lithium ion batteries. *Journal of Alloys and Compounds* **653**, 434–443 (2015).

67. Deng, D. Transition metal oxyfluorides for next-generation rechargeable batteries. *ChemNanoMat* **3**, 146–159 (2017).

68. Kim, S. W. *et al.* Structure Stabilization by Mixed Anions in Oxyfluoride Cathodes for High-Energy Lithium Batteries. *ACS Nano* **9**, 10076–10084 (2015).

69. Stout, J. W. & Reed, S. A. The Crystal Structure of MnF2, FeF2, CoF2, NiF2 and ZnF2. *Journal of the American Chemical Society* **76**, 5279–5281 (1954).

70. Li, L. *et al.* Origins of Large Voltage Hysteresis in High-Energy-Density Metal Fluoride Lithium-Ion Battery Conversion Electrodes. *Journal of the American Chemical Society* **138**, 2838–2848 (2016).

71. Yamakawa, N., Jiang, M., Key, B. & Grey, C. P. Identifying the local structures formed during lithiation of the conversion material, iron fluoride, in a Li ion battery: A solid-state NMR, X-ray diffraction, and pair distribution function analysis study. *Journal of the American Chemical Society* **131**, 10525–10536 (2009).

72. Xie, Z.-h., Jiang, Z. & Zhang, X. Review âĂŤ Promises and Challenges of In Situ Transmission Electron Microscopy Electrochemical Techniques in the Studies of. *Journal of The Electrochemical Society* **164**, 2110–2123 (2017).

73. Wang, C.-m. In situ transmission electron microscopy and spectroscopy studies of rechargeable batteries under dynamic operating conditions : A retrospective and perspective view. *Journal of Materials Research* **30**, 326–339 (2014).

74. Doe, R. E., Meng, Y. S., Ceder, G. & Persson, K. A. First-Principles Investigation of the Li-Fe-F Phase Diagram and\rEquilibrium and Nonequilibrium Conversion Reactions of Iron\rFluorides with Lithium. *Chemistry of Materials* **20**, 5274–5283 (2008).

75. Cosandey, F., Al-Sharab, J. F., Badway, F., Amatucci, G. G. & Stadelmann, P. EELS Spectroscopy of Iron Fluorides and FeFx/C Nanocomposite Electrodes Used in Li-Ion Batteries. *Microscopy and Microanalysis* **13**, 87–95 (2007).

76. Sina, M. *et al.* Investigation of SEI layer formation in conversion iron fluoride cathodes by combined STEM/EELS and XPS. *Journal of Physical Chemistry C* **119**, 9762–9773 (2015).

77. Murray, C. B., Kagan, C. R. & Bawendi, M. G. Synthesis and Characterization of Monodisperse Nanocrystals And Close-Packed Nanocrystal Assemblies. *International Journal of Advances in Engineering & Technology* **2**, 668–676 (2012).

78. Cargnello, M., Doan-Nguyen, V. & Murray, C. Engineering Uniform Nanocrystals: Mechanism of Formation and Self-Assembly into Bimetallic Nanocrystal Superlattices. *American Institute of Chemical Engineers* **62**, 392–398 (2016).

79. Mai, H.-x. *et al.* High-Quality Sodium Rare-Earth Fluoride Nanocrystals : Controlled Synthesis and Optical Properties High-Quality Sodium Rare-Earth Fluoride Nanocrystals : Controlled Synthesis and Optical Properties. *Journal of the American Chemical Society* **128**, 6426–6436 (2006).

80. Park, J. *et al.* Monodisperse Nanoparticles of Ni and NiO : Synthesis , Characterization , Self-Assembled Superlattices , and Catalytic Applications in the Suzuki Coupling Reaction **. *Advanced Materials* **17**, 429–434 (2005).

81. Porter, D. A., Easterling, K. E. & Sherif, M. Y. *Phase Transformations in Metals and Alloys, Third Edition* (Taylor & Francis Group, Boca Raton, FL, 2009), 3 edn.

82. Murray, C. B. *et al.* Colloidal synthesis of nanocrystals and nanocrystal superlattices. *IBM Journal of Research and Development* **45**, 47–56 (2001).

83. Zhang, Y.-w., Sun, X., Si, R., You, L.-p. & Yan, C.-h. Single-Crystalline and Monodisperse LaF 3 Triangular Nanoplates from a Single- Source Precursor. *Mercury* **34**, 5–7 (2005).

84. Boyer, J.-C., Cuccia, L. A. & Capobianco, J. A. Synthesis of Colloidal Upconverting NaYF4: Er3+ /Yb3+ and Tm3+ /Yb3+ Monodisperse Nanocrystals. *Nano letters* **7**, 847–852 (2007).

85. Mourdikoudis, S. & Liz-Marzán, L. M. Oleylamine in nanoparticle synthesis. *Chemistry of Materials* **25**, 1465–1476 (2013).

86. Wade Jr, L. *Organic Chemistry ®*. 7 (Pearson Education, Inc., Boston, MA, USA, 2013), eighth edn. 0605511.

87. Baur, W. H. & Khan, A. A. Rutile-type compounds. IV. SiO2, GeO2 and a comparison with other rutile-type structures. *Acta Crystallographica Section B Structural Crystallography and Crystal Chemistry* **27**, 2133–2139 (1971).

88. Gordon, T. R. *et al.* Nonaqueous synthesis of TiO 2 nanocrystals using TiF 4 to engineer morphology, oxygen vacancy concentration, and photocatalytic activity. *Journal of the American Chemical Society* **134**, 6751–6761 (2012).

89. Roth, H. G., Romero, N. A. & Nicewicz, D. A. Experimental and Calculated Electrochemical Potentials of Common Organic Molecules for Applications to Single-Electron Redox Chemistry. *Synlett* **27**, 714–723 (2016).

90. Mendes, R. G. *et al.* A facile route to coat iron oxide nanoparticles with few-layer graphene. *Journal of Physical Chemistry C* **116**, 23749–23756 (2012).

91. Jiao, Y. *et al.* Fabrication of three-dimensionally interconnected nanoparticle superlattices and their lithium-ion storage properties. *Nature Communications* **6**, 6420 (2015).

92. Dong, A. *et al.* A generalized ligand-exchange strategy enabling sequential surface functionalization of colloidal nanocrystals. *Journal of the American Chemical Society* **133**, 998–1006 (2011).

93. Piché, D. *et al.* Targeted T 1 Magnetic Resonance Imaging Contrast Enhancement with Extraordinarily Small CoFe 2 O 4 Nanoparticles. *ACS Applied Materials and Interfaces* **11**, 6724–6740 (2019).

94. Elgrishi, N. *et al.* A Practical Beginner's Guide to Cyclic Voltammetry. *Journal of Chemical Education* **95**, 197–206 (2018).

95. Newman, J. & Thomas-Alyea, K. E. *Electrochemical Systems* (John Wiley & Sons, Inc., Hoboken, New Jersey, 2004), 3 edn.

96. Krossing, I. *et al.* Why are ionic liquids liquid? A simple explanation based on lattice and solvation energies. *Journal of the American Chemical Society* **128**, 13427–13434 (2006).

97. DeVos, N., Maton, C. & Stevens, C. V. Electrochemical Stability of Ionic Liquids: General Influences and Degradation Mechanisms. *ChemElectroChem* **1**, 1258–1270 (2014).

98. Rakov, D. A. *et al.* Engineering high-energy-density sodium battery anodes for improved cycling with superconcentrated ionic-liquid electrolytes. *Nature Materials* 4–10 (2020).

99. Moreno, M. *et al.* Ionic liquid electrolytes for safer lithium batteries I. investigation around optimal formulation. *Journal of the Electrochemical Society* **164**, A6026–A6031 (2017).

100. Francis, C., Louey, R., Sammut, K. & Best, A. S. Thermal stability of pyrrolidinium-FSI ionic liquid electrolyte and lithium-ion electrodes at elevated temperatures. *Journal of the Electrochemical Society* **165**, A1204–A1221 (2018).

101. Xiao, A. W. *et al.* Electrophoretic Fabrication of Robust Carbon Nanotube âĂIJBuckypapersâĂİ for Flexible Electronics. *ACS Applied Nano Materials* **2**, 5190–5199 (2019).

102. Zhang, L., Zhang, G., Liu, C. & Fan, S. High-Density Carbon Nanotube Buckypapers with Superior Transport and Mechanical Properties. *Nano letters* 4848–4852 (2012).

103. Gauthier, M. *et al.* Electrode-Electrolyte Interface in Li-Ion Batteries: Current Understanding and New Insights. *Journal of Physical Chemistry Letters* **6**, 4653–4672 (2015).

104. Wang, A., Kadam, S., Li, H., Shi, S. & Qi, Y. Review on modeling of the anode solid electrolyte interphase (SEI) for lithium-ion batteries. *npj Computational Materials* **4** (2018).

105. Guitián, B., Nóvoa, X. & Pintos, A. EIS as a Tool to Characterize Nanostructured Iron Fluoride Conversion Layers for Li-Ion Batteries. *Bulgarian Chemical Communications* **50**, 82–89 (2018).

106. Canongia Lopes, J. N., Costa Gomes, M. F. & Pádua, A. A. Nonpolar, polar, and associating solutes in ionic liquids. *Journal of Physical Chemistry B* **110**, 16816–16818 (2006).

107. Periyapperuma, K. *et al.* Towards high rate Li metal anodes: Enhanced performance at high current density in a superconcentrated ionic liquid. *Journal of Materials Chemistry A* **8**, 3574–3579 (2020).

108. Clark, D. T. & Brennan, W. J. AN ESCA INVESTIGATION OF LOW ENERGY ELECTRON BEAM INTERACTIONS WITH POLYMERS. II. PVDF AND A MECHANISTIC COMPARISON BETWEEN PTFE AND PVDF. *Journal of Electron Spectroscopy and Related Phenomena* **47**, 93–104 (1988).

109. Blume, R. *et al.* Characterizing Graphitic Carbon with X-ray Photoelectron Spectroscopy: A Step-by-Step Approach. *ChemCatChem* **7**, 2871–2881 (2015).

110. Tasaki, K. *et al.* Solubility of Lithium Salts Formed on the Lithium-Ion Battery Negative Electrode Surface in Organic Solvents. *Journal of The Electrochemical Society* **156**, A1019 (2009).

111. Tasaki, K. & Harris, S. J. Computational Study on the Solubility of Lithium Salts Formed on Lithium Ion Battery Negative Electrode in Organic Solvents Ken. *Journal of Physical Chemistry C* **114**, 8076–8083 (2010).

112. Graetz, J., Ahn, C. C., Ouyang, H., Rez, P. & Fultz, B. White lines and d-band occupancy for the 3d transition-metal oxides and lithium transition-metal oxides. *Physical Review B - Condensed Matter and Materials Physics* **69**, 1–6 (2004).

113. Cosandey, F., Al-Sharab, J. F., Badway, F., Amatucci, G. G. & Stadelmann, P. EELS spectroscopy of iron fluorides and FeFx/C nanocomposite electrodes used in Li-ion batteries. *Microscopy and Microanalysis* **13**, 87–95 (2007).

114. Dahmen, U. Orientation Relationships in Precipitation Systems. *Acta Metallurgica* **30**, 63–73 (1981).

115. Mitchell, D. R. G. DiffTools: Electron diffraction software tools for DigitalMicrographâĎć. *Microscopy Research and Technique* **71**, 588–593 (2008).

Appendix I: Methods

Colloidal Synthesis of FeF_2 Nanorods.

Trifluoroacetic acid (99%), trifluoroacetic anhydride (99%+), 1-octadecene (ODE, technical grade, 90%), and ethanol (absolute) were purchased from Fisher Scientific. Iron(II) chloride (98%), oleic acid (OLAC, technical grade, 90%), oleylamine (OLAM, technical grade, 90%), n-hexane (anhydrous, 95%), and chloroform (anhydrous, ≥ 99%) were purchased from Sigma-Aldrich. Ethanol was dried over calcium sulfate, filtered and stored over molecular sieves before use. All other chemicals were used as received.

Iron(II) trifluoroacetate, $Fe(CF_3COO^-)_2(CF_3COOH)_2$, was employed as the single source Fe, F precursor in the colloidal synthesis of FeF_2 nanorods. Iron(II) trifluoroacetate was prepared using a method modified from that developed by Guntlin *et al.*[41] Briefly, 3.5 g of iron(II) chloride and 40 ml of trifluoroacetic acid were loaded into a 50 ml Erlenmeyer flask, attached to a Schlenk line via a water-cooled condenser and heated to reflux on a hotplate under nitrogen flow with magnetic stirring for 24 h. Excess trifluoroacetic acid was evaporated under vacuum until a slushy, light brown mixture was obtained; the mixture was then washed three times with 10 ml portions of 5% trifluoroacetic anhydride in anhydrous hexane (v/v) followed by centrifugation. The resultant off-white, crystalline powder was dried under vacuum and transferred to an argon-filled glovebox.

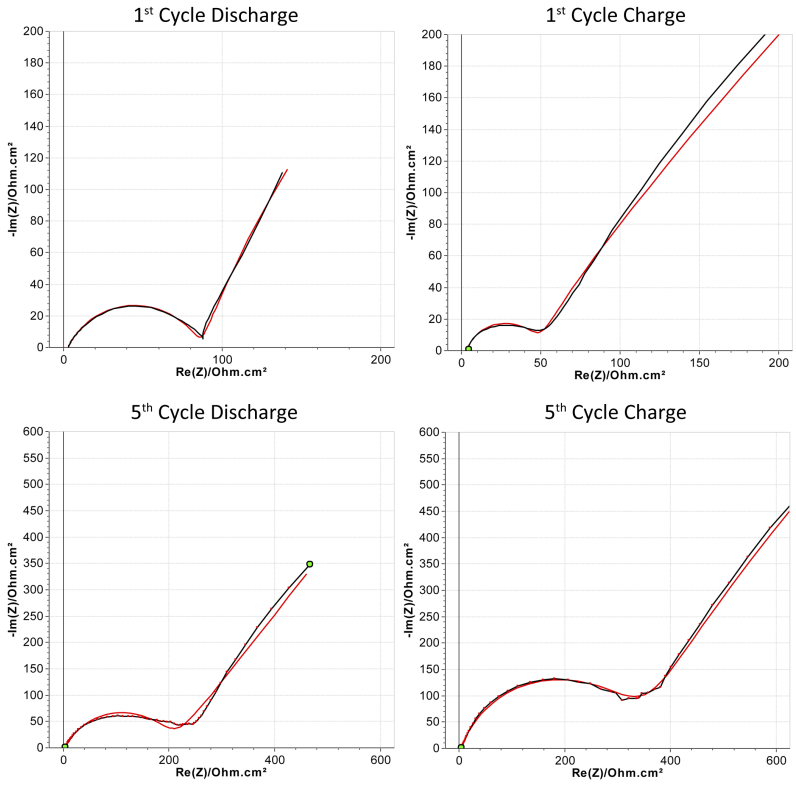
In a typical FeF_2 nanorod synthesis, 1530 mg of the iron(II) trifluoroacetate (3 mmol) was transferred under argon to a 250 ml three-neck, round-bottom flask attached to a Schlenk line. To minimize air exposure, a continuous nitrogen purge was applied as 16 ml of oleic acid, 16 ml of oleylamine, and 28 ml of 1-octadecene were loaded into the flask along with a magnetic stir bar, resulting in a dark red solution. The flask was equipped with an immersion type thermocouple and a PID-controlled heating mantle and sealed

with a ground-glass stopper. The reaction mixture was flushed under vacuum for (5 min) and purged under nitrogen (1 min) three times at room temperature and subsequently degassed under vacuum at 100 °C for 15 min. The flask was then heated to 310 °C (~14 °C min^{-1}) resulting in a color change from dark red to clear yellow and allowed to react for 2 h. The reaction mixture was slowly cooled to room temperature, transferred to a centrifuge tube and washed 3 times by dispersion in anhydrous hexane followed by precipitation with dried ethanol and centrifugation. The washed pellet (260 mg) was redispersed and stored in anhydrous hexane resulting in a pale yellow dispersion.

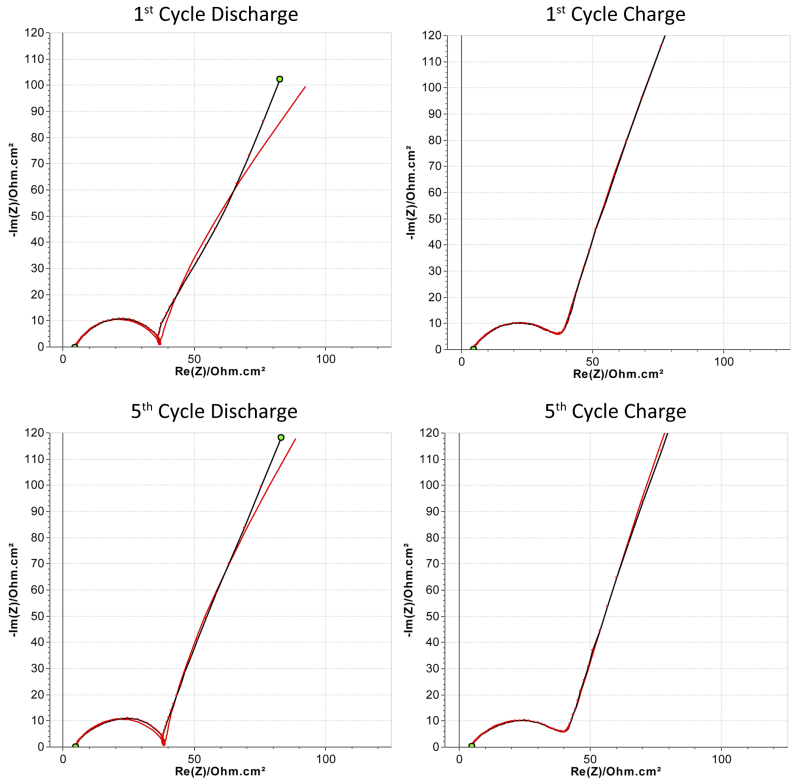
Electrochemical Characterization.

FeF_2 nanorod electrodes were fabricated using a conventional tape casting method. The as-synthesized FeF_2 nanorods were co-dispersed with a suspension of Super-P carbon black in anhydrous chloroform, dried under vacuum and hand ground with additional Super-P before mixing with polyvinylidene fluoride (PVDF) and N-methyl pyrrolidone (NMP). The resulting slurry (7:2:1 FeF_2:Super-P:PVDF by mass) was cast via doctor blade on aluminum foil, allowed to dry and placed under vacuum for 24 h before being punched into circular electrodes (diameter 1 cm). All electrodes tested contained between 1.0-1.3 mg cm^{-2}, corresponding to an areal capacity of 0.57-0.74 mA h cm^{-2} at a current density of 28.6-37.1 µA cm^{-2}.

Galvanostatic cycling tests were conducted at 30 °C between 4.0 and 1.2 V in a 2032 coin cell format using a Biologic BCS-805 battery cycler. Electrochemical impedance spectroscopy was performed in conjunction with galvanostatic cycling using 3-electrode Swagelok type cell and a Biologic VMP3 potentiostat. Impedance spectra in the frequency range 50 mHz–200 kHz were acquired with a frequency distribution of 10 points per decade, with measurements averaged over 5 scans per frequency, using a 10 mV amplitude single sine wave excitation. Each impedance spectra was collected following a 1 h rest period after each discharge/charge half cycle (C/20 rate) to allow cells to return to the equilibrium open-circuit potential. EIS spectra were analyzed using the ZFit tool in the Biologic EC-Lab software; fittings were produced based on the modified Randles circuit shown in Figure 3.11. A constant phase element is introduced in parallel with the semi-infinite Warburg element to account for inhibited diffusion within the metal fluorides.



(a) Impedance spectra in LP30 electrolyte.



(b) Impedance spectra in IL electrolyte.

Figure 5.3: Fitting of IL Impedance Data. Electrochemical impedance spectra of the FeF_2 nanorod electrodes in the LP30 electrolyte (a) and IL electrolyte (b) fitted using the equivalent Randles circuit shown in Figure 3.11. Experimental data is shown in black with the fitted spectrum shown in red.

All cells were assembled in an argon-filled glovebox using glass fiber separators (Whatman, GF/D) and metallic lithium foil (Sigma, 99.9%) as the counter/reference electrodes. The 1 molal IL electrolyte was prepared from LiFSI (TCI, >98%) and dried $Pyr_{1,3}FSI$ (Solvionic, 99.5%) in a glovebox. 1.0 M LP30 was purchased from Sigma-Aldrich.

Powder XRD and Refinement

Higher resolution powder XRD patterns were collected for the as-synthesized FeF_2 nanorod samples. Powder samples were prepared by drying the as-synthesized FeF_2 nanorod dispersion at 70 °C under vacuum for 24 h, followed by grinding in a mortar and pestle. The FeF_2 nanorod powder was then sealed under argon in a borosilicate glass capillary (1.0 mm outer diameter) and measured using a Rigaku Smartlab XRD with a 3 kW monochromated Cukα X-ray source and 0.0002° scan resolution. Scans were collected between 5° to 90°, 2θ, at a scan rate of 0.7 °min^{-1} and a step size of 0.01°. The resultant XRD patterns were refined according to the Rietveld method using the GSAS-II program. An initial refinement was performed for the scale factor and lattice parameters based on the rutile ($P4_{/2}mnm$) space group. The structure was further refined with the atomic coordinates of Fe fixed to the unit cell vertex (0,0,0), while the F position was refined. Atomic displacement factors (U_{iso}) for both Fe and F were also refined. The quality of the refinement was good (R_p = 1.42%, R_{wp} = 2.05%, R_{exp} = 1.27%, and χ^2 = 2.59), indicating that the assumption of a tetragonal space group ($P_{4/2}mnm$) was in good aggreement with the experimental data.

Ex-situ XRD and XPS.

Ex-situ samples from various states of discharge and charge were prepared by setting appropriate cutoff values for either voltage or charge during a galvanostatic cycling test at a C/20 rate. After a 2 h post-cycling rest, coin cells were transferred to an argon-filled glovebox and opened using a hydraulic disassembling press. The working electrodes were removed, patted dry and stored in dimethyl carbonate (DMC). For XRD measurements, electrodes were transferred in sealed vials to a Rigaku Miniflex XRD housed in a nitrogen-filled glovebox. XRD patterns were collected using a monochromated Cu Kα X-ray source from 10° to 60°, 2θ, at a scan rate of 1 °min^{-1} and a step size of 0.05°. Contributions

from the Al current collector were fitted using experimental data from pristine Al foil and subtracted. After measurement, the electrodes were returned to an Ar-filled glovebox and stored under DMC in preparation for ex-situ TEM measurements.

For XPS measurements, electrodes were soaked in DMC for 48 h and subsequently rinsed twice in fresh DMC to ensure removal of residual electrolyte. Electrodes were then transferred to a Schlenk tube under argon and dried under vacuum overnight. The electrodes were sealed under argon during transport and were only exposed to air for <1 min during transfer to the XPS high-vacuum chamber. XPS spectra were collected using a Thermo Scientific K-Alpha XPS with a monochromated Al K-α X-ray source. Data quantification was performed using Casa XPS software. All energy-loss regions in both survey and high-resolution spectra were fitted using Shirley-type backgrounds. A self-consistent peak model (Supplementary Figure 11) was developed for the pristine (uncycled) electrode and propagated to all other spectra with appropriate regions and components added to account for compounds introduced by the electrolyte. All spectra were charge referenced to the disordered C1s component at a binding energy of 284.8 eV.

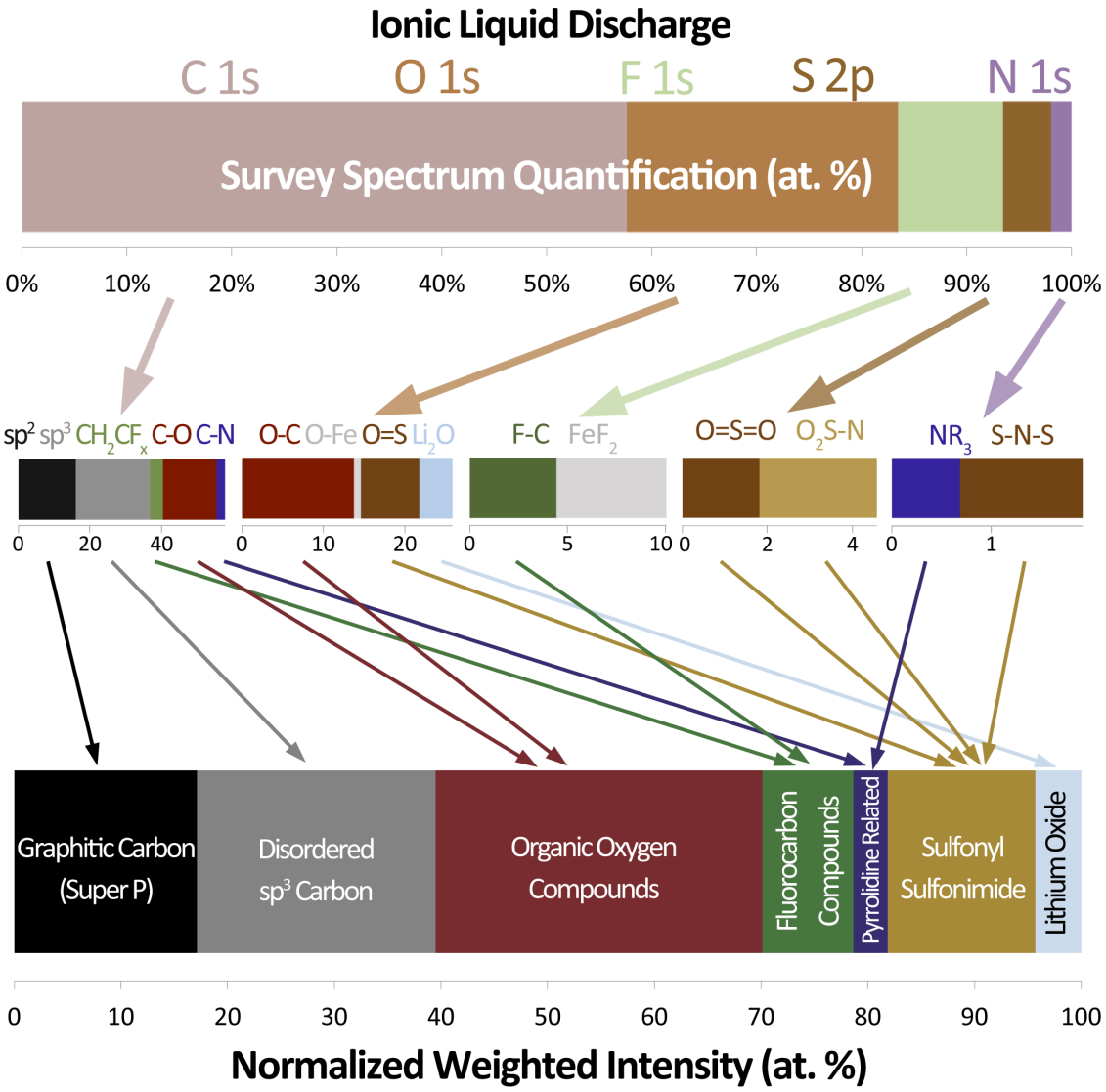


Figure 5.4: Quantification of XPS Data. Diagram describing the quantification of XPS data using the electrode discharged in IL electrolyte as an example. An elemental composition (at.%) is obtained from the survey spectra. The atomic % of each element is subdivided into is different components based on the deconvoluted high-resolution spectra. The relative proportions of different elements belonging to the same group of compounds (i.e. oxidized carbon and oxygen bound to carbon) are combined to give the proportion of different compounds at the electrode surface (at.%).

Ex-Situ TEM/EDX/STEM/EELS.

Following XRD measurements, the cycled electrodes were loaded into a glass vial with anhydrous NMP and a magnetic stir bar and gently stirred for 24 h under argon to remove and redisperse the electrode material. The dispersion was subsequently centrifuged at 14000 rpm for 10 min and the supernatant discarded. The resulting pellet was redispersed in fresh NMP, and drop cast on holey carbon TEM grids (Agar) in a glovebox on an 80 °C hot plate. Alternatively, to preserve the SEI, the electrodes in NMP were placed in an ultrasonic bath for 20 min and the resulting dispersion was immediately drop-cast onto TEM grids. All TEM samples were placed in a Schlenk tube under argon, dried under vacuum at 80 °C overnight, and transported to the TEM in airtight vials under argon. Air exposure was limited to <30 s during transfer to the TEM column.

Bright field TEM/HRTEM imaging was performed on a JEOL 3000F field emission gun transmission electron microscope operated at 300 kV and equipped with a Gatan Ultrascan CCD camera. EDX measurements were acquired in STEM mode with a 1 nm probe size using an Oxford instruments X-Max detector. EDX maps were generated without background subtraction and used only for qualitative analysis of elemental distribution. A high peak to background ratio was observed throughout the measurement. However, quantitative determination of the elemental composition was hindered by low energy of F Kα X-rays and their overlap with Fe Lα and other spurious X-rays. Lattice reflections in the FFTs were measured based on their Gaussian centers of gravity and indexed by comparison with diffraction patterns computed from standard CIF files, using SingleCrystal software. FFTs were colored by changing the RGB values of only the white pixels in the original FFT using the “Selective Color” function in Adobe Photoshop to preserve the original appearance and relative intensity of diffraction spots.

STEM/EELS measurements were conducted using a JEOL ARM 200F atomic resolution analytical microscope equipped with a Gatan GIF Quantum EELS detector. EELS spectra between 650 eV to 750 eV were collected at 200 kV with a 1 nm probe size and a dwell time of 0.5 s. Line scans were collected with a step size of 1.5 nm to minimize the accumulation of beam damage while maintaining acceptable spatial resolution. Spectra were calibrated to the zero-loss peak acquired simultaneously in dual-EELS mode. The backgrounds were subtracted using a power law model. However, to accurately calculate

the L_3/L_2 ratios, the contributions of both the F K-edge and the continuum absorption of the Fe L-edge must accounted for and subtracted from the Fe $L_{2,3}$ region. This was done following the method proposed by Cosandey *et al.* whereby the continuum Fe L-edge removed using a calculated Hartree-Slater cross-section fit to the high-energy side of the white lines.[113] The F contribution was then approximated by a standard LiF K-edge spectra that was scaled to fit the overt F K-peak at ~694 eV. After subtracting both of these contributions, the Fe L_3/L_2 white line intensities were integrated using a 4 eV window centered on the white line maxima. All image processing and EELS analysis was done using Gatan Microscopy Suite 3 software with plugins with the aid of additional scripts written by D. R. G. Mitchell.[115]

In-Situ TEM.

In-situ lithiation experiments were performed using a Nanofactory Instruments Dual-Probe STM-TEM biasing sample holder within an FEI Tecnai G2 F20 X-Twin TEM at an accelerating voltage of 200 kV. The as-synthesized nanorods were dried, redispersed in acetonitrile and loaded onto a Cu wire probe via a simple dipping process. The Li metal counter electrode was prepared by attaching Li metal to a W wire and exposing it to air for ~5 s to generate a thin surface layer of Li_2O, functioning as a solid electrolyte. A relative bias of -1.5 V was applied between the two electrodes to drive migration of Li^+ ions through the solid electrolyte. Video files were recorded through the live-view window in Gatan Digital Micrograph Software.